TECHNISCHE UNIVERSITÄT MÜNCHEN
TUM School of Engineering and Design

Influence of Material Property Changes on Thermoset Automated Fiber Placement Processing

Klaus Heller

Vollständiger Abdruck der von der TUM School of Engineering and Design der Technischen Universität München zur Erlangung des akademischen Grades eines

Doktors der Ingenieurwissenschaften

genehmigten Dissertation.

Declaration

Ich erkläre hiermit ehrenwörtlich, dass ich die vorliegende Arbeit selbstständig und ohne Benutzung anderer als der angegebenen Hilfsmittel angefertigt habe; die aus fremden Quellen (einschließlich elektronischer Quellen) direkt oder indirekt übernommenen Gedanken sind ausnahmslos als solche kenntlich gemacht. Die Arbeit wurde in gleicher oder änlicher Form noch keiner anderen Prüfungsbehörde vorgelegt.

Ort, Datum	Klaus Heller

Acknowledgement

This thesis would not have been possible without the generous support of various people I would like to express my thankfulness to.

First of all, I would like to thank my academic supervisor Prof. Dr.-Ing. Klaus Drechsler, head of the Chair of Carbon Composites, for giving me the opportunity to work on this topic and providing an environment for personal development. I want to thank Prof. Dr. Paul Compston from the Australian National University for being my second supervisor and for his contributions to the thesis.

Apart from my supervisors, I had invaluable scientific advice from several colleagues. I am grateful to Christoph for helping me find my research topic, to Andi K., Benno, and Ralf for helping me refine my research topic and I am particularly grateful to David for answering so many of my technical questions and for being my scientific mentor.

My time at the Chair of Carbon Composites was shaped by the many enjoyable colleagues I had. Besides all my fellow PhD students, I would like to express my gratitude to Swen, deputy head of the chair, and the research group leaders for their daily support. I thank Daniel and Reiner for their support in the practical work and I thank Cigdem, Heli, Katja, and Pelin for their support in the bureaucratic work. Most importantly, I am very happy that I made three close friends during my time at the chair: Benno, David, and Ralf. Thank you, my friends!

Furthermore, I am very thankful for all the students I had who either contributed directly to this thesis or supported me in other tasks so I could focus more on my research.

The path to this thesis would not have been possible without the support from my friends and family. I thank Michael and Selle for helping me finish my studies, motivating me during my PhD, and being great friends. I thank Deniz for being an endless source of advice for personal improvement. Finally, I would like to express my deepest gratitude to my parents, Nele and Peter, my wife, Dariya, and my son, Milen, for their love, support, and encouragement throughout this work.

Abstract

Carbon fiber reinforced plastics (CFRP) play a significant role in the reduction of greenhouse gas emissions in aviation due to their high weight specific mechanical properties. To lower the environmental impact in all stages of an aircraft's life cycle, the resource efficiency of aircraft production has to be considered. The state-of-the-art process thermoset automated fiber placement (TS-AFP) offers low scrap rates. Yet larger amounts of material (pre-impregnated fibers, prepreg) might be discarded as the material properties change due to storage at room temperature (out-time). Hence, a resource-efficient AFP manufacturing can only be achieved with detailed knowledge about the effects of material property changes on the material process interaction. To quantify the influence of material property changes due to out-time and modifications on TS-AFP processing, AFP-relevant prepreg properties are analyzed systematically and their effects on manufacturing are scrutinized within this thesis. The methodology includes test method development, material characterization, lay-up experiments, and analytical defect prediction models.

The developed prepreg characterization procedure comprises test methods for cure-related, tack, thermal, and mechanical properties. It includes a new test method for peel tack measurements which enables a direct comparison of tack to lay-up results. The systematic property analysis reveals that both out-time and modification with graphite fillers lead to a reduction in tack and an increase in both mechanical properties and thermal conductivity. Results of the lay-up experiments display a strong dependence on out-time: the lay-up defects "out-of-plane buckling" and "tape peel-off" increased up to factor 13 and 16 respectively due to fifteen days out-time. The most feasible countermeasure is a reduction in lay-up rate, which increases the material temperature and the time of intimate contact.

Results from material characterization and lay-up experiments serve as inputs for the development of defect prediction models. Models for out-of-plane buckling and tape peel-off are used to assess the manufacturability of an aerospace part — an aircraft nacelle inner fixed structure. The outcomes show that the out-time can be expanded by 50 % compared to manufacturer specification, indicating a high potential for waste reduction. Furthermore, they reveal that the modified research materials are suitable for the manufacturing of the part without the need for lay-

up experiments, enabling a resource-efficient development of new materials. Apart from that, the presented results can be used to assess for which part geometry a material with a certain out-time can be utilized and what process parameters should be set to avoid defects. The findings serve as a framework which can be transferred to other processes like hand lay-up as well as other pre-impregnated materials like towpreg.

Kurzfassung

Carbonfaserverstärkte Kunststoffe (CFK) spielen aufgrund ihrer hohen gewichts-spezifischen mechanischen Eigenschaften eine wesentliche Rolle in der Reduktion von Treibhausgasemissionen in der Luftfahrt. Um die Umweltbelastung in allen Phasen des Lebenszyklus eines Flugzeugs zu minimieren, muss zudem die Ressourceneffizienz der Produktion in Betracht gezogen werden. Mit dem etablierten Fertigungsverfahren Duroplast Automated Fiber Placement (engl.: thermoset automated fiber placement, TS-AFP) werden geringe Verschnittraten erreicht. Jedoch werden teils größere Mengen des verarbeiteten Materials, vorimprägnierte Faserbänder (engl.: Prepreg), zu Ausschuss, da sich die Materialeigenschaften während der Lagerung bei Raumtemperatur ändern. Folglich kann eine ressourceneffiziente AFP-Fertigung nur mit tiefgründigem Verständnis der Wechselwirkung zwischen Materialeigenschaftsänderungen und Material-Prozess-Interaktion erreicht werden. Um die Auswirkungen der Materialänderungen aufgrund der Zeit bei Raumtemperatur und aufgrund von Materialmodifikationen auf die TS-AFP-Verarbeitung zu quantifizieren, werden die AFP-relevanten Prepreg-Eigenschaften innerhalb der vorliegenden Arbeit systematisch untersucht und deren Einfluss auf die Verarbeitung wird analysiert. Die Methodik beinhaltet die Entwicklung von Prüfmethoden, Materialcharakterisierungen, Fertigungsversuche und analytische Defektvorhersagemodelle.

Die entwickelte Prepreg-Charakterisierungsmethodik besteht aus Prüfmethoden für das Aushärteverhalten, die Klebrigkeit sowie für thermische und mechanische Eigenschaften. Sie beinhaltet eine neue Prüfmethode für Klebrigkeitsmessungen, die einen direkten Vergleich der Klebrigkeit zu Fertigungsversuchen ermöglicht. Die systematische Eigenschaftsanalyse ergab, dass sowohl die Zeit bei Raumtemperatur als auch die Modifikation mit Graphit-Füllstoffen zu einer Verringerung der Klebrigkeit und zu einer Erhöhung der mechanischen Eigenschaften und der thermischen Leitfähigkeit führen. Ergebnisse der Fertigungsversuche zeigen eine deutliche Abhängigkeit von der Zeit bei Raumtemperatur: Die Ablagedefekte „Ausbeulen aus der Ebene heraus" und „Abschälen des Faserbandes" nahmen infolge von fünfzehn Tagen bei Raumtemperatur um bis zu Faktor 13 bzw. 16 zu. Die effektivste Gegenmaßnahme gegen die Defektbildung ist die Verringerung

der Legegeschwindigkeit, wodurch die Materialtemperatur und die Einwirkdauer steigen.

Die Ergebnisse der Materialcharakterisierung und der Fertigungsversuche dienen als Eingangsdaten für die Entwicklung der Defektvorhersagemodelle. Mit den Modellen zur Vorhersage des Ausbeulens sowie des Abschälens wird die Fertigbarkeit eines Luftfahrtbauteils, der inneren Struktur einer Triebwerksgondel, bewertet. Die Resultate zeigen, dass die Zeit bei Raumtemperatur im Vergleich zur Herstellerangabe um 50 % erhöht werden kann, was ein großes Potenzial zur Ausschussvermeidung demonstriert. Zudem machen die Ergebnisse deutlich, dass die modifizierten Forschungsmaterialien für das Luftfahrtbauteil geeignet sind, ohne dass Fertigungsversuche mit den Materialien durchgeführt werden mussten, wodurch eine ressourceneffiziente Materialneuentwicklung ermöglicht wird. Die Modelle können außerdem dazu genutzt werden zu bewerten, für welche Bauteilgeometrie Material mit einer bestimmten Zeit bei Raumtemperatur genutzt werden kann und mit welchen Prozessparametern Defekte vermieden werden. Die Erkenntnisse der Arbeit bieten ein grundlegendes Rahmenwerk, das auf andere Fertigungsverfahren wie Handlaminieren sowie andere Materialien wie vorimprägnierte Rovings (Towpregs) übertragen werden kann.

Table of Contents

List of Figures

List of Tables

Nomenclature

List of symbols

Latin letters

A	area	m^2
A_{E2}	parameter of fit — transverse tensile modulus	$\text{Pa}\,\text{s}^{-2}$
A_{edge}	surface area at edge of inner fixed structure	m^2
A_{G12}	parameter of fit — in-plane shear modulus	$\text{Pa}\,\text{s}^{-2}$
A_{ply}	total surface area of a ply	m^2
A_T	parameter of fit — lay-up temperature	$\text{K}\,\text{W}^{-2}$
A_{Tg}	parameter of fit — glass transition temperature	$\text{K}\,\text{s}^{-2}$
A_α	parameter of fit — degree of cure	s^{-2}
b	width	m
b_{track}	track width	m
B	bending stiffness	$\text{N}\,\text{m}^2$
B_{E2}	parameter of fit — transverse tensile modulus	$\text{Pa}\,\text{s}^{-1}$
B_{G12}	parameter of fit — in-plane shear modulus	$\text{Pa}\,\text{s}^{-1}$
B_T	parameter of fit — lay-up temperature	$\text{K}\,\text{W}^{-1}$
B_{Tg}	parameter of fit — glass transition temperature	$\text{K}\,\text{s}^{-1}$
B_α	parameter of fit — degree of cure	s^{-1}
c_p	specific heat capacity	$\text{J}\,\text{kg}^{-1}\,\text{K}^{-1}$
c_p^{saph}	specific heat capacity of sapphire sample	$\text{J}\,\text{kg}^{-1}\,\text{K}^{-1}$
c_p^{sp}	specific heat capacity of specimen	$\text{J}\,\text{kg}^{-1}\,\text{K}^{-1}$
c_{G12}	correction factor shear stiffness in steering defect model	-
$c_{out-time}$	correction factor out-time in steering defect model	-
c_{plast}	correction factor plastic deformation in peel-off model	-
$c_{t,intim}$	correction factor time of intimate contact in steering defect model	-
c_{temp}	correction factor temperature in steering defect model	-
C_{E2}	parameter of fit — transverse tensile modulus	Pa
C_{G12}	parameter of fit — in-plane shear modulus	Pa

C_{Tg}	parameter of fit — glass transition temperature	K
$d_{IR-roller}$	distance between IR emitter and compaction roller	m
D_{50}	particle diameter at 50 % in the cumulative distribution	m
e_{tack}	separation energy to overcome tack per area	$\mathrm{J\,m^{-2}}$
E_1	tensile modulus in fiber direction	Pa
E_2	tensile modulus perpendicular to fiber direction	Pa
E_f	tensile modulus of fiber	Pa
E_{flex}	flexural modulus	Pa
$E_{flex}I$	bending stiffness	$\mathrm{N\,m^2}$
E_m	tensile modulus of matrix	Pa
F	force	N
F_{max}	maximum force	N
F_{probe}	probe tack test compaction force	N
G_{12}	shear stiffness	Pa
$G_{L,TB}$	elastic shear modulus	Pa
h	height	m
h_{IR}	distance of IR emitter from substrate	m
h_{ramp}	ramp height	m
h_{tool}	tool height	m
ΔH	enthalpy of reaction	J
ΔH_r	exotherm of the remaining reactants	J
ΔH_T	total heat of reaction	J
I	second moment of area	$\mathrm{m^2}$
J	torsional constant	$\mathrm{m^4}$
k	thermal conductivity	$\mathrm{W\,m^{-1}\,K^{-1}}$
k_3	thermal conductivity in thickness direction (direction 3)	$\mathrm{W\,m^{-1}\,K^{-1}}$
k_{tack}	tack stiffness	$\mathrm{N\,m^3}$
$k_{tack,\infty}$	long term tack stiffness	$\mathrm{N\,m^3}$
$k_{tack,base}$	tack stiffness from experimental results	$\mathrm{N\,m^3}$
$k_{tack,start}$	initial tack stiffness	$\mathrm{N\,m^3}$
k_{tool}	thermal conductivity of tool	$\mathrm{W\,m^{-1}\,K^{-1}}$
l	arc length over radius	m
L	length	m
$L_{b,free}$	relative buckle-free length	-
L_{edge}	length after edge	m
$L_{p,free}$	relative pull-up-free length	-
L_{roller}	length of pressure area from deformed roller	m
L_{TB}	free specimen length in Torsion Bar Test	m

m	number of waves in a buckling mode	-
m^{saph}	mass of sapphire sample	kg
m^{sp}	mass of specimen	kg
M_{TB}	torque in Torsion Bar Test	N m
P_0	maximum compression load	N m^{-1}
P_{crit}	critical buckling load	N m^{-1}
P_{IR}	infrared emitter power	W
$\dot{Q}_{empty}$	heat flow of empty run	W
$\dot{Q}_{saph}$	heat flow of sapphire sample	W
$\dot{Q}_{sp}$	heat flow of specimen	W
r_{xy}	Pearson correlation coefficient	-
R	steering radius	m
R^2	coefficient of determination	-
R_{crit}	critical steering radius	m
R_{edge}	edge radius	m
$R_{edge,eff}$	effective edge radius	m
s_{temp}	shift factor for material temperature in steering defect model	-
t_{after}	time after lay-up	s
t_{comp}	compaction time	s
t_{intim}	time of intimate contact	s
t_{layup}	lay-up time	s
t_{out}	out-time	s
t_{relax}	relaxation time	s
T	temperature	K
T_0	initial temperature	K
T_{amb}	ambient temperature	K
T_g	glass transition temperature	K
T_{layup}	lay-up temperature	K
T_{tool}	tool temperature	K
U_B	strain energy due to bending	J
$U_{peeloff}$	peel-off energy	J
U_T	separation energy to overcome tack	J
v	lay-up rate/speed/velocity	m s^{-1}
$v_{max,peeloff}$	maximum lay-up rate with regard to tape peel-off	m s^{-1}
$v_{max,steering}$	maximum lay-up rate with regard to steering	m s^{-1}
v_{probe}	probe tack test displacement rate	m s^{-1}
w	conversion factor for critical steering radius	-

| W_{adh} | work of adhesion | J |
| z | distance of neutral axis from centerline | m |

Greek letters

α	degree of cure	-
α_{diff}	thermal diffusivity	$\mathrm{m^2\,s^{-1}}$
α_{load}	load parameter for out-of-plane buckling model	-
α_{ramp}	ramp angle	°
β_{IR}	inclination of IR emitter	°
$\dot{\gamma}$	shear rate	$\mathrm{s^{-1}}$
δ_{roller}	roller compliance	-
ε_{tool}	tool emissivity	-
$\dot{\varepsilon}_2$	strain rate perpendicular to fiber direction	$\mathrm{s^{-1}}$
ε_b	equivalent bending strain	-
ζ_{time}	coefficient for temporal evolvement of tack stiffness	-
η	viscosity	$\mathrm{Pa\,s}$
κ	curvature	$\mathrm{m^{-1}}$
λ	adjustable parameter for modified DiBenedetto equation	-
ν_{xy}	Poisson's ratio	-
ρ	density	$\mathrm{kg\,m^{-3}}$
σ_{probe}	maximum force per probe area	$\mathrm{N\,m^{-2}}$
τ_1	coefficient for temporal evolvement of tack stiffness	$\mathrm{s^{-1}}$
ϕ	fiber volume fraction	-
$\phi_{RH,amb}$	ambient relative humidity	-
ϕ_{TB}	rotational angle in Torsion Bar Test	°
$\dot{\varphi}$	bending rate	$\mathrm{s^{-1}}$
φ_{layup}	lay-up direction	°
ω	angular frequency	$\mathrm{s^{-1}}$

List of abbreviations

AFP	automated fiber placement
ATL	automated tape laying
CFRP	carbon fiber reinforced plastic
CNT	carbon nanotube
DCB	double cantilever beam
DETDA	diethyltoluenediamine
DFP	dry fiber placement
DIC	digital image correlation
DMA	dynamic mechanical analysis
DoC	degree of cure
DSC	differential scanning calorimetry
FEM	finite element method
FOD	foreign object debris
FPP	fiber patch placement
FTIR	Fourier-transform infrared spectroscopy
GPC	gel permeation chromatography
IFS	inner fixed structure
IR	infrared
KES-F	Kawabata evaluation system for fabrics
LFA	laser flash analysis
LVE	linear viscoelastic
OoA	out-of-autoclave
prepreg	pre-impregnated carbon fibers
PSA	pressure-sensitive adhesive
PTD	peltier temperature device
PTFE	polytetrafluoroethylene
RH	relative humidity
RT	room temperature
SDG	Sustainable Development Goals
SEM	scanning electron microscopy
TC	thermocouple
TGMDA	tetraglycidylmethylenedianiline
TP-AFP	thermoplastic automated fiber placement
TS-AFP	thermoset automated fiber placement
TTS	time temperature superposition
UBT	University of Bayreuth

| **UD** | unidirectional |
| **UTM** | universal testing machine |

1 Introduction

1.1 Motivation

In 2015, the United Nations General Assembly adopted seventeen Sustainable Development Goals (SDG) for a sustainable global development [1]. Part of the SDG are goals for the sustainable industrialization (goal 9) and the sustainable production (goal 12) [1]. Both goals emphasize the importance of an efficient use of natural resources. This is of particular importance since the global material footprint — the amount of primary materials used — has increased by 17% from 2010 until 2017 to a total of 85.9 billion metric tons [2]. Therefore, a resource-efficient production with a reduced waste generation has to be applied to all industry sectors. One sector that has been the focus of sustainability demands for a long time is the aerospace sector [3]. Even though the emissions during flight are the largest source of environmental impact in aviation [4], the production of airliners plays a significant role for a sustainable aerospace sector as well. Here, high performance materials like carbon fiber reinforced plastic (CFRP) have to be used to meet the requirements for performance, safety, and eco-efficiency in flight. Commonly used precursors of these materials for aerospace applications are pre-impregnated carbon fibers (prepreg) consisting of carbon fibers impregnated with an uncured epoxy resin. Since prepreg constituents are made from fossil resources in a energy intensive process and since they are hazardous to the environment in the uncured state, wastage of these materials has to be minimized to achieve a resource-efficient production. Yet, the two biggest aircraft manufacturers, Airbus and Boeing, and their supply chain generate about $1000\,t$ of cured and uncured carbon fiber prepreg waste each year [5]. The prepregs for large aerospace components are commonly processed by automated fiber placement (AFP) followed by autoclave curing. During AFP, several unidirectional (UD) prepreg slit-tapes are laid up onto a mold by a placement head which is manipulated by an industrial robot or a gantry system [6]. By individually cutting the narrow slit-tapes a comparably low scrap rate of 2–6% can be achieved at the edges of the component [7]. However, changes in material properties during manufacturing can lead to the necessity to discard larger amounts of material. During manufacturing, prepregs are kept at temperat-

ures above the glass transition temperature (T_g) at which the material properties change due to the ongoing cross-linking process of the resin [8]. Due to these property changes, the slit-tapes might display lay-up defects or might move from the intended position [9]. This leads to machine downtime and eventually discarding of the material after exceeding a certain storage time above T_g (out-time). Fig. 1.1 illustrates the material utilization during part manufacturing via AFP.
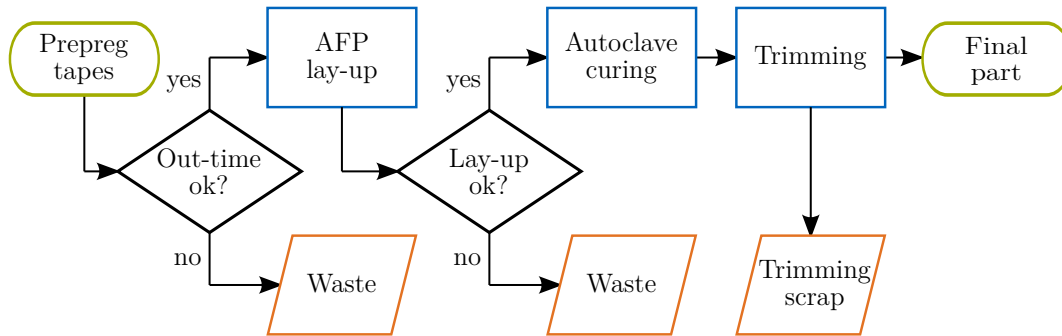
Figure 1.1: Simplified flowchart of material utilization during AFP part manufacturing

Besides the out-time-dependent material changes, material manufacturers also modify the material properties intentionally to expand their field of application. For example, fillers are added to the resin to increase the thermal conductivity of the final part [10]. By this, prepregs can be shaped for new applications like lightweight electric engines [11]. However, modifications influence the material properties both in the cured state and the uncured state which affects the material process interaction during manufacturing. For a resource-efficient material development, newly developed materials have to be characterized and evaluated early in the development phase to prove their suitability for the automated manufacturing of aerospace parts.

1.2 Objective

To maximize the material usage while minimizing manufacturing times, knowledge about the material property changes and their interaction with the process is crucial. However, unlike the material properties in the cured state, there are almost no standards for the material characterization in the uncured state. Therefore, the aim of this thesis is to establish a material characterization procedure for uncured UD prepregs, to quantify the influence of material changes, and to predict the influence on AFP lay-up. By this, the process parameters and the utilization with regard to lay-up complexity can be adapted to the material properties to avoid discarding of the material. Furthermore, recommendations for the development of

new materials can be given. To quantify the material changes and their influence on AFP processing, the following research questions are addressed in this thesis:

Which prepreg properties change because of out-time effects or modifications? How can they be measured?
Prepregs have a variety of properties which result from the prepreg manufacturing process, the fiber properties, the resin properties, the prepreg condition, and others. Only few of these properties are documented in data sheets. Therefore, the objective is to identify all prepreg properties which are relevant for AFP processing. Since there are almost no test standards, existing test methods have to be evaluated and new test methods have to be developed where needed. Once the material characterization procedure is set up, changes of the properties due to out-time effects and modifications are quantified.

How do property changes affect the lay-up quality during AFP?
The influence of prepreg properties on the material process interaction during AFP affects the lay-up quality — potentially leading to lay-up defects or unusability of the material. Hence, the objective is to quantify these effects by conducting lay-up trials at different geometric scenarios with varying prepreg conditions and process parameters.

How can the lay-up quality be predicted?
Even though lay-up trials provide evidence on the material process interaction, the necessary expenses are disadvantageous for industrial applications. Furthermore, they can only be done using prepreg in the final format — slit-tape — which requires the costly process step of slitting the material to the desired width. To ensure a cost-efficient and resource-efficient production and material development, the objective is to predict the lay-up quality with analytical models using input data from the material characterization procedure.

What are the implications for process parameters and part design?
The experimental and analytical findings are used to outline recommendations for practical applications. The objective is to provide guidelines for the process parameter optimization, for the suitability of prepregs in their respective condition for the manufacturing of a part with a certain geometry, and for the development of new prepregs for AFP. To demonstrate the potential for the maximization of material usage and the minimization of manufacturing time and resource demand for the development of new material, the analytical models are applied to a use case.

1.3 Outline

The thesis is structured in six main chapters:

Chapter 2 outlines the state of the art of prepregs and thermoset automated fiber placement (TS-AFP). For the former, the focus is on the prepreg properties and the influence of out-time effects and modifications on them. For the latter, the focus is on the process parameters. Furthermore, the AFP machine from Coriolis Group SAS used in this thesis is described.

Chapter 3 presents the findings on the material characterization. Based on the state of the art the AFP-relevant prepreg properties consisting of tack, mechanical, and thermal properties are identified. Existing characterization methods are evaluated and newly developed methods are presented. Subsequently, the results from the quantification of out-time effects and effects of modifications using the material characterization routine are detailed. The analyzed materials are HexPly IM7/8552, an unmodified research material, and a modified research material.

Chapter 4 describes AFP lay-up trials comprising material deposition experiments along in-plane curved paths (steering) and out-of-plane curved paths (concave and convex edge) with HexPly IM7/8552 prepreg slit-tapes in different conditions. Its analysis focuses on the influences of material changes and process parameter adjustments.

Chapter 5 details the development of analytical models for the defect prediction based on the lay-up trials. The input data for the models are results of the material characterization. The chapter concludes with the application of the models to a use case — an aircraft nacelle inner fixed structure (IFS) — to quantify the effects of material changes on a real part.

Chapter 6 summarizes the work presented, draws conclusions, and evaluates potential future work.

Fig. 1.2 graphically summarizes the structure of the thesis.

Inputs

Materials (all uncured):
- HexPly IM7/8552
- unmodified research
  material
- modified research
  material

Process:
- thermoset AFP
- Coriolis machine

Part:
aircraft nacelle –
inner fixed structure

Thesis structure

Literature review
- prepreg material
- TS-AFP process

Chapter 2

Material characterization
- identification of changes
- test development
- quantification of changes

Chapter 3

AFP lay-up experiments on
- lay-up scenarios
- material property changes
- process parameters

Chapter 4

Modelling and prediction of
lay-up defects

Chapter 5

Application to use case

Chapter 5

Part
Process
Material

Main outputs

Prepreg
characterization
procedure

Quantification
of property
changes

Quantification of
AFP lay-up vs.
property changes

Enhanced defect
prediction for
AFP

Part assessment
- manufacturability
- process parameters

Figure 1.2: Graphic illustration of the thesis structure

2 State of the art

The following chapter pictures the state of the art related to the material process interaction in thermoset automated fiber placement. Sec. 2.1 gives a general description of prepregs, their manufacturing (Sec. 2.1.1), and their properties (Sec. 2.1.2). The existing literature on the influence of out-time effects and intentional modifications on the prepreg properties is outlined in Sec. 2.1.3 while existing characterization methods are detailed in Sec. 2.1.4. Sec. 2.2 presents the state of the art of the investigated process — thermoset automated fiber placement — including the basic principle, the material process interaction (Sec. 2.2.1), and lay-up scenarios (Sec. 2.2.2). Lastly, based on the lay-up scenarios, existing lay-up defect prediction models are covered in Sec. 2.2.3.

2.1 Prepreg

Thermoset pre-impregnated carbon fibers (prepregs) consist of unidirectional or woven fibers which are impregnated with a partially reacted (B-staged) thermosetting system [12]. To inhibit a further reaction before the final processing to a structural part, prepregs require refrigerated storage — typically at $-18\,°C$ [13, 14]. For part manufacturing, prepregs are thawed and laid up by hand lay-up or automated processes like filament winding, pultrusion, automated tape laying (ATL), and AFP [13, 14]. In aerospace applications, the prepreg lay-up is commonly followed by the autoclave curing. Other curing technologies include oven curing, press forming, and curing via induction, microwave heat, or electron beams [13]. The main resin materials include epoxy resins, bismaleimide resins, and phenolic resins [13]. As it is the focus of this thesis, subsequently only aerospace grade UD-prepregs with an epoxy resin laid up by AFP followed by autoclave curing are considered.

2.1.1 Manufacturing of prepregs

UD-Prepregs are usually manufactured using the hot-melt impregnation [15]. The basic principle is depicted in Fig. 2.1.
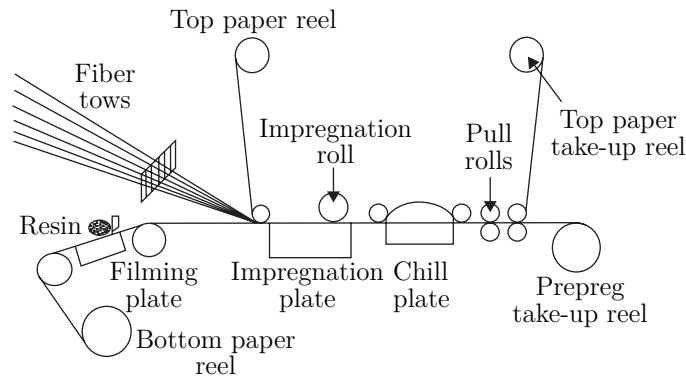
Figure 2.1: Scheme of hot-melt prepreg manufacturing [15]

In the process, the resin is applied to a bottom paper with the help of a filming plate which can be done online, as depicted, or in a separate process [15]. The resin film is then brought into contact with the fibers as well as a top paper or release film and passes the impregnation zone including the impregnation plate, impregnation roll, chill plate, and pull rolls. Here, the resin is heated to control the viscosity and pressure is applied to control the thickness and the degree of impregnation [15]. Subsequently, the prepreg is cooled and wound around the take-up reel either with or without top paper or release film. For AFP applications, the wound UD-prepreg — parent tape — has to be slit to the required width depending on the AFP machine configuration, e. g. 1/8" (3.175 mm), 1/4" (6.35 mm), or 1/2" (12.7 mm) [16]. For this, the parent tape is run through a slitter with the required slitting width and wound on cardboard spools together with a backing film which prevents sticking of the slit-tape to the material below during despooling [16]. A prepreg slit-tape spool is shown in Fig. 2.2.
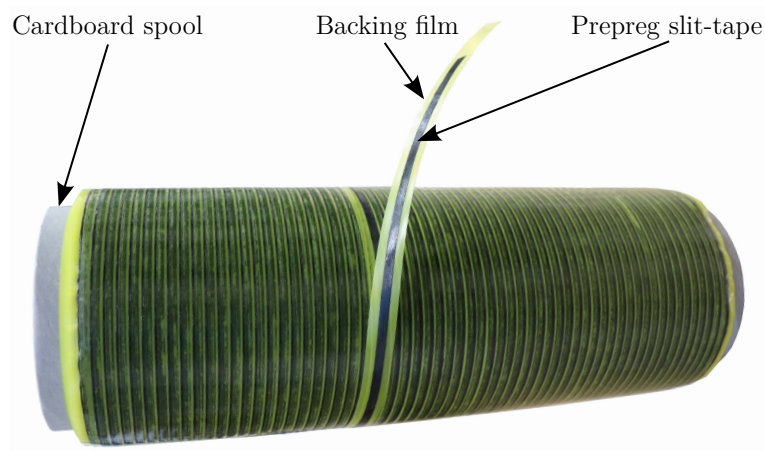
Figure 2.2: Prepreg slit-tape spool

The slitting is the final process step for prepreg slit-tapes and accounts for around 15% of the slit-tape cost [17]. Generally, the prepreg manufacturing process allows for the use of modified resins since fillers can be dispersed homogeneously in the resin before the fiber impregnation [16]. However, the application of the resin film from one side can lead to different properties on the top and the bottom side of the prepreg [18].

2.1.2 Prepreg properties

Uncured prepregs have a variety of properties the following of which are given in data sheets — see Tab. 2.1.

Table 2.1: Prepreg properties given in data sheets from [19, 20]

Composition	Dimensional and gravimetric properties	Mechanical properties	Thermal and electrical properties	Other resin concerning properties
Nominal fiber volume	Prepreg density	Fiber tensile strength	Fiber specific heat capacity	Viscosity
Resin content	Prepreg areal weight	Fiber tensile modulus	Fiber thermal conductivity	Gel time
	Prepreg width	Fiber elong. at failure	Fiber coeff. of thermal exp.	
	Prepreg thickness		Fiber electrical resistivity	
	Fiber density			
	Fiber areal weight			
	Filament diameter			
	Resin density			

Relevant prepreg properties which are not given in data sheets are listed in Tab. 2.2.

Besides common material properties like mechanical, thermal, and electrical properties, prepreg properties include specific composition and exterior properties as well as resin concerning properties. Selected properties relevant for TS-AFP are described in the paragraphs below.

Table 2.2: Prepreg properties not given in data sheets (PP: prepreg)

Composition	Dimensional and gravimetric properties	Mechanical properties	Thermal and electrical properties	Other resin concerning properties
Surface roughness	-	PP tensile strength	PP specific heat capacity	Degree of cure
Slit quality		PP tensile modulus	PP thermal conductivity	Glass trans. temperature
Degree of impregnation		PP transverse tensile strength	PP coeff. of thermal exp.	Enthalpy of reaction
		PP transverse tensile modulus	PP electrical resistivity	Moisture content
		PP in-plane shear strength		Tack
		PP in-plane shear modulus		
		PP Poisson's ratio		
		PP bending stiffness		

The exterior property *surface roughness* influences the contact between prepreg and substrate which affects the tack and the occurrence of interply voidage during lay-up [18]. Poor *slit quality* can lead to protruding fibers and fuzzballs causing contamination in the material feed or even reducing the part quality [13]. The *degree of impregnation* is defined as the percent of spacing between the fibers that is filled with resin and is not pore volume [21]. It affects the deformability and the tack of the uncured prepreg as well as the porosity in the laminate [13].

From the multitude of *mechanical properties*, the *tensile modulus*, the *transverse tensile modulus*, and the *in-plane shear modulus* are the most relevant mechanical properties for AFP processing. They affect the dimensional stability, the deformability, and the occurrence of lay-up defects [13, 22, 23] — see Sec. 2.2.3. The transverse tensile modulus and the in-plane shear modulus are influenced by the resin properties, in particular the viscosity. Because of the high width to thickness ratio of slit-tapes (~ 24), out-of-plane properties like the out-of-plane shear modulus are not considered. The *bending stiffness* is influenced by the tensile modulus,

the width, and the thickness of the material and affects the occurrence of lay-up defects like peel-off [24] — see Sec. 2.2.2. Due to the state of stress in bending and due to through-thickness differences of the prepreg, the bending modulus usually differs from the tensile modulus [16].

The *thermal properties* affect the temperature of the material during processing as it is a function of the heat input, the *specific heat capacity*, and the *thermal conductivity* [25]. The temperature, in turn, has an influence on several other properties like the viscosity, the tack, and the resin influenced mechanical properties like the transverse tensile stiffness or the shear stiffness [8, 24, 26]. The *coefficient of thermal expansion* and the *electrical resistivity* are not expected to have any influence on TS-AFP processing.

The *viscosity* is defined as the internal resistance of a fluid to an externally acting load [27]. For TS-AFP, it is an important property since it affects the tack as well as mechanical properties like the in-plane shear stiffness [28, 29]. A low level of viscosity is desired to achieve a high level of surface wetting for adhesion [30]. Simultaneously, a high level of viscosity mitigates the occurrence of defects [30, 31]. The viscosity is both cure and temperature dependent [8]. The *degree of cure (DoC)* quantifies the resin's extend of transformation from low molecular weight liquid to high molecular weight amorphous solid by means of chemical reactions [32, 33]. It is of particular interest for prepreg processing since properties like the viscosity and the tack change as a function of the DoC [8, 34–37] — see Sec. 2.1.3. The DoC can be referred to the initial state of the resin before B-staging or to the resin state after B-staging. Subsequently, the latter is used if not stated otherwise because it is the relevant DoC reference for the prepreg end user. Typical parameters for the determination of the DoC are the *glass transition temperature* (T_g) or the *enthalpy of reaction* [8] — see Sec. 2.1.4. The *moisture content*, which can be caused by water uptake from the atmosphere, affects properties like the cure rate, the glass transition temperature, and the tack of the uncured resin [35, 38–40]. The *tack* is considered as an intrinsic stickiness or more specifically a measure of mechanical resistance which needs to be overcome to separate the prepreg from a substrate [24]. To ensure a successful lay-up, the prepreg tack has to be high enough for the tapes to remain in the desired position on the lay-up tool or on a preceding ply and to prevent the occurrence of lay-up defects [24, 35] — see Sec. 2.2.2. Simultaneously, the tack has to be low enough to prevent faults in the material feed and to prevent adherence to the placement roller during lay-up [24, 35].

In data sheets, additional information on the storage life of the prepreg is given [19]: the *tack life* is defined as "the time, at room temperature, during which prepreg retains enough tack for easy component lay-up." The *out life* is defined as

"the maximum accumulated time allowed at room temperature between removal from the freezer and cure" and the *shelf life* is defined as the maximum storage life when stored in a sealed bag at $-18\,°C$ [19].

2.1.3 Property changes

Prepreg properties may change due to storage at elevated temperatures (out-time) or due to intentional modifications like adding fillers to the resin. Both of these sources of property changes solely affect the resin concerning properties and do not affect fiber properties. Therefore, only resin concerning properties are considered in this section.

2.1.3.1 Property changes due to out-time

In aerospace prepreg manufacturing, the workshop temperature is typically around $18-24\,°C$ and the relative humidity (RH) is within $25-60\,\%$ [41]. Therefore, these conditions are considered typical out-time conditions. Subsequently, the findings in literature regarding changes of relevant prepreg properties due to out-time are discussed.

Degree of cure

The effects of out-time on the degree of cure of prepregs has been investigated by a variety of authors [34, 36, 42–54]. The temperature range in all publications was between $18-26\,°C$. Where the humidity was stated, it was $49-51\,\%$ [43, 45, 48–51, 53, 54] except for [36] and [52], where it was $<0.1\,\%$ and $<10\,\%$ respectively. The enthalpy of reaction was used in [34, 36, 42–45, 47, 49–52, 54] for the calculation of the degree of cure. Jones et al. [46] used spectra obtained by infrared (IR) photoacoustic spectroscopy while Grunenfelder et al. [48, 53] and de Andrade Raponi et al. [51] used the glass-transition temperature. All authors reported a monotonic increase of degree of cure as a function of out-time. The development was non-linear in [34, 36, 42–44, 46, 47, 49–52, 54] while Grunenfelder et al. [48, 53] reported a linear development. The maximum reported degree of cure ranges from $15\,\%$ [43] to $38\,\%$ [50] both after 60 days out-time.

Moisture content

The prepreg moisture content dependency on the out-time has been investigated by less authors. Sanjana et al. [55] measured the moisture content of an epoxy prepreg after conditioning at room temperature (RT) and 90% RH up to 27 days, which led to a maximum moisture content of $0.8\,wt\%$. Grunenfelder et al. [56] varied the RH from $30-90\%$ at $35\,°C$ for one day out-time of an out-of-autoclave (OoA) prepreg. As expected, the highest RH led to the highest moisture content of around $1\,wt\%$. Kim et al. [57] also varied the RH from $30-90\%$ OoA prepreg. Here, the temperature was $30\,°C$ and the maximum moisture content was around $1\,wt\%$ after 35 days out-time. Recently, Minakuchi et al. [58] measured the moisture content of a epoxy prepreg at $40\,°C$ and 85% RH and reported a saturated level of moisture content of around $0.27\,wt\%$ after seven hours out-time. All above results revealed a non-linear, monotonic increase of moisture content as a function of out-time.

Viscosity

The out-time effects on the viscosity η are the increase in molecular size and the effect of temperature on the molecules [59]. It is usually measured from the neat resin as the viscosity of a prepreg is influenced by the heterogeneous and viscoelastic nature of the prepreg which is dependent on the fiber content [28]. Banks et al. [30] measured the complex viscosity of a epoxy resin up to a DoC (before B-staging) of 57% and reported an increase from the order of magnitude of $10^1\,Pa\,s$ to $10^6\,Pa\,s$. Yu et al. [60] conditioned a neat epoxy resin at $35\,°C$ for 7 days which led to a viscosity increase by factor 3.4. Grunenfelder et al. [61] investigated the influence of 56 days out-time at $20\,°C$ and 50% RH (DoC of 33%) on the viscosity and reported an increase from the order of magnitude of $10^1\,Pa\,s$ to $10^3\,Pa\,s$. Just like the authors above, Gu et al. [52], Kim et al. [54, 62], and Kuliaei et al. [63] also reported a non linear monotonic increase of the viscosity of neat epoxy resins as a function of out-time.

Tack

The out-time affects the flowability and the molecular mobility of the resin which, in turn, affects the tack of the prepreg [34, 35]. Tab. 2.3 gives an overview of the experimental results found in literature. The development of tack over out-time is indicated by the symbols: ↓ indicates monotonic decrease, ↑↓ indicates non-monotonic changes.

Table 2.3: Literature review of investigations of tack as a function of out-time — ↓ indicates monotonic decrease, ↑↓ indicates non-monotonic changes (CF: carbon fiber, EP: epoxy, F: compaction force, GF: glass fiber, RH: relative humidity, RT: room temperature, T: temperature, UTM: universal testing machine, v: velocity/rate)

Ref.	Test type	Material	Out-time conditions	Tack development
[64]	Sticking to vertical steel plate	Narmco 5208/ WC3000	22 °C, 50 % RH up to 66 days	↓
[34]	Probe tack UTM	Hercules 3501-6	25 °C up to 33 days	↑↓ dep. on T
[30]	Foating roller peel test	GF/EP prepreg	RT up to 57 % DoC	↑ ↓
[47]	Sticking to vertical steel plate	CYCOM IM7/ 977-3	RT up to 60 days	↓
[40]	Probe tack UTM	HexPly T700/M21	20 °C, 20, 80 % RH up to 1.4 days	↓
[53]	Probe tack UTM	CF, Cytec 5320	not indicated	↑ ↓
[65]	Lap shear test	CF/EP prepreg	RT up to 16 days	↑ ↓
[49]	T-peel test	CF/EP prepreg	23 °C, 50 % RH up to 120 days	↓
[66]	Friction tack test	HexPly IM7/8552	20 °C, 35 % RH up to 15 days	↑↓ dep. on v,F
[35]	Single-stage peel test	CF/EP prepreg	19 °C, 42 % RH up to 14 days	↑ ↓
[36]	Probe tack rheometer	CF/EP prepreg	21 °C, < 0.1 % RH up to 60 days	↑↓ dep. on T
[51]	Probe tack rheometer	CF/EP prepreg	24 °C, 50 % RH up to 60 days	↑ ↓
[37]	Single-stage peel test	CYCOM T650/ 5276-1	18 °C, 44 % RH up to 35 days	↑↓ dep. on v,T

To visualize the tack development, the resulting graphs of selected publications are pictured in Fig. 2.3. Both, Tab. 2.3 and Fig. 2.3, show that out-time has a strong effect on the tack. No case was found where the tack increased monotonic in all investigated parameter sets as a function of out-time. A monotonic decrease, however, was reported in [40, 47, 49, 64]. The maximum achievable tack declined to a value of zero in [64] (after 25 days out-time), [53] (22 days), [49] (60 days), and [51] (60 days). Studies with varying test parameters like velocity/rate, temperature, compaction force revealed that the maximum tack at a given out-time can be influenced by optimizing the test parameters [35–37]. Endruweit et al. [35], Budelmann et al. [36] and Smith et al. [37] found that either a lower rate or a higher temperature or both is needed to maximize the tack at higher out-times.

Degree of impregnation

No studies have been found on changes of the degree of impregnation due to out-time. Even though the resin viscosity increases which might affect the void content after prepreg processing [61], the degree of impregnation of the unprocessed prepreg is not expected to change due to out-time effects.

Surface roughness

Lukaszewicz and Potter [18] measured the surface roughness of HexPly IMA/M21 and CF-MTM44-1 prepregs over 21 days out-time at room temperature. They could not identify any significant changes since the resin does not flow without external loads.

(a) Probe tack UTM

(b) Floating roller peel test

(c) T-peel test

(d) Probe tack rheometer

(e) Single-stage peel test
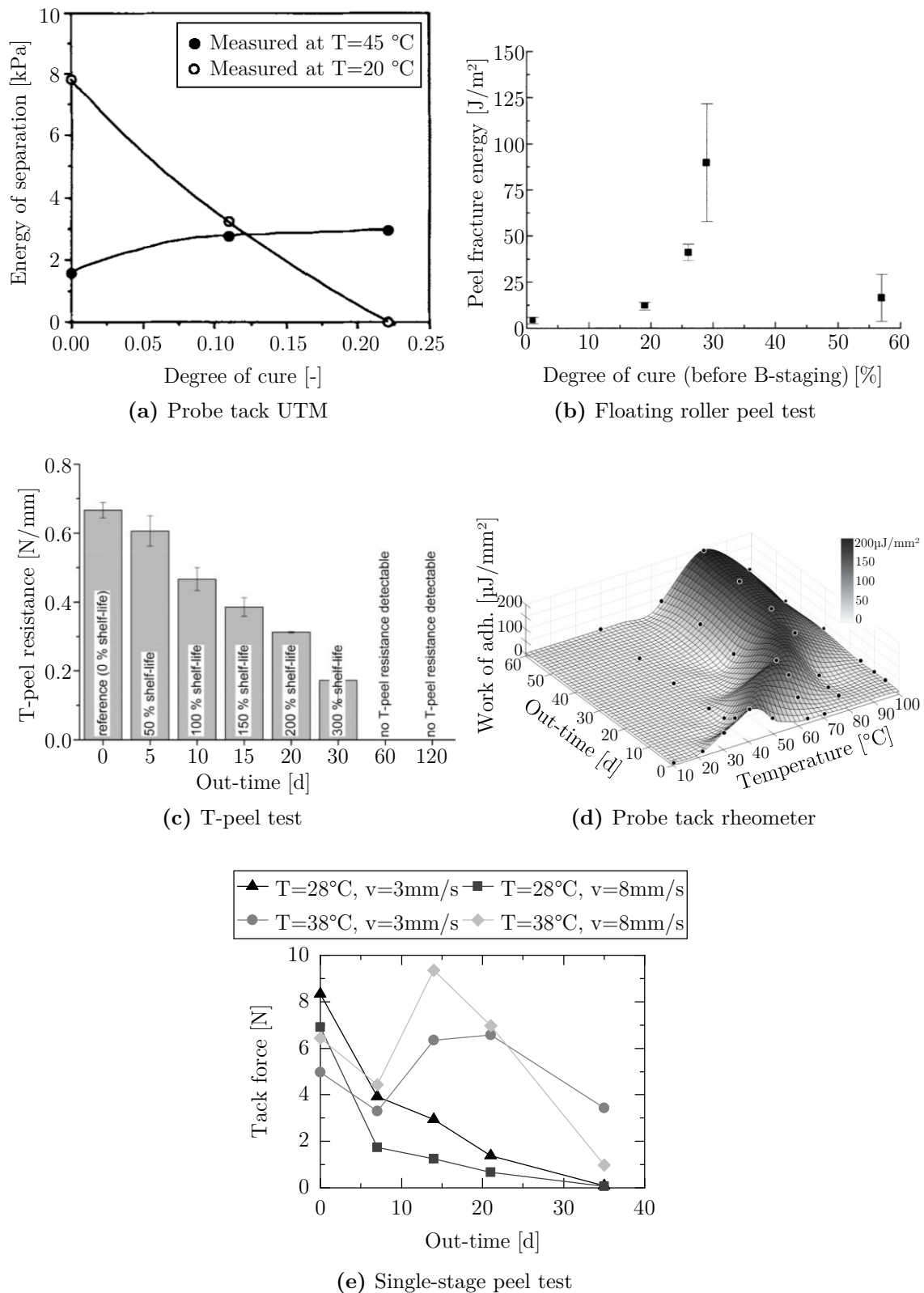
Figure 2.3: Tack vs. out-time from selected publications: (a) [34], (b) [30], (c) [49], (d) [36], (e) data from [37]

Specific heat capacity

No studies on the influence of out-time on the specific heat capacity c_p and thermal conductivity k have been found. However, there are several studies on c_p and k as a function of cure, many of which consider significantly higher temperatures — up to $150\,°C$ — compared to out-time conditions. McHugh and Stark [67] analyzed the specific heat capacity of a carbon/epoxy prepreg as a function of cure. They measured an approximate linear increase up to a DoC of $60\,\%$ which was followed by a sharp decrease due to the vitrification of the resin. The increase in c_p from $0\,\%$ to $30\,\%$ DoC was around $1\,\%$. Whereas Chern et al. [68] analyzed Hercules 3501-6 neat epoxy resin and reported a decrease in c_p by around $1\,\%$ from a DoC of $20\,\%$ to $40\,\%$. Garnier and Sommier [69] tested a glass/epoxy prepreg and found almost no change in c_p up a DoC of $80\,\%$. Tab. 2.4 gives an overview of the above mentioned results including additional investigations. Where available, the c_p development was calculated for a DoC range of $0 - 30\,\%$ which corresponds to typical out-time conditions.

Table 2.4: Literature review of investigations of the specific heat capacity as a function of cure

Ref.	Material	DoC range	$T_{min}[°C]$	c_p development
[70]	CF/Epon 828-mPDA prepreg	$0 - 30\,\%$	78	$+2.3\,\%$
[68]	Hercules 3501-6 neat EP resin	$20 - 40\,\%$	27	$-1\,\%$
[69]	GF/EP prepreg	$0 - 80\,\%$	109	~ 0
[71]	SP Systems SPX8800 GF prepreg	$0 - 30\,\%$	85	$+0.5\,\%$
[67]	CF/EP prepreg	$0 - 30\,\%$	150	$+1\,\%$

Thermal conductivity

McHugh and Stark [67] also analyzed the thermal conductivity of a carbon/epoxy prepreg as a function of cure. Here, a more pronounced increase as a function of DoC was reported compared to the increase in c_p. The increase in k from $0\,\%$ to $30\,\%$ DoC was around $8\,\%$. Garnier and Sommier [69] reported a DoC dependent increase of around $2.4\,\%$ from $0\,\%$ to $30\,\%$ DoC. Again, Chern et al. [68] came to a different conclusion stating that: "Thermal conductivity is found to be only weakly dependent on the degree of cure." They presented a polynomial for the temperature dependent calculation of k of Hercules 3501-6 neat epoxy resin which did not include any consideration of the DoC. Tab. 2.5 gives an overview of the above mentioned results including additional investigations.

Table 2.5: Literature review of investigations of the thermal conductivity as a function of cure

Ref.	Material	DoC range	$T_{min}[°C]$	k development
[72]	DER 332 neat EP resin	$0 - 30\%$	25	$+2.4\%$
[70]	CF/Epon 828-mPDA prepreg	$0 - 30\%$	78	$+3.2\%$
[68]	Hercules 3501-6 neat EP resin	$11 - 100\%$	27	~ 0
[71]	SP Systems SPX8800 GF prepreg	$0 - 30\%$	85	$+3.3\%$
[67]	CF/EP prepreg	$0 - 30\%$	150	$+8\%$
[73]	XU3508/XB3473 neat EP resin	$0 - 80\%$	91	$+13\%$

Tensile modulus and strength

No studies on the influence of out-time on the tensile modulus have been found in literature. Even though the resin does have an influence on the tensile modulus of the prepreg according to the rule of mixture, the influence is negligible since the tensile modulus of the fiber is several orders of magnitude higher than the tensile modulus of the uncured resin. The tensile strength does not affect the material process interaction and is therefore not discussed further.

Transverse tensile modulus and strength

No studies on the influence of out-time on the transverse tensile modulus have been found in literature. Margossian et al. [74] measured the transverse tensile modulus of an carbon/epoxy prepreg. However, they did not consider any material changes due to out-time or cure. The transverse tensile strength does not affect the material process interaction and is therefore not discussed further.

In-plane shear modulus and strength

The in-plane shear or intra-ply shear encompasses the movement of fibers past one another within a ply — either parallel (longitudinal) or orthogonal (transverse) to the fiber direction [75, 76]. The longitudinal intra-ply shear is generally seen as the most important forming mechanism [77, 78] while the transverse intra-ply shear is of lower importance when investigating UD prepreg tapes [77].

No studies on the influence of out-time on the in-plane shear modulus have been found in literature. Several authors investigated the in-plane shear modulus of uncured prepregs [22, 26, 79–84]. However, none of them considered out-time effects. Ersoy et al. [85] calculated and Chen et al. [86] measured the in-plane shear modulus as a function of DoC. The range of DoC was, however, higher than

the range of out-time effects — > 33 % and > 54 % respectively. The in-plane shear strength does not affect the material process interaction and is therefore not discussed further.

Poisson's ratio

No studies on the influence of out-time on the Poisson's ratio ν_{xy} have been found in literature. O'Brien et al. [87] and Saseendran et al. [88] investigated the Poisson's ratio of neat epoxy resins as a function of DoC. However, in both studies the DoC range was higher — > 79 % and > 50 % respectively — than the DoC range caused by out-time. O'Brien et al. reported a Poisson's ratio of $0.4 - 0.4925$ [87] and Saseendran et al. reported a Poisson's ratio of $0.32 - 0.5$ [88]. Ersoy et al. [85] calculated the Poisson's ratio of HexPly AS4/8552 prepreg as a function of DoC. Again, the DoC was higher than the range of out-time effects. The predicted Poisson's ratio in the resin's rubbery state stemming from two different modelling methods was 0.327 and 0.346 respectively [85].

Bending stiffness

Similarly, no studies on the influence of out-time on the bending stiffness $E_{flex}I$ have been found in literature. Potter [22], Banks et al. [30], Wang et al. [89] , Bloom et al. [90], and Alshahrani and Hojjati [91] all did experiments on the out-of-plane deformation or the flexural rigidity of different types of prepregs. However, none of them considered out-time effects.

2.1.3.2 Property changes due to modifications

As mentioned in the introduction, fillers are used to modify the properties of the resin and therefore of the prepreg. Particulate fillers are defined as "inert, solid materials which are physically dispersed in the polymer matrix, without significantly affecting the molecular structure of the polymer" [92]. The modified prepregs covered in this thesis contain $15 \, vol\%$ graphite particles with a platelet-shape and an average size of $18 \, \mu m$ as described by Bard et al. in [10] and [93]. Therefore, the starting point for the literature review are graphite fillers with a size within the μm range.

Degree of cure

Siddiqui et al. [94] measured the curing behavior of a prepreg as a function of carbon nanotube (CNT) filler content. They reported a catalytic behavior caused by the CNT fillers leading to a faster conversion with increasing filler content from $0-1\ wt\%$. Tao et al. [95] stated similar findings for a neat epoxy resin with different types of CNT: CNT initiate cure at lower temperatures but slow the curing process. Puglia et al. [96] also stated that CNT act as a catalyst depending on the filler content, so did Mauro et al. [97] for graphite oxide and high-surface-area graphite fillers. Yang et al. [98] investigated the influence of graphite fillers ($< 20\ \mu m$) on T_g in neat epoxy resin. They found a 4 % increase in T_g with $1\ wt\%$ and a 6.9 % increase with $4\ wt\%$ filler content. In sum, fillers affect the cure kinetics and the extend of the influence depends on the filler type, concentration, and size.

Viscosity

Fillers significantly influence the viscosity of the uncured resin. Studies have shown an exponential increase in viscosity as a function of filler concentration since the interparticle interactions increase [92]. Furthermore, the viscosity depends on the filler size: The smaller the particle the higher the viscosity as smaller particles lead to a network formation of finite strength [92]. Other particle properties influencing the viscosity are the filler type, the distribution, and the surface — see [92]. Additionally, fillers change the temperature dependency of the viscosity. Due to a higher temperature the viscosity decreases because of the greater free volume for molecular motion. The presence of fillers reduces this free volume change [92]. Siddiqui et al. [94] investigated the influence of CNT filler content on the viscosity of epoxy resins. They found an approximately linear increase in viscosity of around 50 % per $1\ wt\%$ CNT content. Several other studies came to similar conclusions [99–101].

Specific heat capacity

Yazman et al. [102] measured the influence of CNT on c_p on neat epoxy resin in the cured state. From a filler content of 0 to $2\ wt\%$ c_p generally decreased up to 39 % due to the decrease in molecular mobility caused by the presence of the fillers [102]. Similar findings were reported in [103].

Thermal conductivity

Bard et al. [10] measured the thermal conductivity of the material covered in the present thesis in the cured state. The 15 $vol\%$ graphite particles in the resin led to an increase in transverse thermal conductivity by factor 3 — from 0.36 W/mK to 0.91 W/mK — of the material. They did not measure the thermal conductivity in the uncured state. However, it is expected that influence of the fillers in the uncured state is similar to the cured state.

Transverse tensile modulus and strength

Besides the T_g, Yang et al. [98] also investigated the influence of graphite fillers ($< 20\ \mu m$) on the tensile stress-strain behavior neat epoxy resin in the rubbery state. They found a 8 % increase in tensile modulus and a 39 % increase in tensile strength with 4 $wt\%$ filler content. Allaoui et al. [104] reported a doubled and quadrupled tensile modulus and strength for filled rubbery epoxy with respectively 1 and 4 $wt\%$ CNT compared to the neat rubbery resin. Bai [105] also found a doubling in tensile modulus and strength for filled soft epoxy with 1 $wt\%$ CNT while Liu and Wagner [106] found a 28 % increase in tensile modulus of a rubbery epoxy with 1 $wt\%$ CNT filler content.

No relevant work was found on the influence of fillers on *moisture content*, *tack*, *degree of impregnation*, *surface roughness*, *tensile modulus and strength*, *Poisson's ratio*, *in-plane shear modulus and strength*, and *bending stiffness*.

2.1.4 Prepreg characterization

Since there are no test standards for many properties of uncured prepregs, different characterization methods have to be considered for each material property as described in the following paragraphs.

Degree of cure

A common measurement method to determine the DoC is differential scanning calorimetry (DSC) with which the enthalpy of reaction ΔH and the glass transition temperature T_g can be determined [8, 16, 27, 32, 107]. Other measurement methods include dynamic mechanical analysis (DMA) [108], gel permeation chromatography (GPC) [109, 110], Fourier-transform infrared spectroscopy (FTIR)

[45], IR photoacoustic spectroscopy [46], and dielectric analysis [111]. The enthalpy of reaction was used in [34, 36, 42–45, 47, 49–52, 54] for the calculation of the degree of cure while several other authors used the glass transition temperature [33, 48, 51, 53, 112]. The measurement procedures are defined in various test standards: [113, 114] for the determination of ΔH, and [115–117] for the determination of T_g. During a DSC run, the difference in heat flow between two encapsulated pans — one empty, one containing the material to be measured — is measured as a function of temperature or time. Both pans are subjected to the same temperature program — e. g. a constant heat rate of $10K/min$ [115]. In the sample pan, reactions take place because of the heating of the sample. Due to the amount of heat dissipated or absorbed by the sample, the amount of heat required to increase the temperature in the sample pan differs from that in the reference pan. This difference results in the evaluated heat flow change in the DSC curve. Using ΔH, the DoC α is calculated as [32]

$$\alpha = 1 - \frac{\Delta H_r}{\Delta H_T} \tag{2.1}$$

with the residual exotherm of the remaining reactants (ΔH_r) and the total heat of reaction (ΔH_T).

T_g is defined as distinctive point of the heat flow-temperature curve where the heat flow decreases and the curve progression passes an inflection point [115]. Fig. 2.4 shows examples of the curve progression including the glass transition temperature of uncured material T_{g0}, glass transition temperature of fully cured material $T_{g\infty}$, and ΔH, which is calculated as the area under the curve at the peak.
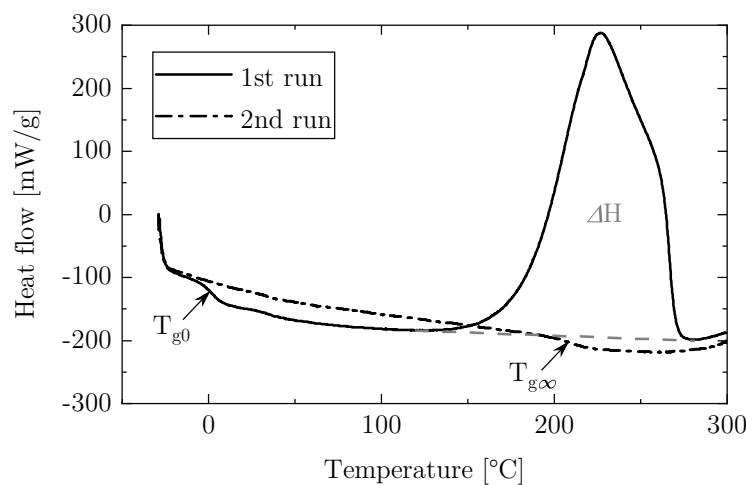
Figure 2.4: Exemplary illustration of heat flow during two DSC runs

The determination of T_g is either done by measuring the midpoint between the heat flow level before the inflection and after the inflection — midpoint method — or by directly measuring the position of the inflection point — inflection method — [8, 115]. The relation between T_g and the degree of cure is commonly described by an equation by DiBenedetto [118] which has been modified by Pascault and Williams [112]. The modified equation is

$$\frac{T_g - T_{g0}}{T_{g\infty} - T_{g0}} = \frac{\lambda\alpha}{1 - (1 - \lambda)\alpha} \tag{2.2}$$

where λ is an adjustable parameter between 0 and 1. Rearranged for the calculation of the DoC Eq. 2.2 becomes

$$\alpha = \frac{T_g - T_{g0}}{T_g(1 - \lambda) + \lambda T_{g\infty} - T_{g0}}. \tag{2.3}$$

The determination of the degree of cure via T_g offers several advantages: T_g can be measured precisely, the test procedure is relatively quick, only a small amount of material is needed, and the accuracy is higher at high levels of conversion compared to ΔH measurements [33, 48, 51].

Moisture content

A straightforward method to measure the moisture uptake or emittance is by gravimetric measurement [55, 58]. The absolute moisture content can be quantified using Coulometric Fischer titration [119], which has been used by Grunenfelder et al. [56] and Kim et al. [57].

Viscosity

The viscosity of neat epoxy resins is typically determined using a rotational rheometer with parallel plates or similar configurations [120]. The resin is subjected to a controlled shear stress or shear rate by the rotational symmetric plates while the velocity gradient and the resulting shear stress respectively are determined to calculate the viscosity [27, 120]. In theory, the parallel plates configuration can also be used to measure prepregs. The presence of the fibers, however, causes a heterogeneous viscoelastic material response which makes a comparison of this measurement to the viscosity of the neat resin inappropriate [28, 37].

Tack

Since there had been no test standard for the measurement of prepreg tack, several
different test methods and measuring principles can be found in literature — see
Tab. 2.6.

Table 2.6: Literature review of tack test methods (DCB: double cantilever beam, UTM: universal
testing machine)

Principle	Test type	Ref.
Hold time	Sticking to vertical plate	[47, 64]
Probe test	Probe tack UTM	[28, 34, 40, 53, 121–124]
	Probe tack rheometer	[36, 51, 125–127]
Peel test	Floating roller peel test	[30, 128]
	T-peel test	[49]
	90° peel test	[129]
	Single-stage peel test	[35, 37, 110, 130, 131]
Others	Lap shear test	[65]
	Shear test	[132]
	Friction tack test	[66]
	Rigid DCB test	[133]

A rather basic tack test method is sticking a prepreg specimen to a vertical steel
plate and measuring the time it holds onto the steel plate before falling off [64].
This test method is sensitive to the application of the specimen to the steel plate,
the level of tack cannot be quantified, and effects of AFP process parameters cannot
be taken into account.

A frequently used principle is the probe tack test method [24]. It is based on the
standard ASTM D2979 for pressure-sensitive adhesive (PSA) [134]. Fig. 2.5 illus-
trates the basic principle: in the compression phase, the probe is pressed onto the
specimen with a controlled force followed by a defined dwell time. In the separation
phase, the probe is removed with a controlled rate and the force counteracting the
separation is measured [134]. Common readings from the probe tack test are the
maximum force F_{max} and the work of adhesion W_{adh} which is the integral under
the force-displacement curve from the start of the separation to full separation [36]
— see Fig. 2.5 right. Another measurement value from probe tack tests is the tack
stiffness F/d which corresponds to the force per displacement from the start of
separation to the maximum force. This value is used as input for analytical and
numerical tack models [31, 126, 135]. To increase comparability, the measurement
values from the probe tack test are commonly divided by the contact area.
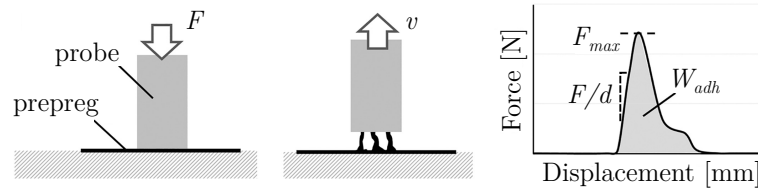
Figure 2.5: Scheme of probe tack test: compression, separation, evaluation (from left to right), adapted from [24]

In early studies, the probe tack test was implemented using a universal testing machine (UTM) combined with heating chambers [28, 34, 40, 53, 121–124]. More recently, rheometers were used to perform the probe tack test which offer reliable temperature control and accurate force measurement at low forces [36, 51, 125–127].

The second frequently used principle is the peel test principle which is also common for PSA — see Fig. 2.6. After applying a specimen to a substrate, the specimen is clamped and peeled off while the peel force is measured. Typical configurations are the 90° peel test [129, 136] — Fig. 2.6 left, the floating roller peel test [30, 128, 137] — Fig. 2.6 middle, and the T-peel test [49, 138]. Readings from peel tests are the average peel force $F_\varnothing$ and in some cases the work of adhesion W_{adh} — see Fig. 2.6 right. To increase comparability, the measurement values from peel tack tests are commonly divided by the width of the specimen. The described peel tests which are based on standards for PSA are sensitive to the specimen application method and the stiffness of the specimen which is considerably higher than that of PSA.
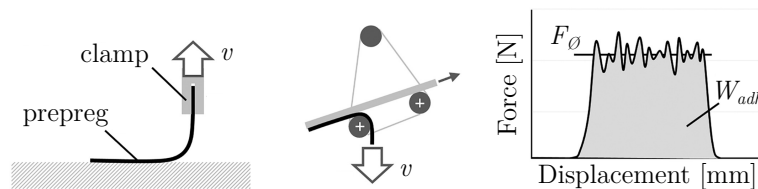
Figure 2.6: Schemes of peel tests: 90° peel test, floating roller peel test, evaluation (from left to right), adapted from [24]

In a frequently cited publication, Crossley et al. [130] introduced a modification of the floating roller peel test: they combined the peel test with a replication of the automated material deposition creating a single-stage peel test — see Fig. 2.7. By this, they are able to investigate the influence of deposition process parameters like lay-up rate and compaction force and to measure the peel force at the moment of deposition instead of afterwards. The test method is implemented in a UTM combined with a heating chamber for temperature control [130]. To account for the bending stiffness of the specimen, the first part of the specimen is covered with

a release film at the bottom and the second part is in contact with the substrate. The difference between measured force between the two parts of the specimen corresponds to the tack force — see Fig. 2.7b. Crossley et al. [110] subsequently carried out rheology measurements on the neat resin of their investigated material to obtain time temperature superposition (TTS) data and create master curves for the process parameter dependent peel force. The single-stage peel test has been used by fellow researchers in recent publications investigating effects of substrate, process parameters, and out-time [35, 37].

(a) Functional principle   **(b)** Evaluation
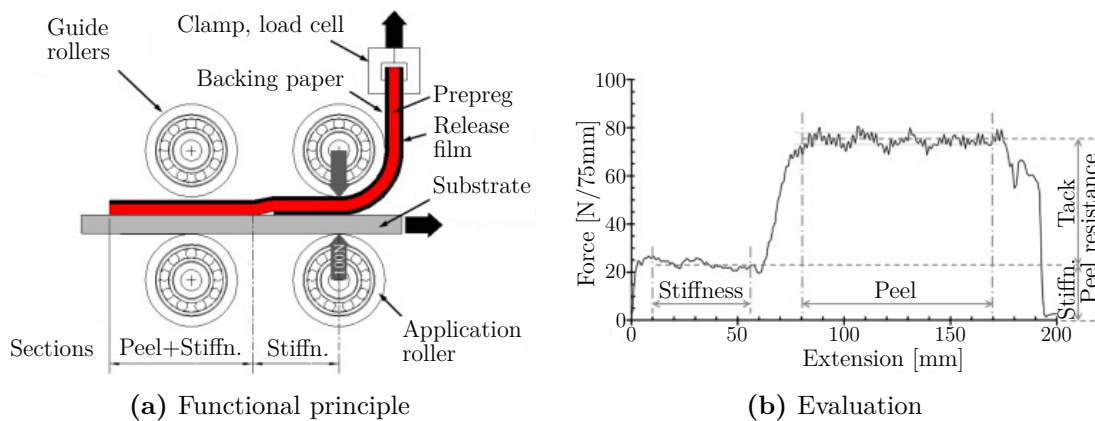
Figure 2.7: Single-stage peel test, adapted from [110]

Besides probe and peel tests, several other measurement principles have been developed. Nguyen and Krombholz [65] manufactured single lap shear specimens via AFP and tested them in a self-constructed test bench. Later, Nguyen and Delisle [132] presented a self-constructed tack measurement system which is mounted on an industrial robot. The system pulls an AFP-manufactured specimen off a substrate in a way that the shear force to remove a laid up prepreg tow from the substrate can be measured. Böckl et al. [66] developed a friction tack test in which the material is conveyed through a loaded pair of rollers and the induced transverse friction force is interpreted as an indicator for the tack. Since it is a continuous measurement principle, the system has the potential to be integrated into the material feed of an AFP machine serving as an online monitoring system for the tack [24]. Rajan et al. [133] introduced a rigid double cantilever beam (DCB) test for the characterization of Mode I and Mode II traction-separation laws for cohesive separation of prepreg tows. By this, they measured the cohesion of two prepreg tows to each other which were pressed together at an elevated temperature using a pneumatic press and a heat gun.

Degree of impregnation

Typical characterization methods for the degree of impregnation are microscopy analyses ranging from optical microscopy to X-ray microtomography — referred to as micro CT — and scanning electron microscopy (SEM) [61, 139]. Other characterization methods include mercury porosimetry [21] and a simple water pickup test which is used during prepreg production [13].

Surface roughness

Lukaszewicz and Potter [18] measured the surface roughness of uncured prepreg optically using a profilometer which allows for a non-contact measurement while Sun et al. [140] used a conventional profilometer which measures tactilely.

Specific heat capacity

The specific heat capacity is generally characterized according to ASTM E1269 - 11 [141] or DIN EN ISO 11357-4 [142] using (temperature modulated) DSC [67, 68, 71].

Thermal conductivity

Characterization methods for the thermal conductivity can be categorized in steady-state and transient methods [73]. The hot-guarded plate technique [143] is a steady-state method which has been used to determine the conductivity of partially cured specimens [144]. In transient methods, the response to periodic heating is measured [73]. Common variants of transient methods are using a planar geometry [69, 71], using a laser flash — laser flash analysis (LFA) [67, 145], or using a hot-wire/line-source method [68, 146]. Struzziero et al. [73] introduced a new transient method and apparatus that allows for the measurement of curing resins in a cylindrical container. Here, periodic heating is applied via a copper block surrounding the cylindrical container while a thermocouple (TC) in the center of the container measures the response. As some of the methods measure the thermal diffusivity α_{diff}, the thermal conductivity k has be calculated using the density ρ and the specific heat capacity c_p as

$$k = \rho \, c_p \, \alpha_{diff}. \tag{2.4}$$

Tensile modulus and strength

Tensile properties in the cured state are usually determined by tensile tests, for instance according to ASTM D3039 / D3039M-17 [147]. Belhaj and Hojjati [31] conducted tensile tests on uncured prepreg samples. Even though they did not report it, slippage of the fibers due to the viscous resin is expected. When resin properties are available, the tensile modulus of the prepreg in fiber direction E_1 can be determined using the rule of mixture as [148]

$$E_1 = \phi \, E_f + (1 - \phi) \, E_m \tag{2.5}$$

where ϕ is the fiber volume fraction, E_f is the tensile modulus of the fibers (given in data sheets), and E_m is the tensile modulus of the matrix.

Transverse tensile modulus and strength

The transverse tensile modulus E_2 can be determined in tensile tests perpendicular to the fiber direction using a universal testing machine combined with a heating chamber or a DMA [22, 74]. Because of the low forces, slippage of the sample is much less likely as compared to E_1 measurements which are mainly influenced by the fiber stiffness. Margossian et al. [74] compared UTM tests to DMA tests indicating good agreement of the compared results. Furthermore, they highlighted advantages of DMA tests: a better control of environmental test conditions, time saving due to reduced efforts to mount/unmount specimens, and material saving since smaller specimens can be used.

In-plane shear modulus and strength

The in-plane shear or longitudinal intra-ply shear modulus has been characterized using several different test principles — see Fig. 2.8.

By using a picture frame — Fig. 2.8a — in which all edges of the specimen are clamped, there is no slippage of the material and the shear properties can be measured via the axial force and the angle of the stretched frame [76]. Leutz [82] conducted picture frame test experiments with uncured UD specimens. However, twisting and bending of the tapes caused by the clamping led to out-of-plane wrinkling and therefore invalid results [82, 83].
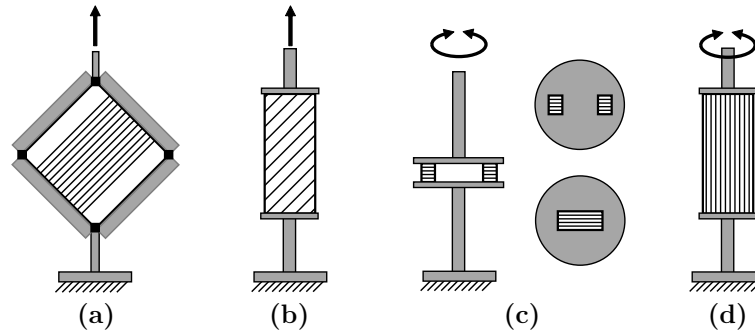
Figure 2.8: Test principles for longitudinal intra-ply shear characterization: a) picture-frame test setup, b) off-axis tension test setup, c) rotational parallel platens test method, d) torsion bar test method, as described in [77, 83, 149]

The principle of off-axis tension — Fig. 2.8b — is used in the bias extension test for cross-ply specimens [26, 79] and in the off-axis test for multilayer UD specimens [22, 84]. In the bias extension test principle, a bidirectional specimen is loaded with a tension force that is non-parallel to the direction of the reinforcing fibers [150–152]. By measuring the displacement and the load, shear properties can be determined. This test method has been used by several authors for cross-ply specimens of uncured UD prepreg material [26, 31, 79]. However, slippage between the layers and uncontrolled distortion of the specimens causing wrinkles can lead to invalid results before the critical load is reached [77].

In the off-axis test introduced by Potter [22] and subsequently used by Wang et al. [84] a multilayer UD specimen is loaded off axis using a UTM. The shear stress is determined by the load-displacement result and the off-axis angle — see [84]. Using this test principle, Wang et al. were able to investigate the influence of test rate and test temperature on the shear properties. This test setup, however, requires a UTM, digital image correlation (DIC), and a heating chamber.

Margossian et al. [81] introduced the Thin Plate Torsion Test which is based on the principle of rotational parallel platens — see Fig. 2.8c. Here, single layer specimens are subjected to a rotational load by parallel platens using a rheometer. By varying the applied shear angle and aspect ratio of the specimens, the shear properties can be determined — see [81].

In the Torsion Bar Test — see Fig. 2.8d, which was developed by Haanappel and Akkermann [77], a prismatic bar is loaded torsionally in a rheometer. By using UD specimens with a square cross-section and aligning the fiber direction parallel to the rotational axis, the shear properties can be determined — see [77]. Haanappel and Akkermann demonstrated the applicability to molten thermoplastic specimens followed by Margossian's demonstration of the applicability to uncured UD prepreg material [83].

Poisson's ratio

The Poisson's ratio of neat resins can be determined either direct or indirect [88]. In direct measurements, the transverse and axial strains are measured optically [153], with strain gauges [154], or with contact extensometers [155]. Limitations of these methods include the direct contact occurring during strain gauge application or extensometer measurement [88]. In indirect measurements, two different independent viscoelastic parameters like the elastic modulus and the shear modulus are measured to determine the Poisson's ratio [155]. Saseendran et al. [88] conducted uniaxial relaxation tests on neat epoxy resin to measure the axial stress relaxation and the lateral strain changes and O'Brien et al. [87] performed uniaxial tension tests combined with measurements by Moiré interferometry.

Bending stiffness

Since there is no test standard for the bending characterization of uncured prepreg material, several different solutions can be found in literature. Tab. 2.7 summarizes the main principles. Because of the shortage of prepreg investigations, tests for molten fiber-reinforced thermoplastics and dry fabrics are considered, too.

Potter [22] bent multilayer UD specimens over a radius forming tool, measured the forming load, and assessed the onset of wrinkles qualitatively. However, he did not determine a bending stiffness. Wang et al. [89] subjected multilayer UD specimens to an axial compression load until buckling occurred and evaluated the load and the shape of the buckled specimen. Through a theoretical model, they contributed to further understanding the bending behavior of viscous composites. Erland et al. [156] introduced a new test principle using a single cantilever configuration in a DMA. Their intention was, however, to determine the shear stiffness instead of the bending stiffness. Rajan et al. [157] conducted short term creep three-point bending experiments with single layer UD specimens in a DMA. They determined the creep compliance and demonstrated that TTS can be used to obtain master curves for the material response. Banks et al. [30] and Bloom et al. [90] used the standard ASTM D1388-18 [158], which is intended for dry fabrics, to characterize woven prepreg specimens. In this straightforward test, the sample is supported at one end on a horizontal surface and is then pushed over the edge of the surface at a predefined speed. Due to gravity, the free end of the sample bends until it reaches a board tilted at a defined angle, i.e. 41.5 °. The measured value is the free length of the sample at the moment of first contact with the board [158]. This test requires the assumption of linear elastic behavior and small deformation

both of which restrict the application to prepregs [91]. Alshahrani and Hojjati [91] introduced a novel single cantilever test in which an external load is applied via a linear actuator. They determined the bending stiffness by measuring the applied load a well as the curvature of the bent specimen following the elastica theory of a flexible uniform cantilever beam [159].

Table 2.7: Literature review of bending test methods (CF: carbon fiber, DMA: dynamic mechanical analysis, EP: epoxy, ext.: external, GF: glass fiber, KES-F: Kawabata evaluation system for fabrics, TP: thermoplastic, UD: unidirectional, UTM: universal testing machine)

Ref.	Test type	Device	Material
[22]	Three-point bending	Custom-built	CF-EP prepreg, UD
[89]	Buckling	UTM	CF-EP prepreg, UD
[156]	Single cantilever, ext. load	DMA	CF-EP prepreg, UD
[157]	Three-point bending	DMA	CF-EP prepreg, UD
[30, 90]	Single cantilever, gravity	Standard test apparatus	GF-, CF-EP prepreg, weave
[91]	Single cantilever, ext. load	Custom-built	CF-EP prepreg, weave
[160]	Single cantilever, gravity	Custom-built	TP
[161, 162]	Single cantilever, ext. load	Rheometer	TP
[163]	Three-point bending	DMA	TP
[162, 163]	Dual cantilever	DMA	TP
[164]	Single cantilever, gravity	Custom-built	Dry fabric
[158]	Single cantilever, gravity	Standard test apparatus	Dry fabric
[165]	Single cantilever, gravity	Custom-built	Dry fabric
[166]	Single cantilever, ext. load	KES-F	Dry fabric
[167]	Single cantilever, ext. load	Custom-built	Dry fabric

Several authors proposed test methods for the characterization of fiber-reinforced thermoplastics including single/dual cantilever tests and three-point bending tests conducted using rheometers, DMAs, or custom-built devices [160–163]. Even though some test principles might be useful for the characterization of uncured thermoset prepreg, limitations result from the low inherent stability of uncured

prepreg during sample mounting (generally at RT) compared to thermoplastics as well as from the tackiness of the specimen.

For dry fabrics, ASTM D1388-18 or variations of it are commonly used [164, 165, 167]. Lomov et al. [166] used single cantilever tests as part of the Kawabata evaluation system for fabrics (KES-F), which is a considered standard tool for a holistic evaluation of textile fabrics deformability [168]. However, due to the prepreg's time-dependent viscoelastic behavior and the handling challenges because of the tackiness, a transfer of dry fabric test principles to uncured prepregs may not be appropriate.

2.2 Thermoset automated fiber placement (TS-AFP)

During thermoset automated fiber placement (TS-AFP), several prepreg slit-tapes are laid up by a placement head with a defined lay-up rate v, applying a defined compaction force F and a defined IR emitter power P_{IR} [6, 13, 169]. The lay-up rate is realized by manipulation of the placement head, the compaction is realized by force application via a compaction roller, and the IR emitter power is applied by an IR emitter — see Fig. 2.9.
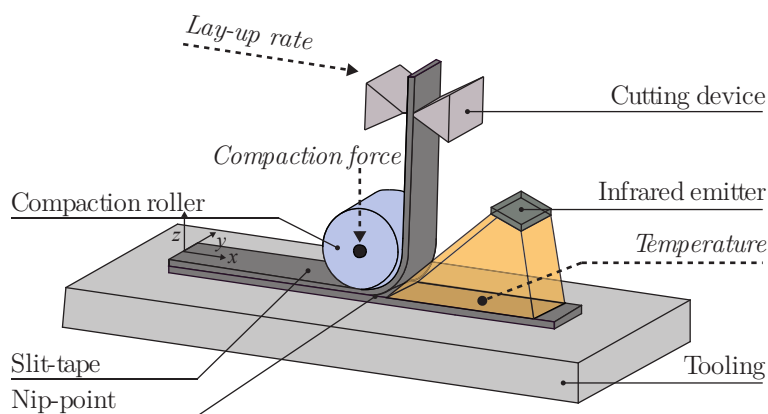
Figure 2.9: Functional principle of thermoset automated fiber placement [149]

The placement head comprises a feed unit to feed each slit-tape individually to the nip-point and a cutting unit to cut each slit-tape individually perpendicular to the fiber direction. The process is used to place tapes track by track and layer by layer automatically on a mold/tooling to build the prepreg preform. Because of the degree of freedom of the placement head, arbitrary fiber directions and even curved paths can be realized. To consolidate the part, the AFP process step is followed by

autoclave curing where the prepreg is cured at defined temperature and pressure conditions. There are several different configurations for AFP machines [6, 13, 169]:

- The placement head can be manipulated by an industrial robot or a gantry system.

- The slit-tape spools can be stored internally — directly at the placement head — or externally — in a cooled creel.

- The maximum number of tapes is determined by the machine architecture. Typically, 8, 16, or 32 tapes are processed simultaneously.

- The tape width — typically 1/8", 1/4", or 1/2" — is determined by the machine architecture.

- Besides IR emitters, other heat sources include hot gas torch, laser, pulsed light, LEDs [170]

The tooling onto which the slit-tapes are placed is usually made of steel, aluminium, rigid foam, or CFRP. Its lay-up surface is either blank, cleaned, and coated with a release agent or covered with a film. Besides TS-AFP, there is thermoplastic automated fiber placement (TP-AFP) with thermoplastic fiber-reinforced slit-tapes and dry fiber placement (DFP) with bindered dry tows [169].

2.2.1 Material process interaction

The general objective of TS-AFP is the defect free lay-up of prepreg slit-tapes. To meet efficiency demands, the lay-up is expected to be as fast as possible. Other demands are a low void content in the laminate, a certain degree of compaction, and no excessive curing of the resin. By this, the optimum part quality can be achieved during autoclave curing. To fulfill these requirements, the interaction of material properties with process parameters and conditions has to be considered. Besides the process parameters v, F, and P_{IR}, the lay-up trajectory (curvature), the compaction roller (compliance, surface), the tool (thermal properties, surface), and the ambiance (temperature, humidity) are essential — see Tab. 2.8.

Table 2.8: Parameters in TS-AFP

Category	Parameter	Symbol
Process parameter	Lay-up rate	v
	Compaction force	F
	IR emitter power	P_{IR}
Lay-up trajectory	Curvature	κ
Roller	Roller compliance	δ_{roller}
	Roller surface	-
Tool	Emissivity	ε_{tool}
	Thermal conductivity	k_{tool}
	Tool surface	-
Ambiance	Temperature	T_{amb}
	Relative humidity	$\phi_{RH,amb}$

The parameters in TS-AFP result in physical properties which, in turn, affect the material properties during manufacturing. Their relation is summarized in Tab. 2.9.

The compaction force F and the time of intimate contact t_{intim} ($f(v, F, \delta_{roller})$), which is the time the roller presses the tape onto the tool, influence the tack as they affect the surface wetting by the resin [24, 35, 171–173]. The lay-up time t_{layup} ($f(v)$) in combination with the material temperature T ($f(v, P_{IR}, T_{tool}, T_{amb})$) affect the degree of cure α of the resin after lay-up as heat input initiates cure [8]. The temperature also affects the viscosity η, the tack, the transverse tensile modulus E_2, the shear modulus G_{12}, the bending stiffness $E_{flex}I$ because of its influence on the molecular mobility and the stiffness of the resin. Furthermore, the temperature affects the specific heat capacity c_p and the thermal conductivity k as they are temperature dependent [67]. The curvature of the lay-up trajectory κ in combination with the lay-up rate v lead to load rates in different directions: the strain rate perpendicular to the fiber direction $\dot{\varepsilon}_2$ affects the transverse tensile modulus [74], the shear rate $\dot{\gamma}$ affects the shear modulus [84], and the bending rate $\dot{\varphi}$ affects the bending stiffness [91]. Several other influences affect the tack: the tool temperature and the tool surface influence the surface wetting, the roller surface influences the adherence to the roller, which should be as low as possible, and the ambient conditions T_{amb} and $\phi_{RH,amb}$ influence the resin and therefore the tack [24, 35].

Table 2.9: Influences of TS-AFP on material properties

Influence	Symbol	Source parameter	Influence on							
			α	η	Tack	c_p	k	E_2	G_{12}	$E_{flex}I$
Compaction force	F	-			●					
Lay-up time	t_{layup}	v	●							
Time of intimate contact	t_{intim}	v, F, δ_{roller}			●					
Material temperature	T	$v, P_{IR},$ T_{tool}, T_{amb}	●	●	●	●	●	●	●	●
Strain rate perp. to fiber direction	$\dot{\varepsilon}_2$	v, κ						●		
Shear rate	$\dot{\gamma}$	v, κ		●					●	
Bending rate	$\dot{\varphi}$	v, κ								●
Tool temperature	T_{tool}	$\varepsilon_{tool}, k_{tool},$ T_{amb}			●					
Tool surface	-	-			●					
Roller surface	-	-			●					
Ambient temperature	T_{amb}	-			●					
Ambient humidity	$\phi_{RH,amb}$	-			●					

Subsequently, only the influences that are adjustable during manufacturing, namely v, F, and P_{IR}, are considered relevant for the optimization of the material usage and the manufacturing time within the scope of this thesis. The influences from roller, tool, and ambiance are considered as given inputs while the lay-up trajectory is used for verification.

2.2.2 Lay-up scenarios

AFP lay-up scenarios can be distinguished by the resulting lay-up trajectory or path. In straight or geodesic paths, the curvature is zero. In non-geodesic paths like constant angle paths or variable angle paths, the curvature is constant or variable, respectively [174]. The cause for a non-geodesic path is determined by the

path planning. On a tool surface with complex geometry, a fixed angle path (with respect to a global coordinate system) can lead to non-geodesic paths. On a flat tool surface, the need to create a variable stiffness laminate can be the motivation to create steered paths. Depending on the path and the tool geometry, several different material property-related lay-up defects can occur [24]. Generalized, these defect causes are steering — leading to in-plane waviness, out-of-plane buckling, tape pull-up, a concave tool geometry — leading to bridging, and a convex tool geometry — leading to tape peel-off. Steering defects are illustrated in Fig. 2.10.
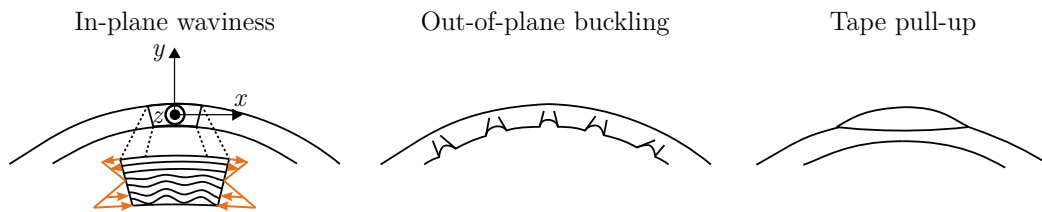
Figure 2.10: Top view of steering defects including simplified load distribution in tape, adapted from [6, 149]

Here, the in-plane defect in-plane waviness is the first occurring defect which is followed by the out-of-plane defects buckling and tape pull-up [149]. In-plane waviness and out-of-plane buckling are caused by the compressive forces at the inside of the tape and pull-up is caused by tensile forces at the outside of the tape [6]. All steering defects affect the mechanical properties of the cured part — see review in [175]. Therefore, they may lead to machine downtime and scrapping of the material when they exceed an acceptable level for the cured part properties. The occurrence of steering defects during AFP has been the subject of numerous studies with different materials, process parameters, defect measurement techniques etc. [23, 31, 149, 176–185].

The defects on concave and convex geometries are shown in Fig. 2.11.
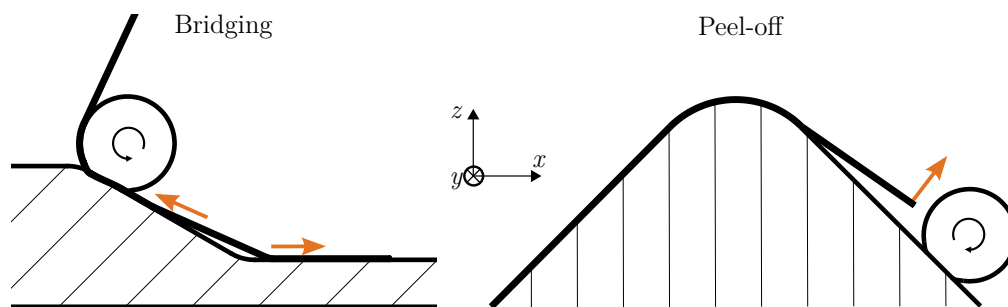
Figure 2.11: Side view of defects due to concave (left) and convex tool geometry (right) including simplified loads

Bridging occurs when a tape does not adhere to the surface of a concave tool. Tensile forces in the tape may lead to a resulting force perpendicular to the surface

which counteracts the tack between tape and substrate [24, 175]. Peel-off occurs due to the stiffness of the tape at a convex corner being higher than the tack. Both defects lead to machine downtime, manual rework, and eventually scrapping of the material [24]. No experimental studies on the occurrence of bridging and tape peel-off have been found in literature. There is only one approach by Lichtinger et al. [186] to describe the deformation of the compaction roller in different geometric constellations.

Among the defects that are generally not related to the material properties are gaps/overlaps, tow misalignment, twisted tow, splice, foreign object debris (FOD), fuzzballs — see reviews in [174, 175, 187, 188].

2.2.3 Lay-up defect prediction

Because of the relevance during AFP manufacturing and the impact on mechanical properties of the cured part, various approaches have been proposed to predict the occurrence of lay-up defects.

2.2.3.1 Steering defects prediction

Out-of-plane buckling is the defect that occurs when loads in the tape cannot be absorbed by in-plane waviness anymore and it is a more common defect than tape pull-up. Therefore, steering defect models focus on the prediction of out-of-plane buckling (also referred to as wrinkling).

Analytical models

In 2011, Beakou et al. [23] introduced an analytical model — describing the out-of-plane buckling as a plate buckling problem — which has been refined by several authors afterwards. In a series of experiments, they found that out-of-plane buckling occurs after falling below a critical steering radius and that the buckles were distributed uniformly. Therefore, they assumed that one buckle can be considered isolated as orthotropic plate buckling with the inner edge of the tape being free and the other three edges being simply supported. The connection between tape and substrate is modelled as an elastic foundation of normal stiffness. The plate is subjected to combined in-plane bending and tension in the tape and the load distribution is dependent on a load parameter α_{load}. This accounts for the fact the neutral axis is not necessarily in the middle of the tape. To derive closed-form solutions, the Ritz method [189] is used to evaluate the critical buckling load at which

the out-of-plane buckling is initiated. Assumptions are that classic laminated plate theory, the Kirchhoff-Love hypothesis (normals to the mid-plane before steering remain normal to the deformed mid-plane) [190], and von Kármán approximations (in-plane effects are infinitesimal compared to the effect of the out-of-plane deflection) [191] apply. Finally, the critical steering radius R_{crit} at which buckling occurs can be determined via a relationship between bending moment and lay-up radius. For the detailed derivation and the exact formulaic relationships, the author refers to Beakou et al.'s publication [23].

A first refinement of Beakou et al.'s model was published by Hörmann [149]. He emphasizes on the determination of the position of the neutral axis, which was only based on assumptions in Beakou et al.'s model. Hörmann states the in-plane waviness, which begins to occur even at small curvatures on the inside of the tape, leads to angular deviations in the fibers which, in turn, leads to a decrease in the stiffness of the tape on the inside. This is accompanied by a displacement of the neutral axis toward the outside of the tape. To determine the position of the neutral axis, Hörmann uses a strain energy formulation. The area from the inside of the tape to the neutral fiber is characterized by compression, normal shear, and shear due to the development of in-plane waviness. The outer region, on the other hand, is dominated by elongation due to tensile stresses. The strain energy thus depends on the position of the neutral axis and the in-plane waviness. By discretizing the tapes along the width, the neutral axis can be shifted step wise. This is used to calculate the strain energy for each possible position of the neutral axis. The constellation with the lowest strain energy finally indicates the position of the neutral axis.

Another refinement of Beakou et al.'s model was implemented by Matveev et al. [177]. Even though their motivation was DFP, their assumptions can still be transferred to TS-AFP. The main adjustment they proposed, was the boundary condition at the radial edges of the orthotropic plate being clamped instead of simply supported. The inner edge of the tape remained free and the outer edge remained simply supported.

Belhaj and Hojjati [31] subsequently refined Matveev et al.'s model. To account for shear related correlations, they modelled the connection between tape and substrate using a Pasternak elastic foundation [192]. In this foundation, one elastic spring layer is connected to an elastic shear layer which accounts for shear interactions in the spring layer. By this, they were able to achieve better agreement between model and experimental results compared to Beakou et al.'s work.

The latest modification of Beakou et al.'s model was published by Bakhshi and Hojjati [181] as a refinement of Belhaj's model, accounting for the time dependence

of the buckle formation. They assume that the foundation is influenced by the viscoelastic behavior of the tack replacing the elastic Pasternak foundation with a viscoelastic foundation. The underlying principle is illustrated in Fig. 2.12.
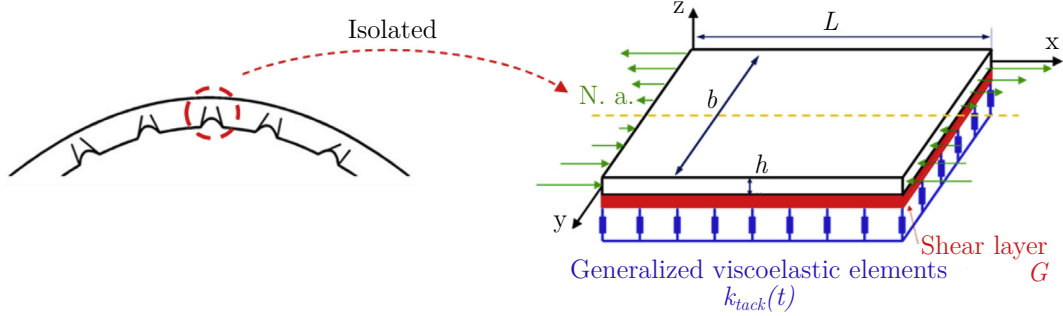
Figure 2.12: Scheme of Bakhshi's model for the prediction of time-dependent out-of-plane buckling formation [181]

The resulting critical load P_{crit} at which buckling occurs is described as

$$
\begin{aligned}
P_{crit}(t) = \frac{1}{6 - \alpha_{load}} \Bigg[& 24D_{11} \left(\frac{\pi m}{L}\right)^2 + 90D_{22} \left(\frac{L}{\pi m b^2}\right)^2 + 160D_{66} \left(\frac{1}{b}\right)^2 \\
& -40D_{12} \left(\frac{1}{b}\right)^2 + G\left(6 + 30\left(\frac{L}{\pi m b}\right)^2\right) + \frac{k_{tack}(t)}{2}\left(\frac{3L}{\pi m}\right)^2 \Bigg]
\end{aligned}
\tag{2.6}
$$

where

$$
D_{11} = \frac{E_1 h^3}{12(1 - \nu_{12}\nu_{21})} \tag{2.7}
$$

$$
D_{12} = \nu_{21} D_{11} \tag{2.8}
$$

$$
D_{22} = \frac{E_2}{E_1} D_{11} \tag{2.9}
$$

$$
D_{66} = \frac{G_{12} h^3}{12} \tag{2.10}
$$

$$
G = G_{12} h \tag{2.11}
$$

and m is the number of waves in a buckling mode, L the length, b the width, h the height of the orthotropic plate, $k_{tack}(t)$ the time-dependent tack stiffness, ν_{12} and ν_{21} the Poisson's ratios. Furthermore, the relation between maximum load at the inner edge of the plate and the steering radius R is

$$P_0 = \frac{E_1 hb}{R\alpha_{load}}. \tag{2.12}$$

For the load parameter α_{load}, they use the same estimation as Beakou et al. [23] which is illustrated in Fig. 2.13.
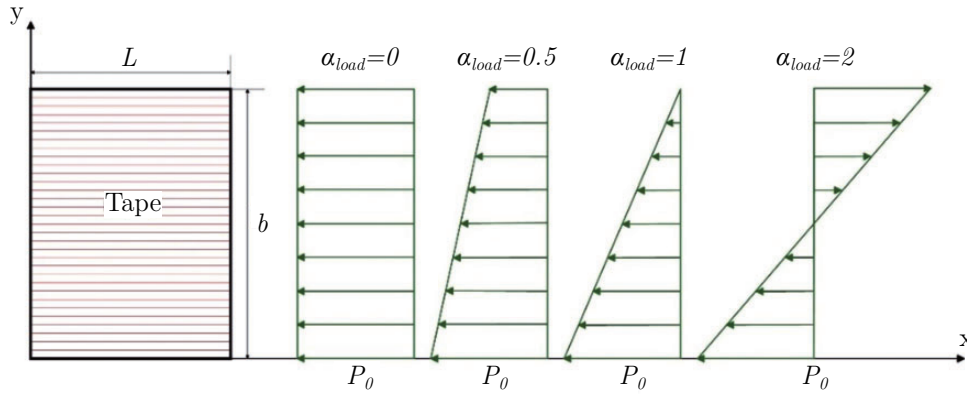
Figure 2.13: Correlation between stress distribution in the tape and load factor α_{load} [31]

The time dependence of the tack is modelled using a Prony series:

$$k_{tack}(t) = k_{tack,\infty} + \sum_{i=1}^{n} k_{tack,i} \cdot exp\left(\frac{-t}{\tau_i}\right) \tag{2.13}$$

where $k_{tack,\infty}$ is the long term modulus once the interface is fully relaxed, τ_i are the relaxation times and $k_{tack,i}$ are the elastic moduli in series with dashpots. Bakhshi and Hojjati state that one term from the series was sufficient to capture the time-dependent behavior of the buckle. The model shows good agreement with experimental investigations on buckling. However, it should be noted that the parameters used for the tack were not determined experimentally, but were adjusted to achieve maximum agreement between model and experiments.

Numeric models

Apart from the analytical models, there are several approaches for the numerical/simulative prediction of steering-related defects.

Bakhshi and Hojjati [180] developed a finite element modeling approach including a surface-based cohesive zone modeling technique using a bilinear traction-separation law to model the tack. They obtained tack data from probe tack tests and assumed the same traction-separation law for both the normal and in-plane shear directions. Rajan et al. [133], however, state that this is not accurate.

Forghani et al. [126] used a similar approach to model defect formation trends. Instead of using cohesive zone modeling for the tack, they developed an individual rate-dependent decohesion tack model describing a mixed-mode opening and an exponential decay for the post-peak decohesion response.

Wehbe et al. [183] developed a numerical solution to visualize buckles on curved paths. They implemented equations for an arbitrary surface, the path, and the buckled tape and used the Ritz method analogously to Belhaj and Hojjati [31] to obtain the buckle wavelength as a function of the path curvature.

Rajan et al. [193] developed a finite element-based tape placement and adhesion model. They model the bonding of the tape to the substrate surface through a sticky contact definition while delamination and wrinkling are predicted through incorporation of measured mixed mode cohesive traction-separation laws for contact and bonding of the tape and substrate.

2.2.3.2 Bridging prediction

To the best of the author's knowledge, there are no models predicting bridging. Lichtinger et al. [186], however, described the deformation of the compaction roller in different geometric constellations at a ramp geometry. Assuming a flexible compaction roller and Hertzian stress [194], the compaction force F is

$$F = \frac{\pi}{4} \cdot \frac{E_{roller}}{1 - \nu_{roller}^2} \cdot b_{roller} \cdot d \tag{2.14}$$

where E_{roller} is the roller's Young's modulus, ν_{roller} is the roller's Poisson's ratio, b_{roller} is the roller width, and d is the required roller indentation. The authors distinguish between geodesic (geo) and non-geodesic (ngeo) paths. From the relation between path angle α_{path} and ramp angle θ_{ramp} result the Dihedral angles φ and the required roller indentation d as follows

$$\varphi_{geo} = \arccos\left(\frac{\frac{-\sin\vartheta}{\tan\theta_{ramp}} - \frac{\cos\vartheta}{\sin\theta_{ramp}\tan\vartheta}}{(\csc^2\vartheta \csc^2\theta_{ramp})^{0.5}}\right) \tag{2.15}$$

$$\varphi_{ngeo} = \arccos\left(\frac{-\csc\vartheta\cot\theta_{ramp}}{(\csc^2\vartheta\cot^2\theta_{ramp} + 1)^{0.5}}\right) \tag{2.16}$$

$$\csc\vartheta = \frac{1}{\sin\vartheta} \tag{2.17}$$

$$\vartheta = 90° - \alpha_{path} \tag{2.18}$$

$$d = \frac{b_{roller}}{2\tan\left(\frac{\varphi}{2}\right)}.$$ (2.19)

Since the Hertzian theory only applies to small deformations and isotropic materials, Lichtinger et al. also implemented a finite element method (FEM) model with which they were able to obtain a better prediction of the roller deformation. However, the occurrence of bridging was not directly addressed. Other works regarding roller deformation have been published by Chu et al. [173], Jiang et al. [195, 196], Bakhshi and Hojjati [172], and Qu et al. [197]. Again, none of them considered the lay-up defect bridging.

2.2.3.3 Peel-off prediction

To the best of the author's knowledge, there are no models predicting the tape peel-off in TS-AFP. One possible approach is the use of the strain energy due to bending U_B assuming elastic bending [198]:

$$U_B = \frac{1}{2}B \int_{\frac{1}{2}l}^{-\frac{1}{2}l} \kappa^2 dx$$ (2.20)

where B presents the bending stiffness, l is the arc length over the radius, and κ is the curvature.

2.3 TS-AFP system used in this thesis

The TS-AFP machine used in this thesis is a unique machine from CORIOLIS GROUP SAS (Queven, France) designated "Coriolis 1/8-TS-AFP." It is depicted in Fig. 2.14. The main components are the lay-up head which is manipulated by an industrial robot and the creel in which the material is stored during manufacturing. Details of the lay-up head are shown in Fig. 2.15.

The head is equipped with two IR emitters. Combined with the possibility to tilt the suspension of the silicone compaction roller, a bidirectional lay-up without turning the head can be realized. Within the creel, the material feed, and the lay-up head, the prepreg slit-tapes are cooled to around $10 - 15\ °C$ to avoid process errors resulting from the prepreg tack. The main AFP-related technical data of the machine are summarized in Tab. 2.10.

All eight tapes can be fed and cut individually enabling a near-net-shape lay-up at the edges of the laminate. The path planing and programming of the machine is done using the offline programming software CATFiber from CORIOLIS GROUP SAS which is fully integrated in CATIA V5 by Dassault Systèmes.
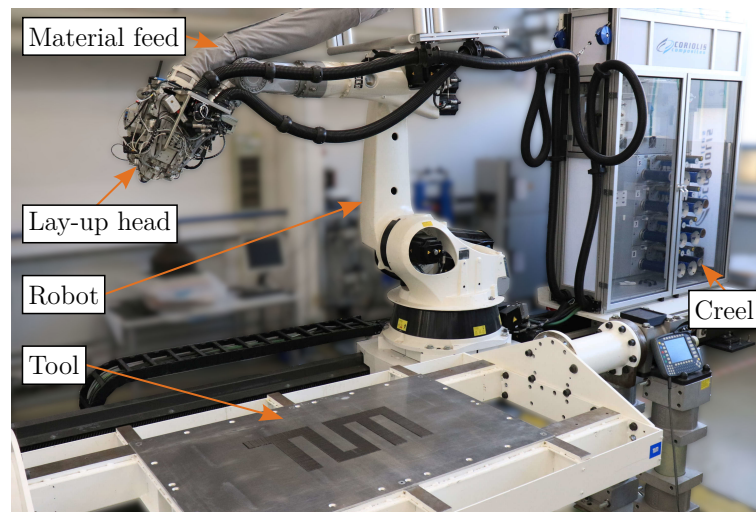
Figure 2.14: Coriolis 1/8-TS-AFP machine used in this thesis
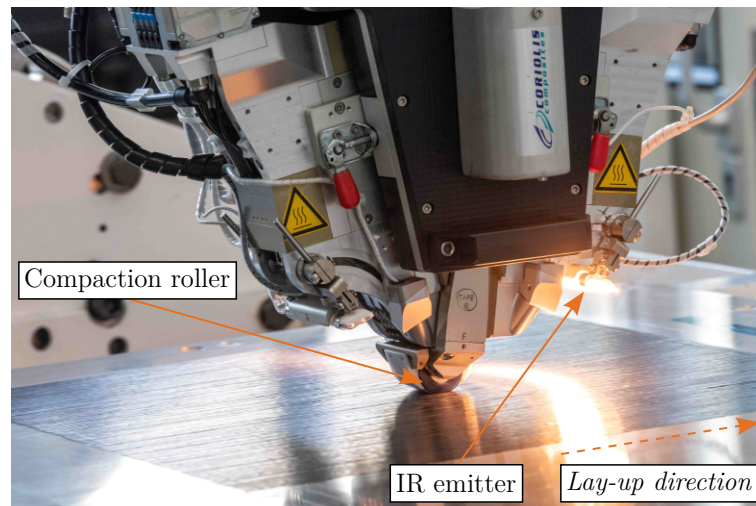
Figure 2.15: Coriolis 1/8-TS-AFP lay-up head

Table 2.10: Main characteristics of Coriolis 1/8-TS-AFP machine

Characteristic	Value
No. of tapes	8
Tape width	1/8"
Heat source	IR emitter
Max. IR emitter power	430 W
Max. compaction force	500 N
Min. tape length	63 mm
Max. lay-up rate	0.5 m/s
Lay-up direction	bidirectional

3 Material characterization

As discussed in the state of the art, prepregs are subject to changes affecting several different properties. To quantify the extent of these changes and to provide inputs for defect prediction models, the relevant prepreg properties and their dependence on out-time and material modification are characterized systematically. This chapter presents the obtained experimental results for the degree of cure (Sec. 3.2), the tack (Sec. 3.3), the thermal properties specific heat capacity and thermal conductivity (Sec. 3.4) as well as for the mechanical properties transverse tensile modulus, in-plane shear modulus, and bending stiffness (Sec. 3.5). Each section is divided into test method and results. The test methods may either be available from a standard or existing methods have to be evaluated — e. g. in-plane shear Sec. 3.5.2. In case no existing methods are available, new methods are developed and implemented — e. g. peel tack Sec. 3.3.2, bending stiffness Sec. 3.5.3. Subsequently, the elaborated prepreg characterization procedure is applied to the investigated properties and the influence of out-time and of modification through fillers in the matrix are discussed in the results sections. The chapter concludes with a summary of important outcomes in Sec. 3.6.

Tab. 3.1 summarizes the prepreg properties that are considered for the material characterization. The degree of cure DoC is the baseline property for the monitoring of out-time effects and therefore the aging of the material. In case the out-time is unknown, it can be estimated using the DoC as a reference. Even though the moisture content and the viscosity change, they are not considered in the material characterization as they are primary properties affecting other properties like tack and mechanical properties. Their influence on AFP defects is covered by the measurement of the affected properties. The tack is one of the main influences on the lay-up quality and the lay-up efficiency and it is strongly affected by material changes. Hence, the tack characterization is a focal point of the material characterization. According to results found in literature — see Sec. 2.1.3, the degree of impregnation and the surface roughness are not expected to change. This observation has been verified in preliminary trials [S6]. Therefore, they are not considered in the material characterization. The thermal properties are subjected to changes,

especially due to modification by fillers, which is why they are considered in the material characterization. They are no direct input parameters for the defect models — symbol ○ in Tab. 3.1, however, they affect other properties because of their temperature dependence: if thermal properties change and the same IR emitter power is used during AFP processing, the material temperature will be affected which, in turn, affects all temperature dependent material properties. Thus, the thermal properties are considered. Generally, mechanical properties in the uncured state of the prepreg are subjected to changes and they are relevant for defect models underlining the need to characterize them. Yet, there are two exceptions: the influence of change on the tensile modulus is negligible — see Sec. 2.1.3 — and the relevance of the Poisson's ratio on defect models is negligible as Rajan at el. [193] investigated in a parameter study of their model. Therefore, these two properties are not considered in the material characterization.

Table 3.1: Properties considered for material characterization (symbol ●: direct dependence, symbol ○: indirect input affecting other inputs)

Category	Property	Changing	Input for AFP models	Considered
Resin baseline	Degree of cure	●		●
	Moisture content	●		
	Viscosity	●		
	Tack	●	●	●
	Degree of impreg.			
Exterior	Surface roughness			
Thermal	Specific heat	●	○	●
	Thermal conductivity	●	○	●
Mechanical	Tensile modulus		●	
	Transv. tensile modulus	●	●	●
	In-plane shear modulus	●	●	●
	Poisson's ratio	●	●	
	Bending stiffness	●	●	●

3.1 Materials and process parameters

3.1.1 Materials

Three materials have been investigated: HexPly IM7/8552, an unmodified research material, and a modified research material. The research materials were manufac-

tured by the Department of Polymer Engineering of the University of Bayreuth
(UBT) who analyzed material properties in the cured state [10]. Tab. 3.2 gives an
overview of the materials.

Table 3.2: Characterized materials (D_{50}: particle diameter at 50 % in the cumulative distribution, FVC: fiber volume content, Mfr.: manufacturer, UBT: University of Bayreuth)

Mfr.	Fiber	Matrix	FVC	Name
Hexcel	IM7	8552	0.577	IM7/8552
UBT	Tenax HTS40	EPIKOTE Resin 496, XB3473	0.48	unmodified material
UBT	Tenax HTS40	EPIKOTE Resin 496, XB3473 with 15 $vol\%$ graphite $D_{50} = 18.4\ \mu m$	0.53	modified material

HexPly 8552 is a high performance amine cured, toughened epoxy resin [19] and
IM7 is a continuous, high performance, intermediate modulus, PAN based fiber
($E_1 = 276\ GPa$) [20] from Hexcel Corporation. Both are certified for the use in
primary aerospace structures. According to the data sheet, the tack life of 8552 is
ten days at room temperature and the out life is 30 days at room temperature [19].
To measure the influence of controlled out-time conditions on the material properties, IM7/8552 specimens were kept in a climate chamber (MKF 56 from BINDER
GmbH) at 21 °C and 40 % RH and tests were conducted at several different out-times. The *unmodified material* consists of Tenax HTS40 fibers ($E_1 = 240\ GPa$)
from Teijin Carbon Europe GmbH [199] and the tetraglycidylmethylenedianiline
(TGMDA) resin EPIKOTE Resin 496 from Hexion Inc. [200] which is cured with
the diethyltoluenediamine (DETDA) hardener XB3473 from Huntsman International LLC. The *modified material* consists of the same constituents as the unmodified material with the addition of 15 $vol\%$ platelet-shape graphite fillers from
Imerys Graphite & Carbon Switzerland Ltd. with a size of 18.4 μm (D_{50}: particle
diameter at 50 % in the cumulative distribution) [201]. The two research materials
had not been b-staged by the manufacturer. Therefore, they were b-staged at 60 °C
for six hours before the material characterization. Depending on the application,
IM7/8552 was used as 1/8" slit-tape or as parent tape from which specimens were
cut out. The unmodified and modified materials were not available as slit-tapes.
Therefore, specimens were cut out from parent tapes.

3.1.2 Process parameters

As described in Sec. 2.2.1, the process parameters have a significant influence on the material properties because of their temperature and rate dependence. To consider this influence within the material characterization, a set of TS-AFP process parameters was defined which was used during lay-up trials — see Chapter 4 — and which served as the framework for test parameters within the material characterization. The process parameters are listed in Tab. 3.3.

Table 3.3: TS-AFP process parameters for lay-up trials

Parameter	Symbol	Unit	Values
Lay-up rate	v	m/s	0.03; 0.06; 0.1
Compaction force	F	N	200; 400
IR emitter power	P_{IR}	W	150; 350

All parameters result from experiences from preliminary lay-up trials. During AFP, the lay-up rate v is supposed to be as high as possible to minimize manufacturing time. The upper limit, however, is determined by the occurrence of lay-up defects. Based on the preliminary trials, 0.1 m/s proved to be a lay-up rate where defects would occur depending on the material properties and the trajectory. To investigate to which extent a reduction of lay-up rate would reduce defects, 0.06 m/s and 0.03 m/s were defined. For the compaction force F and the IR emitter power P_{IR}, two values each were defined which are within the general operating range of the used AFP machine ($F_{max} = 500\ N$, $P_{IR,max} = 430\ W$, see Tab. 2.10). By varying F and P_{IR}, their influence on the material properties and the lay-up outcome can be quantified. From the production viewpoint, reducing the compaction force could reduce wear and tear of the roller and reducing the IR emitter power reduces the overall energy consumption. Three levels for the lay-up rate were defined because it was expected to have a significant influence on the defect occurrence and because it affects the physical properties like the time of intimate contact t_{intim} and the temperature T.

To quantify t_{intim} and T resulting from the process parameters and the roller compliance, measurements with the AFP machine were performed. The length of the pressure area resulting from the deformation of the silicone roller during lay-up was measured using a pressure-mapping sensor film "type 5101" from Tekscan Inc. (Boston, USA) [202] in [S1]. The results are shown in Tab. 3.4.

Table 3.4: Length of pressure area vs. compaction force

Compaction force $[N]$	Length of pressure area $[mm]$
210	15.4
307	16.3
354	17.3
402	18.2
500	19.3

Within the investigated range, the length of pressure area L_{roller} approximately increases linearly with the compaction force as

$$L_{roller} = 1.41 \cdot 10^{-2} \, \frac{mm}{N} \, F + 12.306 \, mm \qquad (3.1)$$

with a coefficient of determination of $R^2 = 0.9805$. The quotient of L_{roller} divided by the lay-up rate v equals the time of intimate contact t_{intim}.

The temperature is dependent on the lay-up rate and the IR emitter power P_{IR}. To quantify its changes as a function of the process parameters, the substrate temperature was measured using type K thermocouples — see Fig. 3.1.
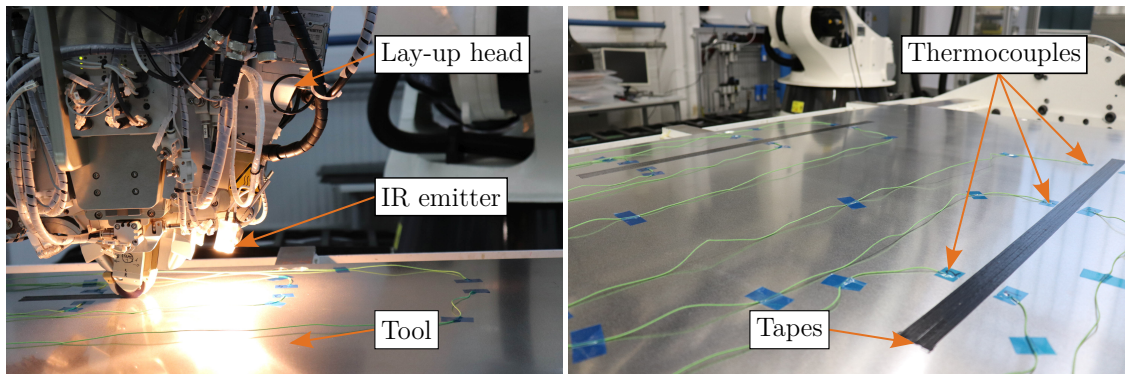
Figure 3.1: Temperature measurements with AFP machine

The measurements were conducted five times and the ambient temperature was 22.6 °C. Detailed results are listed in Tab. A.1 in the appendix. The relevant results from the measurements of t_{intim} and T are summarized in Tab. 3.5.

With the assumption that the tape temperature during first contact between tape and substrate equals the substrate temperature [184], the test temperatures in the material characterization were set to 20 °C and 40 °C to cover the relevant range. The lower limit 20 °C represents processing at ambient temperature with no additional heat input. The upper limit 40 °C is just above the highest temperature of the AFP investigations and it is the nominal processing temperature for IM7/8552 [157].

Table 3.5: Time of intimate contact and temperature resulting from process parameters

v [m/s]	F [N]	P_{IR} [W]	t_{intim} [s]	T [°C]
0.03	200	150	0.50	26.3
0.03	200	350	0.50	39.0
0.03	400	150	0.60	26.3
0.03	400	350	0.60	39.0
0.06	200	150	0.25	25.5
0.06	200	350	0.25	34.3
0.06	400	150	0.30	25.5
0.06	400	350	0.30	34.3
0.10	200	150	0.15	24.8
0.10	200	350	0.15	31.3
0.10	400	150	0.18	24.8
0.10	400	350	0.18	31.3

Wherever appropriate, the symbols and colors listed in Tab. 3.6 were used to represent the process parameters in graphs:

Table 3.6: Symbols and colors for result illustration

Process parameter	Level	Symbol/color
Rate	low mid high	triangle △ square □ circle ◯
Compaction force	low high	small symbol large symbol
IR emitter power / temperature	low high	blue red

The symbols for the rate are inspired by a rolling movement — triangle: slow rolling movement, circle: fast rolling movement. The symbol size is analogous to the pressure area of the compaction roller.

3.2 Degree of cure

The glass transition temperature and therefore the degree of cure is a standard value for the incoming goods inspection and the quality control of prepreg in the aerospace industry [13]. Being widely used, it is predestined as a reference value

for the out-time of the prepreg and the correlation between out-time and material properties.

3.2.1 Test method

DSC runs according to existing test standards — DIN EN ISO 11357 [115] and ASTM E1356-08 [116] — were used for the determination of the DoC. During the measurements, the glass transition temperature T_g was determined by the midpoint method — midpoint between the heat flow level before the inflection and after the inflection [8, 115]. The relation between T_g and the DoC α was calculated using the modified DiBenedetto equation [112] — Eq. 2.3.

3.2.2 Experimental procedure

The T_g measurements were part of the student thesis [S11] and they were published in [J2]. All measurements were done using a TA Instruments Q200 DSC with a heating rate of 10 K/min. Each time, around 20 mg prepreg material was used. The DSC sample pans were Tzero with Tzero lids [203]. The T_g of five samples each was measured at 0, 1, 5, 11, 15, and 20 days out-time.

3.2.3 Results

The results for T_g as well as the calculated DoC α are depicted in Fig. 3.2.

(a) Glass transition temperature

(b) Degree of cure
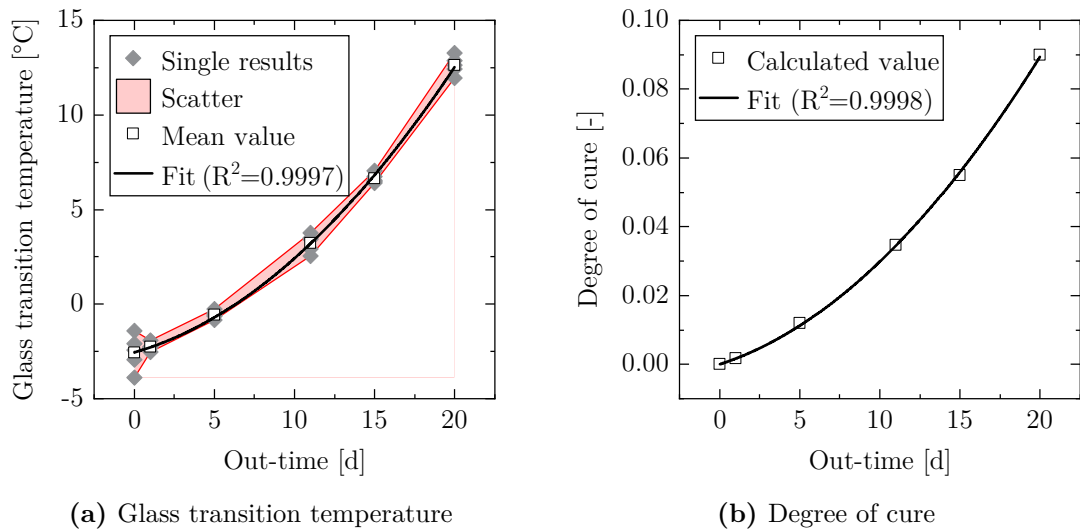
Figure 3.2: Cure-related properties of IM7/8552 as a function of out-time

The input values for the calculation of the DoC using Eq. 2.3 are listed in Tab. 3.7.

Table 3.7: Input values for DoC calculation

Parameter	Symbol	Unit	Value	Source
Glass transition temp. of uncured material	T_{g0}	$°C$	-2.548	Own measurement
Glass transition temp. of fully cured material	$T_{g\infty}$	$°C$	209.51	Own measurement
Adjustable parameter	λ	-	0.78	[204]

Both the dependence of T_g and α on the out-time t_{out} [d] can be expressed with a parabolic fitting within the measured range with Eq. 3.2, Eq. 3.3, and the corresponding parameters listed in Tab. 3.8.

$$T_g = A_{Tg} \cdot t_{out}^2 + B_{Tg} \cdot t_{out} + C_{Tg} \tag{3.2}$$

$$\alpha = A_\alpha \cdot t_{out}^2 + B_\alpha \cdot t_{out} \tag{3.3}$$

Table 3.8: Cure-related properties — parameters of fits

Symbol	Unit	Value
A_{Tg}	$°C/d^2$	$2.57 \cdot 10^{-2}$
B_{Tg}	$°C/d$	$2.4 \cdot 10^{-1}$
C_{Tg}	$°C$	-2.548
A_α	d^{-2}	$1.485 \cdot 10^{-4}$
B_α	d^{-1}	$1.5029 \cdot 10^{-3}$

The coefficients of determination are $R^2 = 0.9997$ and $R^2 = 0.9998$, respectively. The results show a quadratic dependence of T_g and α on the out-time at 21 $°C$ and 40 % RH. Similar results can be found in literature, e. g. [51]. The DoC after 20 days out-time (twice as much as the tack life) is around 9 % which is in agreement with findings in literature, e. g. [34, 48].

3.3 Tack

Prepreg tack is one of the most important material properties regarding AFP lay-up efficiency and defect occurrence. Therefore, the determination of tack is an essential part of the material characterization. Since no standard for the determination of prepreg tack existed during the development of this thesis, approaches from

literature have to be considered. Two principles have been used extensively: the probe tack test and the peel tack test. Both principles deserve consideration since data from probe tack tests has been used by several authors as an input for defect prediction models [31, 126, 180, 181] while peel tests allow for a better relation to the peel mechanisms in automated lay-up processes compared to probe tack tests [130]. The tack is not only dependent on the material and the test parameters but also on the substrate that the material is in contact with. TS-AFP related substrates include a blank metal tool surface, a base film on a metal tool, or a previously laid up ply. To focus the investigations in this study on the effects of prepreg changes instead of different substrates, only a blank metal tool was taken into account as the substrate. This case, which is considered the *first-ply problem*, is more sensitive to changes and more relevant since the low expected tack induces a higher risk of lay-up defects.

3.3.1 Probe tack

3.3.1.1 Test method

In literature, the probe tack test has been conducted using two types of devices — universal testing machine (UTM) and rheometer. The latter allows for an accurate force and temperature control. Apart from that, the expected measured forces are comparably low and the material demand is expected to be lower for rheometer measurements. Therefore, a rheometer has been chosen to conduct the probe tack tests.

3.3.1.2 Experimental procedure

All probe tack measurements were done using an Anton Parr MCR 302 rheometer. The general experimental procedure was adopted from Budelmann et al.'s publication [36]. The test procedure — illustrated in Fig. 3.3 — comprises the compaction phase, where the probe is pressed onto the specimen, the relaxation phase, and the measurement phase, where the probe is pulled away from the specimen and the counteracting force is measured.

The test preparation — see Fig. 3.4 — includes placing the specimen (size: $30\ mm \times 30\ mm$) inside the lower plate and covering the specimen with a downholder. All specimens were placed with the tackier side down to avoid a pull up of the whole specimen and great care was taken to avoid entrapped air between specimen and lower plate surface. The downholder was fixed with adhesive tape also serving as a way to avoid a pull up of the whole specimen. The used probe was

a flat aluminium probe with a 10 *mm* diameter replicating the first-ply tack on an
aluminium tool — see Fig. 3.5. The probe was cleaned thoroughly using isopropyl
alcohol before and after each test. The temperature was controlled by a peltier
temperature device (PTD) in combination with a hood covering the experimental
chamber.
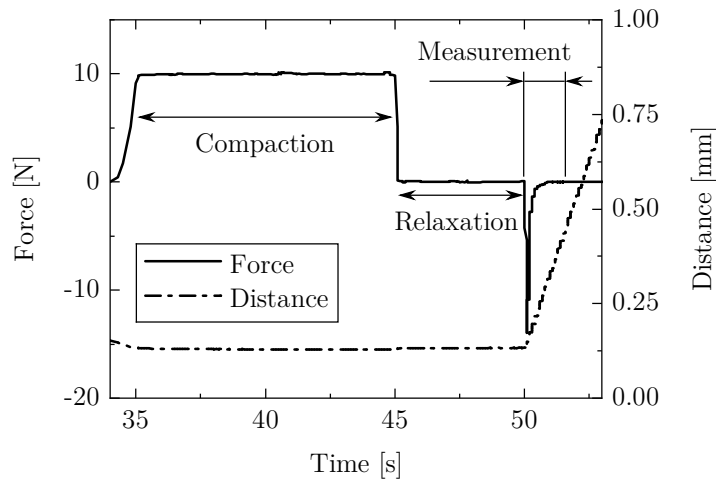
Figure 3.3: Probe tack test — test procedure
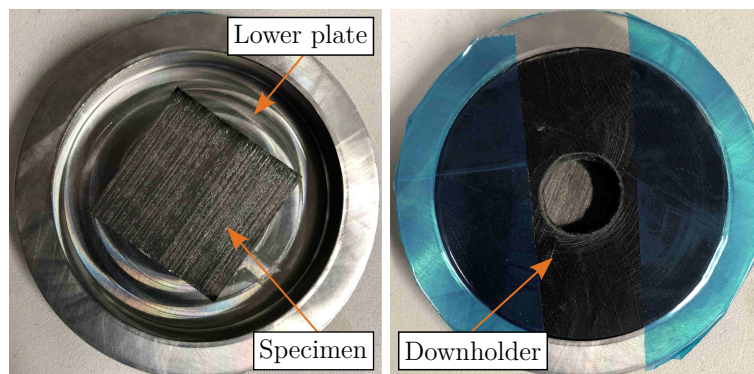
Figure 3.4: Probe tack test — specimen in lower plate

The test parameters were derived from Budelmann et al.'s publication [36]. They
are listed in Tab. 3.9. The compaction force was kept constant at 10 *N* (resulting
in a pressure of 0.127 N/mm^2). Since the compaction pressure during AFP is
comparably high — 0.43 N/mm^2 to 0.86 N/mm^2, the highest value of [36] was
used. The compaction and relaxation time where kept constant as they were not
expected to have a significant influence on the probe tack. The IM7/8552 material
was aged to out-times of 1, 5, 10, and 15 days. The test temperatures were set
to 20 °*C* and 40 °*C* to cover the relevant range for TS-AFP processing. The
displacement rates cover the same range as in [36]. Besides aged IM7/8552 at 1 *d*,

5 *d*, 10 *d*, and 15 *d* out-time, all experiments were carried out with the unmodified and the modified material. For each material and test parameter combination five to six samples were tested.
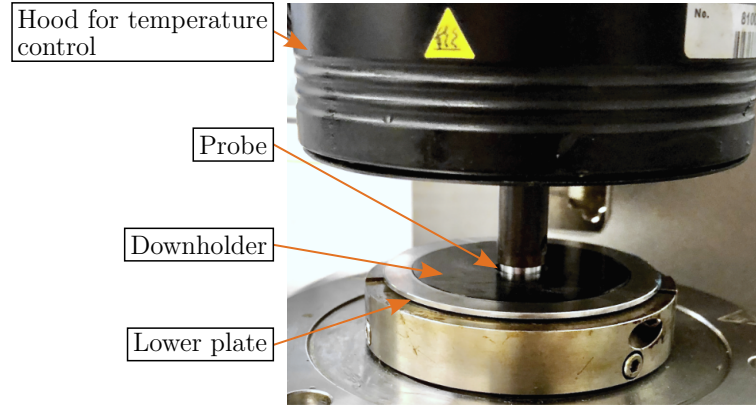
Figure 3.5: Probe tack test — setup in rheometer

Table 3.9: Probe tack test — test parameters

Parameter	Symbol	Unit	Values
Compaction force	F_{probe}	N	10
Compaction time	t_{comp}	s	10
Relaxation time	t_{relax}	s	5
Temperature	T	$°C$	20; 40
Displacement rate	v_{probe}	mm/s	0.02; 0.2; 2

3.3.1.3 Results

The experiments were evaluated in accordance with previous publications as described in Sec. 2.1.4 and Fig. 2.5. The assessed values were the maximum force per probe area σ_{probe}, the tack stiffness per probe area σ_{probe}/d, and the work of adhesion per probe area W_{adh}/A. The tack stiffness is defined as the force per displacement from the start of separation to the maximum force. The work of adhesion is defined as the integral under the force-displacement curve from the start of separation to full separation.

Out-time effects on IM7/8552

The probe tack measurements with IM7/8552 were part of the student thesis [S12] and the publication [J2]. Fig. 3.6 shows the results for the maximum force per probe area σ_{probe}.

In Fig. 3.6, error bars have been omitted to increase readability. A considerable scatter was, however, present during most measurements. Fig. 3.7 visualizes two examples of the single and mean values while the remaining results can be found in the appendix — see Tab. A.2. A certain degree of scatter was observed during the other single-layer based experiments, too. Prepreg tapes exhibit a local variability in properties like resin content [18] which directly influences the scattering of the tack related measurements.
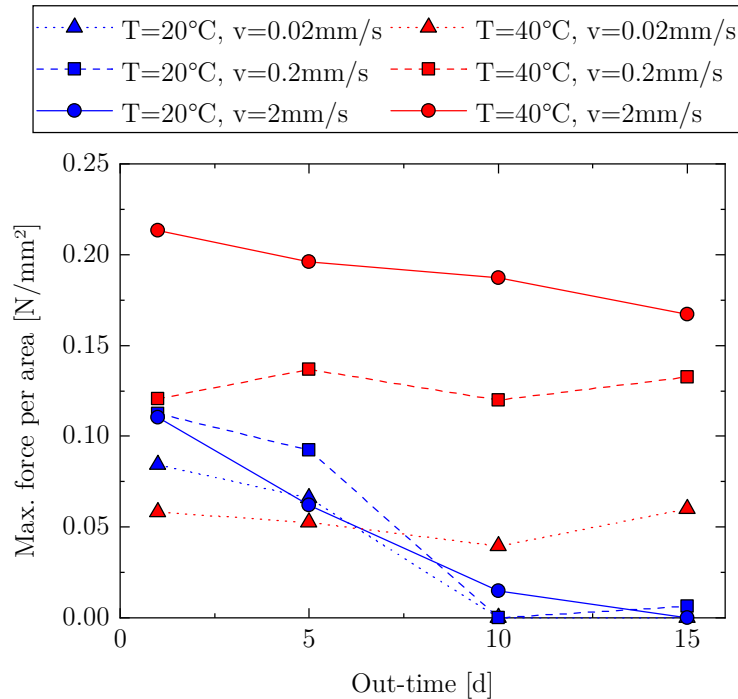
Figure 3.6: Maximum force per probe area of IM7/8552

Fig. 3.6 reveals several trends regarding the material response. Except for the high temperature and slow rate ($T = 40$ °C, $v = 0.02$ mm/s) at 1 and 5 d out-time, the maximum force σ_{probe} is higher at the high test temperature. The increase in temperature generally improves the surface wetting of the substrate due to the decrease in viscosity [24]. However, the decrease in viscosity also leads to a lower shear resistance during debonding, which, after a certain point, outweighs the increase in surface wetting leading to a decrease in tack [24]. This fact may explain the higher maximum force at $T = 20$ °C at out-times 1 d and 5 d where the viscosity is lower than at later out-times. At the high test temperature, σ_{probe} is clearly dependent on the displacement rate with the highest value at the highest test rate ($v = 2$ mm/s) and vice versa corresponding to the viscoelastic behavior of the tack. Budelmann et al. [36] assumed that at higher rates, the short debonding time does not allow the interface to relieve stresses by relaxation.
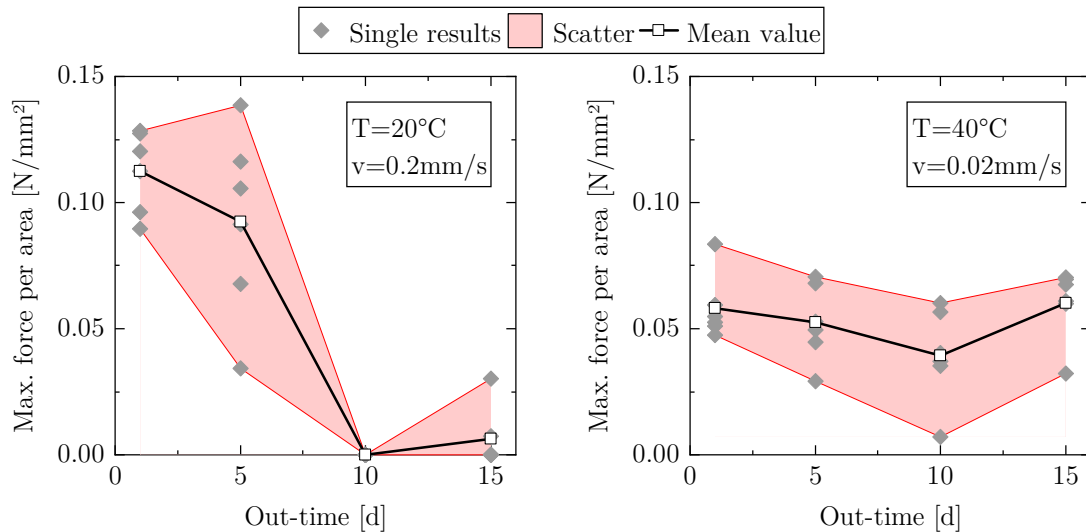
Figure 3.7: Maximum force per probe area of IM7/8552 at $T = 20\,°C$, $v = 0.2\,mm/s$ (left) and $T = 40\,°C$, $v = 0.02\,mm/s$ (right)

At the low test temperature ($T = 20\,°C$), the effect of the rate is much smaller and there is no clear trend whether σ_{probe} increases or decreases with the rate. A clear trend, on the other hand, is evident for the out-time dependence of σ_{probe} at $T = 20\,°C$: it decreases by 18 to 44% from 1 to 5 d out-time — depending on the displacement rate — and drops to almost zero at 10 and 15 d out-time which corresponds to the tack life specified by the manufacturer. Due to the increase in viscosity / decrease in molecular mobility at higher out-times, the surface wetting worsens leading to a decrease in tack. At $T = 40\,°C$, there is no strong dependence on the out-time as the higher temperature decreases the viscosity [8], counteracting the increase due to out-time effects. Budelmann et al., whose test parameters were used, used different materials which makes a comparison of the absolute values difficult. Yet, Wohl et al. [125] also conducted probe tack measurements with IM7/8552. Even though their test parameters were different, the results for the maximum force per probe area were in the same order as the presented results. Relevant results range from 0.13 N/mm^2 to 0.79 N/mm^2.

The results for the work of adhesion per probe area W_{adh}/A are shown in Fig. 3.8. Examples of the single results are shown in Fig. 3.9. Further details are given in Tab. A.3 in the appendix. Similarly to the maximum force, the work of adhesion is rate-dependent at the high temperature while no clear rate dependence at the low temperature can be seen. The work of adhesion is higher at the high test temperature at all out-times and rates. At the high temperature, a large amount of separation energy is dissipated during debonding due to the prevailing viscous behavior of the material [36] leading to a higher work of adhesion.
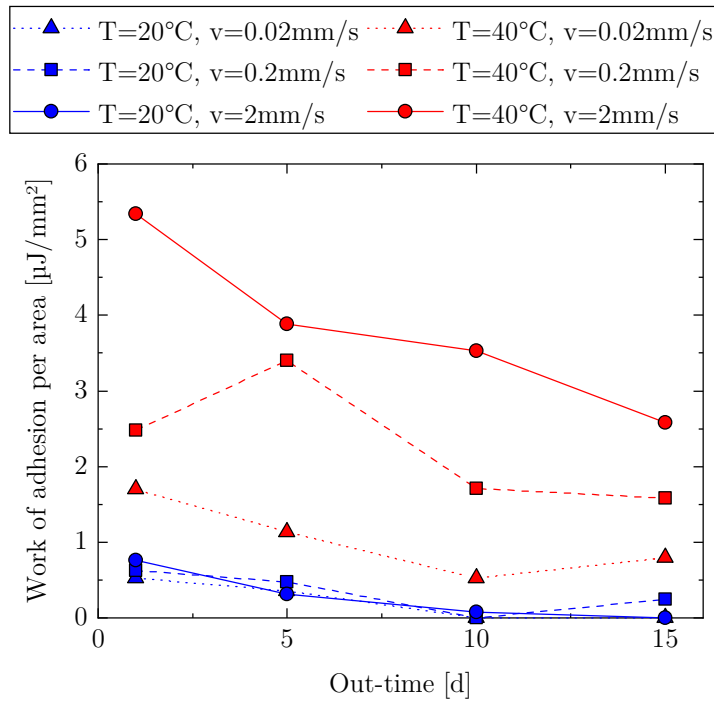
Figure 3.8: Work of adhesion per probe area of IM7/8552
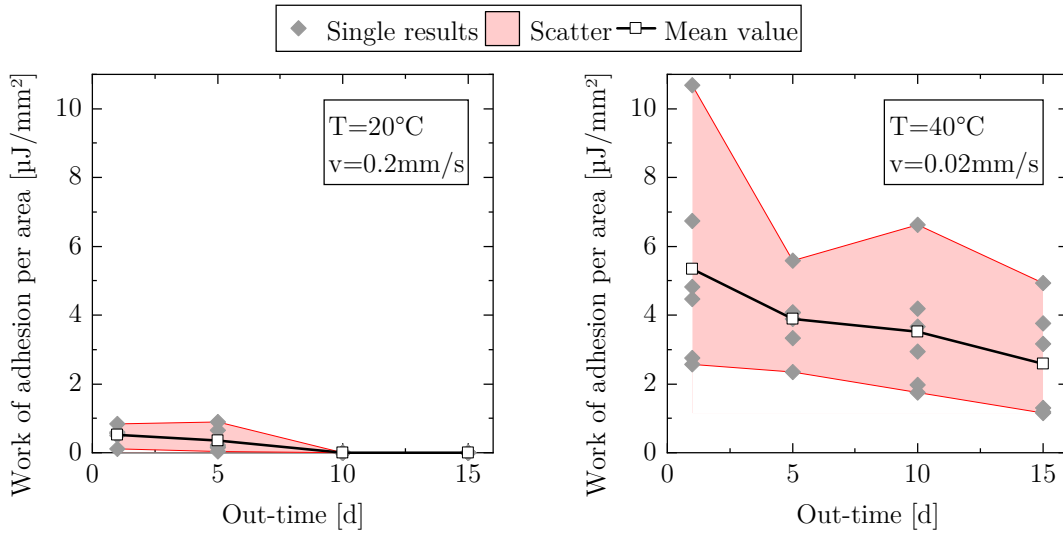
Figure 3.9: Work of adhesion per probe area of IM7/8552 at $T = 20$ °C, $v = 0.2$ mm/s (left) and $T = 40$ °C, $v = 0.02$ mm/s (right)

At both test temperatures, the out-time dependence is apparent with the same assumed root causes as for the maximum force. Besides some deviations ($T = 20$ °C, $v_{probe} = 0.2$ mm/s, $t_{out} = 15$ d; $T = 40$ °C, $v_{probe} = 0.2$ mm/s, $t_{out} = 5$ d; $T = 40$ °C, $v_{probe} = 0.02$ mm/s, $t_{out} = 15$ d), the work of adhesion generally decreases as a function of out-time as the poorer surface wetting leads to a smaller

effective debonding area. As a comparison, relevant examples of Wohl et al.'s results [125] range from 8.3 µJ/mm^2 to 20.8 µJ/mm^2. These results are higher than the presented findings, yet they are within the same order of magnitude.

Fig. 3.10 shows the results for the tack stiffness σ_{probe}/d. Examples of the single results are shown in Fig. 3.11. Further details are given in Tab. A.4 in the appendix.
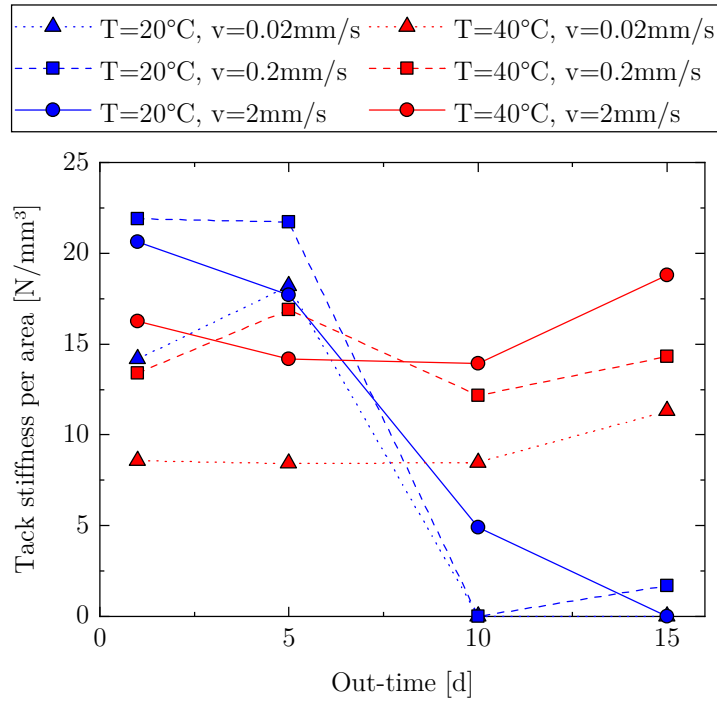
Figure 3.10: Tack stiffness per probe area of IM7/8552
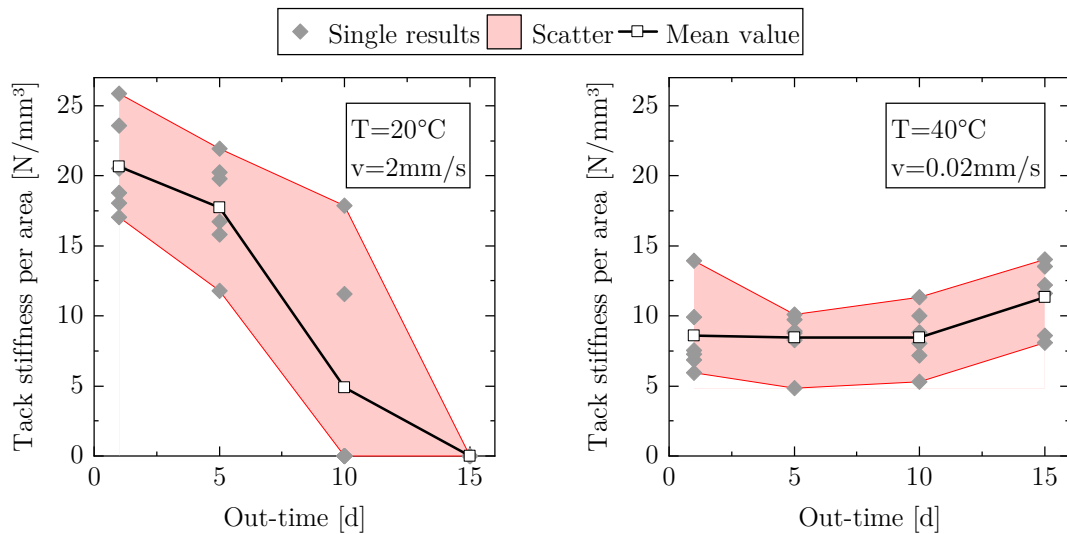
Figure 3.11: Tack stiffness per probe area of IM7/8552 at $T = 20\ °C$, $v = 2\ mm/s$ (left) and $T = 40\ °C$, $v = 0.02\ mm/s$ (right)

Similar to the maximum force, there is no strong out-time dependence at $T = 40\ °C$ for the tack stiffness. At $T = 20\ °C$, however, the tack stiffness is generally even higher than at $T = 40\ °C$ for out-times 1 d and 5 d before dropping off sharply from 5 d to 10 d. The tack stiffness is assumed to be dependent on the elastic component of the material behavior which may be lower at $T = 40\ °C$ and low out-times due to the low viscosity. The sharp decrease is attributed to the poor surface wetting at high out-times. Again, there is no clear trend concerning the influence of rate at the low temperature. At the high temperature, a higher rate generally leads to a higher tack stiffness with the exception of $v_{probe} = 0.2\ mm/s$ and $v_{probe} = 2\ mm/s$ at 5 d out-time with the same assumed reasons as explained for the maximum force. As a comparison, relevant examples of Wohl et al.'s results [125] range from 0.74 N/mm^3 to 5.12 N/mm^3. Here, the measured results are higher, yet, the difference in test parameters has to be acknowledged.

Effects of modification

The probe tack measurements with the research materials were part of the student thesis [S14]. Fig. 3.12 gives an overview of the maximum force results in comparison with IM7/8552 at 1 d out-time.
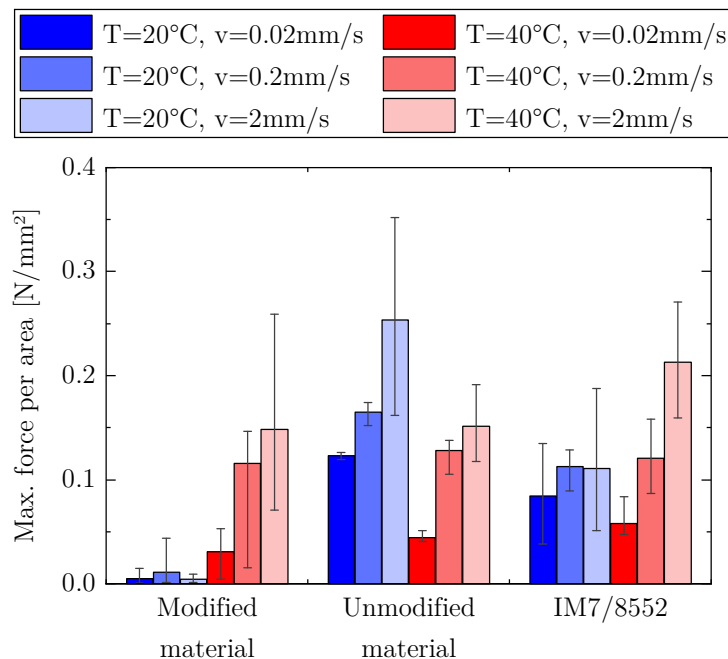
Figure 3.12: Maximum force per probe area of the research materials in comparison with IM7/8552 at 1 d out-time (error bars represent the minimum and maximum values of the respective test series)

The error bars in Fig. 3.12 represent the minimum and maximum values of the respective test series. In addition to the prepreg variability described above, the research materials displayed several material imperfections like gaps, fiber distortions, and local deviations in resin content as exemplified in Fig. 3.13.
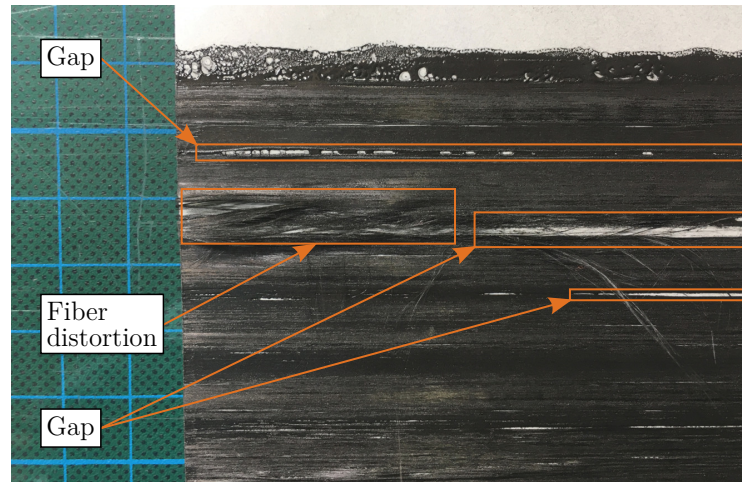
Figure 3.13: Imperfections of research material (top view of single ply)

Since these imperfections appeared periodically and the available material amount was limited, it was not possible to select only specimens without imperfections. Yet, several observations can be made from Fig. 3.12. Except for one deviation, the maximum force of the research materials increases as a function of rate corresponding to the viscoelastic material behavior. The temperature dependence of the modified material is the opposite of the unmodified material. At $T = 20\ °C$, the maximum force of the modified material is very low whereas at $T = 40\ °C$ it is almost identical to the maximum force of the unmodified material and both were in the same range as the reference (IM7/8552 at $1\ d$ out-time). The fillers in the modified material deteriorate the molecular mobility which, in turn, deteriorates the capability of surface wetting. Therefore, at $T = 20\ °C$ the resin viscosity is too high to ensure sufficient surface wetting. The maximum force of the unmodified material is higher at $T = 20\ °C$ than at $T = 40\ °C$ indicating that the temperature for maximum tack of this material is lower than $T = 40\ °C$ and that cohesive failure occurs at $T = 40\ °C$. Compared to the reference, the maximum force of the unmodified material at $T = 20\ °C$ is higher, yet, within the same order of magnitude.

The results for the work of adhesion are shown in Fig. 3.14.
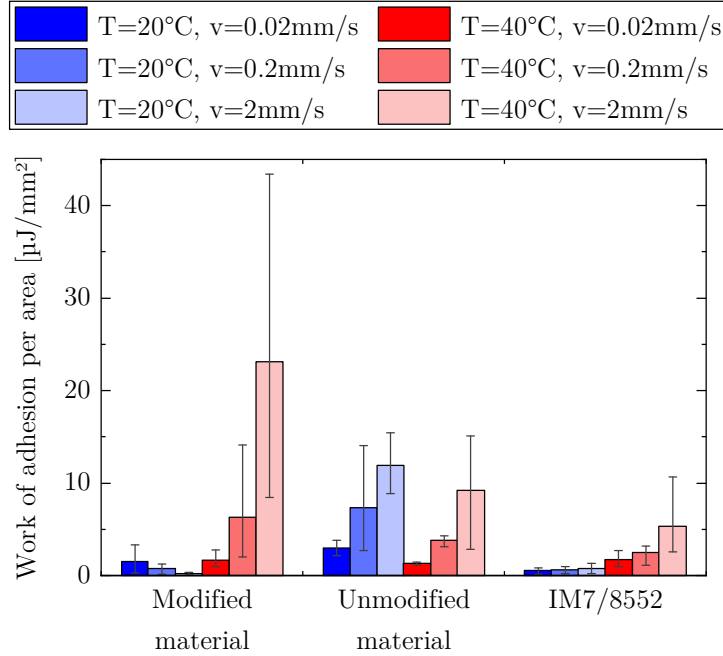
Figure 3.14: Work of adhesion per probe area of the research materials in comparison with IM7/8552 at 1 d out-time (error bars represent the minimum and maximum values of the respective test series)

Similar to the maximum force, the work of adhesion of the unmodified material is higher at $T = 20\,°C$ than at $T = 40\,°C$ and the work of adhesion of the modified material is significantly lower compared to the unmodified material at $T = 20\,°C$. In comparison to the reference, the work of adhesion of the research materials is generally higher with a peak at $T = 40\,°C$, $v_{probe} = 2\ mm/s$ of the modified material. As the scatter is rather high in this case, the unexpected peak is the result of two outliers with $W_{adh}/A = 43.38\ \mu J/mm^2$. Excluding these outliers would lead to an average of $W_{adh}/A = 12.96\ \mu J/mm^2$. The higher work of adhesion compared to the reference might be caused by the lower fiber volume content of the research materials (unmodified material: $\phi = 0.48$, modified material: $\phi = 0.53$, IM7/8552: $\phi = 0.577$). At a lower fiber volume content, the amount of resin on the prepreg surface is higher leading to a prolonged adhesion of the probe to the specimen and therefore to a prolonged force-displacement curve progression in probe tack measurements [36].

Fig. 3.15 depicts the tack stiffness results.
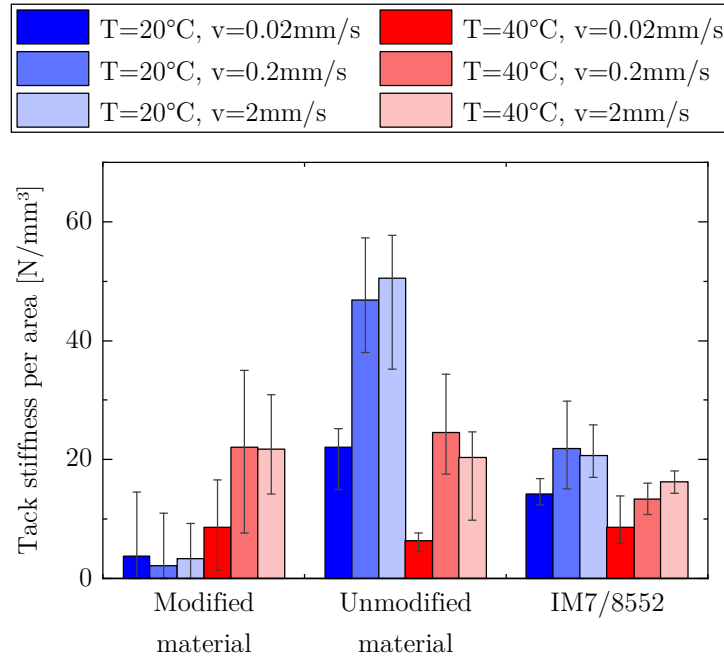
Figure 3.15: Tack stiffness per probe area of the research materials in comparison with IM7/8552 at 1 *d* out-time (error bars represent the minimum and maximum values of the respective test series)

The tack stiffness results are on the lines of the maximum force results as the general observations are comparable.

Conclusion

The probe tack test provides useful information on the out-time dependence on tack and the effect of material modification. To give an overview of the impacts of the test parameters and the material changes, the Pearson correlation coefficient as per [205] was determined using the single measurement values. The Pearson correlation coefficient $-1 \leq r_{xy} \leq 1$ quantifies the linear correlation between two sets of data. A correlation coefficient close to -1 indicates a strong negative correlation while a correlation close to 1 indicates a strong positive correlation and 0 indicates no correlation [205]. Fig. 3.16 illustrates the results. The temperature is the most influential test parameter for the reference material followed by the rate. While the maximum force and the work of adhesion have a similar maximum correlation to the temperature followed by the rate, the tack stiffness has a weaker correlation to the test parameters and a stronger correlation to the out-time. As the tack stiffness is assumed to be influenced by the elastic component of the viscoelastic material

behavior, apparent stiffening effects due to out-time may be more significant than for the other readings. The investigation of out-time effects reveals a significant influence and a strong decrease in tack after 10 d which is also the tack life stated by the material manufacturer. The rate dependence of all three readings is a result of the viscoelastic behavior. Implications for AFP processing are, however, difficult to derive, as the debonding rate during AFP lay-up is difficult to estimate and it is highly dependent on the type of defect [36]. In contrast, implications for AFP processing from the temperature dependence observed in probe tack tests are more straightforward. At prolonged out-times, the higher test temperature leads to a higher tack implying that a temperature increase — within the investigated range — can be used to increase tack at these out-times. Comparing the reference material to the research materials, it becomes evident that the unmodified material generally has a higher tack — particularly at the low test temperature (20 °C). The modified material has a considerably lower tack at $T = 20$ °C and a similar to higher tack level at $T = 40$ °C. The correlation coefficients — Fig. 3.16b — reveal that the tack is more related to the rate than the temperature. Out of the three probe tack readings, the material modification mostly affects the maximum force and has no influence on the work of adhesion. Assuming that the reference material is well suited for AFP processing, the modified material should be processed at a higher temperature than the reference. The unmodified material's tack may be so high that it leads to issues in the material feed which might even arise in a cooled down material feed.

(a) IM7/8552   **(b)** Research materials
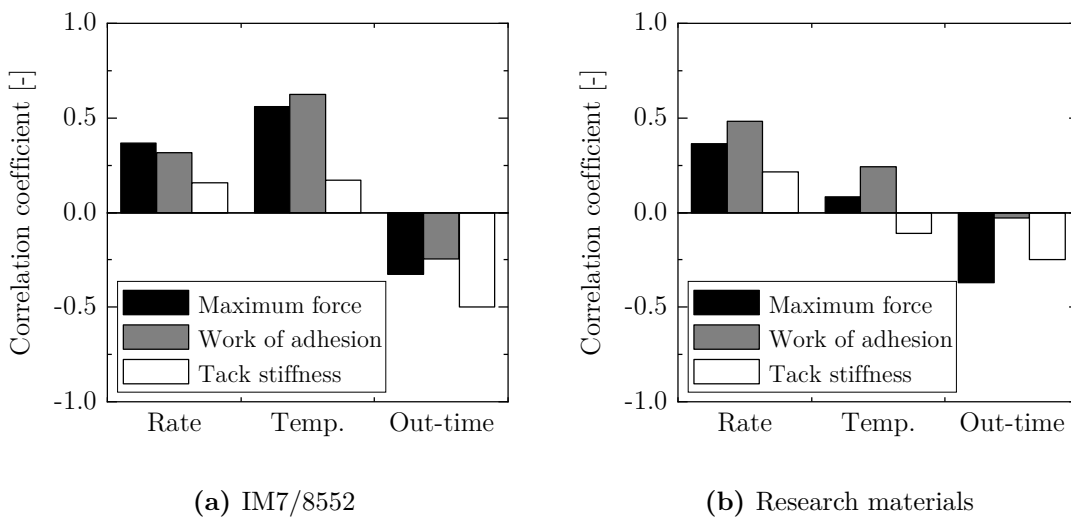
Figure 3.16: Probe tack correlation coefficients

Despite the findings stated above, the probe tack test does not relate to the peel mechanisms during AFP [130] and the adjustable test parameters cannot be converted directly to the AFP process parameters. An attempt to do so was not successful as it is difficult to estimate the rate occurring during AFP lay-up and out-of-plane buckling of the tape. Furthermore, the rheometer characteristics limit the maxima of parameters like rate, acceleration, and compaction force.

3.3.2 Peel tack

3.3.2.1 Test method

The first attempts to measure the peel tack were done using an existing test bench presented in [206] and [207]. Even though significant effort was put into improving the test bench — see [S1] and [S4], the accuracy and repeatability of the measurements were not satisfactory. The kinematic setup of the test bench made a smooth movement of the movable components difficult and the integrated compaction roller affected the force measurement when applying compaction force.

A frequently used peel test is the single-stage peel test [35, 37, 110, 130, 131]. Although the test is based on a standard floating roller method, it has been modified significantly from the standardised test. The fact that the peel measurement and the lay-up replication are executed simultaneously determines two characteristics of the test method: the peel rate and the lay-up rate cannot be uncoupled and measurements can only be done at the moment of lay-up and not afterwards. The former is a limitation since the peel force is expected to be dependent on both the peel rate and the lay-up rate. The latter is a limitation since prepreg tack exhibits time-dependent viscoelastic behavior [181, 182]. To fill the gap for peel tack measurements of prepreg tapes, the author developed a novel post lay-up tack peel test which was implemented within [S8] and presented in [C3]. The test is based on a test standard for pressure-sensitive adhesives (PSA) — DIN EN ISO 29862 [208] — and the specimen deposition is independent of the peel test. The test method was implemented in a standalone test bench resulting in the following principal benefits:

- capability to measure the influence of tack on the deposition rate independent of the peel rate,

- capability to measure tack at different times after material deposition,

- standardised procedure,

- capability to position test bench next to placement machine and prepare specimens with placement machine,

- applicability to other material deposition processes.

The functional principle is pictured in Fig. 3.17. It is based on a 90° peel test. The specimen is positioned on a sample carrier which is fastened on a movable sled. The front end of the specimen is clamped and pulled upwards using a linear axis while a load cell measures the peeling force. The slide of the linear axis is connected to the movable sled with a wire. Therefore, it moves forward while the specimen is pulled upwards. In order to ensure a 90° peeling of the specimen from the sample carrier, the specimen passes a pulley directly underneath the clamp. The first half of the specimen's lower side is covered with a release film while the second half is in direct contact with the surface of the sample carrier. By this, the force caused by the stiffness of the specimen can be measured separately and subtracted from the total force which is measured when the second half of the specimen is peeled. The difference between total force and force caused by stiffness equals the tack — in accordance with the single stage peel test [130]. The described test principle is identical to the test standard DIN EN ISO 29862 with the exception of the specimen passing the aforementioned pulley. The test procedure consists of the following steps:

1. specimen deposition on sample carrier — for example AFP or hand lay-up,

2. fastening of sample carrier on movable sled,

3. clamping of specimen in clamping jig,

4. start of peel test.

Fig. 3.18 shows the post lay-up peel tack test bench. The drive system is a linear axis with a spindle drive which is powered by a stepper motor and ensures a low level of vibration. The initial peel rate is constant at 5 mm/s which is equal to the peel rate in DIN EN ISO 29862 and the travel is 300 mm which is determined by the linear axis. The load cell has a nominal force of 50 N with an accuracy class of 0.02 since peel forces are expected to be comparably low. The clamping jig is designed in such a way that the specimen can be clamped quickly. Likewise, the fastening mechanism for the sample carrier on the movable sled is designed to enable a quick and accurate positioning of the sample carrier in the test bench. The forward movement of the sled is controlled by two retention springs avoiding an uncontrolled forward sliding. The pulley is pivoted and it is coated

with a polytetrafluoroethylene (PTFE) shrinking tube so that it interferes as little as possible with the specimen movement — see Fig. 3.18b.
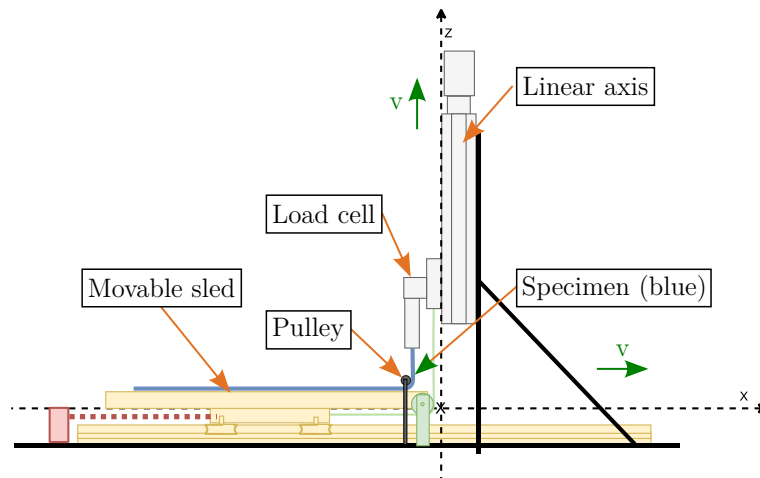
Figure 3.17: Functional principle of the post lay-up peel tack test

(a) Overview

(b) Details
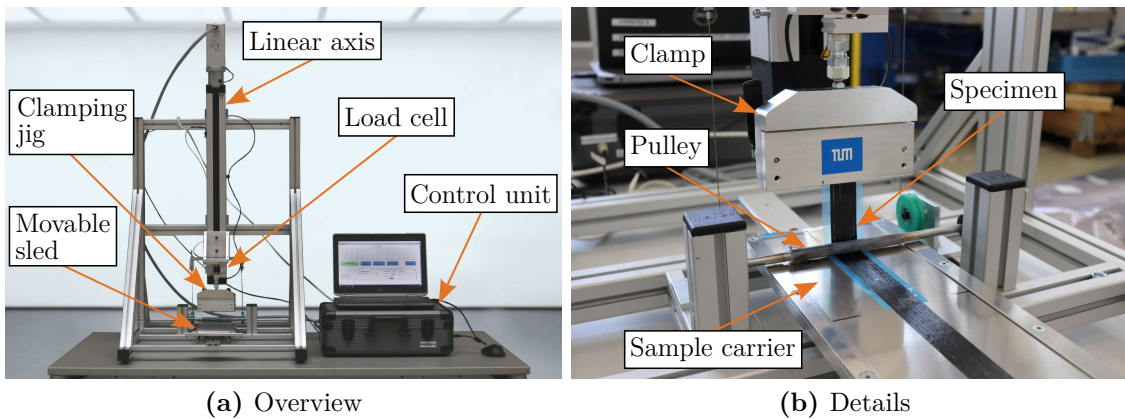
Figure 3.18: Post lay-up peel tack test bench

The sample carriers are aluminium sheets in order to replicate the first-ply problem on metal substrates. For the described test bench, the sample carrier size is $360 \ mm \times 120 \ mm$. The type of sample carrier can easily be changed to other materials or other substrates like a previously laid up prepreg layer. The control unit of the test bench is comparably small and the needed power supply for the test bench is a standard $230 \ V$ AC grid. Further information on the conceptual design of the test bench are detailed in [S8].

3.3.2.2 Experimental procedure

As described above, the experimental procedure includes specimen deposition on sample carrier, fastening of sample carrier on movable sled, clamping of specimen

in clamping jig, start. Since the test bench is transportable, it was positioned in close proximity to the AFP machine — see Fig. 3.19a — and specimens were deposited directly with the AFP machine — see Fig. 3.19b. Thus, there is no need for converting process parameters from a jig or deposition test bench to the AFP machine parameters.

(a) Test bench next to AFP machine   **(b)** Lay-up on sample carrier
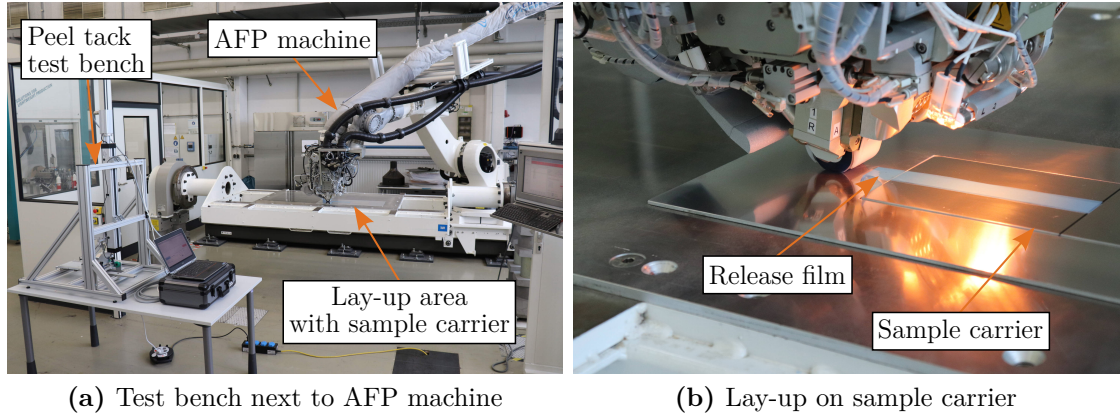
Figure 3.19: Peel tack test — specimen preparation

Just as the probe tack test, the out-time effects on IM7/8552 and the effects of modification were investigated. The AFP process parameters listed in Tab. 3.3 were used for a full factorial experimental design. All tack measurements were done 1.5 min after material deposition (t_{after}). It is desirable to measure as soon as possible after material deposition. Yet, the time needed for the transfer of the sample carrier and the clamping of the specimen has to be accounted for. To investigate the influence of time after lay-up, additional experiments were conducted at $t_{after} = 40\ min$ which is the time for defect development after steering — see Sec. 4.1.2. These additional experiments were done with the expected best and worst parameters regarding tack as per Tab. 3.10.

Table 3.10: Peel tack test — test parameters for time after lay-up

Lay-up rate [m/s]	Compaction force [N]	IR emitter power [W]	Time after lay-up [min]
0.03	400	350	1.5; 40
0.1	200	150	1.5; 40

The IM7/8552 specimens consisted of eight slit-tapes with a total width of 25.4 mm and a length of 350 mm. As the research materials were not available as slit-tapes, specimens with a size of 350 $mm \times 25\ mm$ were cut from the respective parent tapes. Hence, it was not possible to process the material directly with the AFP

machine. Instead, the research material specimens were placed on the sample carrier manually and the lay-up head of the AFP machine passed over with the same process parameters as in the IM7/8552 experiments. Five specimens each were deposited and tested.

3.3.2.3 Results

Out-time effects on IM7/8552

The experiments were conducted within [S13] and a part of the results was published in [J2]. Fig. 3.20 shows the mean values for the peel tack normalized to the tape width. Again, errors bars have been omitted to increase readability but a considerable scatter was present during most measurements — see Fig. 3.21 as well as Tab. A.5 and Tab. A.6 in the appendix. Besides the prepreg variability described above, there is a second source of variability for specimens prepared via AFP: it cannot be controlled which prepreg side is in contact with the substrate since the narrow tapes can be twisted at several locations of the AFP machine's material feed. As the prepreg side plays a significant role for resin distribution and tack [35], it will affect the peel tack of AFP specimens.
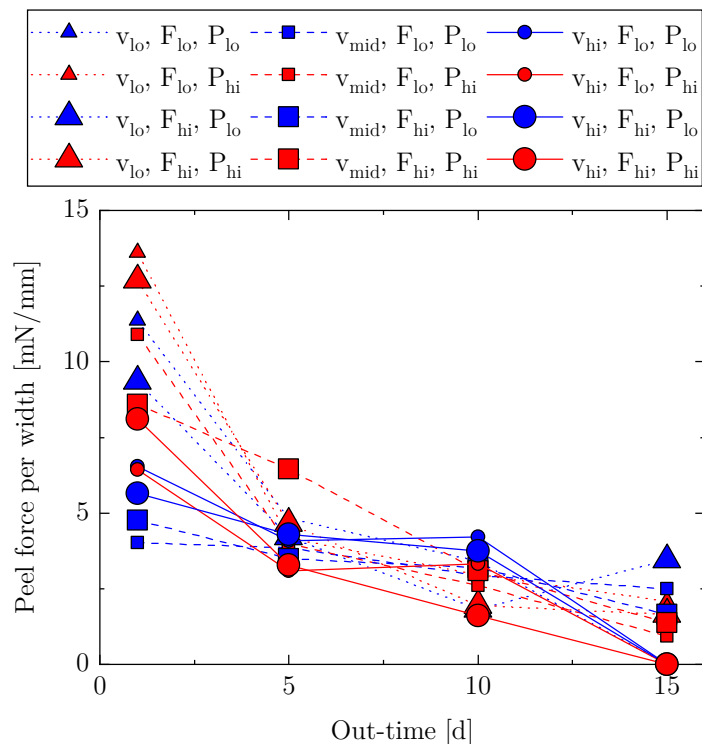
Figure 3.20: Peel tack per width of IM7/8552 ($v_{lo} = 0.03\ m/s$, $v_{mid} = 0.06\ m/s$, $v_{hi} = 0.1\ m/s$, $F_{lo} = 200\ N$, $F_{hi} = 400\ N$, $P_{lo} = 150\ W$, $P_{hi} = 350\ W$)
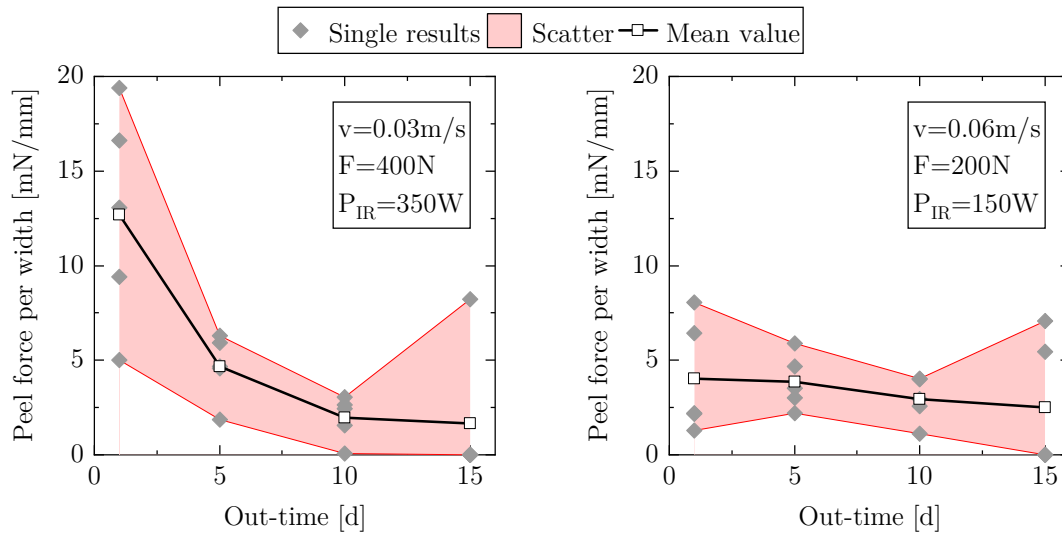
Figure 3.21: Peel tack per width of IM7/8552 at $v = 0.03\ m/s$, $F = 400\ N$, $P_{IR} = 350\ W$ (left) and $v = 0.06\ m/s$, $F = 200\ N$, $P_{IR} = 150\ W$ (right)

Yet, several trends can be identified from Fig. 3.20. The range of the peel tack is rather large at 1 *d* out-time with values from 4 *mN/mm* to 13.6 *mN/mm* (range of 9.6 *mN/mm*). At the other days of out-time, this range is significantly smaller — 3.3 *mN/mm*, 2.6 *mN/mm*, and 3.4 *mN/mm*, respectively. This indicates that the impact of varying process parameters is higher at 1 *d* out-time than the other days. Except for one deviation ($v = 0.03\ m/s$, $F = 400\ N$, $P_{IR} = 350\ W$ at 15 *d* out-time), the peel tack decreases as a function of out-time. Here, the deviation is caused by one outlier with a peel tack of 12.4 *mN/mm*. Without the outlier, the average value would be 1.2 *mN/mm* instead of 3.4 *mN/mm* which would lead to a monotonic decrease as a function of out-time just as at the other process parameter combinations. This again, is explained by the increase in viscosity leading to a poor surface wetting. All specimens exhibited adhesive failure indicating that the temperature for maximum tack was not exceeded. As the influence of process parameters is not clearly visible from Fig. 3.20, it is discussed in the conclusion paragraph below in conjunction with the correlation coefficients.

The peel tack at different times after lay-up is illustrated in Fig. 3.22. It generally increases as a function of time after lay-up. The resin wets and penetrates the substrate surface — depending on the surface roughness — during deposition and subsequently the molecular mobility decreases as the material temperature decreases increasing the adhesion in the wetted area. Similar to the influence of process parameters at 1 *d* out-time, the increase in peel tack as a function of time after lay-up is the highest at 1 *d* out-time — factor $5.6 - 6.0$.

(a) Process parameters favorable for tack

(b) Process parameters unfavorable for tack
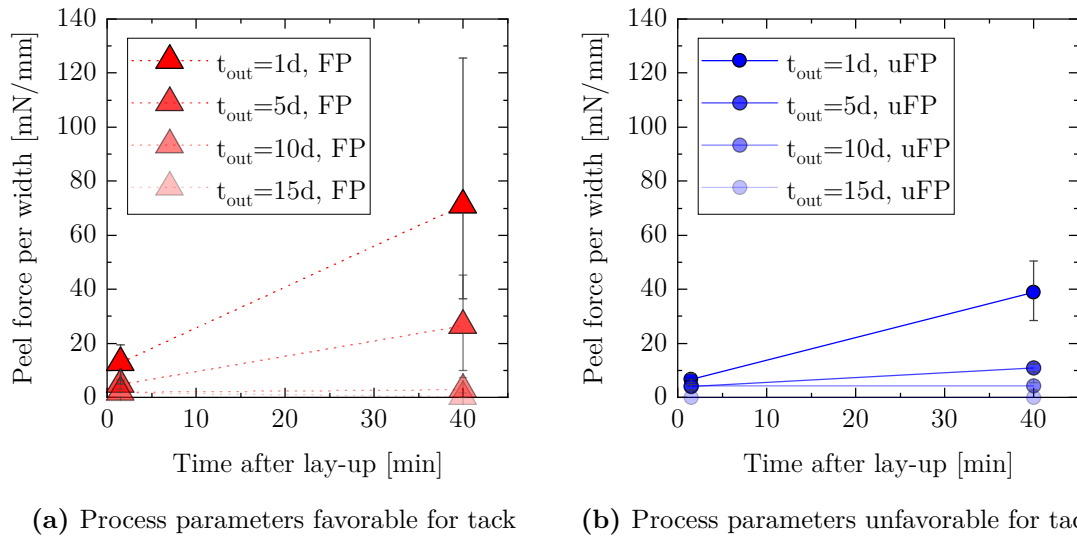
Figure 3.22: Peel tack as a function of time after lay-up (FP: favorable parameters, uFP: unfavorable parameters; error bars represent the minimum and maximum values of the respective test series)

This influence decreases as a function of out-time — factor $2.7 - 5.7$ at $5\ d$, factor $1.0 - 1.4$ at $10\ d$, factor $0 - 0.2$ at $15\ d$ — as the difference between molecular mobility shortly after deposition and at prolonged times after deposition is smaller.

Effects of modification

The results for the research materials in comparison with IM7/8552 at $1\ d$ out-time are shown in Fig. 3.23. The overview indicates that the tack of the modified material is lower and the tack of the unmodified material is significantly higher than the tack of the reference material which is similar to the probe tack results. Again, the results of the research materials are subjected to substantial scattering due to the material imperfections. Yet, the failure modes provided further insight in the tack characteristics: the reference and the modified material displayed adhesive failure indicating that the combination of lay-up rate and temperature was below the values for the tack maximum [24]. Similar to the probe tack results, the unmodified material displayed cohesive failure in several cases indicating that the combination of lay-up rate and temperature exceeded the values for the tack maximum. The dependence on the process parameters is not clearly visible and it does not seem to correlate to the dependence on the process parameters of the reference material. The correlation coefficients of the process parameters will be discussed on the conclusion paragraph. On average, the material modification leads to a reduction

in peel tack of -79 %. Comparing the process parameter results one by one, the range of reduction goes from -31 % to -94 %.
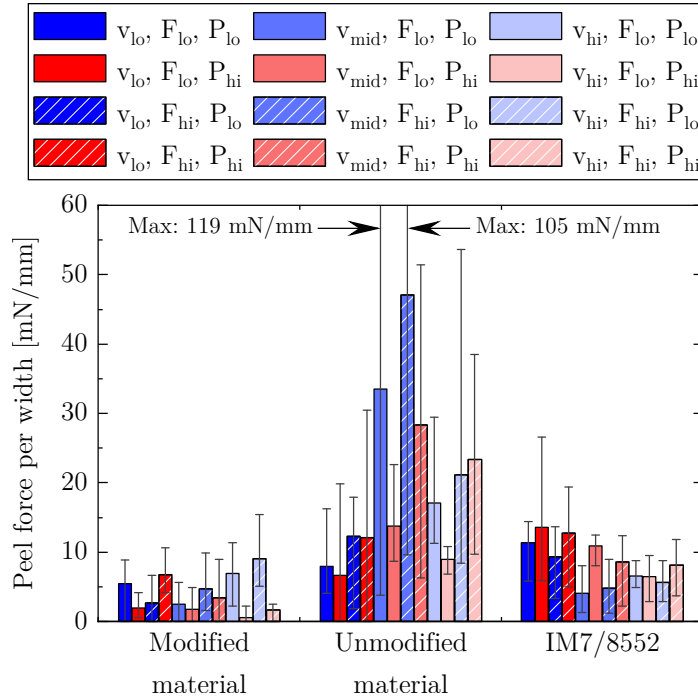
Figure 3.23: Peel tack of the research materials in comparison with IM7/8552 at 1 d out-time ($v_{lo} = 0.03$ m/s, $v_{mid} = 0.06$ m/s, $v_{hi} = 0.1$ m/s, $F_{lo} = 200$ N, $F_{hi} = 400$ N, $P_{lo} = 150$ W, $P_{hi} = 350$ W; error bars represent the minimum and maximum values of the respective test series)

Conclusion

The presented peel tack test proved to be valuable for the tack measurement of AFP deposited specimens enabling an immediate process parameter optimization. Fig. 3.24a — showing the correlation coefficients of IM7/8552 — points out that the peel tack of IM7/8552 has the highest correlation with the rate followed by the IR emitter power. The compaction force has a negligible correlation with the peel tack. Considering the physical properties resulting from the process parameters, it can be seen that the peel tack has a slightly higher correlation with the time of intimate contact t_{intim} than with the temperature T as t_{intim} generally leads to a higher tack [28, 35]. Yet, all process parameters have a significantly lower correlation than the out-time which underlines the importance of the investigation of out-time effects. As stated above, the peel tack of IM7/8552 decreases monotonically as a function of out-time. Countermeasures are decreasing the lay-up rate and increasing the IR emitter power.

(a) IM7/8552

(b) Research materials
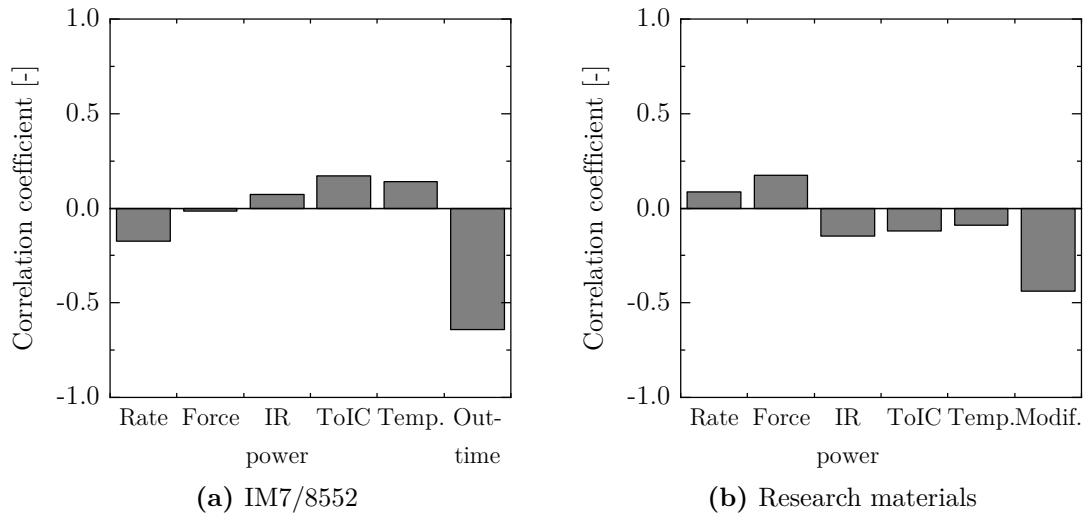
Figure 3.24: Peel tack correlation coefficients (ToIC: time of intimate contact)

Fig. 3.24b — showing the correlation coefficients of the research materials — indicates that the modification reduces the peel tack and that it has a higher correlation than the process parameters. The correlation coefficients of the process parameters are unexpectedly contrary to the ones of IM7/8552. A higher rate and lower IR emitter power — and therefore lower temperature — leading to a higher tack would be in accordance with probe tack measurements for the unmodified material, though, not for the modified material. Apparent trends in the results may be affected by the scattering due to material imperfections. Furthermore, the difference in specimen preparation — see Sec. 3.3.2.2 — may be relevant as the heat input is different when the tapes are passed over instead of deposited directly. Yet, the suitability of the research materials can be assessed with the peel tack results. Similar to the probe tack results, they show that the unmodified material is likely too tacky potentially leading to difficulties in the material feed. For the modified material, process parameters have to be optimized to achieve sufficient tack during lay-up for robust manufacturing.

3.4 Thermal properties

3.4.1 Specific heat capacity

3.4.1.1 Test method

The specific heat capacity was characterized according to DIN EN ISO 11357-4 [142] by means of DSC measurements. The measurements were conducted within [S11] in conjunction with the DoC measurements using the TA Instruments Q200.

3.4.1.2 Experimental procedure

All measurements were done at a heating rate of 10 K/min. Each time, around 20 mg prepreg material was used. The DSC sample pans were Tzero with Tzero lids. The c_p of five samples each of IM7/8552 (out-times 1 d, 5 d, 10 d, 15 d) and of the research materials was measured. In accordance with DIN EN ISO 11357-4, an empty run calibration and a reference run with sapphire were conducted to determine the specific heat capacity of each specimen c_p^{sp} using the continuous scanning method as per

$$c_p^{sp} = c_p^{saph} \cdot \frac{m^{saph}(\dot{Q}_{sp} - \dot{Q}_{empty})}{m^{sp}(\dot{Q}_{saph} - \dot{Q}_{empty})} \tag{3.4}$$

with the specific heat capacity of sapphire c_p^{saph}, the masses of specimen and sapphire m^{sp} and m^{saph}, and the heat flows of the empty run, the sapphire run, and the specimen $\dot{Q}_{empty}$, $\dot{Q}_{saph}$, and $\dot{Q}_{sp}$.

3.4.1.3 Results

Out-time effects on IM7/8552

Fig. 3.25 depicts the results for the specific heat capacity of IM7/8552. The specific heat capacity of IM7/8552 remains nearly the same within the range of 1 d to 15 d out-time. At $T = 20$ °C, the change from 1 d to 15 d out-time is -0.1 %, at $T = 40$ °C it is $+0.4$ %. This generally coincides with results found in literature – see Sec. 2.1.3.1. The temperature dependence of the specific heat capacity is clearly visible in Fig. 3.25. Depending on the out-time, the increase from 20 °C to 40 °C is 6.3 % to 6.9 %. In comparison for the absolute values, Saad et al. [209] measured the c_p of fully cured IM7/8552 i. a. at $T = 25$ °C and $T = 50$ °C and reported values of 0.857 J/gK and 0.92 J/gK, respectively.

(a) As a function of temperature

(b) As a function of out-time at $T = 20 \,°C$ and $T = 40 \,°C$
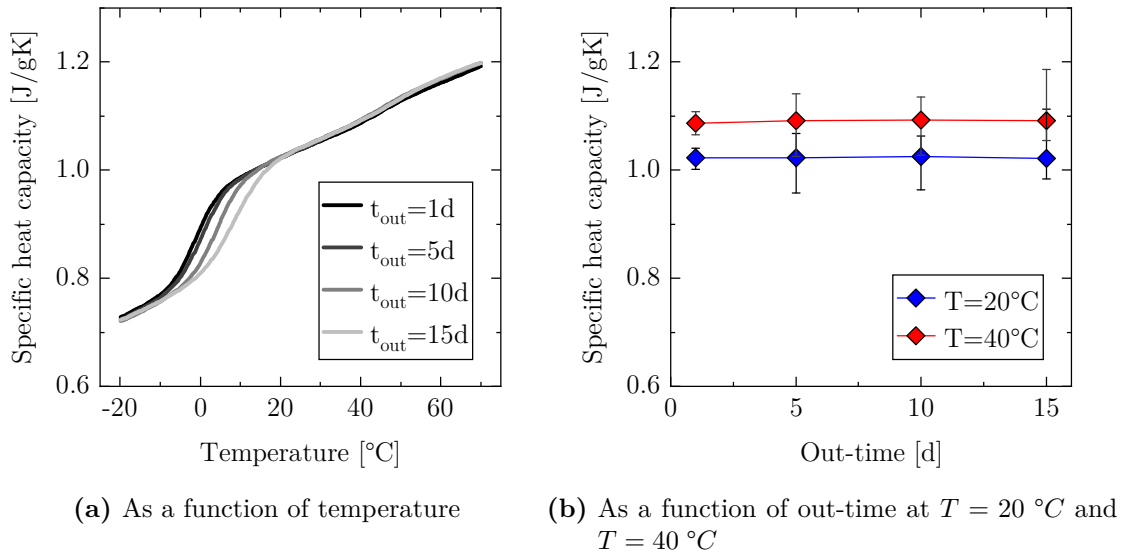
Figure 3.25: Specific heat capacity of IM7/8552 (error bars represent the minimum and maximum values of the respective test series)

Effects of modification

The results for the research materials in comparison with IM7/8552 at 1 d out-time are shown in Fig. 3.26.

The specific heat capacity of the modified material is 6.5 % lower at $T = 20 \,°C$ and 4.9 % lower at $T = 40 \,°C$ compared to the unmodified material. In literature, this decrease is explained by the decrease in molecular mobility caused by the presence of the fillers [102]. Compared to the reference material, the specific heat capacity of both research materials is slightly higher, yet within the same order of magnitude. The temperature dependence is similar to the one of the reference: from 20 $°C$ to 40 $°C$, the modified material's c_p increases by 7.6 % and the unmodified material's c_p increases by 5.8 %.

Conclusion

The c_p measurements reveal that there is no dependence on out-time for IM7/8552 within the investigated range. The modification of the research material leads to a slight decrease in c_p. This, as well as the temperature dependence of all investigated materials have to be considered in thermal simulation models.
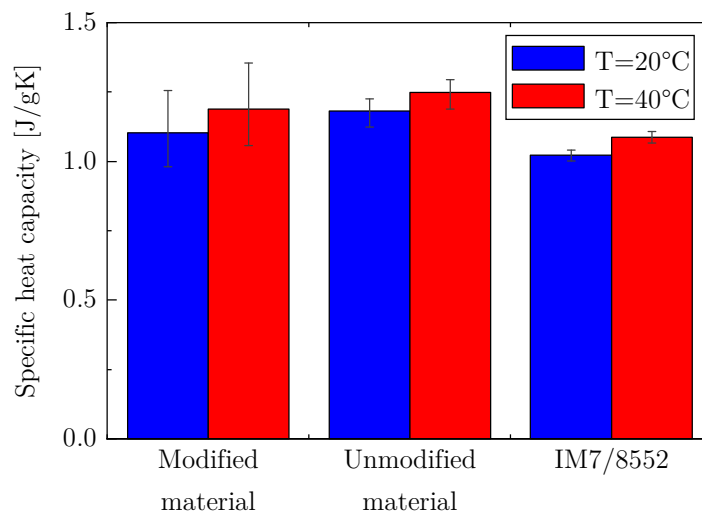
Figure 3.26: Specific heat capacity of the research materials in comparison with IM7/8552 at 1 *d* out-time (error bars represent the minimum and maximum values of the respective test series)

3.4.2 Thermal conductivity

3.4.2.1 Test method

The thermal diffusivity α_{diff} in thickness direction (direction 3) was measured using the laser flash analysis LFA following ASTM E1461-13 [145]. It was used to calculate the thermal conductivity k_3 in combination with density measurements and the c_p results as per Eq. 2.4. The thermal conductivity in thickness direction was considered since it is more likely to be affected by the resin changes due to out-time or modification than the thermal conductivity in fiber direction. Furthermore, increasing the thermal conductivity in thickness direction was the main objective of the material development by UBT [10].

3.4.2.2 Experimental procedure

The LFA measurements were conducted using a NETZSCH LFA 457 MicroFlash from NETZSCH-Gerätebau GmbH (Selb, Germany) [210]. Here, a laser heats the sample from the bottom side and a detector on top detects the time-dependent temperature rise in a vertical setup measuring the rate of heat transfer from the bottom side to the top side — i. e. the thermal diffusivity. The average of three shots each were used to determine α_{diff}. The density of the specimens was determined by measuring the dimensions with a caliper and weighing them with a precision scale. The specimen size was 10 *mm* × 10 *mm* with a thickness of 1 *mm*. The specimen thickness was reached using a procedure presented in [J1]: stacking

larger layers manually, compacting the layers by applying vacuum at room temperature for 35 *min*, and cutting the layers into the specimen size using an NC cutting machine. To obtain a thickness of 1 *mm*, seven layers of IM7/8552 and eleven layers of the research materials were compacted. Before each test, the specimens were coated with a graphite spray for homogeneous laser absorption. The intended test temperatures were 20 °*C* and 40 °*C*. Yet, due to issues with the temperature control, the actual test temperatures were about 21.3 °*C* and 41.4 °*C*, respectively. The thermal diffusivity of five samples each of IM7/8552 (out-times 1 *d*, 5 *d*, 10 *d*, 15 *d*) and of the research materials was measured.

3.4.2.3 Results

Out-time effects on IM7/8552

Fig. 3.27 shows the results for the thermal conductivity of IM7/8552 as a function of out-time.
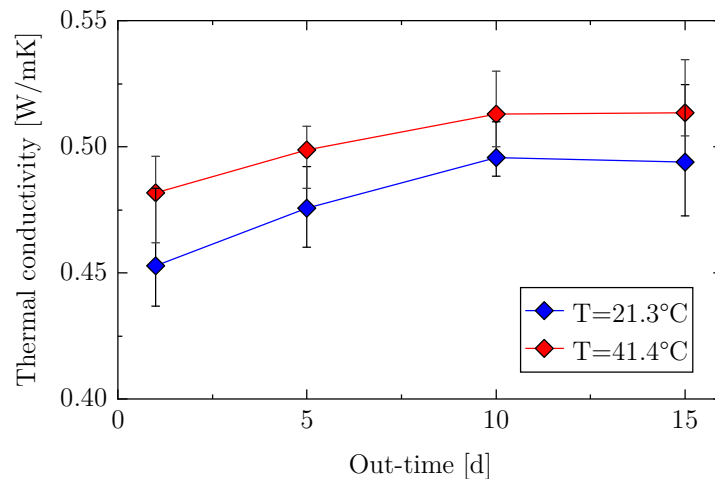
Figure 3.27: Thermal conductivity in thickness direction of IM7/8552 (error bars represent the minimum and maximum values of the respective test series)

The values for thermal diffusivity, density, and specific heat capacity used to calculate the thermal conductivity k_3 are listed in Tab. A.7 and Tab. A.8 in the appendix. The average density was 1.5 g/cm^3. Fig. 3.27 reveals both the temperature and the out-time dependence of the thermal conductivity of IM7/8552. Yet, for both the difference is rather small. From $T = 21.3$ °*C* to $T = 41.4$ °*C*, k_3 increases by 3 % to 6 % depending on the out-time. The thermal conductivity increases monotonic from 1 *d* to 10 *d* out-time and remains almost the same from 10 *d* to 15 *d*. The increase from 1 *d* to 15 *d* at $T = 21.3$ °*C* is 9 % and at $T = 41.4$ °*C* it

is 7 %. McHugh and Stark [67] found that the thermal diffusivity is influenced by the cross-linking reaction caused by the rise in degree of cure. According to their findings, the strongest increase in k_3 is expected at $\alpha > 50$ %. In comparison to absolute values, Saad et al. [209] measured the k_3 of fully cured IM7/8552 i. a. at $T = 25\,°C$ and $T = 50\,°C$ and reported values of $0.841\,W/mK$ and $0.882\,W/mK$, respectively.

Effects of modification

The comparison of k_3 of the research materials with IM7/8552 at $1\,d$ out-time is illustrated in Fig. 3.28.
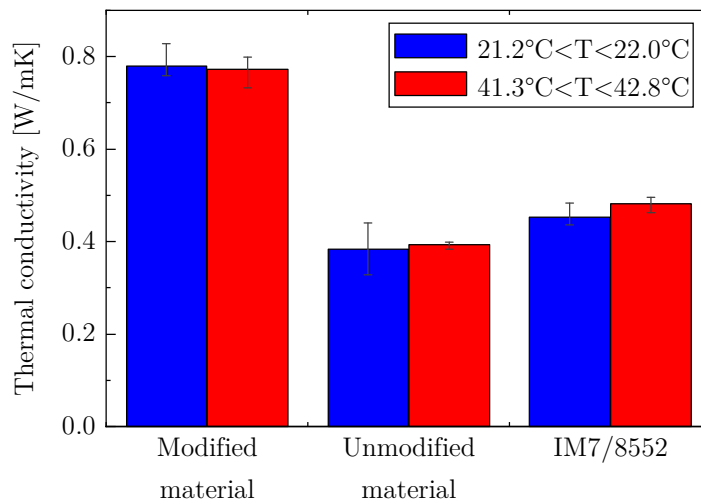
Figure 3.28: Thermal conductivity in thickness direction of the research materials in comparison with IM7/8552 at $1\,d$ out-time (error bars represent the minimum and maximum values of the respective test series)

The values for thermal diffusivity, density, and specific heat capacity used to calculate the thermal conductivity k_3 are listed in Tab. A.9 in the appendix. The average density of the modified material was $1.37\,g/cm^3$ and the average density of the unmodified material was $1.33\,g/cm^3$. The temperature dependence within the investigated range is slightly less pronounced than at the reference material with a relative change of 3 % and -1 % of the unmodified and modified material respectively. Compared to the reference, the thermal conductivity of the unmodified material is 15 % to 18 % lower — depending on the test temperature. In contrast, the modified material's k_3 is 60 % to 72 % higher than the reference's — depending on the test temperature — and it is twice as much as the unmodified material's k_3. In comparison to absolute values, Bard et al. [10] measured $k_3 = 0.91\,W/mK$

for the fully cured modified material and $k_3 = 0.36\ W/mK$ for the fully cured unmodified material.

Conclusion

The results for the thermal conductivity reveal a slight dependence on out-time for IM7/8552 within the investigated range. The modification of the research material leads to a doubling of k_3 which has to be considered since different thermal properties lead to different material temperatures if process parameters are not adapted. Compared to that, the temperature dependence for all investigated materials plays a subordinate role.

3.5 Mechanical properties

As discussed in the introduction of Chapter 3, the mechanical properties transverse tensile modulus, in-plane shear modulus, and bending stiffness are expected to change due to out-time effects or modification and they are input parameters for AFP defect prediction models. Therefore, they are analyzed within the material characterization.

3.5.1 Transverse tensile modulus

3.5.1.1 Test method

The transverse tensile modulus was measured in accordance with measurements by Margossian et al. [74] who compared DMA transverse tensile measurements to UTM transverse tensile measurements. The DMA measurements were reliable and reproducible and the DMA system allows for a straightforward temperature control. Furthermore, the amount of needed material is considerably less: $< 2\ \%$ of UTM specimen demand. Therefore, DMA measurements were chosen to determine the transverse tensile modulus.

3.5.1.2 Experimental procedure

The DMA system used for the experiments was a TA Instruments Q800 with tension clamps – see Fig. 3.29 right. The specimens — size $23\ mm \times 6.5\ mm \times 1\ mm$ — were covered with an aluminium tape in the area of clamping to avoid contamination of the clamps — see Fig. 3.29 left. To reach the thickness of $1\ mm$, multi-layer specimens were prepared in the same manner as the thermal conduct-

ivity specimens — see Sec. 3.4.2.2. During clamping of the specimens, great care
was taken to ensure a fiber orientation perpendicular to the direction of tension
and to avoid pretensioning of the specimen. The free measuring length was about
10 *mm* and the test parameters are listed in Tab. 3.11. Two of the loading rates
Margossian et al. used were chosen to investigate the influence of rate in addition
to the temperature. Besides aged IM7/8552 at 1 *d*, 5 *d*, 10 *d*, and 15 *d* out-time,
all experiments were carried out with the unmodified and the modified material.
For each material and test parameter combination five samples were tested.
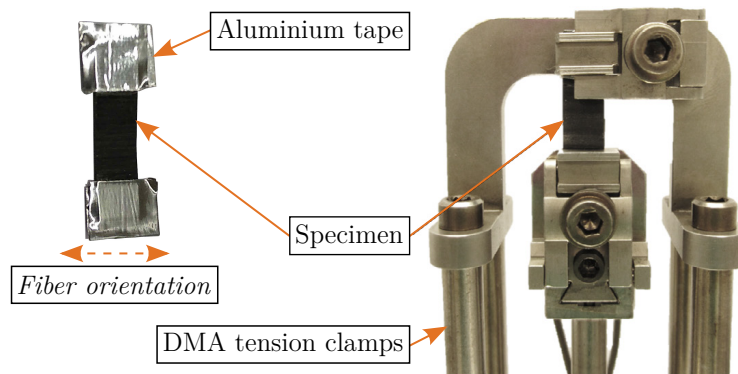
Figure 3.29: Transverse tensile specimen and DMA setup, adopted from [74]

Table 3.11: Transverse tensile modulus test — test parameters

Parameter	Symbol	Unit	Values
Loading rate	$\dot{F}$	N/min	0.05; 0.1
Temperature	T	$°C$	20; 40

The readings from the tensile tests were stress-strain curves. To obtain the trans-
verse tensile modulus E_2, the slope of the stress-strain curve was measured in the
region where there was a linear stress-strain response of the material in accordance
with Margossian et al.'s proposition [74].

3.5.1.3 Results

Out-time effects on IM7/8552

The transverse tensile measurements with IM7/8552 were part of the student thesis
[S12] and the publication [J2]. The results for E_2 of IM7/8552 as a function of out-
time are shown in Fig. 3.30. The scatter of the results was a lot less compared to
the tack measurements as variabilities in a single layer have less severe effects in
multi-layer specimens. Furthermore, E_2 is not dependent on the prepreg surface

which otherwise might be a source of variability. The mean standard deviation was 0.06 MPa. Detailed data is provided in Tab. A.10 in the appendix.
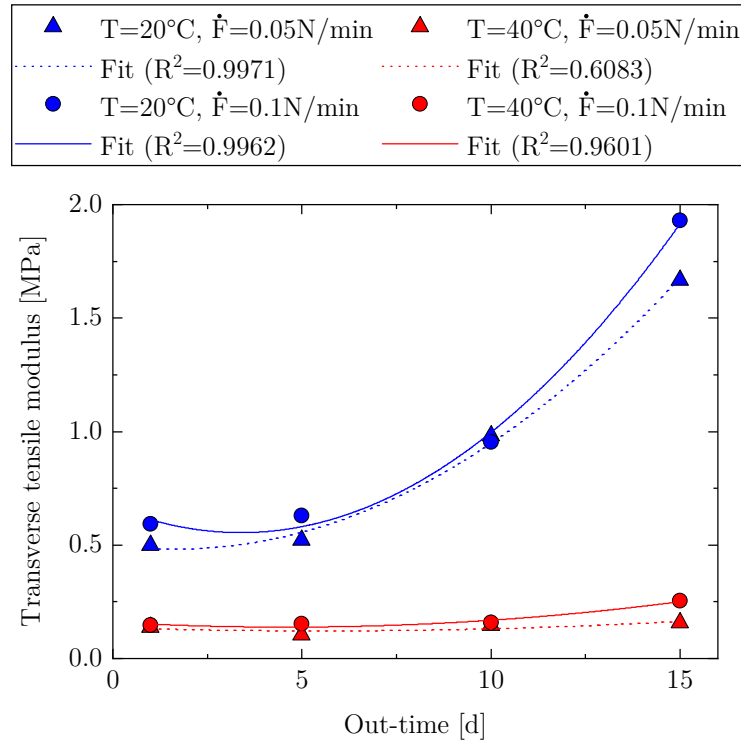
Figure 3.30: Transverse tensile modulus of IM7/8552

The transverse tensile modulus is generally higher at the higher loading rate ($\dot{F} = 0.1$ N/min) due to the viscoelasticity. Yet, the influence is comparably small — factor 1.0 to 1.6. In comparison, there is a pronounced temperature dependence as the higher temperature ($T = 40$ °C) leads to a reduction of E_2 of 72 to 90 %. This is in agreement with the expected temperature dependence of the viscosity which affects the transverse tensile stiffness [8]. E_2 generally increases with increasing out-time, as expected, as the viscosity increases due to the increase in molecular size and decrease in molecular mobility [8, 35, 59]. From 1 d to 15 d out-time, the increase is around factor 3.3 at $T = 20$ °C and around factor 1.2 to 1.7 at $T = 40$ °C. The dependence on out-time can be expressed as second order polynomial curve fits as

$$E_2(T, \dot{F}) = A_{E2}(T, \dot{F}) \cdot t_{out}^2 + B_{E2}(T, \dot{F}) \cdot t_{out} + C_{E2}(T, \dot{F}). \tag{3.5}$$

The parameters of the fits and the coefficients of determination are listed in Tab. 3.12. The coefficients of determination are rather high — 0.9971, 0.9962, and 0.9601 — except for $E_2(T = 40$ °$C, \dot{F} = 0.05$ $N/min)$ where the coefficient is 0.6083. Here, the transverse tensile modulus is lower at 5 d than at 1 d. In

comparison, in literature two values were found: $E_2 = 1\ MPa$, which was set by
Wang et al. [211] for a numerical study of IM7/8552, and $E_2 = 350\ MPa$ which
was measured by Rajan et al. [193] testing single-layer specimens in a table-top
test frame and evaluating the stress-strain relation up to 0.0001 strain. Rajan
et al. analyzed a different part of the stress-strain curve than Margossian et al.'s
test procedure [74] which explains the differing order of magnitude of the results.

Table 3.12: Transverse tensile modulus — parameters of fits

T [°C]	$\dot{F}$ [N/min]	A_{E2} [MPa/d^2]	B_{E2} [MPa/d]	C_{E2} [MPa]	R^2 [-]
20	0.05	$6.74 \cdot 10^{-3}$	$-2.264 \cdot 10^{-2}$	$5.013 \cdot 10^{-1}$	0.9971
20	0.1	$1.008 \cdot 10^{-2}$	$-6.815 \cdot 10^{-2}$	$6.699 \cdot 10^{-1}$	0.9962
40	0.05	$4.669 \cdot 10^{-4}$	$-5.14 \cdot 10^{-3}$	$1.357 \cdot 10^{-1}$	0.6083
40	0.1	$1.03 \cdot 10^{-3}$	$-9.47 \cdot 10^{-3}$	$1.6 \cdot 10^{-1}$	0.9601

Effects of modification

The results for the transverse tensile modulus of the research materials are depicted
in Fig. 3.31.

(a) All test parameters   **(b)** Excluding modified material at $T = 20$ °C
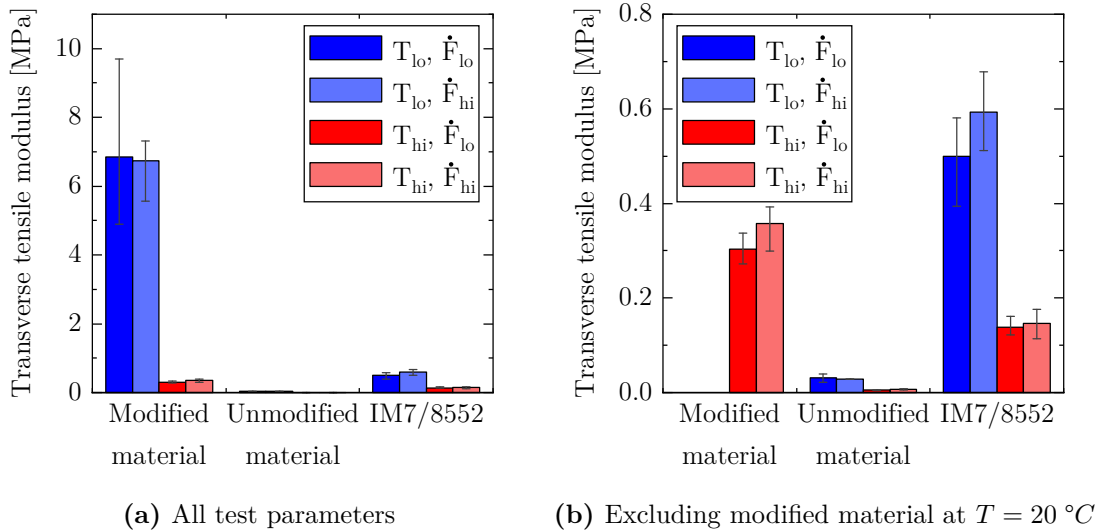
Figure 3.31: Transverse tensile modulus of the research materials in comparison with IM7/8552
at 1 d out-time ($T_{lo} = 20$ °C, $T_{hi} = 40$ °C, $\dot{F}_{lo} = 0.05\ N/min$, $\dot{F}_{hi} = 0.1\ N/min$;
error bars represent the minimum and maximum values of the respective test series)

The results including all test parameters — Fig. 3.31a — reveal that the transverse tensile modulus of the modified material at $T = 20\ °C$ extraordinarily exceeds the transverse tensile modulus of both the unmodified material and the reference. E_2 is mainly dependent on the resin viscosity as it is explained by rheology data of the neat resins from UBT: the complex viscosity of the modified resin at $T = 25\ °C$ is around 85 Pas while at $T = 50\ °C$ it is around 8 Pas. In comparison, the complex viscosity of the unmodified resin is around 80 % lower. Another indicator for the high transverse tensile modulus of the modified material at $T = 20\ °C$ was the condition at the end of the experiment: no failure of the specimens was visible. Albeit, it was possible to evaluate the linear stress-strain response of the resulting curve in accordance with Margossian et al.'s publication [74]. At $T = 40\ °C$, the specimens were torn apart and the specimens of the unmodified material were elongated until the maximum travel of the DMA. Omitting the results of the modified material at $T = 20\ °C$, facilitates the comparison of the remaining results — see Fig. 3.31b. E_2 of the modified material at $T = 40\ °C$ is more than twice as high as the reference, yet it is lower than the reference at $T = 20\ °C$. E_2 of the unmodified material is significantly lower compared to the reference and the modified material. The modification therefore leads to an increase of E_2 of more than factor 200 at $T = 20\ °C$ and more than factor 50 at $T = 40\ °C$.

Conclusion

The transverse tensile modulus of IM7/8552 is clearly out-time-dependent following a second order polynomial fit. The correlation to test parameters can be seen in Fig. 3.32a revealing that E_2 correlates strongly with temperature caused by the temperature dependent viscoelastic behavior of the resin and weakly with rate. An increase in temperature could therefore be used to compensate out-time effects.

For the research materials, the correlation to the test parameters is similar to the reference and the modification has a strong correlation to the transverse tensile modulus — see Fig. 3.32b. The results provide an overview of the effects of material changes on E_2 and serve as inputs for defect prediction models.

(a) IM7/8552   **(b)** Research materials
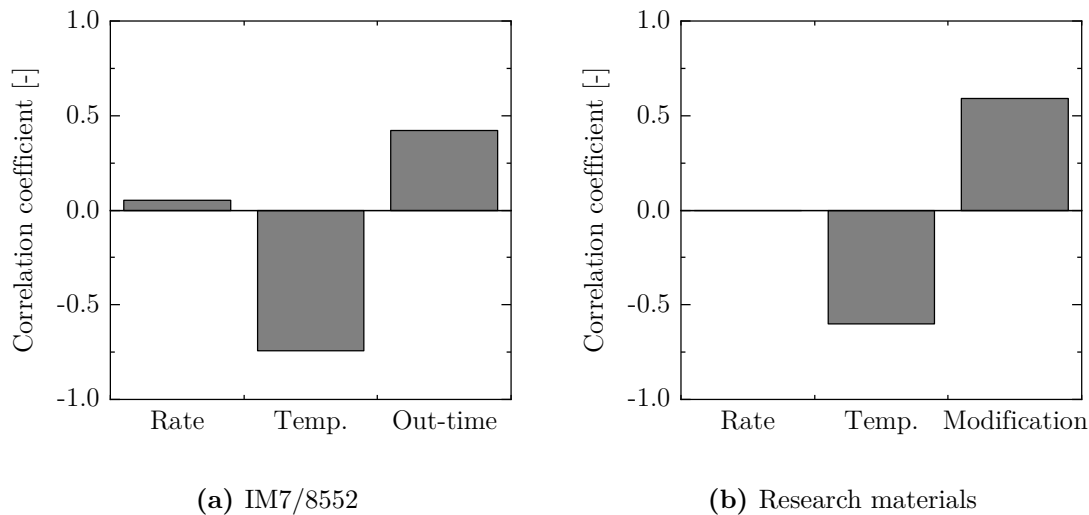
Figure 3.32: Transverse tensile modulus correlation coefficients

3.5.2 In-plane shear modulus

3.5.2.1 Test method

A comparison of test methods for the characterization of the in-plane shear modulus G_{12} of uncured prepreg tapes was subject of [J1]. The investigation revealed that test principles like the picture-frame test setup and the off-axis tension test setup were disadvantageous regarding the reliability of results, the needed equipment, and the material demand — see Sec. 2.1.4 and [J1]. In [J1], two test principles were analyzed experimentally — the rotational parallel platens test method (Thin Plate Torsion Test) and the torsion bar test method (Torsion Bar Test). As the former displayed several sources of variability in the results and the number of experiments to be performed is comparably high, it was not pursued further [J1]. The Torsion Bar Test was less susceptible to inaccuracies and scatter and the number of experiments to be performed is comparably low. Therefore, it was selected as the test method for all in-plane shear tests.

3.5.2.2 Experimental procedure

The approach for the Torsion Bar Test is based on the correlation between the torque M_{TB} and the rotation angle ϕ_{TB} for a prismatic bar with the fiber direction parallel to the rotation axis and linear elastic material behavior:

$$M_{TB} = G_{L,TB}\, J\, \frac{\phi_{TB}}{L_{TB}} \tag{3.6}$$

where $G_{L,TB}$ corresponds to the elastic shear modulus, J to the torsional constant, and L_{TB} to the free specimen length. For the measurements, a multilayered specimen with a square cross section is positioned inside the rheometer (Anton Parr MCR 302) using the standard torsion clamps — see Fig. 3.33. The specimen is subjected to an oscillating torsional load within the linear viscoelastic (LVE) region by the upper clamp while the lower clamp remains fixed. Frequency sweeps are conducted and the generated data for the storage modulus and the loss modulus are used to calculate the stress-strain response — see [J1] and [77]. The in-plane shear modulus is subsequently determined by linearization of the stress-strain curve.
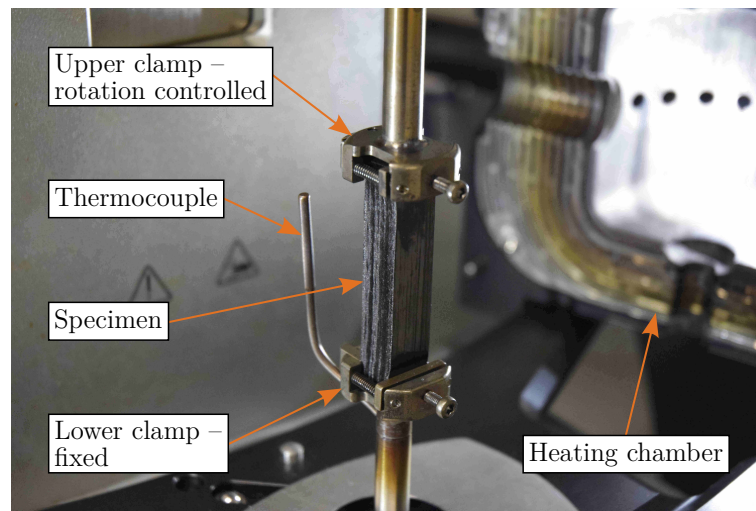
Figure 3.33: In-plane shear modulus test — setup in rheometer

60-layer IM7/8552 specimens — see Fig. 3.34 — were prepared in the same manner as the thermal conductivity specimens to obtain the desired specimen thickness of 12 mm (length: 60 mm, width: 12 mm). Because of the limited available amount of research materials, the specimen size for the research materials was reduced to 60 $mm \times$ 5 $mm \times$ 5 mm. To account for the difference in fiber stiffness between IM7 (276 GPa) and the fibers of the research materials (HTS40, 240 GPa), results from [J1] with AS4/8552 were used to evaluate the influence of fiber stiffness. The AS4 fiber has a tensile stiffness of 231 GPa. To evaluate the influence of specimen size on the results, additional 5 $mm \times$ 5 mm specimens with AS4/8552 were prepared and tested. For all test parameters, five specimens each were tested. The IM7/8552 specimens were subjected to out-times of 1 d, 5 d, 10 d, and 15 d.

The test parameters for the experimental design including two test temperatures and the range for the frequency sweeps are listed in Tab. 3.13. In accordance with the test method theory, the shear behavior at different shear rates, which are the product of angular frequency and maximum shear amplitude, were assessed.
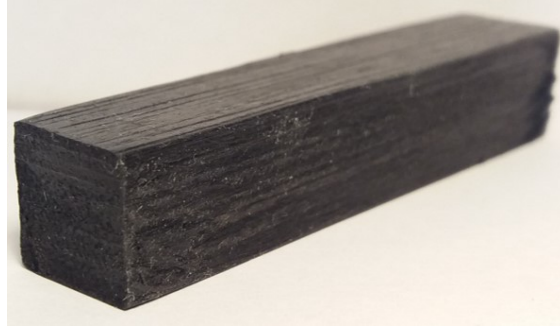
Figure 3.34: In-plane shear modulus test — specimen

Table 3.13: In-plane shear modulus tests — test parameters

Parameter	Symbol	Unit	Values
Angular frequency	ω	rad/s	0.1...500
Temperature	T	$°C$	20; 40

3.5.2.3 Results

Out-time effects on IM7/8552

The in plane shear modulus results are depicted in Fig. 3.35. The values were calculated at shear rates of 0.001 s^{-1}, 0.005 s^{-1}, and 0.01 s^{-1}. The in plane shear modulus G_{12} obtained from the Torsion Bar Test is a result of several conversion steps based on the mean values of the measured storage and loss modulus. Therefore, the measured values storage and loss modulus serve as an indicator for the variation of the converted results: their mean coefficient of variation was 5.3 % indicating that the scatter was significantly lower compared to experiments with single-layer specimens. Fig. 3.35 demonstrates that the obtained shear modulus is rate dependent since it is affected by the viscous behavior of the resin. At both test temperatures, G_{12} increases with increasing shear rate. At $T = 20$ °C, the increase from $\dot{\gamma} = 0.001$ s^{-1} to $\dot{\gamma} = 0.01$ s^{-1} is around factor 1.7 to 2.1 — depending on the out-time — and at $T = 40$ °C the increase is around factor 1.4. The temperature dependence of G_{12} is clearly evident, too. The higher temperature ($T = 40$ °C) leads to a reduction of G_{12} of 58 to 86 % depending on rate and out-time. Similar to E_2, the in plane shear modulus increases with increasing out-time as the viscosity increases due to the increase in molecular size and decrease in molecular mobility. The dependence on out-time can be expressed as second order polynomial curve fits at $T = 20$ °C as

$$G_{12}(T, \dot{\gamma}) = A_{G12}(T, \dot{\gamma}) \cdot t_{out}^2 + B_{G12}(T, \dot{\gamma}) \cdot t_{out} + C_{G12}(T, \dot{\gamma}) \tag{3.7}$$

while at $T = 40$ °C, the out-time dependence appeared rather linear so that $A_{G12}(T = 40$ °$C)$ was set to zero. The parameters of the fits and the coefficients of determination are listed in Tab. 3.14.
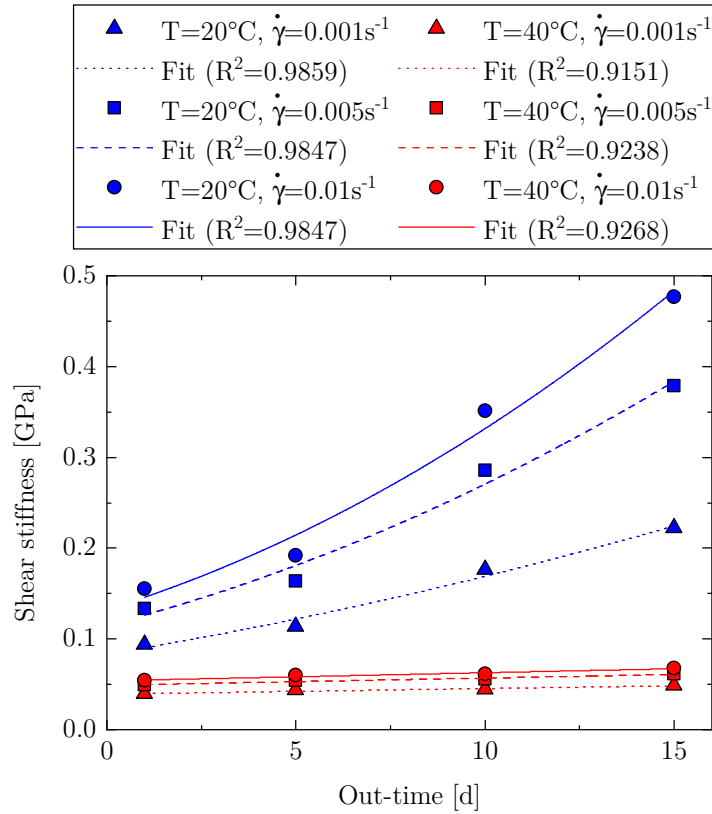
Figure 3.35: In-plane shear modulus of IM7/8552

Table 3.14: In-plane shear modulus — parameters of fits

T [°C]	$\dot{\gamma}$ [s^{-1}]	A_{G12} [GPa/d^2]	B_{G12} [GPa/d]	C_{G12} [GPa]	R^2 [-]
20	0.001	$1.660 \cdot 10^{-4}$	$6.920 \cdot 10^{-3}$	$8.319 \cdot 10^{-1}$	0.9859
20	0.005	$4.724 \cdot 10^{-4}$	$1.089 \cdot 10^{-2}$	$1.150 \cdot 10^{-1}$	0.9847
20	0.01	$6.957 \cdot 10^{-4}$	$1.298 \cdot 10^{-2}$	$1.323 \cdot 10^{-1}$	0.9847
40	0.001	0	$6.168 \cdot 10^{-4}$	$3.918 \cdot 10^{-2}$	0.9151
40	0.005	0	$7.958 \cdot 10^{-4}$	$4.896 \cdot 10^{-2}$	0.9238
40	0.01	0	$8.880 \cdot 10^{-4}$	$5.389 \cdot 10^{-2}$	0.9268

In comparison, in literature Wang et al. [84] presented values between 14 MPa and 24 MPa at $T = 25$ °C obtained from an off axis tensile test. Contrary to that, Rajan et al. [193] did a parametric study with their numerical model for buckle formation where they used values from 0.5 GPa to 5 GPa and eventually assumed $G_{12} = 5 \, GPa$, which is significantly higher than the presented findings.

Effects of modification

Fig. 3.36 shows the results for the research materials compared to IM7/8552 at 1 d out-time. Because of the material imperfections, the scatter of the measured values storage and loss modulus was higher compared to the reference. For the unmodified material, the mean coefficient of variation was 25 % and for the modified material it was 10 %. To contextualize the difference in specimen size and fiber, the relative change from IM7 fibers to AS4 fibers and from 12 mm × 12 mm specimens to 5 mm × 5 mm specimens was calculated from the results. The lower stiffness of the AS4 fibers led to a reduction in G_{12} (up to 36 %) and the smaller specimen size led to an increase in G_{12} (up to 63 %). In conclusion, the in-plane shear modulus of AS4/8552 5 mm × 5 mm specimens was on average 8 % higher than the in-plane shear modulus of IM7/8552 12 mm × 12 mm specimens. Because of this comparably small difference, a direct comparison of the research material specimens to IM7/8552 12 mm × 12 mm specimens seems feasible.

Similar to the E_2 results, the in-plane shear modulus of the modified material at $T = 20$ °C is significantly higher than the the in-plane shear modulus of the unmodified material and the reference — see Fig. 3.36a. Again, the root cause attributed to the high viscosity of the modified resin at the lower temperature. To compare the remaining results, the in-plane shear modulus of the modified material at $T = 20$ °C was omitted in Fig. 3.36b.

(a) All test parameters   **(b)** Excluding modified material at $T = 20$ °C
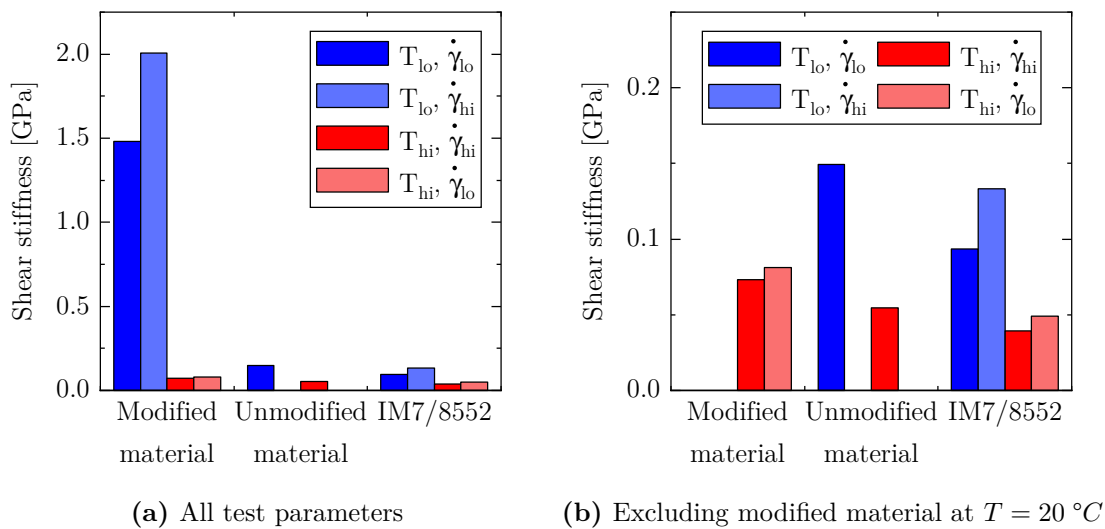
Figure 3.36: In-plane shear modulus of the research materials in comparison with IM7/8552 at 1 d out-time ($T_{lo} = 20$ °C, $T_{hi} = 40$ °C, $\dot{\gamma}_{lo} = 0.001$ s^{-1}, $\dot{\gamma}_{hi} = 0.005$ s^{-1})

The results for the unmodified material were only calculated up to $\dot{\gamma} = 0.001\ s^{-1}$ because of the low maximum shear rate determined by the maximum shear strain and the angular frequency. The maximum shear strain — defined by the LVE region in the amplitude sweep — of the unmodified material is only 0.0005 %. In comparison, the maximum shear strain of the modified material and the reference are 0.002 % and 0.003 %, respectively. At $\dot{\gamma} = 0.001\ s^{-1}$, G_{12} of both research materials are 39 to 87 % higher than the reference. The increase due to modification at $T = 40\ °C$, $\dot{\gamma} = 0.001\ s^{-1}$ is 35 % while at $T = 20\ °C$ it is 890 %.

Conclusion

The in-plane shear modulus of IM7/8552 is clearly out-time-dependent following a second order polynomial fit. The correlation to test parameters can be seen in Fig. 3.37a revealing that G_{12} correlates strongly with temperature caused by the temperature dependent viscoelastic behavior of the resin and moderately with rate. An increase in temperature could therefore be used to compensate out-time effects.

(a) IM7/8552 **(b)** Research materials
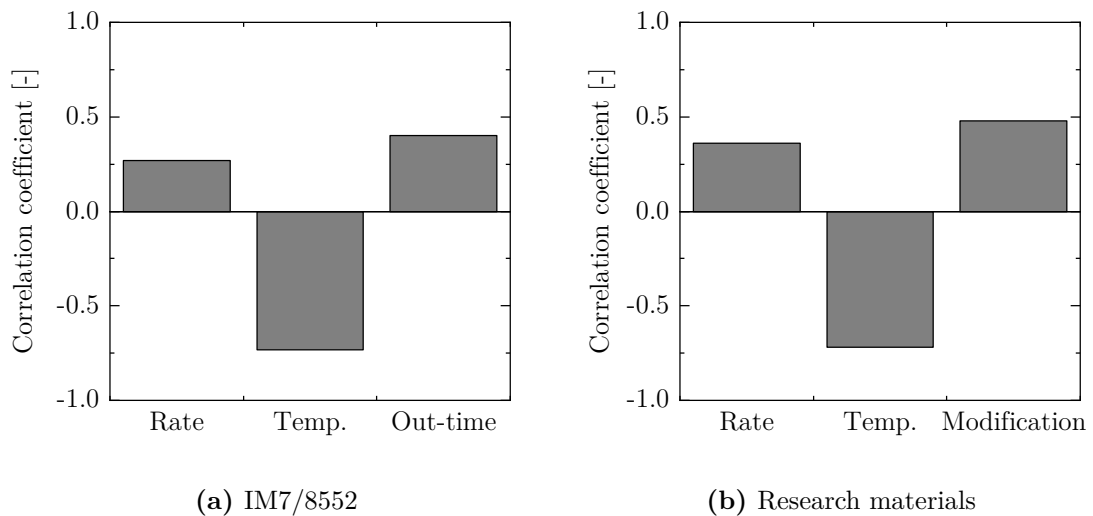
Figure 3.37: In-plane shear modulus correlation coefficients

For the research materials, the correlation to the test parameters is similar to the reference and the modification has a moderate to strong correlation to the transverse tensile modulus — see Fig. 3.37b. The results provide an overview of the effects of material changes on G_{12} and serve as inputs for defect prediction models.

3.5.3 Bending stiffness

3.5.3.1 Test method

First bending tests were carried out using a double cantilever fixture in a DMA in accordance with [163] — see [S6]. However, due to the high tensile stiffness of the fibers, measurements with a double cantilever fixture do not ensure a pure bending measurement. Furthermore, to comply with the DMA's geometric requirements, multilayer specimens had to be used which are prone to unquantifiable inter-ply displacements. To provide reliable bending measurements with single-layer specimens, within [S9] a new test method was developed which was derived from a bending test device for fiber-reinforced hinges [212]. The test principle is illustrated in Fig. 3.38.
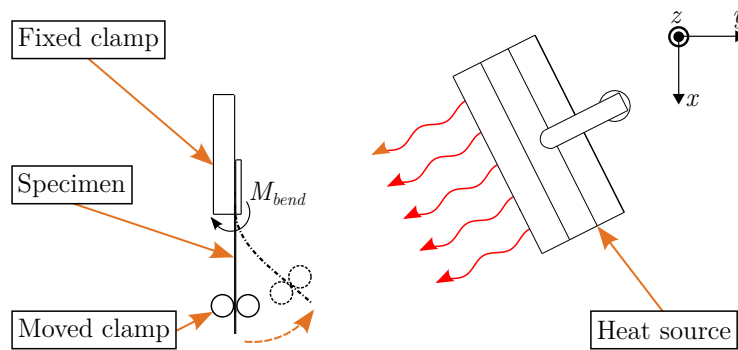
Figure 3.38: Bending test principle (top view)

The test is based on a single cantilever test where the specimen is deflected in a circular motion initiated by a stepper motor. In the end position of the deflection — e. g. 30 ° — the material response is measured via a torque sensor (D-D2452/M210-G21 from Lorenz Messtechnik GmbH, Germany) and the deflection curve of the specimen is captured via digital image acquisition. By this, the bending stiffness $E_{flex}I$ can be determined in accordance with the Euler-Bernoulli beam theory. Furthermore, the flexural modulus E_{flex} can be determined as the quotient of bending stiffness and second moment of area I. The test is implemented in a standalone test bench which is shown in Fig. 3.39. Here, the camera for image acquisition is mounted above the specimen. It is equipped with telecentric lenses which enables orthoscopic image acquisition. As the bending stiffness is expected to be dependent on the test temperature, a heat source — IR emitter — combined with temperature monitoring were implemented to enable measurements at different temperatures. The analysis of the measured data is implemented in a MATLAB script as developed in [S9] using the input values specimen size, deflection angle, specimen deflection curve, and measured torque. To validate the

functional principle of the test bench, measurements with steel specimens were conducted resulting in a flexural modulus of 209.6 GPa.
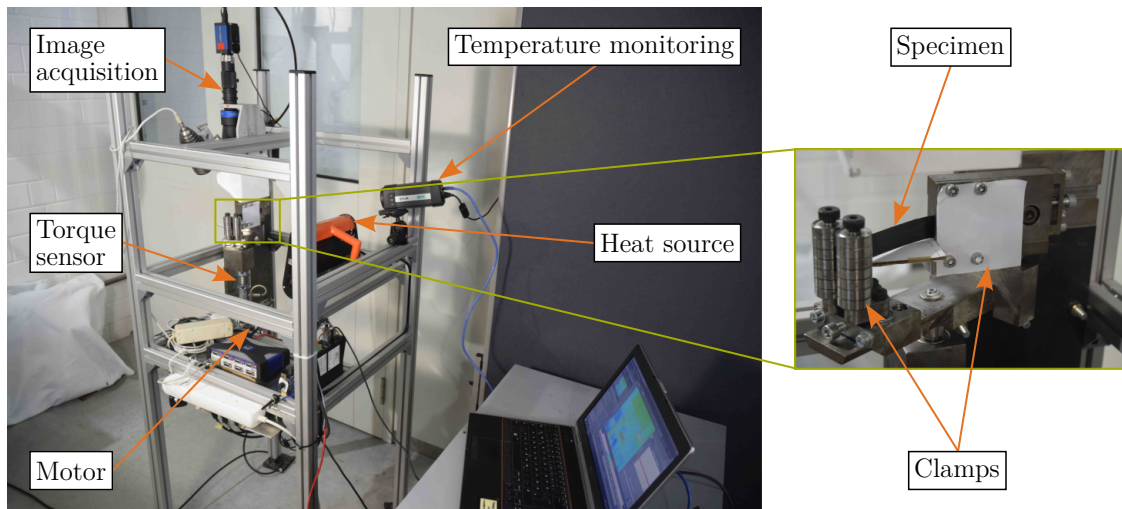
Figure 3.39: Bending test bench

3.5.3.2 Experimental procedure

The experiments were defined as quasi-static measurements. The specimens were deflected and the torque measurement directly after reaching the end position was used for the analysis. The deflection angle was set constant to 30 °. The specimen were single-layer specimens with a length of 130 mm and a width of 20 mm. The thickness of each layer was measured using a caliper. Measurements were conducted at room temperature — i. e. at around 23.5 $°C$ — and at 40 $°C$. To account for the difference in fiber stiffness between reference and research materials, additional measurements with AS4/8552 were conducted. In the case of the bending stiffness specimens, it was not possible to age them in the environmental chamber at 21 $°C$ and 40 % RH. Instead they were aged in an oven at 60 $°C$ and T_g measurements were conducted to calculate the equivalent out-time at 21 $°C$ and 40 %RH according to Eq. 3.2. The resulting equivalent out-times were 4.9 d, 8.1 d, 10.5 d, and 15 d. Again, for each material five specimens were tested.

3.5.3.3 Results

Out-time effects on IM7/8552

The bending stiffness and flexural modulus of IM7/8552 as a function of out-time is depicted in Fig. 3.40.

(a) Bending stiffness

(b) Flexural modulus
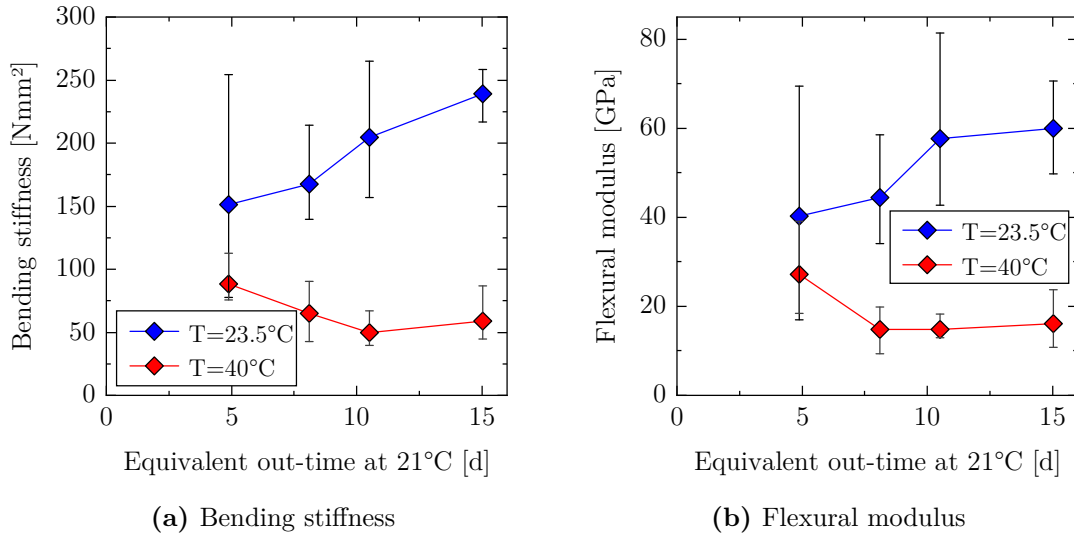
Figure 3.40: Bending properties of IM7/8552 (error bars represent the minimum and maximum values of the respective test series)

Similar to other single-layer measurements, a certain degree of scatter was present. Yet, the effects of out-time and test temperature are clearly visible. At room temperature, the bending stiffness increases monotonically as a function of out-time. $E_{flex}I$ at 15 d out-time was 58 % higher than at 4.9 d out-time. Again, the increase is explained by the decrease in molecular mobility at higher out-times. In contrast, at $T = 40\,°C$ the bending stiffness decreases up to 10.5 d out-time followed by a slight increase from 10.5 d to 15 d out-time. In this case, the temperature rise apparently compensates all out-time effects. Yet, no cause was found explaining the decrease from 4.9 d to 10.5 d out-time. Comparably to the results for E_2 and G_{12}, the effect of temperature increases as a function of out-time. At 4.9 d out-time, the ratio between the bending stiffness at room temperature and $T = 40\,°C$ is 1.7 and at 15 d out-time it is 4.1.

The results for the theoretical flexural modulus — see Fig. 3.40b — show similar dependencies as the bending stiffness.

Effects of modification

Fig. 3.41 summarizes the results for the research materials compared to IM7/8552 and AS4/8552.

(a) Bending stiffness

(b) Flexural modulus
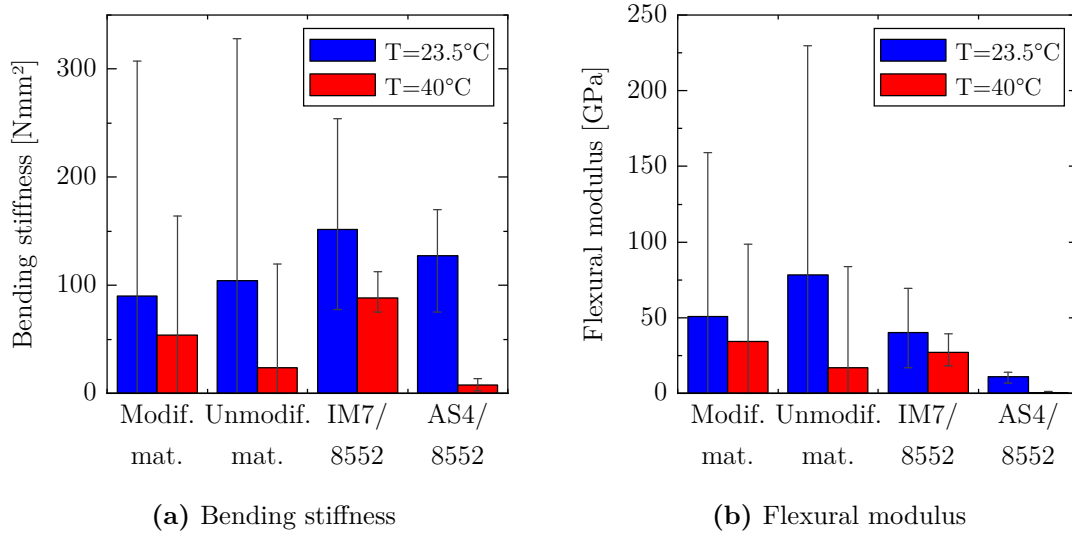
Figure 3.41: Bending properties of the research materials in comparison with IM7/8552 at 4.9 *d* equivalent out-time and AS4/8552 at 1 *d* out-time (error bars represent the minimum and maximum values of the respective test series)

The research material results were affected by material imperfections leading to very high scatter. Additionally, the high tack of the unmodified specimens led to handling difficulties. As Fig. 3.41 indicates, the mean values of the research materials were affected by extraordinary outliers. Since extraordinary outliers are not expected when the material is fully developed for serial production, the outliers of the research materials were omitted in Fig. 3.42 in order to compare the expected material characteristics to the reference. Therefore, the mean values for the research materials in Fig. 3.42 were calculated with three instead of five measurements excluding the outliers.

Fig. 3.42a reveals that the bending stiffness of the reference is generally higher than the bending stiffness of the research materials. Since the specimen thickness and therefore the second moment of area differ — research materials thickness: 0.095 *mm*, IM7/8552 thickness: 0.13 *mm*, AS4/8552 thickness: 0.19 *mm* — a comparison of the flexural modulus is more feasible than a comparison of the bending stiffness. In this regard, Fig. 3.42b shows that E_{flex} of the modified material is considerably higher than E_{flex} of AS4/8552 and slightly lower than that of IM7/8552. In contrast, E_{flex} of the unmodified material is significantly lower compared to the other materials. While the different specimens can be compared directly, the differences in fiber stiffness and fiber volume content have to be respected.

At $T = 40$ °*C*, the unmodified material did not have any measurable bending stiffness as the resin viscosity was seemingly too low to provide sufficient dimensional stability of the specimens. At room temperature, the flexural modulus of

the unmodified material was 9 % of the modified materials modulus and 27 % of the AS4/8552 modulus.

(a) Bending stiffness   **(b)** Flexural modulus
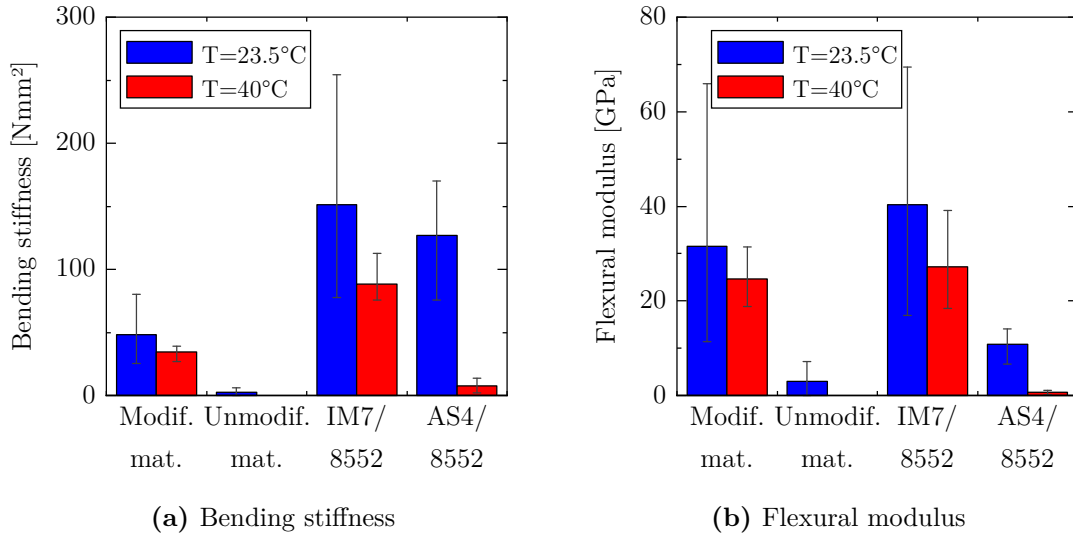
Figure 3.42: Bending properties of the research materials without outliers in comparison with IM7/8552 at 4.9 *d* equivalent out-time and AS4/8552 at 1 *d* out-time (error bars represent the minimum and maximum values of the respective test series)

Conclusion

The bending stiffness and flexural modulus of IM7/8552 display an expected out-time dependence at room temperature. Both bending stiffness and flexural modulus are significantly lower at $T = 40\ °C$. This indicates that a temperature increase can be used as a countermeasure to the out-time effects similar to the conclusions drawn for E_2 and G_{12}. The results of the research materials reveal that the single-layer specimens of the unmodified material have a low dimensional stability. The modification leads to a rise in flexural modulus of factor 11 at room temperature. The flexural modulus of the modified material is almost as high as the flexural modulus of IM7/8552 even though the fiber stiffness is lower. Bending stiffness characteristics have to be considered in lay-up scenarios on convex or concave surfaces. Here, an increase in bending stiffness caused by the material changes can lead to a higher defect probability — particularly in combination with a decrease in tack.

3.6 Intermediate summary

The findings presented in the material characterization chapter answer the questions

- which prepreg properties are relevant for AFP,

- how can these properties be measured, and

- what are the effects of material changes due to out-time and modification on the prepreg properties.

The relevant properties and the way they can be measured is summarized in the prepreg characterization procedure in Fig. 3.43 which lists the properties and their respective test methods and test devices. The depicted tabs visualize the implementation of the procedure for each out-time or material condition.
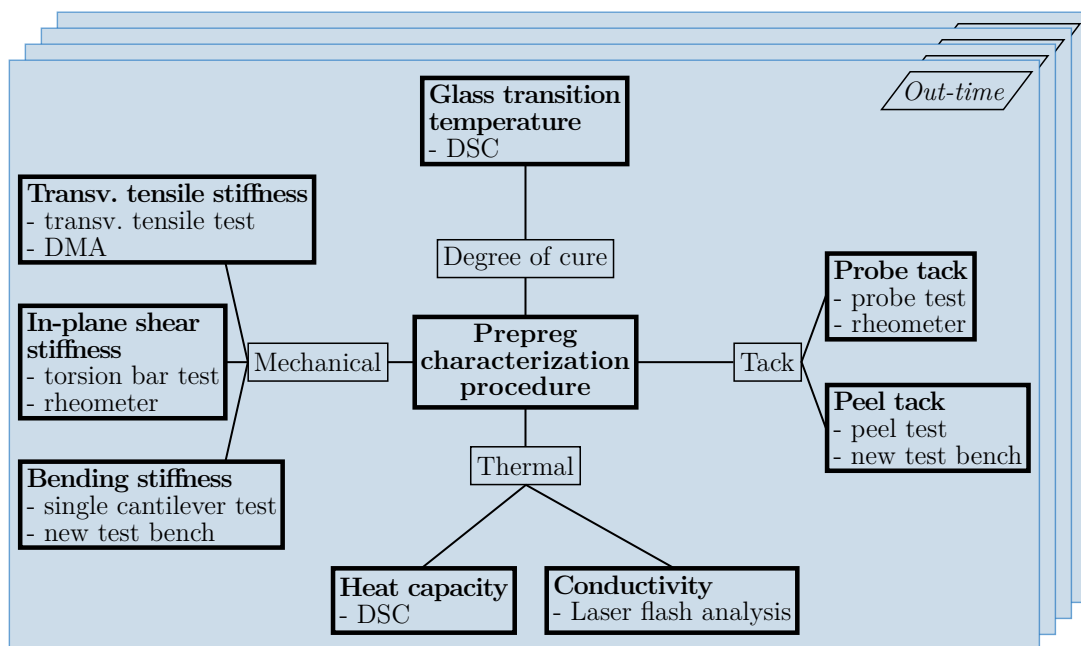
Figure 3.43: Prepreg characterization procedure

The AFP-relevant properties comprise tack, thermal properties, and mechanical properties while the degree of cure is used to quantify the out-time. Test methods for tack and mechanical properties are not standardized. Therefore, test methods from literature were evaluated and new test methods were developed to complete the prepreg characterization procedure.

The effects of material changes due to out-time and modification on the prepreg properties as well as the most influential test parameters are summarized in Tab. 3.15 where the filling of the Harvey balls correspond to the correlation coefficient.

Table 3.15: Overview of correlation coefficient r for all material properties with regard to out-time, modification, and the respective most influential test parameter (the filling of the Harvey balls correspond to the correlation coefficient: clockwise filling in black $0 < r \leq 1$, counterclockwise filling in grey $-1 \leq r < 0$, no filling $r = 0$; F: compaction force, T: temperature, TP: test parameter, v: lay-up rate, v_{probe}: debonding rate)

Property	Out-time			Modification		
	r(out-time)	TP	r(TP)	r(modif.)	TP	r(TP)
Probe tack max. force	◔	T	◑	◔	v_{probe}	◑
Probe tack work of adh.	◔	T	◑	○	v_{probe}	◑
Probe tack tack stiffness	◐	T	◔	◔	v_{probe}	◔
Peel tack	◕	v	◔	◐	F	◔
Heat capacity	○	T	●	◕	T	◕
Thermal conductivity	◕	T	◐	●	T	○
Transv. tensile modulus	◑	T	◔	◑	T	◑
In-plane shear modulus	◑	T	◔	◐	T	◔
Bending stiffness	◔	T	◔	●	T	◔

Both out-time and modification lead to a reduction in tack and to an increase in mechanical properties and thermal conductivity. The temperature is the most influential test parameter for most properties which is explained by the viscoelastic behavior of the prepregs.

An overview of the properties of the investigated research materials in comparison with the reference IM7/8552 is given in Tab. 3.16.

Table 3.16: Qualitative comparison of properties of research materials to properties of IM7/8552 (↑: significantly higher, ↗: higher, —: comparable level, ↘: lower, ↓: significantly lower)

Property	Unmodified material	Modified material
Probe tack — max. force	↗	↘
Probe tack — work of adh.	↑	↑
Probe tack — tack stiffness	↗	—
Peel tack	↗	—
Heat capacity	—	—
Thermal conductivity	—	↑
Transv. tensile modulus	↓	↑
In-plane shear modulus	—	↑
Bending stiffness	↓	↗

The unmodified material has significantly higher tack and lower mechanical properties than the reference. The modified material has a comparable tack and significantly higher mechanical properties. In conclusion, both materials seem suitable for AFP processing, yet the high tack of the unmodified material may lead to unwanted adhesion in the material feed which causes process interruptions.

The prepreg characterization procedure was conducted at four different out-times — as indicated in Fig. 3.43 — and two different filler contents. The outcomes on the effects of out-time and modification can be used to reduce the experimental design for future investigations as it is assumed that the dependencies can are valid for other prepregs as well.

4 Experimental investigations on AFP lay-up defects

Since prepreg material properties significantly change due to out-time and modifications, it is expected that these changes affect the material process interaction and therefore the lay-up quality during AFP. To quantify these effects and to lay the foundation for defect predictions, lay-up experiments at different geometric scenarios with varying prepreg conditions and process parameters were conducted. By analyzing the effects of material changes and process parameter adjustments, their impact on the lay-up quality can be deduced directly. To implement that, the relevant lay-up scenarios steering, concave tool geometry, and convex tool geometry were addressed and the same out-time conditions for the reference material IM7/8552 as in the material characterization were used. Due to the fact that the research materials were not available as slit-tapes, all lay-up experiments were conducted with the reference material. Yet, combined with the results of the material characterization, conclusion for the lay-up behavior of the research materials can be drawn.

The steering defect investigations — Sec. 4.1 — include experiments on the types of defects occurring, on the temporal evolvement of the defects, and on the effects of process parameter adjustments. In Sec. 4.2, the lay-up defect occurring during lay-up on a concave tool geometry — bridging — is analyzed including various tool geometries. Sec. 4.3 describes the investigations on defects resulting from a convex tool geometry — tape peel-off — including process parameter and geometry variations. The chapter concludes with the intermediate summary in Sec. 4.4.

4.1 Steering defect investigations

Steering induced defects play a significant role in the analysis of AFP lay-ups as it is shown by the number of publications on the topic [23, 31, 149, 176–185]. Furthermore, they affect the mechanical properties of the cured part [175]. Therefore, steering defect investigations are the main focus of the investigations on AFP lay-up defects.

4.1.1 Investigation on defect type and steering radius

In a first study published in [C1], the effects of out-time and steering radius on the type and amount of defect were investigated.

4.1.1.1 Experimental procedure

The experiments were conducted with the Coriolis 1/8-TS-AFP machine described in Sec. 2.3. The process parameters listed in Tab. 4.1 were kept constant to focus on out-time effects and steering radii.

Table 4.1: Steering investigation on defect type and steering radius — process parameters

Parameter	Symbol	Unit	Value
Lay-up rate	v	m/s	0.05
Compaction force	F	N	250
IR emitter power	P_{IR}	W	258

Single slit-tapes were laid up onto a flat aluminium plate with three different steering radii — 400 mm, 600 mm, 800 mm — and a constant arc length of 400 mm. By laying up single slit-tapes instead of multiple slit-tapes, interferences between adjacent tapes could be avoided. To avoid fiber straightening within the arc, each track started and ended with a 70 mm straight. An evaluation method from literature [149] was adapted for the analysis of defects resulting from steering (out-of-plane buckling, in-plane fiber waviness, tape pull-up). The procedure includes (see also Fig. 4.1):

- laying-up tape,

- marking of buckles and tape pull-up five minutes after lay-up (as conducted in [149]),

- taking photographs from above of each tape section with a reference length (graph paper),

- measuring buckles and tape pull-up as well as marking and counting locations with in-plane fiber waviness using the image processing software ImageJ.

The material — IM7/8552 — had been unfrozen at around 10 °C for 4.5 days prior to the start of the investigations. During the investigations the material was stored at 21.8 °C and 33 % relative humidity in between the experiments. Therefore, the absolute values of the out-time differs slightly from the standard conditions during

the other investigations. Nonetheless, interpretations of the relative changes are thoroughly valid. Each experiment was repeated five times.
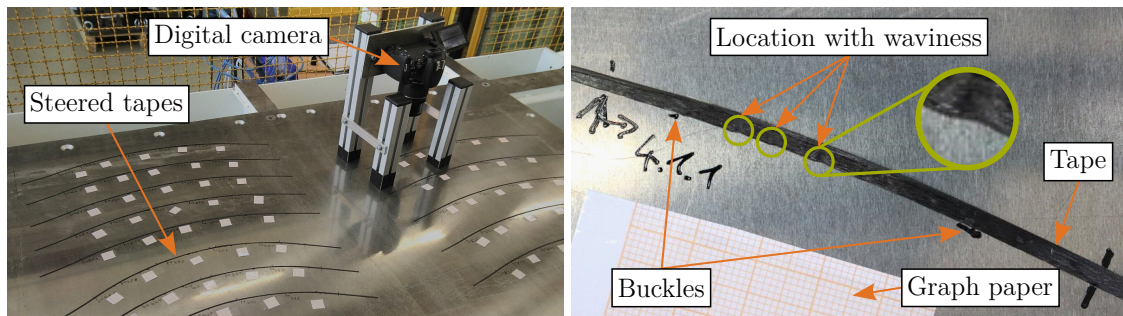
Figure 4.1: Steering investigation on defect type and steering radius — image capturing (left), image analysis (right)

4.1.1.2 Results

The results for out-of-plane buckles, in-plane waviness and tape pull-up are summarized in Fig. 4.2. It shows that the defects due to steering vary as a function of the steering radius and as a function of the material's out-time. The results also show that all three steering defects occur. The highest total buckled length and the highest number of buckles occur at the highest state of aging — 14 d. The lowest total buckled length and number of buckles, however, occur at 7 d instead of 2 d out-time. This could be attributed to an increase in tack in that out-time range as several authors had identified in their studies [30, 34–37, 51, 53, 65, 66]. The tack measurements presented in Sec. 3.3, however, do not suggest that the tack would increase in that out-time range. Furthermore, in a later study on steering defects — see Sec. 4.1.3 — there was no decrease in defects as a function of out-time. Yet, several differences have to be considered which may cause different results: the material batch and the material's pre-condition were different, the time of defect marking was five minutes instead of 40 minutes after lay-up, and the ambient temperature at 7 d out-time was around 1 °C higher than at 2 d out-time.

The dependence of buckles on the steering radius is as expected at 2 d out-time — smaller steering radius, more defects (a smaller steering radius induces a higher stress in the tape). At 14 d out-time, the dependence seems inverse — larger steering radius, more defects. However, at 14 d out-time several tapes did not adhere at all due to the low tack as shown in Fig. 4.3. As published in [C1], they were not included in the calculation of the defects which affects the statements in the results. Yet, considering them as defects improves the validity of the results with regard to the lay-up quality. Therefore, considering them as buckled length

over the full arc length leads to the following total buckled lengths: 329.4 *mm* at 400 *mm*, 146.2 *mm* at 600 *mm*, and 118.3 *mm* at 800 *mm* which is in agreement with the expected dependence on the steering radius. The fact that four out of five tapes did not adhere at 14 *d* out-time indicates that it is not possible to lay-up a steering radius of 400 *mm* at this material age.

(a) Total buckled length

(b) No. of buckles

(c) Locations with waviness

(d) Tape pull-up
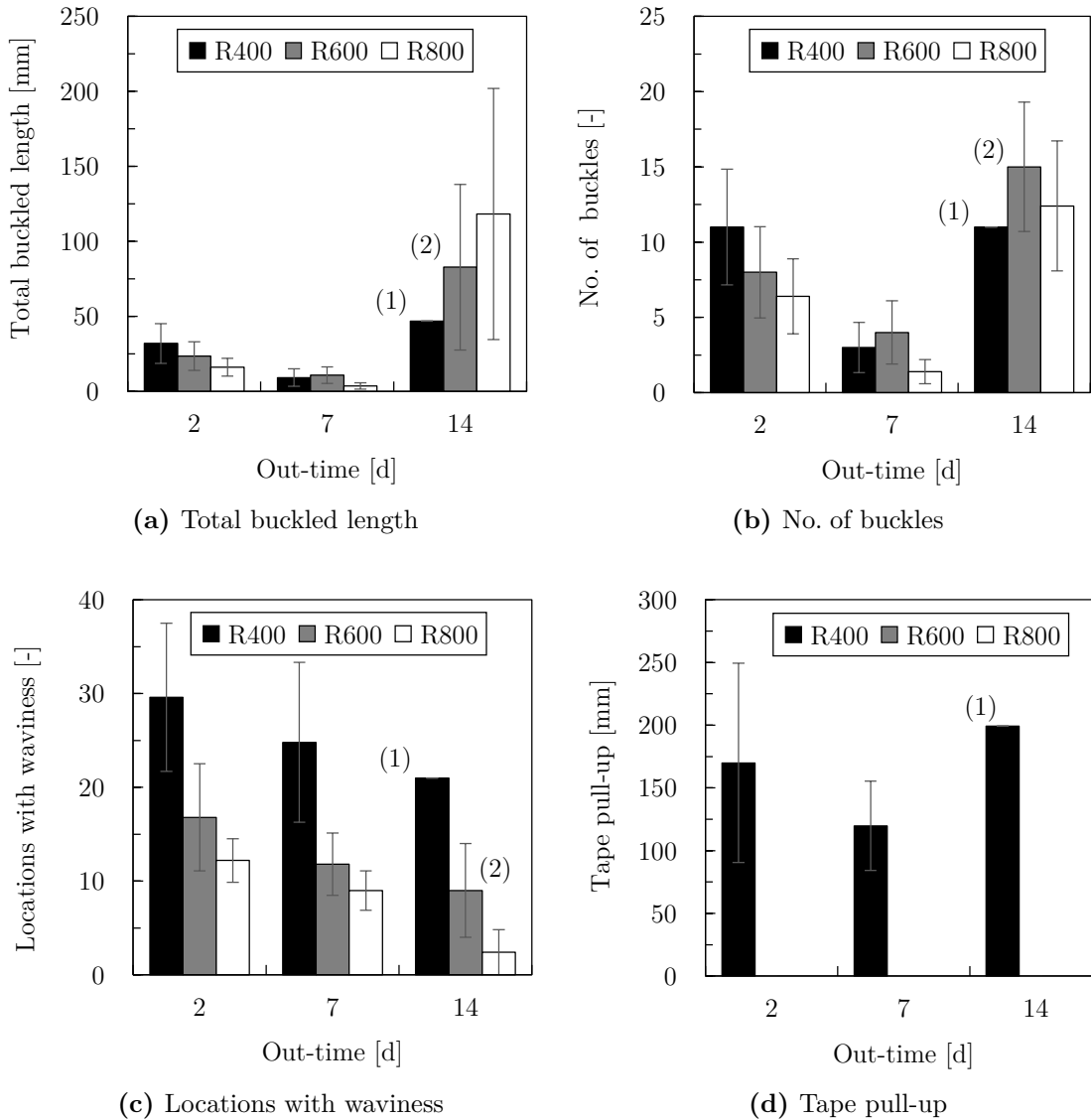
Figure 4.2: Steering investigation on defect type and steering radius — results ((1): 4 out of 5 tapes did not adhere at all, (2): 1 out of 5 tapes did not adhere at all; error bars represent the standard deviation of the respective test series)

The number of locations with in-plane fiber waviness decreases as a function of the material aging. It is the initial defect due to steering. Once the compressive stress at the inner radius of the tape is too high or the tack is too low the defect

converts into out-of-plane buckling [149]. Therefore, at lower tack more buckles and less in-plane waviness occurs.
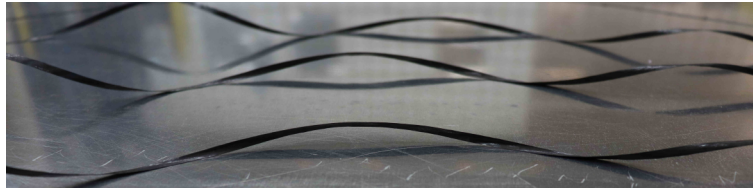
Figure 4.3: Steering investigation on defect type and steering radius — non-adhering tapes

Tape pull-up only occurred at $R400$ due to the tensile stress at the outer edge of the tape. The decrease at 7 d out-time followed by the highest value at 14 d out-time demonstrates a similar trend as it is for buckling.

4.1.1.3 Conclusion

The presented results demonstrate that the occurrence of steering induced defects is affected by the material's out-time. Out-of-plane buckles first decrease moderately followed by a significant increase after 14 d out-time which is beyond the material's tack life. The overall lay-up behavior worsens once the material clearly exceeds its tack life leading even to the fact that tapes did not adhere at all at $R400$ after 14 d out-time. The in-plane waviness decreases as a function of out-time as it is the initial defect which converts to out-of-plane buckling. Both defects are dependent on the steering radius with an increasing steering radius leading to less defects. Tape pull-up only occurs at $R400$ indicating that there is a threshold for the steering radius below which tape pull-up occurs.

4.1.2 Investigation on temporal defect evolvement

Due to the time-dependent viscoelastic behavior of the prepreg during processing, steering induced defects are subject to a time-dependent evolvement [181, 182]. This defect evolvement is relevant during part manufacturing as the acceptable amount of defects might not be exceeded right after lay-up but at a later point in time after lay-up. Laying up the subsequent ply or conducting vacuum debulking within that time span could therefore prevent the exceedance of the critical defect amount. To quantify the temporal defect evolvement during steering, a series of lay-up experiments was conducted and the defect amount and size was measured at different times after lay-up.

4.1.2.1 Experimental procedure

The experiments were part of the student thesis [S12]. Besides the time after lay-up t_{after}, the steering radius was varied and a screening of process parameters was conducted. Preliminary investigations revealed that there is no significant defect evolvement at $t_{after} > 40\ min$. Therefore, the defects were measured at 1.5 min, 5 min, 10 min, 20 min, and 40 min after lay-up. The steering radius and the process parameters were varied in a fractional factorial experimental design as listed in Tab. 4.2.

Table 4.2: Steering investigation on temporal defect evolvement — experimental design

$v\ [m/s]$	$P_{IR}\ [W]$	$F\ [N]$	$R\ [mm]$
0.03	150	200	400
0.06	150	400	400
0.1	350	400	400
0.03	350	200	400
0.06	150	200	600
0.1	150	200	600
0.03	350	400	600
0.06	350	400	600
0.1	150	400	800
0.03	150	400	800
0.06	350	200	800
0.1	350	200	800

The material used was IM7/8552 slit-tapes at out-times 1 d, 5 d, 10 d, and 15 d. Again, single slit-tapes were laid up onto a flat aluminium tool to investigate the first-ply lay-up as depicted in Fig. 4.4. On the lines of the investigation on defect type and steering radius, the out-of-plane defects out-of-plane buckling and tape pull-up were marked at the predefined times after lay-up and the markings were captured together with a reference — graph paper — using a digital camera — see Fig. 4.4. All experiments were conducted five times.

4.1.2.2 Results

An overview of the results for the out-of-plane buckling is illustrated in Fig. 4.5. Non-adhering tapes were not considered in this overview. Though at 15 d out-time, 35 % of the tapes did not adhere at all. Error bars have been omitted to increase readability. The mean standard deviation of the proportion of buckled length was 0.046. Further details on the variation of the results can be found in the appendix in Tab. A.11–Tab. A.17.
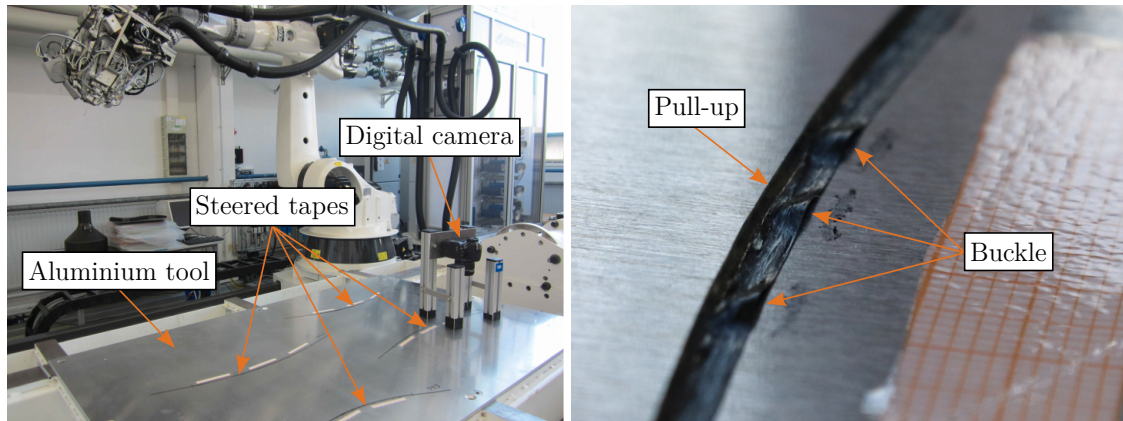
Figure 4.4: Steering investigation on temporal defect evolvement — experimental setup

Fig. 4.5 visualizes the temporal evolvement of the out-of-plane buckling which is consistent at all out-times and process parameter combinations. The relative buckled length (cumulative buckled length divided by total arc length) increases strongly shortly after lay-up up to 10 *min* followed by a moderate to weak increase from 10 *min* to 40 *min* due to viscoelastic effects in the prepreg tack [182]. Comparing curve progressions of fits for the temporal evolvement reveals the highest congruence with exponential fits (with the exponent being < 1). The increase of the relative buckled length is caused rather by the appearance of new buckles than by the enlargement of buckles that formed shortly after lay-up. From 1.5 *min* to 40 *min* the number of buckles rises by 77 % and the average buckle length rises by 26 %.

Besides the temporal evolvement, the results help estimate the dependence on out-time and steering radius as shown in Fig. 4.6. Here, the results for each steering radius regardless of the process parameters are summarized. Furthermore, non-adhering tapes are included in the analysis as both buckles and tape pull-up to understand the effects of out-time on the lay-up quality at all investigated out-times. Fig. 4.6 visualizes the effect of time after lay-up as it leads to an increase in cumulative buckled length at all out-times and steering radii. The effect of steering radius observable in Fig. 4.6 are comparable to the observations in the first study — Sec. 4.1.1. At all out-times, the smallest steering radius leads to more defects than the other radii. Additionally, at 15 *d* out-time, the largest steering radius leads to the least defects. In contrast at 1 *d*, 5 *d*, and 10 *d* out-time, the largest steering radius leads to less cumulative buckle length. Even though the difference is small, the result is unexpected. Yet, results may be affected by the fractional factorial experimental design. At $R800$, two of the four parameter sets include the highest lay-up rate whereas at $R600$ and $R400$ only one of the four parameter sets

include the highest lay-up rate. As the lay-up rate has the largest influence on the buckling result — see Sec. 4.1.2.3 — the fractional factorial experimental design may affect the result concerning steering radius.
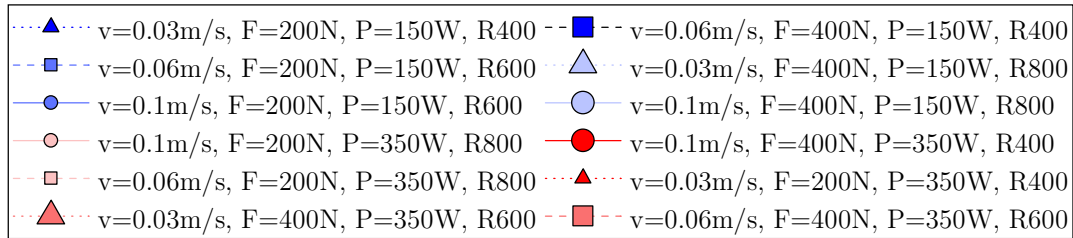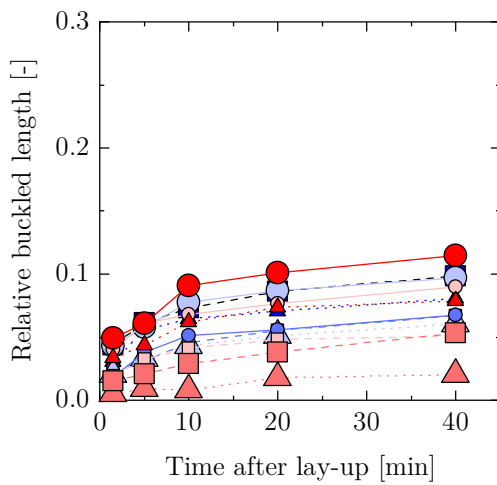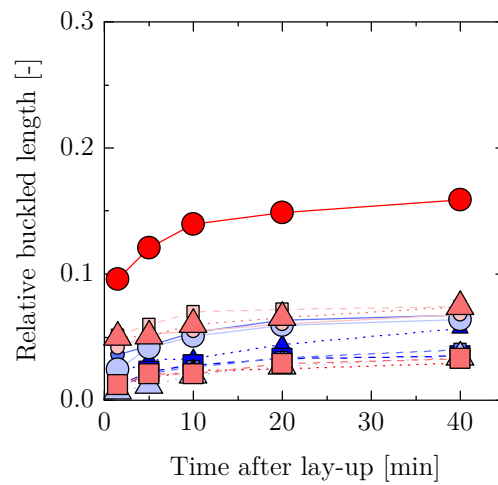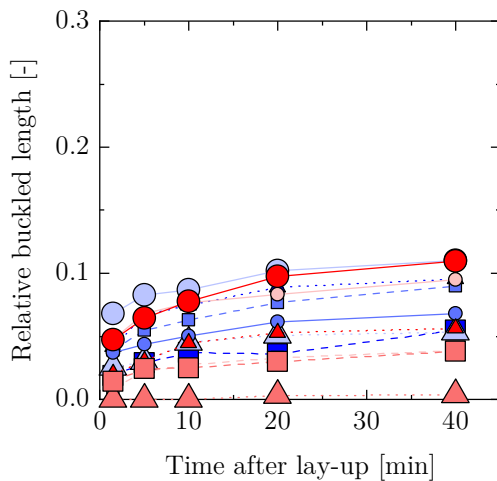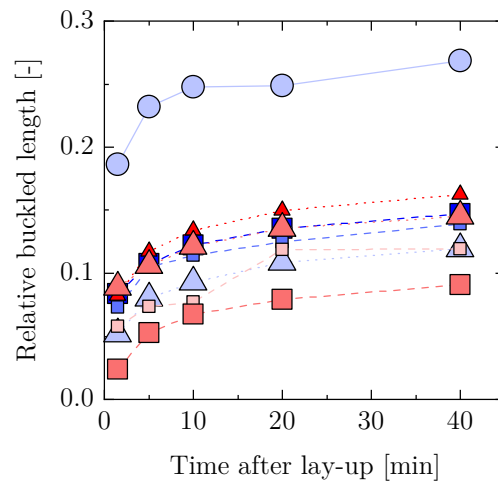
(a) Legend

Figure 4.5: Steering investigation on temporal defect evolvement — buckling results (excluding non-adhering tapes)

(a) $t_{after} = 1.5\ min$ **(b)** $t_{after} = 40\ min$
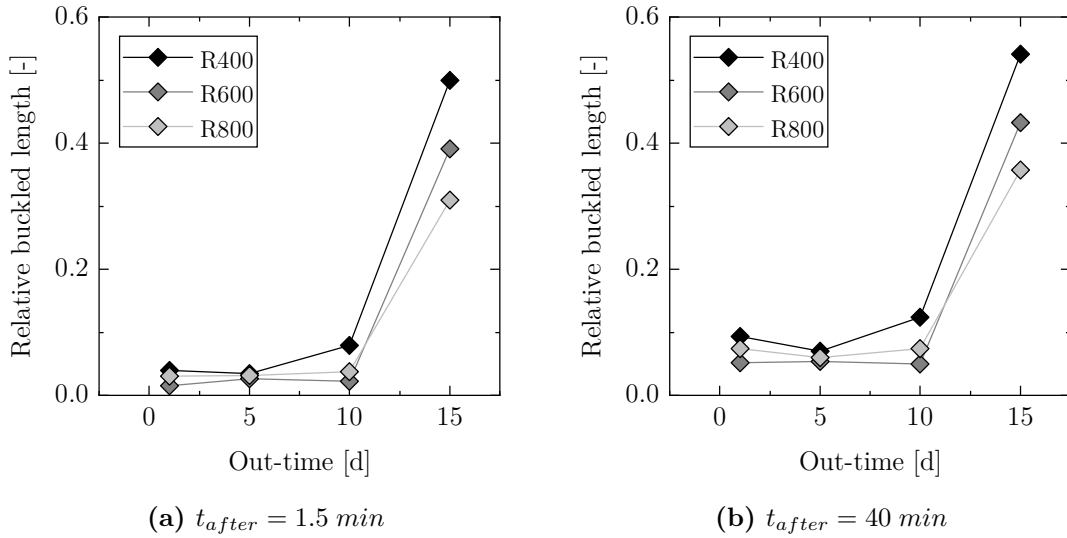
Figure 4.6: Steering investigation on temporal defect evolvement — buckling results relating to out-time and steering radius (including non-adhering tapes)

The effects of out-time are also apparent in Fig. 4.6. Up to 10 d out-time, the changes are comparably small whereas the buckled length increases significantly from 10 d to 15 d out-time as the material's tack life is exceeded. Between 1 d and 10 d, the buckled length does not increase monotonically which may be attributed to a temporal tack increase similar to the investigations in Sec. 4.1.1. However, the increase in tack is most likely caused by the differences in ambient temperature which were: 24.9 $°C$ at 1 d, 27.0 $°C$ at 5 d, 27.9 $°C$ at 10 d, and 27.2 $°C$ at 15 d. Since these temperatures are just in the range where the influence of temperature on tack is the highest, they undoubtedly affect the tack and therefore the steering results. To obtain more reliable results, the effects of out-time were addressed in a subsequent observation — see Sec. 4.1.3 — where the ambient temperature was $21.1 \pm 0.7\ °C$.

The results for the pull-up are collocated in Fig. 4.7. Again, non-adhering tapes were not considered in this overview. The mean standard deviation of the proportion of tape pull-up was 0.18. The result reveal a slight increase of the pull-up length due to t_{after} — yet not as pronounced as in the buckle results. At $R400$ and $R600$, the relative cumulative pull-up length is rather high — even at 1 d out-time. This dependence on the steering radius becomes evident in Fig. 4.8, too, where the results for each steering radius regardless of the process parameters were summarized and non-adhering tapes were included in the analysis. The pull-up length varies significantly due to the steering radius while the effects of out-time is less pronounced than in the buckle results. At $R400$, there is only a weak dependence

on out-time as the pull-up length is already high at 1 d out-time. At $R600$ and $R800$, a strong increase starts after 10 d out-time.
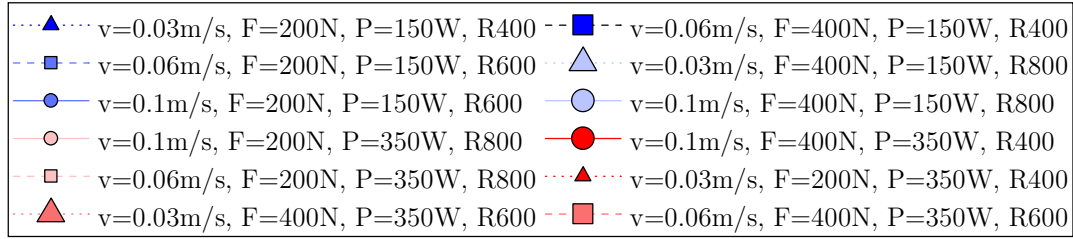
(a) Legend
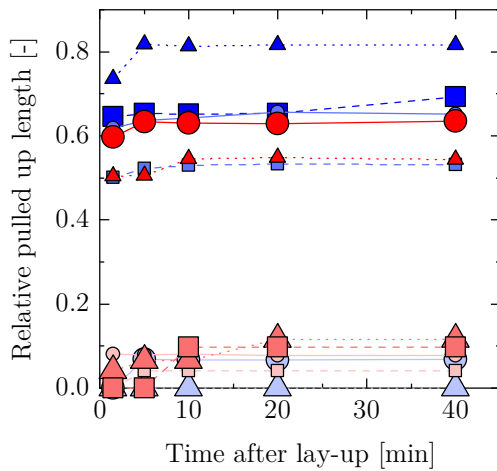
(b) $t_{out} = 1\ d$
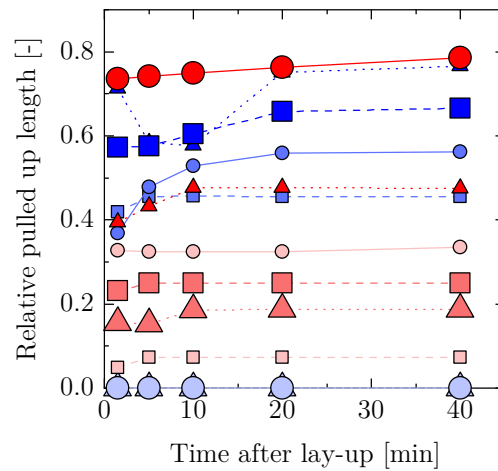
(c) $t_{out} = 5\ d$
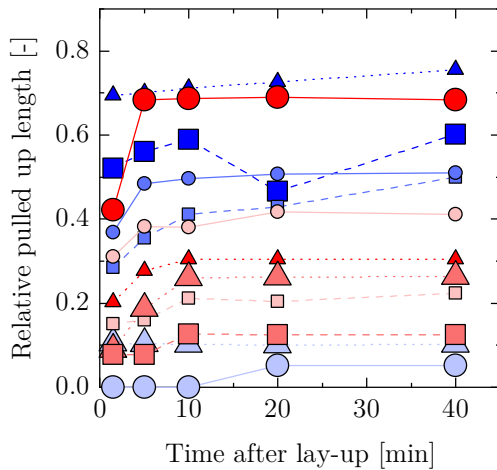
(d) $t_{out} = 10\ d$
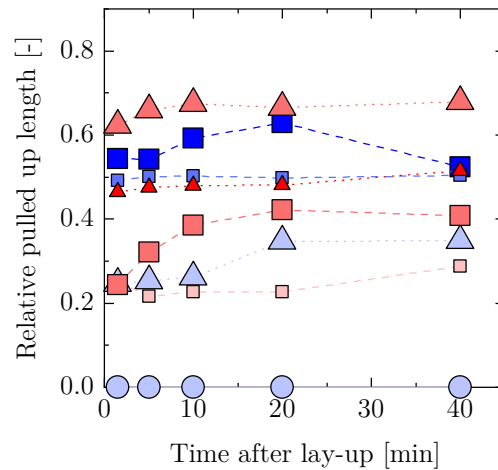
(e) $t_{out} = 15\ d$

Figure 4.7: Steering investigation on temporal defect evolvement — tape pull-up results (excluding non-adhering tapes)

(a) $t_{after} = 1.5\ min$ **(b)** $t_{after} = 40\ min$
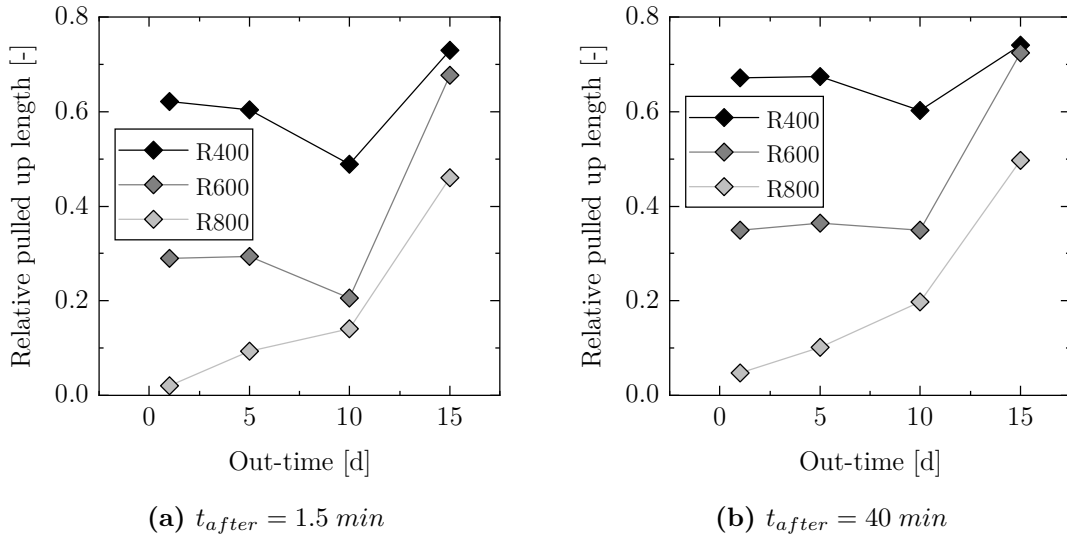
Figure 4.8: Steering investigation on temporal defect evolvement — tape pull-up results relating to out-time and steering radius (including non-adhering tapes)

4.1.2.3 Conclusion

The steering investigation on temporal defect evolvement reveals a distinct effect on out-of-plane buckling within the investigated range of 1.5 *min* to 40 *min* after lay-up. The increase in cumulative buckled length in a tape is primarily caused by the development of new buckles followed by the enlargement of existing buckles. Regrading out-time effects, the experiments led to similar results as the initial investigation: the most significant increase in out-of-plane buckling occurs from 10 *d* to 15 *d* out-time when the material's tack life is exceeded. The influence of process parameters was addressed in a fractional factorial experimental design combined with the steering radius which makes a detailed interpretation of the process parameter influences difficult. Yet, to obtain a preliminary overview of the process parameter influences, the correlation coefficients are shown in Fig. 4.9.

Among the process parameters, the cumulative buckled length has a moderate correlation to the lay-up rate while there is only a weak correlation to the compaction force and the IR emitter power. Similarly, there is only a weak correlation to the steering radius. In contrast, the correlation to out-time is moderate to strong caused by the strong increase of buckling at 15 *d* out-time.

The correlation to process parameters is slightly different for the tape pull-up. Here, there is a stronger correlation to the compaction force than to the lay-up rate. Fig. 4.9 clearly illustrates that the tape pull-up has the strongest correlation to the steering radius. For both defects, the induced load is dependent on the steering radius. The compressive stress at the inner edge of the tape can be compensated

by intra-ply shear or in-plane waviness before buckling occurs. The tensile stress at the outer edge, however, can hardly be compensated because of the high stiffness of the fibers leading to a sudden tape pull-up after exceeding a certain tensile stress threshold which is dependent on the steering radius.
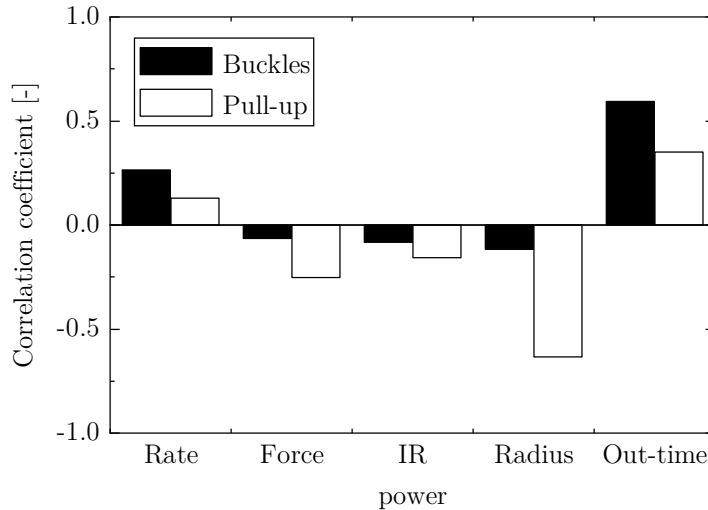
Figure 4.9: Steering investigation on temporal defect evolvement — correlation coefficients (including non-adhering tapes)

4.1.3 Investigation on process parameters

Based on the findings from the investigations on defect type, steering radius, and temporal defect evolvement a systematic investigation on the influence of process parameters including an investigation on out-time effects was conducted. The results of this study were published in [J2].

4.1.3.1 Experimental procedure

The experimental procedure resembles the procedure of the investigation on temporal defect evolvement. Single slit-tapes were laid up onto the flat aluminium tool and the analysis procedure remained the same. As the influence of time after lay-up and steering radius had already been investigated, they were kept constant at $t_{after} = 40\ min$ and $R = 600\ mm$ (arc length $400\ mm$). The experimental design was a one-factor-at-a-time design including all process parameters listed in Tab. 3.3. The baseline parameters were $v = 0.06\ m/s$, $F = 400\ N$, $P_{IR} = 350\ W$. The material used was IM7/8552 at out-times $1\ d$, $5\ d$, $10\ d$, and $15\ d$. In contrast to the investigation on temporal defect evolvement the ambient temperature did

not vary significantly during the experiments at 21.1 ± 0.7 °C increasing the validity of the investigation on out-time effects. All experiments were conducted five times.

4.1.3.2 Results

Fig. 4.10 gives an overview of the results of the occurrence of buckles during steering. The results are defined in a positive expression: relative buckle-free length $L_{b,free}$ which equals the total arc length minus the cumulative buckle length divided by the total arc length. Additional data is listed in Tab. A.18 in the appendix. The mean standard deviation was 0.11.
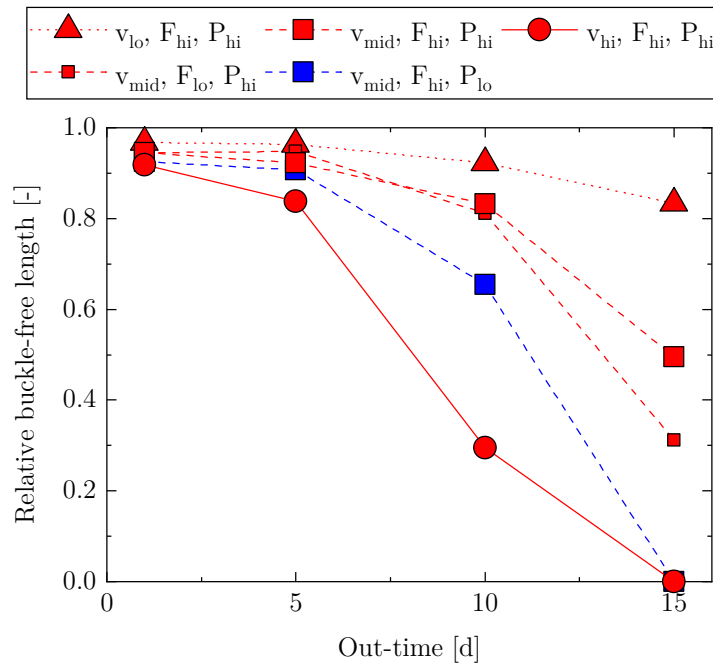
Figure 4.10: Steering investigation on process parameters — relative buckle-free length ($v_{lo} = 0.03$ m/s, $v_{mid} = 0.06$ m/s, $v_{hi} = 0.1$ m/s, $F_{lo} = 200$ N, $F_{hi} = 400$ N, $P_{lo} = 150$ W, $P_{hi} = 350$ W; including non-adhering tapes)

On average, there were buckles in every out-time and process parameter setting. The setting with the least buckling is $v = 0.03$ m/s, $F = 400$ N, $P_{IR} = 350$ W at 1 d out-time with a relative buckle-free length of 0.968. The buckle-free length is dependent on the lay-up rate as a lower lay-up rate leads to less buckles at all out-times. While the difference at 1 d out-time is comparably small — $L_{b,free}(v = 0.03$ $m/s) = 0.968$ and $L_{b,free}(v = 0.1$ $m/s) = 0.919$ — the influence increases with increasing out-time — e. g. $L_{b,free}(v = 0.03$ $m/s) = 0.833$ and $L_{b,free}(v = 0.1$ $m/s) = 0$ at 15 d out-time. The reason for this is that the compaction time and temperature — both dependent on the lay-up rate — significantly affect the bond between tape and substrate [28, 35]. A similar dependence

on the IR emitter power was observed. The low IR emitter power ($P_{IR} = 150\ W$) leads to a smaller buckle-free length at all out-times. Again, the influence is more pronounced at higher out-times. Except for a deviation at $5\ d$ out-time, the higher compaction force ($F = 400\ N$) leads to a higher buckle-free length while the influence is less pronounced than the lay-up rate and IR emitter power influences. The out-time effects are clearly visible, too, in Fig. 4.10. The buckle-free length generally decreases monotonically as the out-time increases caused by the decrease in molecular mobility leading to poor surface wetting. While the difference between $1\ d$ and $5\ d$ out-time is comparably small, the buckle-free length decreases considerably after $10\ d$ out-time and even more after $15\ d$ out-time. At $15\ d$ out-time, none of the tapes adhered to the substrate at the high rate ($v = 0.1\ m/s$) and at the low IR emitter power ($P_{IR} = 150\ W$).

Fig. 4.11 shows the results of the occurrence of tape pull-up during steering. The results are defined in a positive expression, too: relative pull-up-free length $L_{p,free}$ (total arc length minus cumulative pull-up length divided by total arc length). Additional data is listed in Tab. A.19 in the appendix. The mean standard deviation was 0.17.
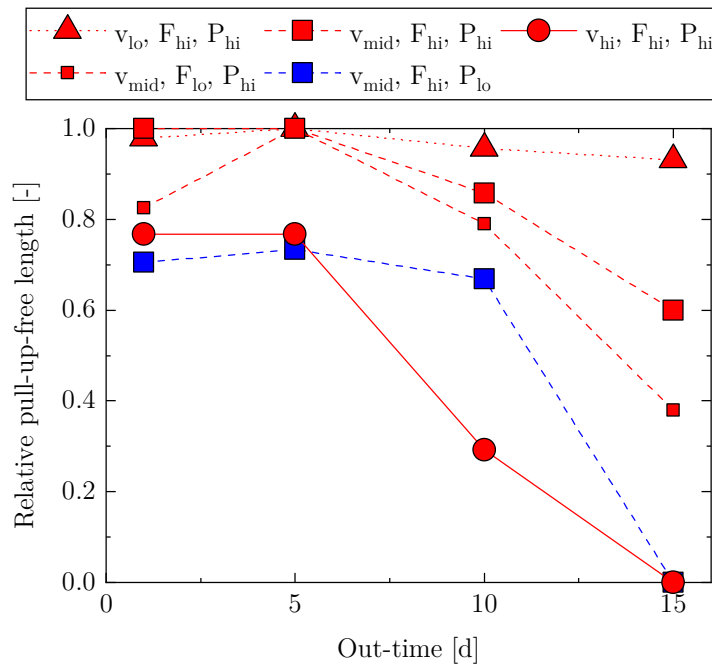
Figure 4.11: Steering investigation on process parameters — relative pull-up-free length ($v_{lo} = 0.03\ m/s$, $v_{mid} = 0.06\ m/s$, $v_{hi} = 0.1\ m/s$, $F_{lo} = 200\ N$, $F_{hi} = 400\ N$, $P_{lo} = 150\ W$, $P_{hi} = 350\ W$; including non-adhering tapes)

Tape pull-up occurred either once per tape — with varying length — or not at all. The dependence of the relative pull-up-free length on process parameters and

out-time is quite similar to the case of the buckle-free length. The pull-up-free length remained almost the same from 1 d to 5 d out-time in most settings and even increased at $v = 0.06$ m/s, $F = 200$ N, $P_{IR} = 350$ W and $v = 0.06$ m/s, $F = 400$ N, $P_{IR} = 150$ W. Apart from that, the observations are comparable to the ones of the buckle-free length.

Since the presented process parameter combinations have also been used in the peel tack investigations — see Sec. 3.3.2 — and the material and the machine are the same, a direct relation of steering defect results to the peel tack is possible. The comparison is illustrated in Fig. 4.12 where the defect-free lengths are shown as a function of peel tack.

(a) Out-of-plane buckles   (b) Tape pull-up
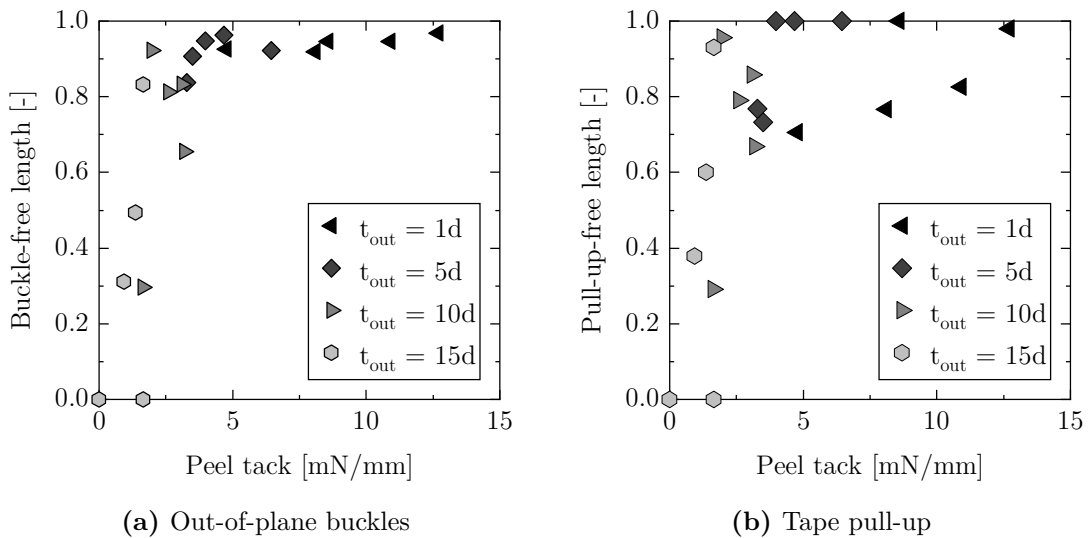
Figure 4.12: Steering investigation on process parameters — steering induced defects as a function of peel tack (including non-adhering tapes)

The data points demonstrate that there is a correlation between relative buckle-free length and peel tack. In the peel tack range from 12.7 mN/mm to 3.5 mN/mm, the buckle free length decreases only slightly from 0.968 to 0.907. Below a peel tack of 3.5 mN/mm, the buckle-free length begins to drop significantly, indicating that this value marks a critical value for the magnitude of buckle occurrence (without considering other material properties) in the investigated case. The relation between relative pull-up-free length and peel tack is less clear — see Fig. 4.12 b). In the peel tack range from 12.7 mN/mm to 1.6 mN/mm, the pull-up-free length ranges from 1 to 0.669 and drops off at lower peel tack values mainly due to the tapes not adhering at all. The findings from Fig. 4.12 underline that peel tack measurements are a useful indicator to experimentally predict the

lay-up behavior during AFP processing with a particular correlation to out-of-plane buckles during steering.

4.1.3.3 Conclusion

The investigation on process parameters and out-time reveal a pronounced dependence of the steering induced defects on out-time which can be influenced by adjusting the process parameters. Fig. 4.13 combines the correlation coefficients for the lay-up defects with the ones for the peel tack. Since the same material, machine, and process parameters were used in both experiments, correlation coefficients can be compared directly.
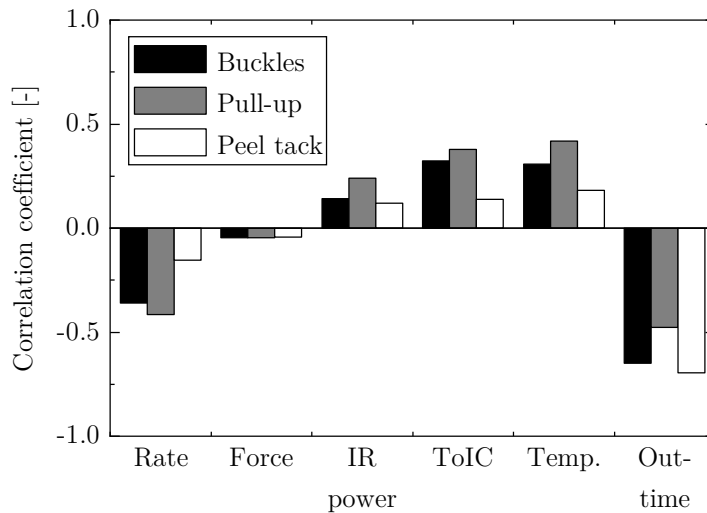
Figure 4.13: Steering investigation on process parameters — correlation coefficients (including non-adhering tapes; ToIC: time of intimate contact)

The general trend of the correlation coefficients is similar for all three results underlining that peel tack results can be used to predict the lay-up behavior. There is almost no correlation of the compaction force with the lay-up defects and the peel tack. The strongest process parameter correlation for all three results is the lay-up rate followed by the IR emitter power. This demonstrates that the lay-up rate can be used as the main process parameter to reduce the occurrence of steering induced lay-up defects. As implied by the steering defect results — Fig. 4.10 and Fig. 4.11 — reducing the lay-up rate leads to a lay-up with very little defects even at 10 *d* out-time while increasing the lay-up rate significantly worsens the lay-up result. Since reducing the lay-up rate decreases the productivity of the manufacturing process, an increase in IR emitter power should be considered, too, as a countermeasure for defect occurrence. The influence of rate is explained by the interpretation of

the correlation to the time of intimate contact and the temperature. Both the peel tack and the steering defects display a considerable correlation with t_{intim} and T who are both dependent on the lay-up rate. The strongest correlation coefficient evident in Fig. 4.13 is between the out-time and the three results — peel tack, buckle, pull-up. This underlines the importance of the consideration of out-time effects on AFP processing.

4.2 Bridging investigations

Besides steering, the lay-up on a concave geometry is a typical lay-up scenario during AFP manufacturing — e. g. during lay-up over a ramp of a sandwich part. At this, the lay-up defect bridging occurs when the resulting force perpendicular to the surface caused by the tensile stress in the tape exceeds the adherence to the substrate — see Sec. 2.2.2. To investigate the influence of out-time on the occurrence of bridging, a series of lay-up experiments on ramps with different geometries as shown in Fig. 4.14 was conducted. The results were published in [C1].
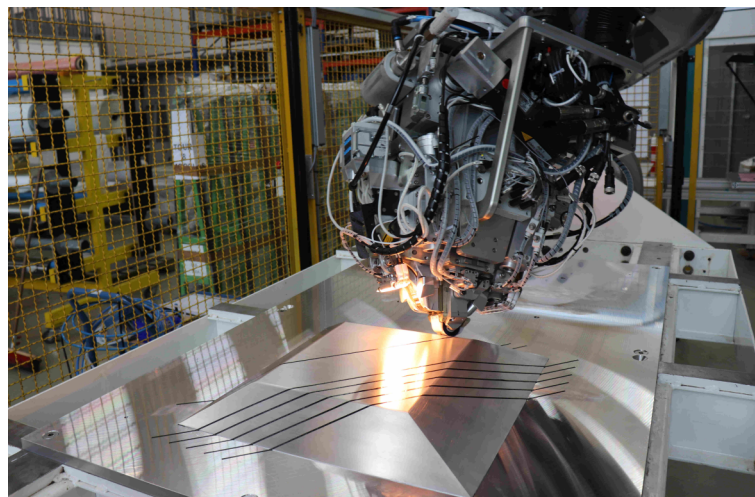
Figure 4.14: Bridging investigation — lay-up on ramp

4.2.1 Experimental procedure

The experiments were conducted with the same material, material conditions, and process parameters as the steering investigation on defect type and steering radius — see Sec. 4.1.1. The geometrical base for the experiments were two aluminum ramp tools which were attached to an aluminum plate as shown in Fig. 4.14. To study the influence of different ramp geometries, tapes were laid up on different ramp heights and angles as listed in Tab. 4.3. The lay-up direction was 45 °

referred to the ramp edge. Preliminary studies, in which the bridged length was investigated as a function of the fiber orientation, showed that 45 ° lay-ups lead to more pronounced bridging effects than other lay-up directions.

Table 4.3: Bridging investigation — parameters of ramp geometry

Parameter	Symbol	Unit	Values
Ramp height	h_{ramp}	mm	25; 50
Ramp angle	α_{ramp}	°	25; 35

On the lines of the steering experiments, the defects were marked after lay-up and photographs were taken perpendicular to the surface followed by the measuring of the bridged length with ImageJ. For this, the tool carrier was tilted 90 ° so images could be taken parallel to both the flat plate and the ramps. Fig. 4.15 illustrates the image capturing and the image analysis. For the analysis of the bridged length it was differentiated between the small opening angle between tape and ramp edge and the large one as the position of the compaction roller leads to different compaction behavior on these two sides — see Fig. 4.15 right. All experiments were conducted five times.
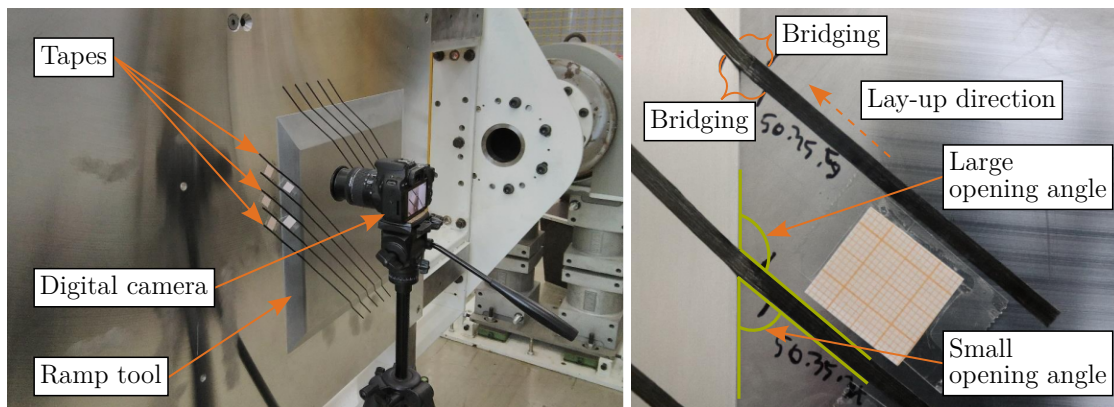
Figure 4.15: Bridging investigation — image capturing (left), image analysis (right)

4.2.2 Results

Fig. 4.16 shows the results of the bridging investigation grouped in small and large opening angle. The results demonstrate a difference between bridging at the small opening angle compared to the large opening angle at $h_{ramp} = 25\ mm$, $\alpha_{ramp} = 35$ °. During 45 ° lay-up on the ramp, the lay-up head including the compaction roller is tilted. By this, the roller axis is moved closer to the surface in the area of the large opening angle and further away in the area of the small opening angle.
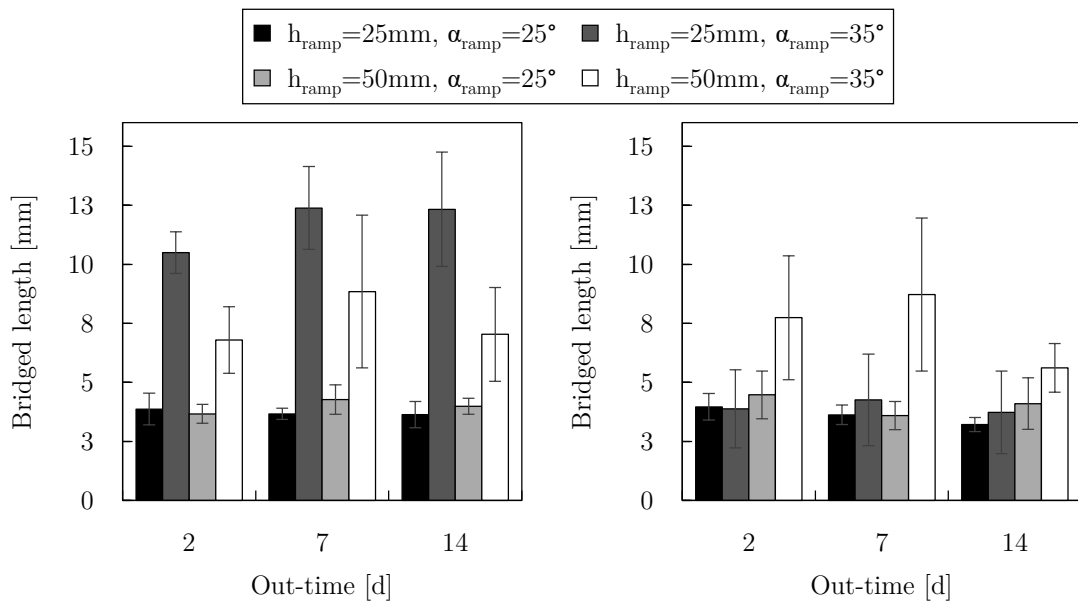
Figure 4.16: Bridging investigation — results for small opening angle (left) and large opening angle (right) (error bars represent the standard deviation of the respective test series)

Due to the roller compliance, the roller adaption to the surface is better at the large opening angle. Fig. 4.16 further reveals that there is a pronounced difference in bridged length with regard to the ramp angle. At the small opening angle, the higher ramp angle leads to an increase in bridged length of up to factor 3.4 at $h_{ramp} = 25\ mm$ and up to factor 2.1 at $h_{ramp} = 50\ mm$. At the large opening angle, the difference is less distinct: at $h_{ramp} = 25\ mm$, there is barely any change and at $h_{ramp} = 50\ mm$ the increase is up to factor 2.4. The higher ramp angle leads to a more pronounced tilting of the compaction roller which affects the pressing of the tape onto the substrate — particularly at the small opening angle. The ramp height did not affect the bridged length significantly as the bridging is dependent on the transition from the flat plate to the ramp rather than the trajectory before and after that. Another parameter with no significant effect was the out-time. Even though there were some changes of the bridged length due to out-time, the changes were comparably small and the mean of all changes at the respective ramp geometries was 1 %. Lay-up defects are an interplay of material properties and loads induced in the tapes. During steering at constant steering radius, the loads lead to tensile and compressive stress along the entire tape. During lay-up on a ramp with geodesic trajectories before and after the ramp, there is only a stress induction at the transition from the flat plate to the ramp. Therefore, bridging is not affected significantly by the material's out-time since the adherence of the tapes to the substrate in geodesic trajectories is less affected by the material's out-time.

4.2.3 Conclusion

The bridging investigation reveal that the bridged length is significantly affected by the ramp angle, yet not by the ramp height. Furthermore, the effect of out-time on the bridged length is negligible. These findings are affirmed by the analysis of the correlation coefficients as shown in Fig. 4.17 displaying a strong correlation to the ramp angle and no correlation to the ramp height and the out-time.
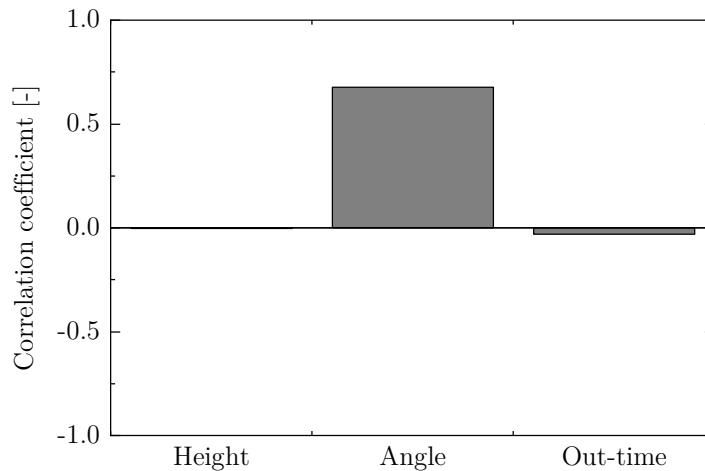
Figure 4.17: Bridging investigation — correlation coefficients

Though being a relevant lay-up defect for AFP in general, bridging apparently is of no relevance regarding material changes in the investigated range.

4.3 Tape peel-off investigations

The third relevant lay-up scenario causing defects is the lay-up on convex geometries which leads to tape peel-off when the stiffness of the tape is higher than the tack — see Sec. 2.2.2. To investigate the influence of out-time and geometry and to assess the influence of process parameters, a series of lay-up experiments was conducted using an aluminium edge tool. The experiments were part of the student thesis [S12].

4.3.1 Experimental procedure

On the lines of the other lay-up experiments, the peel-off investigations were performed using the Coriolis 1/8-TS-AFP machine described in Sec. 2.3. The edge

tool was attached to the horizontal positioner in the robot cell enabling the tilting of the tool as shown in Fig. 4.18.
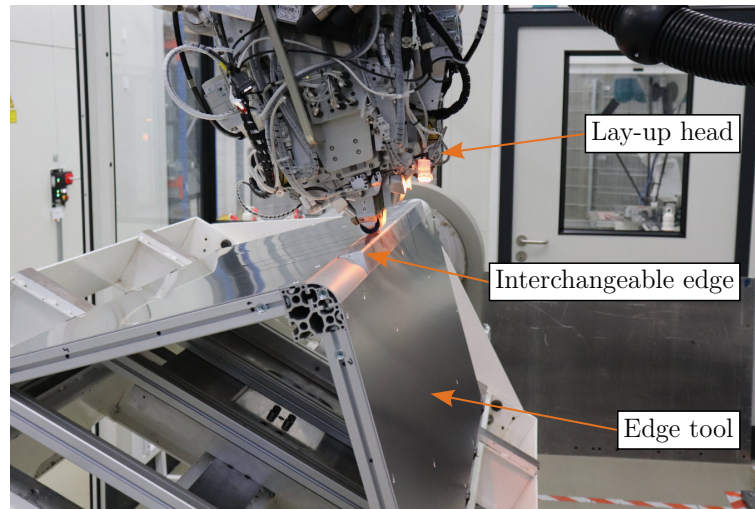
Figure 4.18: Tape peel-off investigation — lay-up on edge tool

As the edge tool was equipped with interchangeable edges with different edge radii, experiments were conducted with different edge radii R_{edge} in addition to the variation of the length after the edge L_{edge} and lay-up direction (in reference to the edge) φ_{layup}. The geometric parameters were combined with the process parameters listed in Tab. 3.3 in a fractional factorial experimental design as specified in Tab. 4.4.

Table 4.4: Tape peel-off investigation — experimental design

v [m/s]	P_{IR} [W]	F [N]	L_{edge} [mm]	R_{edge} [mm]	φ_{layup} [°]
0.06	150	400	20	40	45
0.03	150	200	60	40	45
0.1	150	400	100	40	45
0.03	350	400	20	40	90
0.1	350	200	100	40	90
0.06	150	200	60	40	90
0.06	350	200	100	5	45
0.1	350	400	60	5	45
0.03	350	200	20	5	45
0.1	150	200	20	5	90
0.03	150	400	100	5	90
0.06	350	400	60	5	90

The lay-up direction was defined with the edge as the reference direction (Fig. 4.18 shows the lay-up of 90 ° tapes). The length before the edge was 300 *mm* and the

trajectory was geodesic to ensure sufficient adhesion to the substrate before the edge. The defect evolvement of each experiment was monitored for up to 40 *min*. Again, the material was IM7/8552 slit-tapes at out-times 1 *d*, 5 *d*, 10 *d*, and 15 *d*. All experiments were conducted five times.

4.3.2 Results

During the experiments, three different lay-up results were observed after the edge. The peel-off was either formed up to the edge — see Fig. 4.19 left — or it formed over a certain length, yet not up to the edge — see Fig. 4.19 middle. Both results were counted as peeled off tapes. In some cases, the tapes did not adhere fully to the surface because of a small step between interchangeable edge and side face of the edge tool — see Fig. 4.19 right. These tapes were not counted as peeled off.
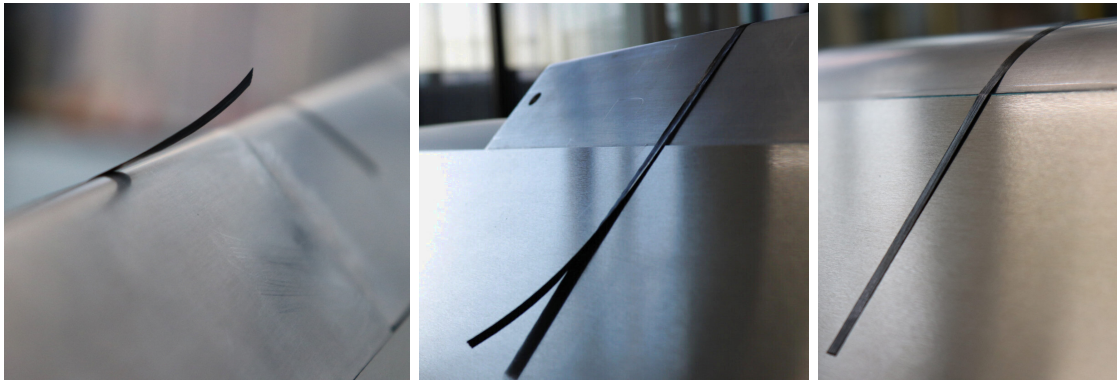
Figure 4.19: Tape peel-off investigation — lay-up peculiarities: fully peeled off tape (left), partly peeled of tape (middle), incomplete adhesion due to inaccurate edge tool (right)

The results of the investigation are shown on Fig. 4.20 where error bars have been omitted as all minima equal 0 and all maxima equal 1. At 15 *d* out-time, 20 % of the tapes did not adhere at all — even before the edge. They were not included in the evaluation. All defects occurred directly after lay-up indicating that there is no relevant time-dependent mechanism. Peel-off rather depends on the tape stiffness and the adhesion to the substrate in the moment of lay-up. Assuming that the bending stiffness is rate dependent, the highest stiffness is expected in the moment of lay-up causing the peel-off right after lay-up.

Fig. 4.20 as well as Fig. 4.21 and Fig. 4.22, where the results per parameter are collated as mean values, display some expected and some unexpected results. The occurrence of tape peel-off is clearly affected by out-time. At 1 *d* and 5 *d* out-time, there are almost no cases of peel-off while at 15 *d* out-time more than half of the tapes peeled off. This observation is in accordance with the out-time effects on the associated material properties: the bending stiffness increases as a function of

out-time — see Sec. 3.5.3 — while the tack decreases as a function of out-time — see Sec. 3.3.
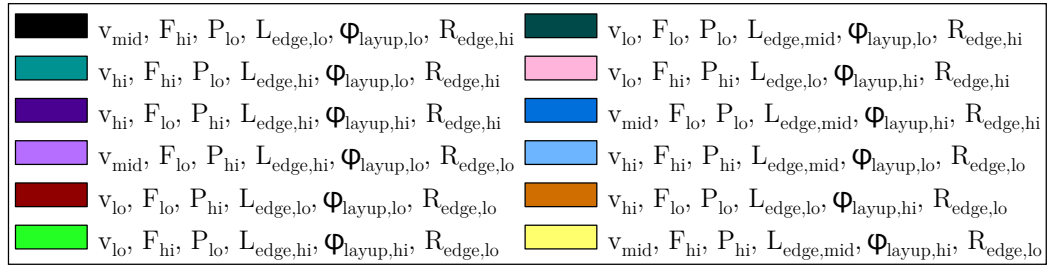
(a) Legend
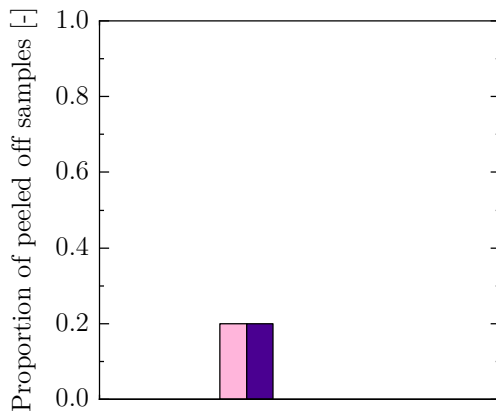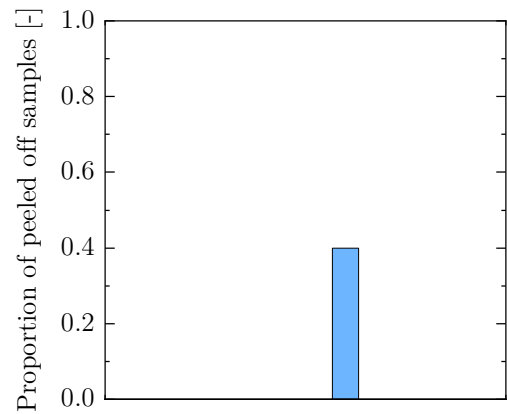
(b) $t_{out} = 1\ d$

(c) $t_{out} = 5\ d$
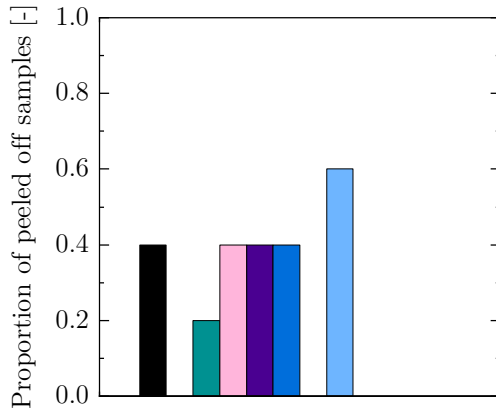
(d) $t_{out} = 10\ d$
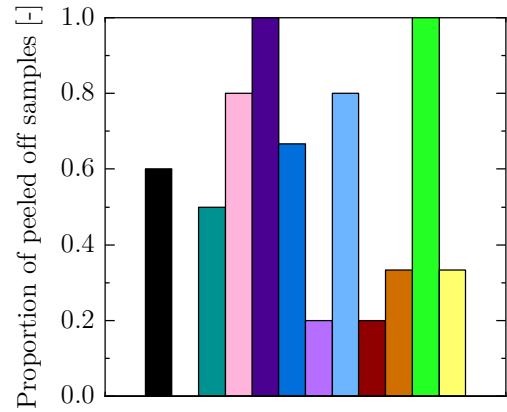
(e) $t_{out} = 15\ d$

Figure 4.20: Tape peel-off investigation — results ($v_{lo} = 0.03\ m/s$, $v_{mid} = 0.06\ m/s$, $v_{hi} = 0.1\ m/s$, $F_{lo} = 200\ N$, $F_{hi} = 400\ N$, $P_{lo} = 150\ W$, $P_{hi} = 350\ W$, $L_{edge,lo} = 20\ mm$, $L_{edge,mid} = 60\ mm$, $L_{edge,hi} = 100\ mm$, $\varphi_{layup,lo} = 45°$, $\varphi_{layup,hi} = 90°$, $R_{edge,lo} = 5\ mm$, $R_{edge,hi} = 40\ mm$)

(a) Lay-up rate

(b) Compaction force

(c) IR emitter power

(d) Length aftetr edge

(e) Lay-up direction

(f) Edge radius
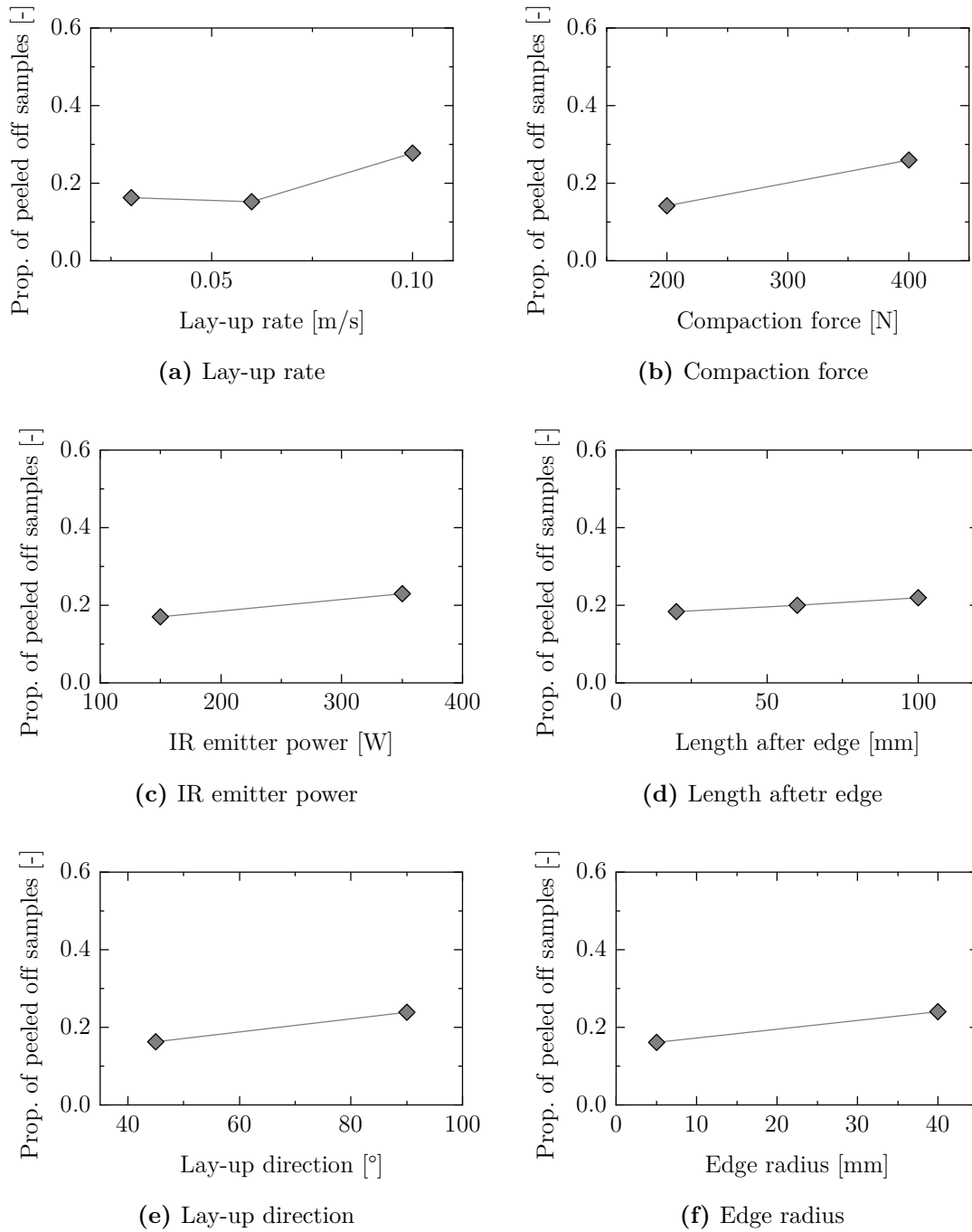
Figure 4.21: Tape peel-off investigation — results for each experimental parameter

The amount of peeled off tapes increases sightly as a function of length after edge which is an unexpected result as a longer tape length would lead to a larger adherend surface. Yet, the results for L_{edge} are affected by the size of the interchangeable edge and the transition from interchangeable edge to the side face.
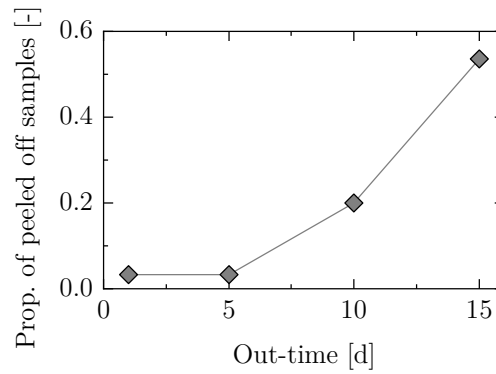
Figure 4.22: Tape peel-off investigation — results as a function of out-time

At $L_{edge} = 20\ mm$, the tapes ended on the interchangeable edge and therefore were not affected by the transition as shown in Fig. 4.19 right. Furthermore, the results were influenced by the robot movement of the AFP machine. Due to the complex movement around the edge, the robot inevitably slowed down below the desired lay-up rate to avoid exceeding velocity constraints of the individual robot axes. At $L_{edge} = 60\ mm$ and $L_{edge} = 100\ mm$, the path was long enough to accelerate the lay-up head up to the desired lay-up rate before the end of the lay-up. At $L_{edge} = 20\ mm$, however, the lay-up rate was below the desired lay-up rate at the end of the path. As a lower lay-up rate is expected to cause less peel-off, the deviation from the desired lay-up rate affects the results for length after edge.

Similar to the length after edge, the larger edge radius leads to slightly more peel-off than the smaller edge radius. The curvature of the smaller edge radius is higher — $\kappa = \frac{1}{R} = 0.2\ mm^{-1}$ — compared to the larger edge radius — $\kappa = 0.025\ mm^{-1}$ — which could lead to a higher probability of peel-off. In contrast, the tape length along which stress is induced is higher at the larger edge radius — $62.8\ mm$ (arc length of quarter circle at R_{edge}) — than at the smaller edge radius — $7.9\ mm$. In accordance with the assumption made for bridging — meaning that a smaller area of stress induction leads to less defects — the stress induction over a larger tape length may explain the higher defect occurrence at $R_{edge} = 40\ mm$.

Besides the edge radius, the fiber orientation towards the edge also has a positive correlation with the occurrence of peel-off as the results show that peel-off is more likely to happen at $\varphi_{layup} = 90\ °$ than at $\varphi_{layup} = 45\ °$. This may be explained by the effective edge radius which is dependent on the orientation of the path towards the edge. For a fixed opening angle of the edge tool of 90 °, the effective edge radius can be calculated as

$$R_{edge,eff} = \sqrt{\left(R_{edge} \cdot \frac{\pi}{2}\right)^2 + \left(R_{edge} \cdot \frac{\pi}{2} \cdot \tan(90° - \varphi_{layup})\right)^2}. \qquad (4.1)$$

In the investigated case, the effective edge radius at $\varphi_{layup} = 45\ °$ is $\sqrt{2}$ times higher than the effective edge radius at $\varphi_{layup} = 90\ °$ which therefore leads to a curvature $\sqrt{2}$ times smaller. At the same time, the effective length along which stress is induced is $\sqrt{2}$ times higher. It is therefore not possible to draw a comprehensive conclusion. A full factorial experimental design on the geometric parameters is likely to provide more insights on the interdependence, yet, the focus of the presented work lies on the effects of material changes.

The lay-up rate has only a minor influence on the occurrence of peel-off from $v = 0.03\ m/s$ to $v = 0.06\ m/s$. From $v = 0.06\ m/s$ to $v = 0.1\ m/s$ though, the occurrence of peel-off increases distinctly as the higher lay-up rate negatively affects the tack. However, the results on lay-up rate have to be treated with caution as the lay-up rate was not constant when passing over the edge. At the end of tracks with $L_{edge} = 60\ mm$ and $L_{edge} = 100\ mm$, the lay-up head was accelerated up to the desired speed increases the validity of these results.

An increase in IR emitter power leads to more cases of peel-off, which is unexpected at first sight since the bending stiffness decreases as a function of temperature. The result may be explained by the slow robot movement around the edge in combination with the constant IR emitter power leading to a significantly higher temperature. The temperature was most probably above the temperature for maximum tack of the material leading to a decrease in tack. An extrapolation of the temperature measurements described in Sec. 3.1.2 gives $T(P_{IR} = 350\ W) = 43.3\ °C$ at an exemplary rate of $v = 0.01\ m/s$ which is above the nominal processing temperature of IM7/8552 being $T = 40\ °C$.

The compaction force also has a positive correlation to the occurrence of peel-off. However, no explanation for this relation was found. There is either an unknown effect or the results are biased by the fractional factorial experimental design.

4.3.3 Conclusion

The peel-off investigation reveals a strong dependence of the defect occurrence on the material's out-time. All other studied parameters also have a positive correlation to the peel-off occurrence as it is underlined by the correlation coefficients shown in Fig. 4.23. The correlation coefficients of all process parameters and geometric parameters are comparably small indicating that they are of minor relevance compared to the out-time which has a strong correlation of > 0.66. Similar to the

steering results, the most adjuvant countermeasure against the peel-off occurrence among the process parameters is the reduction in lay-up rate.
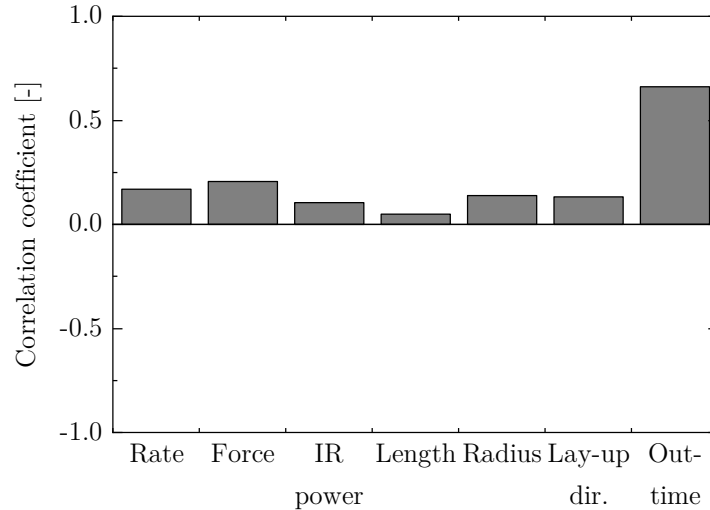
Figure 4.23: Tape peel-off investigation — correlation coefficients

4.4 Intermediate summary

The results of the lay-up experiments quantify the effects of out-time and AFP process parameters on the occurrence of lay-up defects. Three different lay-up scenarios were investigated: non-geodesic lay-up on a flat tool geometry causing steering defects, lay-up on a concave tool geometry causing bridging, and lay-up on a convex tool geometry causing tape peel-off. The effects of out-time on the occurrence of lay-up defects as well as the most influential process parameters are summarized in Tab. 4.5 where the filling of the Harvey balls correspond to the correlation coefficient.

The out-time has a strong influence on the occurrence of out-of-plane buckling due to steering and the occurrence of tape peel-off. Furthermore, it has a moderate to strong influence on the occurrence of tape pull-up due to steering. In all three cases, the reduced tack at high out-times affect the adhesion to the substrate increasing defect probability. In contrast, the correlation between out-time and bridging occurrence is negligible since the trajectory is geodesic before and after the concave edge reducing the sensitivity to a lower tack.

Table 4.5: Overview of correlation coefficient r for all lay-up defects with regard to out-time and the respective most influential process parameter (the filling of the Harvey balls correspond to the correlation coefficient: clockwise filling in black $0 < r \leq 1$, counter-clockwise filling in grey $-1 \leq r < 0$, no filling $r = 0$; F: compaction force, v: lay-up rate)

Lay-up defect	r(out-time)	Process parameter	r(process parameter)
Steering — buckling	◗	v	◔
Steering — pull-up	◖	v	◖
Bridging	◔	-	-
Tape peel-off	◕	F	◔

The most influential process parameter during steering is the lay-up rate which affects the time of intimate contact and the temperature which, in turn, affect the tack. Its influence increases with increasing out-time up to a correlation coefficient of 0.63 at 15 d out-time. Therefore, adjusting the lay-up rate to the material condition and the lay-up path is the most adjuvant countermeasure against defect occurrence. The initial defect is in-plane fiber waviness which becomes out-of-plane buckling when the tack or the steering radius decrease. Experiments on the temporal defect evolvement revealed that the buckles evolve over time up to 40 min after lay-up. The increase in cumulative buckled length in a tape is primarily caused by the development of new buckles followed by the enlargement of existing buckles.

The use of the newly developed peel tack test method — see Sec. 3.3.2 — made it possible to obtain further insights on the correlation between out-of plane buckling and tack. Since the process parameters for peel tack measurements and steering experiments were the same, a direct comparison of the results is possible as shown in Fig. 4.24. The cumulative buckle length per tape (normalized to the tape length) increases sharply at a peel tack < 3.5 mN/mm. This guide value can be used to assess the lay-up behavior of a material without doing lay-up experiments and it is a reference for the development of new materials.
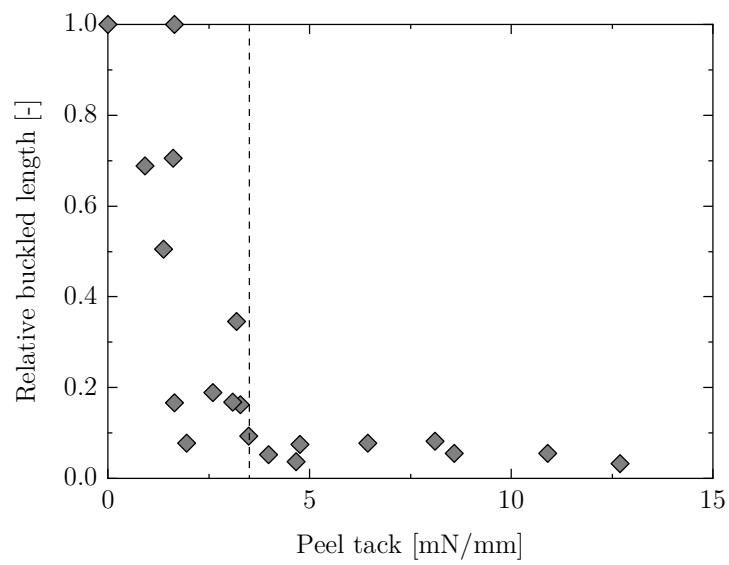
Figure 4.24: Relative cumulative buckle length as a function of peel tack

5 Theoretical models predicting lay-up defects

The material characterization and the AFP lay-up investigations have shown that material properties change due to out-time and modifications via fillers and that these changes significantly affect the occurrence of lay-up defects. Lay-up experiments are the most direct way of analyzing said effects. However, they are time and resource consuming and therefore cost-intensive. Furthermore, they can only be done using prepreg in the final format — slit-tape — which requires the costly process step of slitting the material to the desired width. To enable a cost-efficient and resource-efficient assessment of the lay-up behavior of prepreg materials, analytical models for the defect prediction were implemented as shown in the following chapter. Combined with the results from the material characterization, the analytical models allow for the evaluation of a characterized material for the lay-up of a part with a specific geometry, changes of the suitability depending on out-time effects, and countermeasures against the defect occurrence via process parameter adjustments. Moreover, they help assess new materials at an early stage of the material development process as the results of the material characterization are sufficient for a meaningful prediction of the lay-up behavior.

A thermal simulation was conducted, to account for the changes of thermal properties which affect the material temperature and, in turn, affect the temperature dependent material properties. Its output is the material temperature as a function of material properties and process parameters — see Sec. 5.1. The results from the thermal simulation are used to calculate the input parameters for the steering defect model — Sec. 5.2 — and the tape peel-off model — Sec. 5.3. The former is based on existing models from literature which were enhanced to increase accuracy with regard to the lay-up experiments and to broaden the scope by including process parameter influences. The tape peel-off model was newly developed as there are no existing models. The defect bridging was not considered as the lay-up experiments revealed that the material property changes do not affect this defect occurrence — compare Sec. 4.2. The application of the models to a use case is presented in Sec. 5.4. There, the model results are used to illustrate the impacts

of material property changes and process parameter adjustments on actual part manufacturing for an aircraft nacelle inner fixed structure. The chapter concludes with the summary of the main outcomes in Sec. 5.5.

5.1 Thermal simulation

5.1.1 Model description

For the thermal simulation, a 2D finite differences thermal model developed by Lichtinger [207] was used. The model is used to determine the time- and position-dependent temperature distribution within the prepreg tapes and the tool. Model enhancements and calculations were carried out within [S11]. The main properties used in the model are shown in Fig. 5.1.
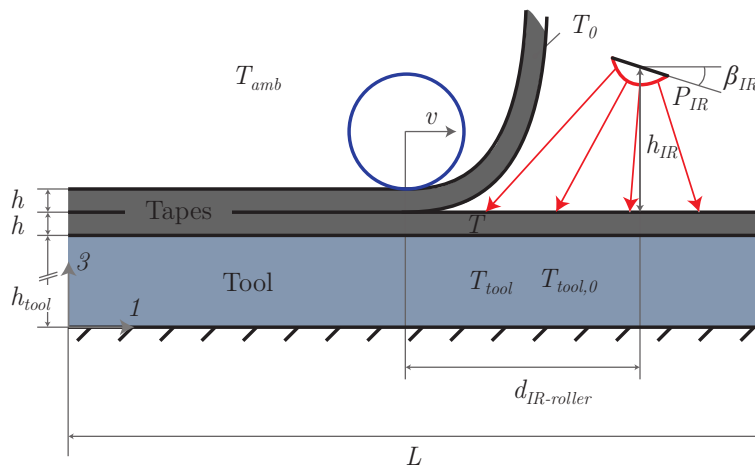
Figure 5.1: Thermal simulation model, adapted from [213]

The input parameters include geometric parameters like the length L, the thickness of tape h and of the tool h_{tool}, the distance between IR emitter and compaction roller $d_{IR-roller}$, the distance of the IR emitter from the substrate h_{IR}, the inclination of the IR emitter β_{IR}. Further inputs are the process parameters lay-up rate v and the IR emitter power P_{IR}, the initial temperatures of tape and tool T_0, $T_{tool,0}$, and the ambient temperature T_{amb} while the resulting temperatures of tapes and tool T, T_{tool} are the outputs. To model the thermal behavior, transient heat transfer equations including the the general law of energy conservation are used. As the material models are both dependent on temperature and on the degree of cure, the considered problem is transient and the system is discretized both spatially and temporally. The movement of the head is modeled with constant velocity, with updated view factor every time step. The model is solved implicitly transient.

The overall model includes material models on the following properties: degree of cure, glass transition temperature, specific heat capacity, thermal conductivity, and viscosity. A detailed description of the model is given in [S11].

5.1.2 Results

The thermal model can be used to simulate the time-dependent temperature distribution during lay-up of several plies. The included material models allow for the analysis of the change of the degree of cure, the thermal properties, and the viscosity during lay-up. Preliminary runs showed that there is no significant long-term change of said properties due to the heat input during lay-up. The presented results therefore focus on the maximum temperature of the material during lay-up which serves as input for the temperature-dependent material properties like mechanical properties and tack.

5.1.2.1 Model verification

To analyze the material temperature, virtual thermocouples on the first ply were used while the lay-up of the second ply was simulated. The results deviate slightly from the experimental measurements of the tool temperature listed in Tab. 3.5 as depicted in Fig. 5.2.

(a) As a function of lay-up rate   **(b)** As a function of IR emitter power
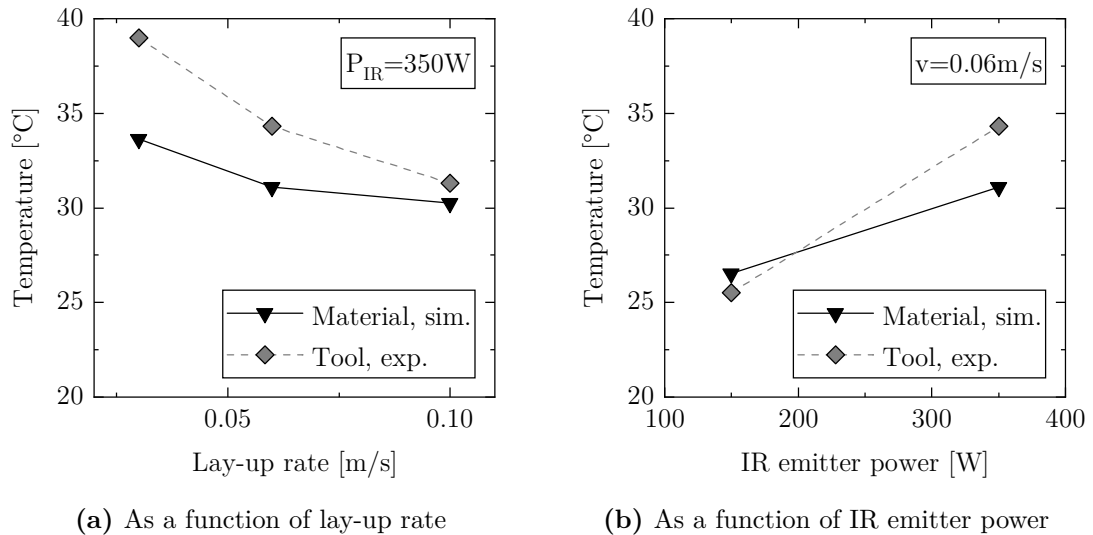
Figure 5.2: Material temperature (IM7/8552 at 1 *d* out-time) from simulation and tool temperature from experimental measurements

At $P_{IR} = 350\ W$, the experimentally measured tool temperature is higher than the simulated material temperature. This is plausible as the IR emitter is directed

at the tool surface which, in turn, heats the material underneath the compaction roller. Reflection of the IR radiation is not included in the model. At $P_{IR} = 150\,W$, the two temperatures are almost identical. Both Fig. 5.2a and Fig. 5.2b reveal that the dependence on process parameters is quite similar in both cases proving that the simulation can be used to predict the effects of process parameter adjustments on material temperature.

5.1.2.2 Out-time effects on IM7/8552

The simulated maximum material temperature during lay-up of IM7/8552 at different out-times is shown in Fig. 5.3.

(a) As a function of lay-up rate   **(b)** As a function of IR emitter power
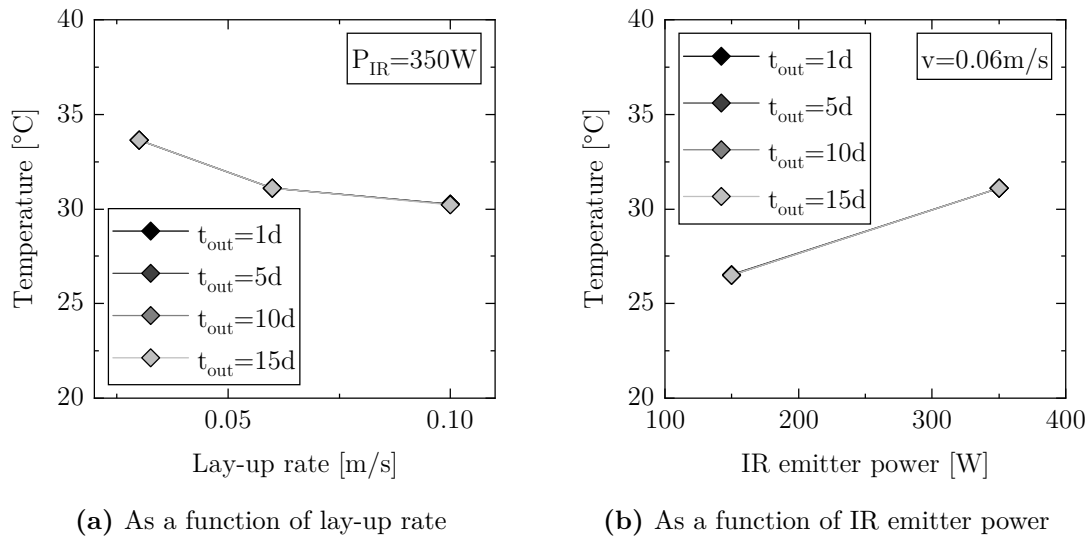
Figure 5.3: Simulated temperature of IM7/8552

Even at an adapted axis scaling, there is no visible difference between the different out-times. It is expected as the thermal properties of IM7/8552 barely change within the investigated out-time range — see Sec. 3.4.

5.1.2.3 Effects of modification

Fig. 5.4 illustrates the simulated maximum material temperature during lay-up of the research materials in comparison with IM7/8552 at 1 *d* out-time. The dependence of the temperature on the process parameters lay-up rate and IR emitter power is rather similar for all analyzed materials. Both process parameters have a significant influence on the material temperature. The temperature of IM7/8552 is higher than the temperature of the research materials at all process parameter combinations.

(a) As a function of lay-up rate

(b) As a function of IR emitter power
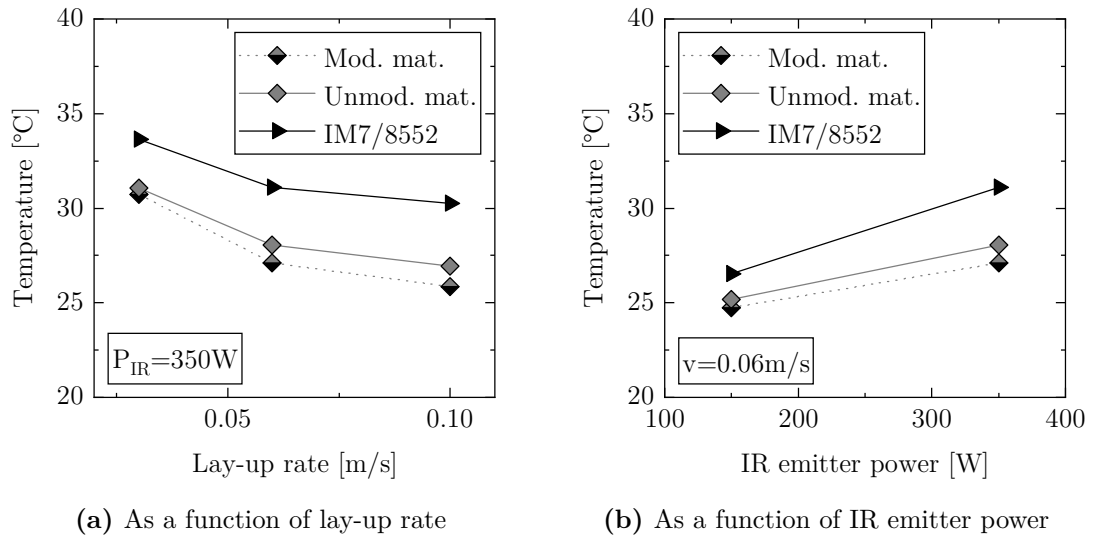
Figure 5.4: Simulated temperature of the research materials in comparison with IM7/8552 at 1 d out-time

Besides differences in fiber volume fraction — see Tab. 3.2, the different thermal properties of the fibers affect the results. The thermal properties of IM7 given in the data sheet are: $k = 5.4\ W/mK$, $c_p = 879\ J/kgK$ [20]. The thermal properties of HTS40 given in the data sheet are: $k = 10\ W/mK$, $c_p = 710\ J/kgK$ [214]. Yet, the effect of fiber difference is of secondary interest as the investigation of the effects of modification on temperature is the principal motivation for the thermal simulation. Fig. 5.4 reveals that the temperature of the unmodified material is higher than the temperature of the modified material at all process parameter combinations. Yet, the difference is relatively small: the maximum temperature decrease due to modification is 4 % at $v = 0.1\ m/s$, $P_{IR} = 350\ W$. The main difference in thermal properties is the thermal conductivity in thickness direction k_3 which is twice as high for the modified material compared to the unmodified material — see Sec. 3.4.2.3. Though, the effect on the material temperature during lay-up is small.

5.1.2.4 Conclusion

The thermal simulation shows that the influences of process parameter adjustments on the material temperature are comparable to the influences measured during lay-up experiments. The analysis of IM7/8552 at different out-times reveal no out-time effects on the material temperature as the out-time effects on the thermal properties are insignificant. The material modification via fillers, however, does affect the temperature as the modified material is heated up to a lower temperature than the

unmodified material at constant process parameters. Yet, the effect is comparably small ($1.1 - 4$ %). In conclusion, the difference in material temperature between IM7/8552 and the research materials has to be considered for lay-up defect models with regard to the temperature-dependent material properties.

5.2 Steering defect model

The objective of the steering defect model is the prediction of steering induced out-of-plane buckling. The presented model is based on Bakhshi and Hojjati's model [181] — see Sec. 2.2.3.1. The model was enhanced with regard to the lay-up experiments described in Chapter 4 increasing accuracy and broadening the scope by including process parameter influences. Parts of the model enhancements were developed within the student thesis [S12].

5.2.1 Model description

Bakhshi and Hojjati's model allows for the calculation of the critical steering radius R_{crit} which is the minimum steering radius at which no buckling occurs. It is calculated using Eq. 2.6 and Eq. 2.12 as

$$R_{crit}(t) = \frac{E_1 h b (6 - \alpha_{load})}{\alpha_{load}} \left[24 D_{11} \left(\frac{\pi m}{L} \right)^2 + 90 D_{22} \left(\frac{L}{\pi m b^2} \right)^2 + 160 D_{66} \left(\frac{1}{b} \right)^2 \right.$$
$$\left. -40 D_{12} \left(\frac{1}{b} \right)^2 + G \left(6 + 30 \left(\frac{L}{\pi m b} \right)^2 \right) + \frac{k_{tack}(t)}{2} \left(\frac{3L}{\pi m} \right)^2 \right]^{-1}.$$
$$(5.1)$$

5.2.1.1 Input parameters

The material input parameters needed for the model are listed in Tab. 5.1. The width and height are either taken from the data sheet or measured directly. The tensile modulus in 1 direction E_1 is determined using the rule of mixture Eq. 2.5 and the inverse rule of mixture Eq. 5.2 [148]

$$E_m = (1 - \phi) \left(\frac{1}{E_2} - \frac{\phi}{E_f} \right)^{-1} \tag{5.2}$$

where E_f is taken from the material's data sheet and E_2 is the result of the transverse tensile tests — Sec. 3.5.1. A parameter study revealed that the influence of changes of E_2 within the measured range on the critical steering radius is negligible.

Table 5.1: Steering defect model — input parameters material

Parameter	Symbol	Unit	Source
Width	b	mm	Own measurement
Height	h	mm	Own measurement
Tensile modulus in 1 direction	E_1	MPa	Eq. 2.5, Eq. 5.2
Tensile modulus in 2 direction	E_2	MPa	Own measurement
Shear stiffness	G_{12}	MPa	Own measurement
Poisson's ratio in 12-plane	ν_{12}	-	[193]
Poisson's ratio in 21-plane	ν_{21}	-	Eq. 5.3
Tack stiffness	k_{tack}	N/mm^3	Own measurement
Out-time	t_{out}	d	*User input*

As a measure of data reduction, E_2 is kept constant using the mean value of all results described in Sec. 3.5.1.3 for the respective material. For the shear stiffness G_{12}, the experimental results presented in Sec. 3.5.2.3 are used. The shear stiffness is dependent on temperature and shear rate. During lay-up the material is heated for a short time followed by a temperature decrease back to ambient temperature. Similarly, a high shear rate is applied in the moment of lay-up caused by the movement of the lay-up head. It is followed by a low shear rate caused by the load within the tape. The steering defect model is used to evaluate the temporal evolvement of the buckles after lay-up rather than in the moment of lay-up. Therefore, the input for the model is G_{12} at ambient temperature and minimum measured shear rate (here: $\dot{\gamma} = 0.001 \ s^{-1}$). It is measured at each out-time and for each material. For temperatures between the measurement temperatures $T = 20 \ °C$ and $T = 40 \ °C$, G_{12} is interpolated linearly. The Poisson's ratio in 12-plane ν_{12} is taken from Rajan et al. [193] who stated that buckle formation is unaffected for values of ν_{12} in the range $0.1 \leq \nu_{12} \leq 1$ and determined $\nu_{12} = 0.24$ for IM7/8552. The Poisson's ratio in 21-plane is calculated as

$$\nu_{21} = \nu_{12} \left(\frac{E_2}{E_1} \right).$$ (5.3)

For the tack stiffness k_{tack}, the experimental results presented in Sec. 3.3.1.3 are used. Just as for the shear stiffness, k_{tack} at ambient temperature is used to represent the material properties after lay-up and values for temperatures between the measurement temperatures are interpolated linearly. The tack stiffness did not display a pronounced dependence on debonding rate. Furthermore, the exact debonding rate during AFP lay-up is difficult to estimate. Therefore, the mean value of all debonding rates was used as the input parameter for each temperature, out-time, and material as a measure of data reduction. This input from the

experimental results is referred to as $k_{tack,base}$. The absolute values of the material inputs are listed in the appendix in Tab. A.20 and Tab. A.21.

The input parameters regarding process and ambience are shown in Tab. 5.2.

Table 5.2: Steering defect model — input parameters process and ambience

Parameter	Symbol	Unit	Source
Lay-up rate	v	m/s	*User input*
Compaction force	F	N	*User input*
IR emitter power	P_{IR}	W	*User input*
Temperature	T	$°C$	Eq. 5.4, Tab. 5.3
Time of intimate contact	t_{intim}	s	Eq. 3.1, Eq. 5.5
Ambient temperature	T_{amb}	$°C$	*User input*

The process parameters v, F, P_{IR} as well as the ambient temperature T_{amb} are values put in by the user. The material temperature T and the time of intimate contact t_{intim} are a result of the process parameters as described in Sec. 3.1.2. Within the model, T is calculated using the experimental results listed in Tab. 3.5. The dependence of the temperature on the lay-up rate and the IR emitter power can be be expressed with a parabolic fitting within the measured range as

$$T(v) = A_T(v) \cdot P_{IR}^2 + B_T(v) \cdot P_{IR} + T_{amb} \tag{5.4}$$

with the corresponding parameters listed in Tab. 5.3.

Table 5.3: Steering defect model — input parameter temperature: parameters of fits

v $[m/s]$	A_T $[°C/W^2]$	B_T $[°C/W]$
0.03	$1.116 \cdot 10^{-4}$	$7.947 \cdot 10^{-3}$
0.06	$6.830 \cdot 10^{-5}$	$9.723 \cdot 10^{-3}$
0.10	$5.140 \cdot 10^{-5}$	$7.035 \cdot 10^{-3}$

For values of v outside the measured values, the temperature is determined using a piecewise cubic interpolation. As the temperature of the research materials is expected to be lower than the temperature of IM7/8552 at the same process parameters — see Sec. 5.1.2.3, a constant value s_{temp} is defined to shift the temperature to the expected value of the research materials. Using the mean value of the relative temperature difference between the research materials as shown in Sec. 5.1.2.3, leads to $s_{temp} = 0.893$. The time of intimate contact is calculated using the length of the pressure area from the deformed roller L_{roller} as described in Eq. 3.1 divided by the lay-up rate:

$$t_{intim} = \frac{L_{roller}}{v}. \tag{5.5}$$

Instead of the process parameters v, F, P_{IR} the resulting properties T and t_{intim} can also be used as a direct input for the model.

5.2.1.2 Model enhancements

A first enhancement of Bakhshi and Hojjati's model is the determination of the position of the neutral axis. Even though the load factor α_{load} is a significant factor for the buckling prediction [31], Bakhshi and Hojjati used a constant, estimated value in their model. To calculate the position of the neutral axis, an approach proposed by Francis [215] is implemented: similar to Hörmann's approach [149], the approach is based on minimizing the strain energy. A sensitivity analysis revealed that the energy components dependent on the in-plane waviness are negligible. The remaining energy components are used to derive an explicit solution for the distance of the neutral axis from the centerline of the tape z by searching for minima as per

$$z = \frac{b}{2} \left[1 + \frac{1}{\varepsilon_b \frac{E_1}{G_{12}}} \left(1 - \sqrt{1 + 4 \, \varepsilon_b \, \frac{E_1}{G_{12}}} \right) \right] \tag{5.6}$$

$$\varepsilon_b = \frac{b \, \kappa}{2} = \frac{b}{2 \, R_{crit}} \tag{5.7}$$

$$\alpha_{load} = \frac{b}{0.5 \, b + z} \tag{5.8}$$

where ε_b is the equivalent bending strain. Since the critical steering radius is dependent on the distance of the neutral axis and vice versa, the distance of the neutral axis is calculated iteratively using MATLAB.

Enhancements regarding time after lay-up, process parameters, and out-time are implemented within the time-dependent tack stiffness $k_{tack}(t)$. As proposed by Bakhshi and Hojjati, the temporal evolvement of the tack stiffness can be expressed by the first term of a Prony series as [181]:

$$k_{tack}(t) = k_{tack,\infty} + k_{tack,1} \cdot exp\left(\frac{-t}{\tau_1} \right) \tag{5.9}$$

where $k_{tack,\infty}$ is the long term tack stiffness and $k_{tack,1}$ and τ_1 express the time-dependent behavior. Both $k_{tack,\infty}$ and $k_{tack,1}$ depend on the initial value of the tack stiffness $k_{tack,start}$ and the coefficient ζ_{time} for the description of the temporal evolvement as

$$k_{tack,\infty} = k_{tack,start} \cdot \zeta_{time} \tag{5.10}$$

$$k_{tack,1} = k_{tack,start} - k_{tack,\infty} = k_{tack,\infty} \cdot \left(\frac{1}{\zeta_{time}} - 1 \right). \tag{5.11}$$

The initial value of the tack stiffness $k_{tack,start}$ is defined as

$$k_{tack,start} = k_{tack,base} \cdot c_{temp} \cdot c_{t,intim} \cdot c_{out-time} \tag{5.12}$$

with the correction factors c_{temp}, $c_{t,intim}$, and $c_{out-time}$ accounting for the influences of temperature, time of intimate contact, and out-time on the tack stiffness which cannot be expressed by the experimental data.

Besides the tack-related enhancements a correction factor for the shear stiffness c_{G12} is defined. A sensitivity study revealed that the influence of G_{12} is overvalued [J2] underlining the need for a correction factor to increase accuracy. The value resulting from the sensitivity study is $c_{G12} = 0.1$.

The coefficients of temporal evolvement are determined empirically based on the results of the lay-up experiments on the temporal defect evolution presented in Sec. 4.1.2. The resulting values are $\zeta_{time} = 0.93$ and $\tau_1 = 7\ s^{-1}$. The correction factors c_{temp}, $c_{t,intim}$, $c_{out-time}$, and c_{G12} are determined empirically based on the results of the lay-up experiments on process parameters influences presented in Sec. 4.1.3. The correction factor for the temperature c_{temp} is defined as

$$c_{temp} = \frac{k_{tack,base}(T_{layup})}{k_{tack,base}(T_{amb})}. \tag{5.13}$$

By this, the temperature-related experimental data is utilized directly to account for the temperature influence on the critical steering radius. Within the model, the lay-up temperature T_{layup} is calculated using Eq. 5.4.

The correction factor for the time of intimate contact $c_{t,intim}$ is defined as

$$c_{t,intim} = 1.3009\ s^{-1} \cdot t_{intim}^{0.2282}. \tag{5.14}$$

Plotting the results of the lay-up experiments on process parameter influences over t_{intim} reveals that the results for critical steering radius have the highest congruence with power function fits (with the exponent being < 1). The parameters of Eq. 5.14 are determined empirically with the results at $1\ d$ out-time as a reference. Using the temperature and the time of intimate contact instead of the process parameters as inputs for the model enhancements increases the transferability to

other machine configurations where process parameter inputs might lead to other values for temperature and time of intimate contact.

The correction factor $c_{out-time}$ accounts for the observation that $k_{tack,base}$ leads to unexpected results for the critical steering radius at $5 - 15\ d$ out-time. The obtained values are $c_{out-time}(1d) = 1$, $c_{out-time}(5d) = 0.859$, $c_{out-time}(10d) = 1.076$, and $c_{out-time}(15d) = 0.270$. All coefficients and correction parameters for the model enhancement are listed in Tab. 5.4.

Table 5.4: Steering defect model — coefficients and correction parameters

Parameter for	Symbol	Unit	Value/source
Temporal evolvement	ζ_{time}	-	0.93
Temporal evolvement	τ_1	s^{-1}	7
Temperature	c_{temp}	-	Eq. 5.13
Time of intimate contact	$c_{t,intim}$	-	Eq. 5.14
Out-time	$c_{out-time}$	-	1 (1d); 0.859 (5d); 1.076 (10d); 0.270 (15d)
Shear stiffness	c_{G12}	-	0.1

The overall model is implemented in a MATLAB script which is included in the appendix — see Fig. A.1–Fig. A.3.

5.2.2 Results

5.2.2.1 Model verification

The underlying model outputs the critical steering radius at which no defects occur — see Eq. 5.1 — whereas the lay-up experiments have been conducted at constant steering radii with varying defect lengths. Therefore, experimental results have to be converted to an equivalent critical steering radius. For this, the conversion factor w is defined as

$$w = \frac{R_{crit}}{R} - 1. \tag{5.15}$$

It is presumed that w equals the relative buckled length measured in the steering experiments. Namely, at $w \leq 0$ there should not be any buckling while at $w = 10\ \%$, for example, the buckled length should be around 10 % of the total arc length. By determining the equivalent critical steering radius using Eq. 5.15, experimental results and calculated critical steering radii can be compared directly.

To evaluate the accuracy of the model regarding temporal defect evolvement, the critical steering radius as a function of time after lay-up is assessed. For this, the time dependent critical steering radius $R_{crit}(t)$ is normalized by the maximum critical steering radius $R_{crit}(t \to \infty)$ at a given parameter set enabling the analysis of the relative time-dependent change. Fig. 5.5 illustrates the normalized critical steering radius calculated with two different parameter sets and compares them to the minima and maxima from the experimental investigation described in Sec. 4.1.2.
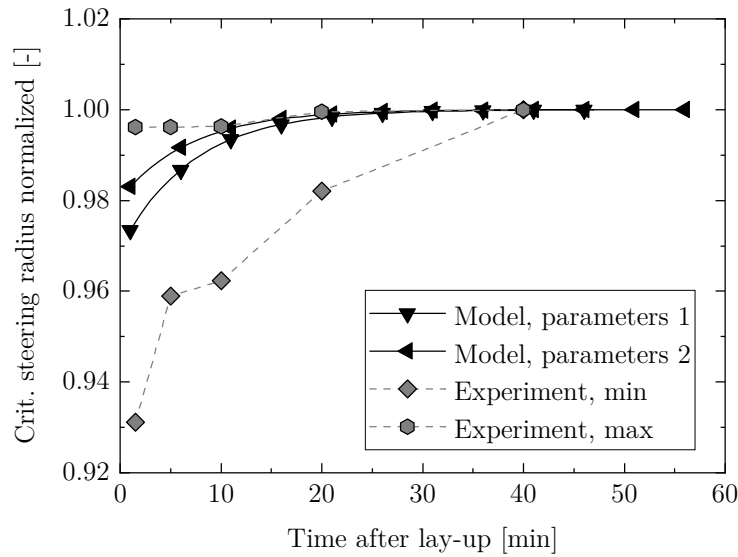
Figure 5.5: Steering model — verification of normalized critical steering radius (material: IM7/8552; parameters 1: $v = 0.1\ m/s$, $F = 200\ N$, $P_{IR} = 150\ W$, $t_{out} = 10\ d$, $T_{amb} = 21\ °C$; parameters 2: $v = 0.03\ m/s$, $F = 400\ N$, $P_{IR} = 150\ W$, $t_{out} = 5\ d$, $T_{amb} = 21\ °C$)

Both model results are well within the experimental range and display a similar curve progression indicating that the model is capable of reproducing the temporal defect evolvement.

To evaluate the accuracy of the model regarding absolute results for R_{crit}, out-time effects, and process parameter influences, the results for the maximum critical steering radius is compared to the experimental results of the process parameter variation as described in Sec. 4.1.3 with the help of the conversion factor w. Fig. 5.6 shows the comparison of model and experiment for each process parameter set used in the experiments. It reveals that the model results are in good agreement with the experimental results with regard to both out-time effects and process parameter influences. At 15 d out-time, the influence of the lay-up rate seems to be underestimated as the calculated critical steering radius is too high at $v = 0.03\ m/s$ — Fig. 5.6a — and too low at $v = 0.1\ m/s$ — Fig. 5.6e. Besides that, the deviation is either very small or within the range of the experimental results.

(a) $v = 0.03 \ m/s$, $F = 400 \ N$, $P_{IR} = 350 \ W$

(b) $v = 0.06 \ m/s$, $F = 200 \ N$, $P_{IR} = 350 \ W$

(c) $v = 0.06 \ m/s$, $F = 400 \ N$, $P_{IR} = 150 \ W$

(d) $v = 0.06 \ m/s$, $F = 400 \ N$, $P_{IR} = 350 \ W$

(e) $v = 0.10 \ m/s$, $F = 400 \ N$, $P_{IR} = 350 \ W$
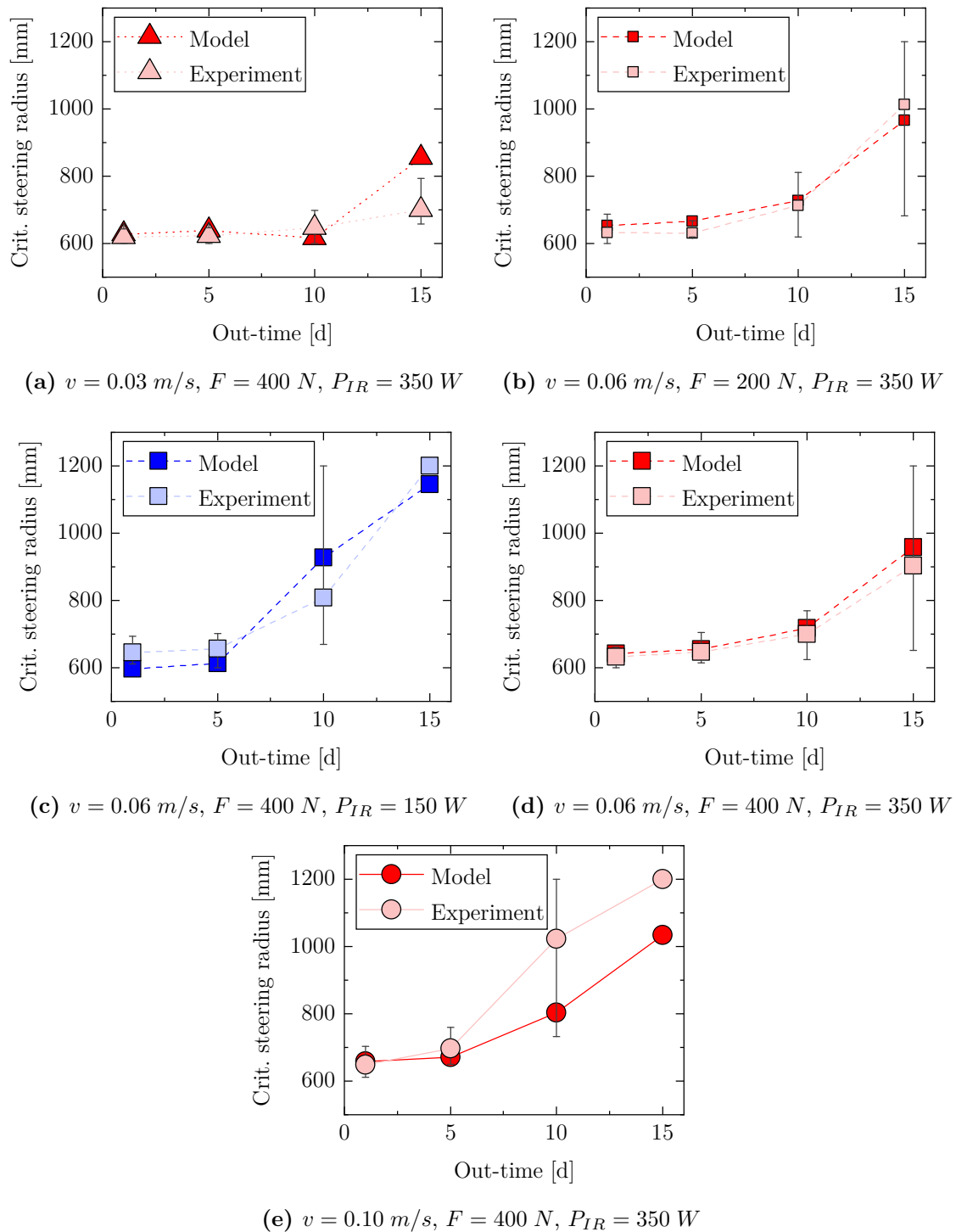
Figure 5.6: Steering model — verification of out-time and process parameters on critical steering radius (error bars represent the minimum and maximum values of the respective experimental test series)

This verifies the overall suitability of the model for the prediction of steering induced out-of-plane buckling at various out-times and process parameters. At 1 d and 5 d out-time it has to be noted that the tack stiffness is higher at $T = 20\ °C$ than at $T = 40\ °C$ — see Sec. 3.3.1.3 — leading to a smaller critical steering radius at lower temperatures. This is contrary to the experimental results, yet, this influence on the R_{crit} result is comparably small within the investigated range.

5.2.2.2 Out-time effects on IM7/8552

The model was used to quantify the out-time effects on the critical steering radius and to identify countermeasures for the out-of-plane buckling occurrence. A full factorial parametric study was conducted using the parameters listed in Tab. 5.5.

Table 5.5: Steering model — parameter variation IM7/8552

Parameter	Symbol	Unit	Values
Lay-up rate	v	m/s	0.01; 0.06; 0.13; 0.20
Compaction force	F	N	50; 200; 400; 600
IR emitter power	P_{IR}	W	0; 150; 350; 500
Out-time	t_{out}	d	1; 5; 10; 15
Ambient temperature	T_{amb}	$°C$	21

Four levels of out-time and four levels of each process parameter were investigated. Besides the range covered in the experiments, the process parameters were extended to very low values, e. g. $v = 0.01\ m/s$, or values out of the scope of the used AFP machine, e. g. $F = 600\ N$, $P_{IR} = 500\ W$, to analyze the benefits of extending the range of the process parameters.

The process parameter with the lowest impact on the critical steering radius is the compaction force. The average decrease of critical steering radius due to increased compaction force between $F = 50\ N$ and $F = 600\ N$ was 4.4 % at 1 d out-time, 4.3 % at 5 d, 3.1 % at 10 d, and 1.6 % at 15 d. Therefore, a further increase in compaction force may not be necessary given the fact that a higher compaction force may lead to increased wear of the compaction unit. To provide an overview of the findings for IM7/8552, Fig. 5.7 shows the results at $F = 400\ N$. It details the critical steering radius at $t_{after} = 40\ min$ as a function of lay-up rate and IR emitter power for each out-time. Contour plots for all values of the compaction force are displayed in the appendix in Fig. A.4, Fig. A.5, Fig. A.6, and Fig. A.7.

Fig. 5.7 highlights the significant impact of the process parameters lay-up rate and IR emitter power on the critical steering radius. At 1 d and 5 d out-time, R_{crit} ranges from around 490 mm to around 780 mm.

(a) Legend

(b) $t_{out} = 1\ d$

(c) $t_{out} = 5\ d$

(d) $t_{out} = 10\ d$

(e) $t_{out} = 15\ d$
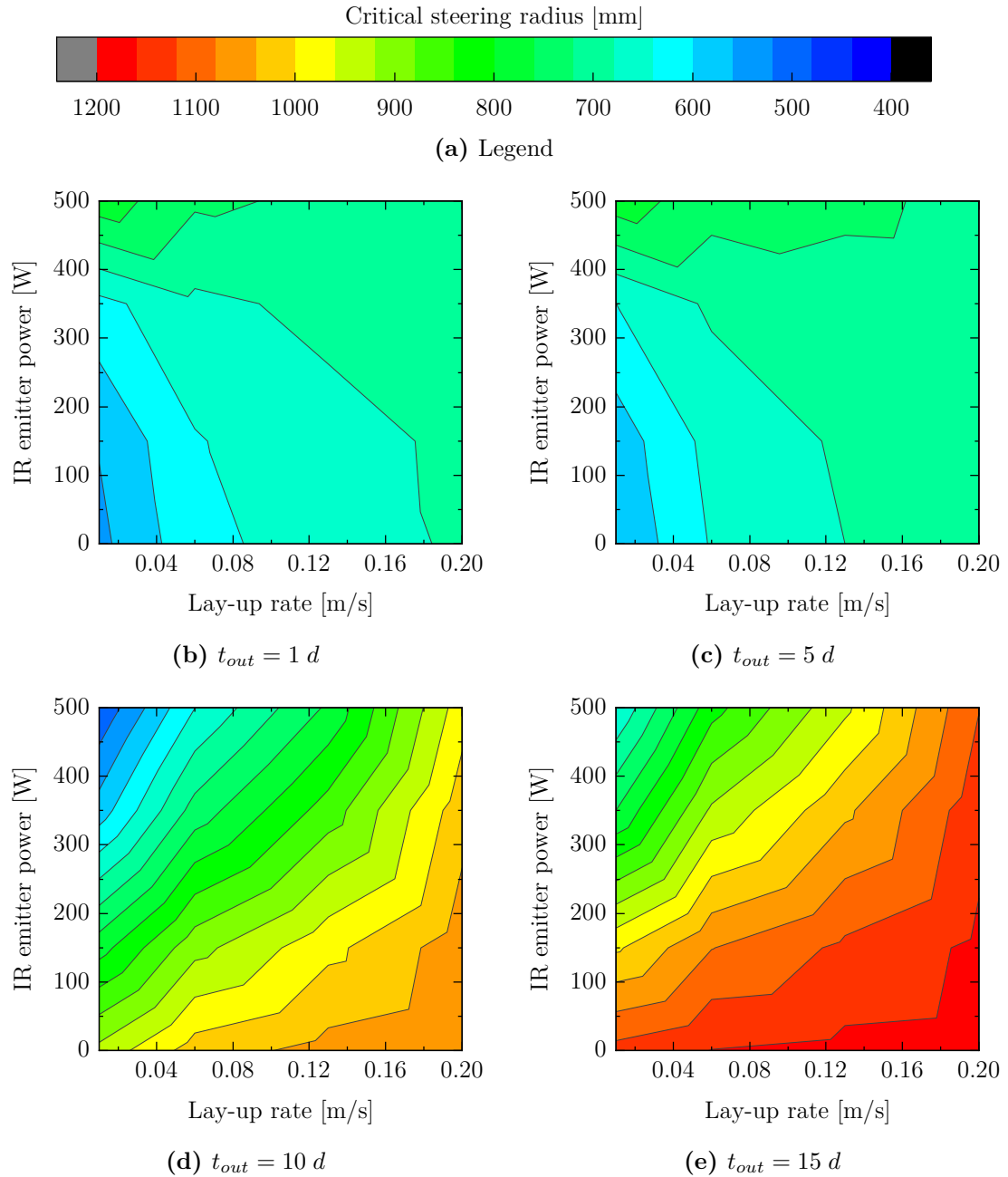
Figure 5.7: Steering model — critical steering radius at $t_{after} = 40\ min$ as a result of process parameter variation for IM7/8552 at $F = 400\ N$

A comparably small steering radius can therefore be achieved even up to a lay-up rate of $0.2\ m/s$. Fig. 5.7b and Fig. 5.7c further reveal that the impact of IR emitter power is higher at lower lay-up rates and becomes negligible at $v > 0.18\ m/s$. At elevated out-times — $10\ d$ and $15\ d$ — the influence of v and P_{IR} on the critical steering radius is even higher as shown in Fig. 5.7d and Fig. 5.7e. R_{crit} ranges from around $410\ mm$ to around $1140\ mm$ at $10\ d$ and from around $600\ mm$ to around $1270\ mm$ at $15\ d$ out-time. As the molecular mobility of the resin decreases, the

parameters temperature and time of intimate contact become more important to achieve sufficient surface wetting for proper adhesion to the substrate. Therefore, v and P_{IR} have to be set accurately to minimize the critical steering radius or — in other words — to minimize out-of-plane buckling at a given steering radius. Fig. 5.7d and Fig. 5.7e further reveal that v has to be minimized and P_{IR} has to be maximized within the investigated range to achieve a minimum critical steering radius. Yet, it has to be considered that a low lay-up rate leads to a higher manufacturing time and very high temperatures may cause cohesive failure resulting in a decline in tack. At a given steering radius, the findings illustrated in Fig. 5.7 can be used to optimize the process parameters by determining the maximum lay-up rate at which no defects occur which therefore reduces manufacturing time. At a given out-time, the results can be used to optimize the process parameters or to determine whether the material is suitable for a part with given steering radii.

5.2.2.3 Effects of modification

On the lines of the IM7/8552 study, the critical steering radius at $t_{after} = 40\ min$ for the research materials was determined. Again, the compaction force was the process parameter with the least impact on R_{crit}. Fig. 5.8 shows the result at $F = 400\ N$. Contour plots for all values of the compaction force are displayed in the appendix in Fig. A.8 and Fig. A.9.

Fig. 5.8c reveals that the critical steering radius of the unmodified material displays a comparably small dependence on v and P_{IR} over a large range of the respective parameters and a drastic dependence when $v < 0.06\ mm$ and $P_{IR} > 350\ W$. The unmodified material has a very high tack at $T = 20\ °C$ — see Sec. 3.3.1.3 — which leads to a comparably low critical steering radius. At low values for the lay-up rate and high values for the IR emitter power, the high resulting temperature leads to a low tack caused by cohesive failure. This, in turn, leads to a steeply increasing critical steering radius. Besides that, the unmodified material can be processed at a wide range of lay-up rate without a significant increase in R_{crit}.

The modified material's results for R_{crit} — Fig. 5.8b — are comparably low, too. The maximum critical steering radius in the investigated range is 361 mm and the minimum is 230 mm. At $T = 20\ °C$, the tack stiffness is significantly lower compared to both the unmodified material and the reference IM7/8552 while at $T = 40\ °C$ it is in the same order of magnitude — see Sec. 3.3.1.3. The low critical steering radius of the modified material is caused by the very high in-plane shear modulus — see Sec. 3.5.2.3. The buckling model is formulated as a plate buckling problem.

(a) Legend

(b) Modified material

(c) Unmodified material
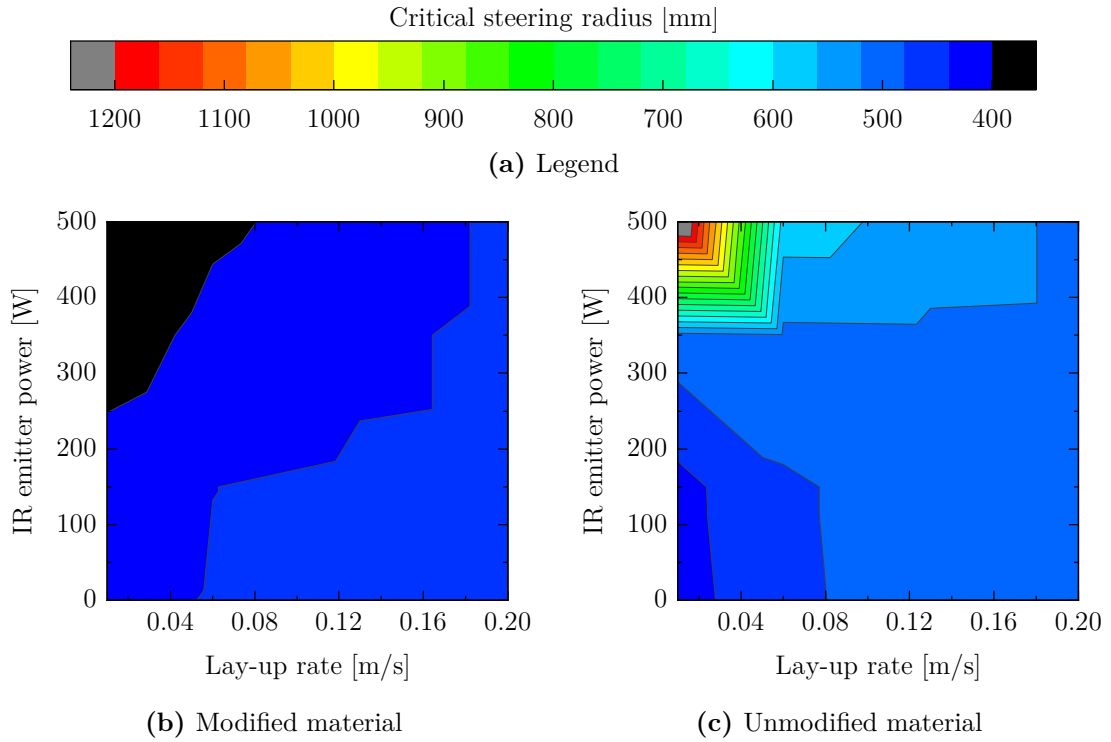
Figure 5.8: Steering model — critical steering radius at $t_{after} = 40\ min$ as a result of process parameter variation for research materials at $F = 400\ N$

Therefore, a higher in-plane shear modulus leads to a smaller critical steering radius since the load for buckle development has to be higher to overcome the shear modulus. Fig. 5.8b suggests that the modified material can be processed at a wide range of lay-up rate and IR emitter power without even exceeding $R_{crit} = 400\ mm$. Yet, the buckling model accounts for the state when the tape is already placed onto the substrate without considering the exact moment when the tape is laid up. In the moment of lay-up, the shear stiffness has to be overcome to position the tape along the curved path. In this case, a high shear stiffness hinders steering whereas it counteracts defect occurrence after the tape is laid onto the substrate. Therefore, the high in-plane shear modulus of the modified material may lead to additional loads in the tape during steered lay-up at low temperatures which are not covered in the steering model. This can be overcome at high lay-up temperatures as the in-plane shear modulus decreases at the moment of lay-up and increases again after lay-up when the material cools down.

5.2.2.4 Conclusion

The steering defect model allows for the prediction of the critical steering radius taking material properties, material changes due to out-time or modification, tem-

poral evolvement, and process parameters into account. The model is in good agreement with experimental steering results and allows for the prediction of R_{crit} beyond the experimental scope. Due to the fact that the input parameters can be obtained using offline characterization methods, the lay-up behavior of new materials can be predicted without doing lay-up experiments. The introduction of a conversion factor allows for the conversion between critical steering radius at which no defects occur to the estimation of the quantity of defects at a given steering radius.

The parametric study for IM7/8552 confirms the strong influence of out-time, lay-up rate, and IR emitter power on the critical steering radius. Even though increasing the compaction force leads to a decrease in critical steering radius, the impact is comparably small. The findings help identify the optimal process parameters at a given out-time and steering radius which allows for the reduction of manufacturing time and material scrapping.

The parametric study for the research materials reveals that the critical steering radius for both materials is comparably low. The unmodified material exhibits a very high tack causing a low critical steering radius and the modified material exhibits a very high in-plane shear stiffness causing a low critical steering radius. As pointed out in the material characterization, the high tack of the unmodified material may be detrimental in the material feed where components of the feeding unit may be contaminated eventually jamming the material feed. The effects of the high in-plane shear stiffness of the modified material in the moment of lay-up are not yet fully understood. Yet, after the tape is placed the high in-plane shear stiffness helps prevent defect evolvement. In conclusion, it is inferred that the modified material is well suited for AFP lay-up even at comparably small steering radii.

5.3 Tape peel-off model

The objective of the newly developed peel-off model is the prediction of the tape peel-off on a convex edge with regard to material properties, lay-up path, and process parameters. Parts of the model were developed within the student thesis [S12].

5.3.1 Model description

The selected approach is the use of the difference between strain energy due to bending U_B and separation energy U_T which is needed to overcome the tack as

$$U_{peeloff} = U_B - U_T. \tag{5.16}$$

If the peel-off energy $U_{peeloff}$ is greater than zero, the defect peel-off is likely to happen while it is less likely the lower $U_{peeloff}$ is below zero. Assuming elastic bending, U_B is defined as [198]

$$U_B = \frac{1}{2} B \int_{\frac{1}{2}l}^{-\frac{1}{2}l} \kappa^2 dx \tag{5.17}$$

where B presents the bending stiffness $E_{flex}I$, l is the arc length over the radius, and κ is the curvature. The curvature is defined as

$$\kappa = \frac{1}{R_{edge,eff}} \tag{5.18}$$

with the effective edge radius described in Eq. 4.1 which accounts for the lay-up direction towards the edge. For a fixed opening angle of the tool edges of 90 °, the arc length l is

$$l = R_{edge,eff} \cdot \frac{\pi}{2} \tag{5.19}$$

leading to a rephrased description of U_B as follows:

$$U_B = \frac{1}{2} \cdot c_{plast} \cdot E_{flex}I \cdot \frac{\pi}{2} \cdot \frac{1}{R_{edge,eff}}. \tag{5.20}$$

Eq. 5.20 includes a correction factor for plastic deformation c_{plast} as it is expected that a considerable part of the strain energy is converted into plastic deformation in the case of severe bending.

The separation energy U_T for a fixed opening angle of the tool edges of 90 ° is defined as

$$U_T = b \left(L_{edge} + R_{edge,eff} \cdot \frac{\pi}{2} \right) e_{tack} \tag{5.21}$$

where b is the tape width, L_{edge} is the length after the edge, and e_{tack} is the separation energy per area of the tack. As the peel-off is caused by a peeling load, the peel tack determined in Sec. 3.3.2 is used to represent e_{tack}.

5.3.1.1 Input parameters

The material input parameters needed for the model are listed in Tab. 5.6.

Table 5.6: Peel-off model — input parameters material

Parameter	Symbol	Unit	Source
Width	b	mm	Own measurement
Height	h	mm	Own measurement
Flexural modulus	E_{flex}	MPa	Own measurement
Peel tack	e_{tack}	N/mm^3	Own measurement
Out-time	t_{out}	d	*User input*

The second moment of area I for a tape with rectangular cross section is calculated as

$$I = \frac{bh^3}{12}.$$ (5.22)

The flexural modulus E_{flex} is taken from the measurements of the bending stiffness as described in Sec. 3.5.3. Values differing from the measurement temperatures are interpolated linearly. The peel tack e_{tack} is taken from the respective measurements as described in Sec. 3.3.2. The values are implemented as a function of the process parameters during testing. Values differing from the measured process parameters are interpolated using the modified Akima interpolation, makima, in MATLAB which performs cubic interpolation to produce piecewise polynomials [216].

The input parameters for process and ambience are the same as the ones for the steering defect model — see Tab. 5.2. Furthermore, the model incorporates the following parameters regarding the tool geometry and lay-up path as user inputs: the edge radius R_{edge}, the length after edge L_{edge}, and the lay-up direction φ_{layup}.

5.3.1.2 Model enhancements

The peel-off model was enhanced by adjusting the correction factor for plastic deformation c_{plast} with regard to the lay-up experiments presented in Sec. 4.3. Comparing model results with $c_{plast} = 1$ to experimental observations revealed that the strain energy due to bending U_B was likely overvalued at the smaller edge radius of $R_{edge} = 5 \, mm$. According to Eq. 5.20, U_B has a hyperbolic dependence on the edge radius. Yet, the experimental observations did not reveal such a strong dependence on the edge radius and indicated that the tapes would deform plastically to some extent. Hence, the correction factor for plastic deformation was determined by a sensitivity analysis as

$$c_{plast} = 0.1 + R_{edge,eff} \, \frac{1 - 0.1}{0.04}.$$ (5.23)

The overall model is implemented in a MATLAB script which is included in the appendix — see Fig. A.10 and Fig. A.11.

5.3.2 Results

5.3.2.1 Model verification

To verify the model, all parameter sets investigated in the experiments — Sec. 4.3 — were calculated with the model and results are compared as shown in Fig. 5.9 and Fig. 5.10. Individual results per parameter are collated as mean values regardless of the other parameters to increase readability.

A higher lay-up rate leads to a higher probability of peel-off in both the experiments and the model caused by the lower peel tack. Similarly, the comparison reveals a slightly higher probability of peel-off at higher IR emitter power. Even though the influence is small, it is an unexpected result as a higher IR emitter power decreases bending stiffness and generally increases peel tack. The peel tack results for IM7/8552 revealed a low positive correlation to the IR emitter power — see Fig. 3.24. Yet, in some process parameter combinations the peel tack decreased with increasing IR emitter power which influences the peel-off model results.

The compaction force does not affect the peel-off energy since there is no influence on bending stiffness and the influence on peel tack is negligible. As described in Sec. 4.3.2, a positive correlation with the compaction force was not expected.

The peel-off energy decreases significantly as the length after the edge increases which is the expected result since a greater length increases the area of adhesion to the substrate. The contrary experimental results are explained in Sec. 4.3.2 by the deviation from the lay-up rate due to the robot movement at the edge.

In the model, a higher edge radius leads to a lower probability of peel-off as it leads to a lower strain energy due to bending. The contrary experimental results are explained in Sec. 4.3.2 by the assumption that stress induction over a larger tape length leads to a higher defect probability which is not covered in the model. In both cases, the lower angle towards the edge leads to a lower defect probability as the effective edge radius is higher at $\varphi_{layup} = 45$ ° than at $\varphi_{layup} = 90$ ° — see Sec. 4.3.2.

The comparison with regard to out-time reveals a similar curve progression for the experimental and the model results. Both factors are low at 1 d and 5 d out-time and increase after that up to 15 d out-time. At 15 d out-time, the mean peel-off energy is greater than zero indicating that peel-off is rather likely. This correlates to the high proportion of peeled samples of 54 %.
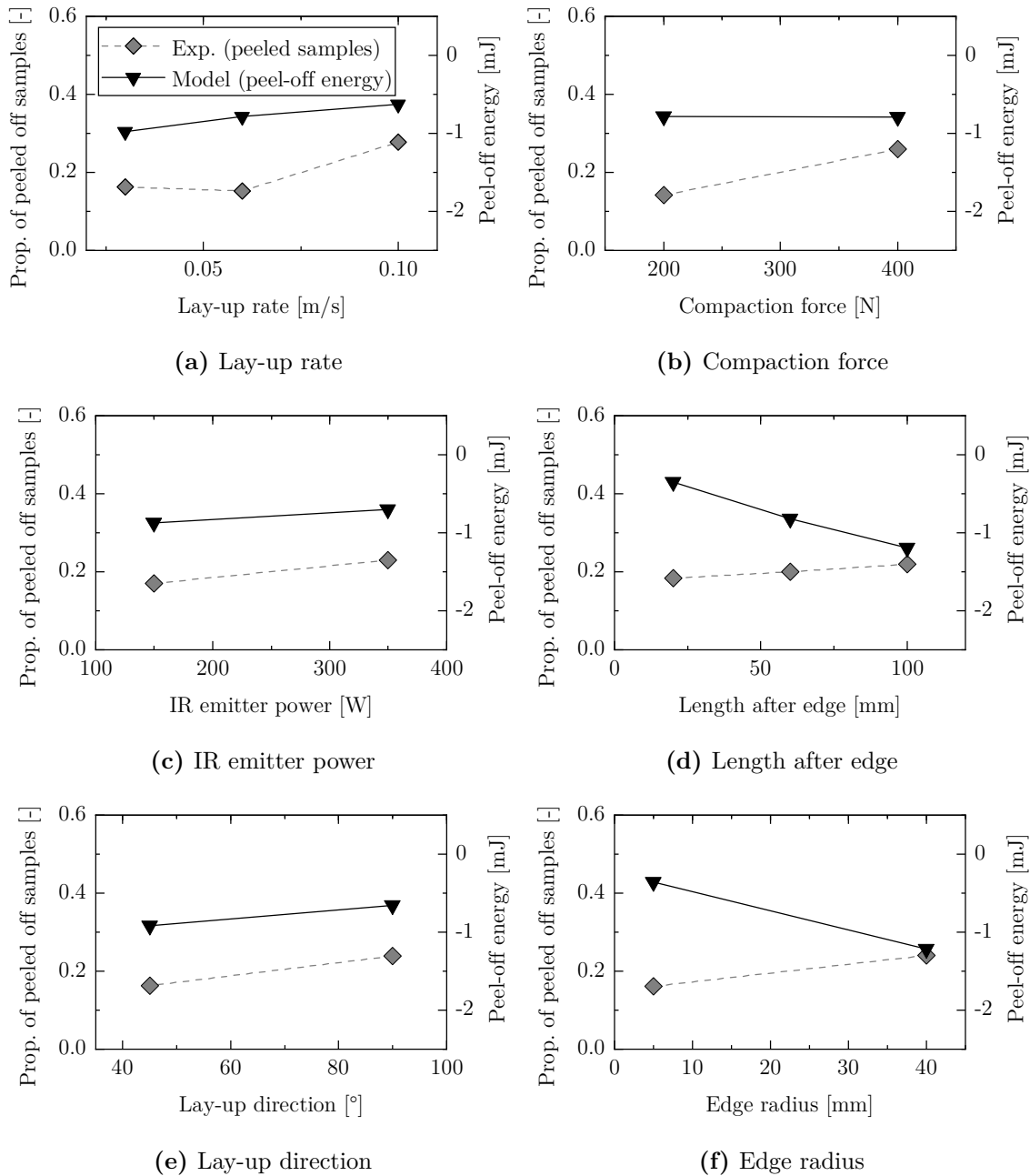
Figure 5.9: Peel-off model — comparison to experimental results for each experimental parameter

In summary, the peel-off model delivers expected results. Where parameter influences differ from experimental results, the experimental results displayed some irregularities caused by the robot movement and other sources. Therefore, the model seems to be suitable to predict the probability of peel-off. Most notably, out-time effects observed during lay-up experiments seem to be addressed adequately.
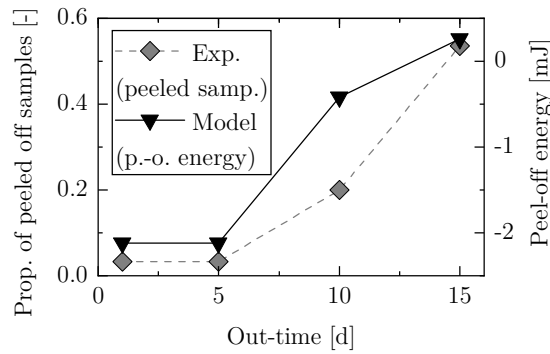
Figure 5.10: Peel-off model — comparison to experimental results as a function of out-time

5.3.2.2 Out-time effects on IM7/8552

The model was used to quantify the out-time effects on tape peel-off and to identify countermeasures. A full factorial parametric study was conducted using the parameters listed in Tab. 5.7. The selected process parameters are within the scope of the parameters of the peel tack measurements since an extrapolation of the parameters led to invalid results. Input parameters for e_{tack} and E_{flex} are listed in the appendix in Tab. A.22, Tab. A.23, and Tab. A.24. The tape width was 3.175 mm and the thickness was 0.125 mm.

Table 5.7: Peel-off model — parameter variation IM7/8552

Parameter	Symbol	Unit	Values
Lay-up rate	v	m/s	0.03; 0.06; 0.10
Compaction force	F	N	200; 300; 400
IR emitter power	P_{IR}	W	150; 250; 350
Out-time	t_{out}	d	1; 5; 10; 15
Ambient temperature	T_{amb}	$°C$	21
Edge radius	R_{edge}	mm	40
Length after edge	L_{edge}	mm	100
Lay-up direction	φ_{layup}	$°$	45

Fig. 5.11 shows the peel-off energy results of IM7/8552 at different out-times as a function of lay-up rate and IR emitter power at the compaction force $F = 400\ N$. Similar to the steering results, the compaction force had the least impact on the defect occurrence. Results for $F = 200\ N$ and $F = 300\ N$ are included in the appendix — see Fig. A.12–Fig. A.15. Fig. 5.11 reveals that the dependence on v and P_{IR} differs for each out-time. The flexural modulus becomes more temperature dependent at higher out-times and the peel tack's dependence on the process parameters varies for each out-time.

(a) Legend

(b) $t_{out} = 1\ d$

(c) $t_{out} = 5\ d$

(d) $t_{out} = 10\ d$

(e) $t_{out} = 15\ d$
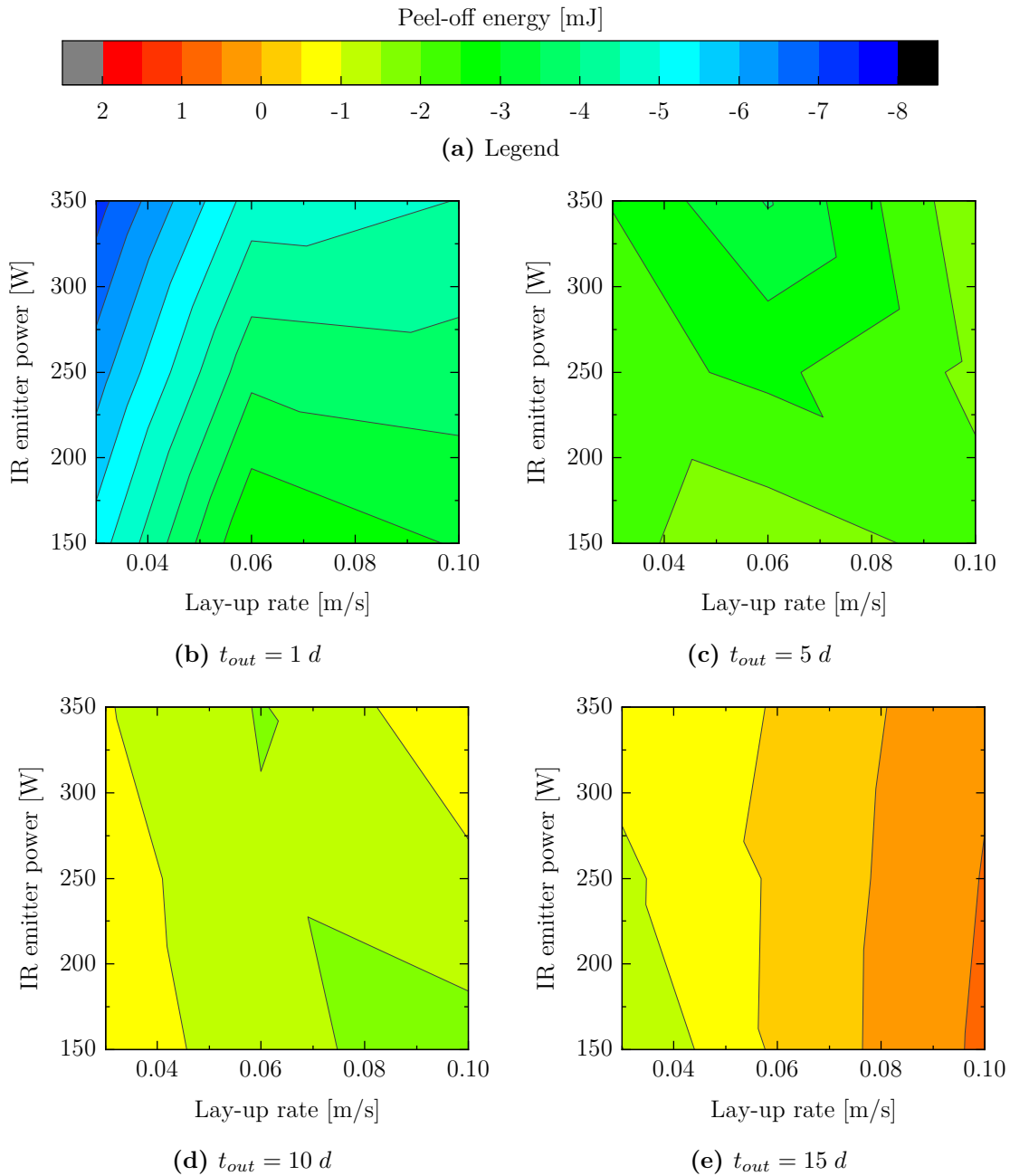
Figure 5.11: Peel-off model — peel-off energy as a result of process parameter variation for IM7/8552 at $F = 400\ N$

At 1 d out-time, $U_{peeloff}$ is the lowest at the minimum lay-up rate and the maximum IR emitter power as this leads to a high peel tack and a low flexural modulus. The maximum is reached at $P_{IR} = 150\ W$ and $v = 0.06\ m/s$ where $U_{peeloff} = -2.5\ mJ$. Fig. 5.11b helps finding the optimum lay-up rate and IR emitter power. It shows that the peel-off energy is clearly below zero in the investigates range indicating that the probability for peel-off is low.

At 5 d out-time, the peel-off energy is still below zero at all investigated parameter sets, yet the range is smaller than at 1 d out-time being $-3.5 \ mJ \leq U_{peeloff} \leq -1.6 \ mJ$. The highest sensitivity to the process parameters can be seen at the high IR emitter power and the middle lay-up rate which coincides with the peel tack results.

At 10 d out-time, the influence of the process parameters on the peel-off energy is comparably small with a range of $-1.7 \ mJ \leq U_{peeloff} \leq -0.6 \ mJ$. Yet the higher values of $U_{peeloff}$ underline the importance of process parameter setting to avoid defect occurrence. The minimum of $U_{peeloff}$ is reached at $P_{IR} = 150 \ W$ and $v = 0.1 \ m/s$ where the peel tack is the highest in the investigated case.

At 15 d out-time, there is a strong dependence of the peel-off energy on the lay-up rate while the influence of the IR emitter power is negligible. At $v = 0.1 \ m/s$, the peel-off energy is greater than zero indicating a high probability of peel-off. Therefore, the lay-up rate should be reduced at 15 d out-time to avoid tape peel-off, yet a defect-free lay-up can still be achieved at 15 d out-time.

5.3.2.3 Effects of modification

Using the same parameters as in the IM7/8552 study, the peel-off energy for the research materials was determined. Input parameters for e_{tack} and E_{flex} are listed in the appendix in Tab. A.23 and Tab. A.24. The tape width was 3.175 mm and the thickness was 0.09 mm. The results for the unmodified and the modified material at $F = 400 \ N$ as a function of lay-up rate and IR emitter power are depicted in Fig. 5.12. Results for $F = 200 \ N$ and $F = 300 \ N$ are included in the appendix — Fig. A.16 and Fig. A.17.

Fig. 5.12c pictures a strong dependence of the unmodified material's peel-off energy on the lay-up rate. The lowest peel-off energy is achieved at $v = 0.06 \ m/s$ since a higher lay-up rate leads to a lower time of intimate contact and a lower lay-up rate leads to cohesive failure. Furthermore, Fig. 5.12c reveals that the peel-off energy is remarkably low being $-28.2 \ mJ \leq U_{peeloff} \leq -7.2 \ mJ$ caused by the very low flexural modulus and the very high peel tack of the material. Tape peel-off is therefore very unlikely to occur.

As the modified material has a higher flexural modulus and a lower peel tack than the unmodified material, the probability for peel-off occurrence is higher — see Fig. 5.12b. All values of the peel-off energy are below zero being $-5.3 \ mJ \leq U_{peeloff} \leq -0.9 \ mJ$. Yet, $U_{peeloff}$ is significantly higher indicating a higher risk for defect occurrence. The dependence on v and P_{IR} is comparably low over a wide range of the parameters.

Peel-off energy [mJ]

(a) Legend

(b) Modified material

(c) Unmodified material
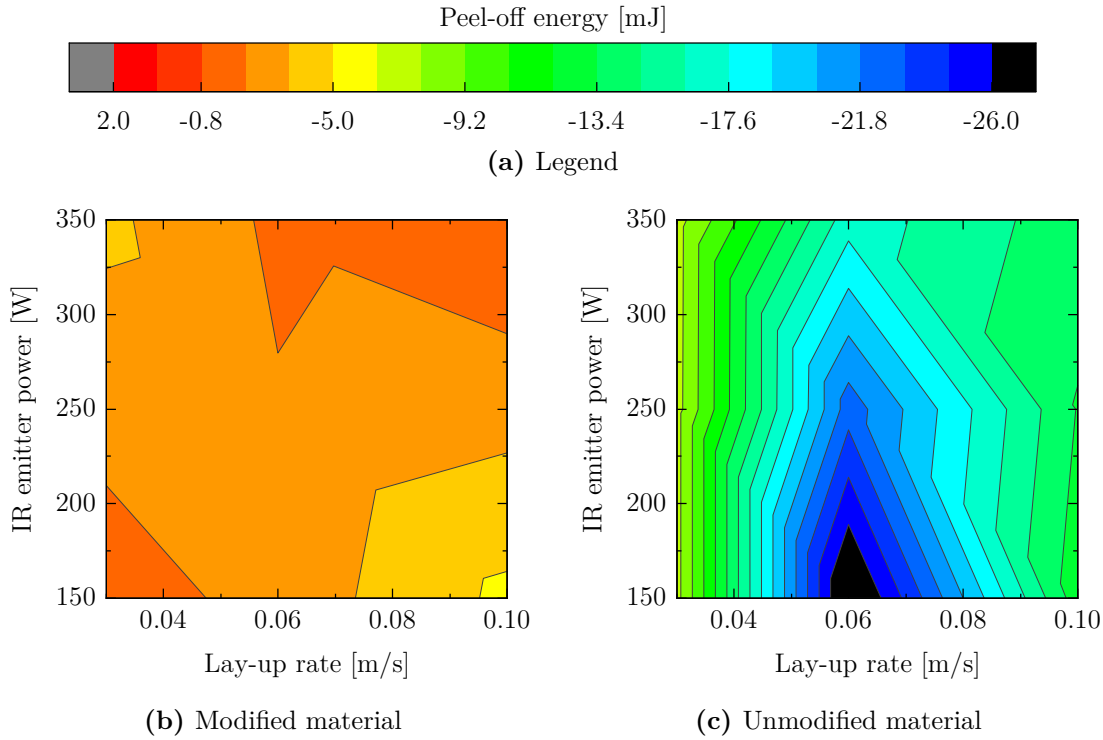
Figure 5.12: Peel-off model — peel-off energy as a result of process parameter variation for research materials at $F = 400\ N$

The lowest values of peel-off energy are reached at $P_{IR} = 350\ W$, $v = 0.03\ m/s$ and at $P_{IR} = 150\ W$, $v = 0.1\ m/s$ while the highest is reached at $P_{IR} = 350\ W$, $v = 0.1\ m/s$. The causes for these results are not fully understood. The results are influenced by the measured peel tack results which, in turn, were affected by the imperfections of research material. Nonetheless, the results for $U_{peeloff}$ help evaluate the risk of tape peel-off for the modified material.

5.3.2.4 Conclusion

The developed peel-off model is capable of indicating the risk of tape peel-off on a convex edge taking material properties, lay-up path, and process parameters into account. The model is based on the difference between the strain energy due to bending and the separation energy to overcome tack using the bending stiffness and the peel tack of the material as the main input parameters. The comparison of the model results to experimental results reveals a very good agreement with regard to the influence of out-time on the defect occurrence. A threshold for peel-off occurrence was identified: where the model results were greater zero — $U_{peeloff} > 0$, the corresponding experimental proportion of peeled samples was $> 50\ \%$ indicating a high probability of peel-off. The variation of the other input parameters was used

to quantify some expected results like an increase in defect risk with increasing lay-up rate, decreasing length after edge, and decreasing edge radius.

The parametric study for IM7/8552 affirms the strong influence of out-time on the peel-off occurrence at out-times $> 5\ d$. Furthermore, it reveals that reducing the lay-up rate is the main countermeasure to avoid tape peel-off — e. g. at $15\ d$ out-time, tape peel-off can be avoided by reducing the lay-up rate to $0.06\ m/s$ or lower.

The parametric study for the research materials reveals that peel-off is very unlikely to occur processing the unmodified material as its flexural modulus is comparably low and its peel tack is comparably high. Processing the modified material, peel-off is more likely due to its higher flexural modulus and lower peel tack. Yet, in all investigated cases the peel-off energy was below zero indicating a low probability of tape peel-off and by that a high suitability of the material for AFP processing.

5.4 Use case: aircraft nacelle inner fixed structure

To visualize the benefit of the presented findings for practical applications, the defect models were applied to an aerospace component which is manufactured via AFP — an aircraft nacelle inner fixed structure (IFS). The IFS is located at the rear part of the engine where the thrust reverser is. Inside the IFS the core stream flows and outside the IFS the bypass stream flows [217]. Fig. 5.13 shows the AFP manufacturing of one half of the IFS at Safran Nacelles Ltd, (Burnley, UK) which is used in the CFM International LEAP-1A engines on Airbus A320neo airliners [218].
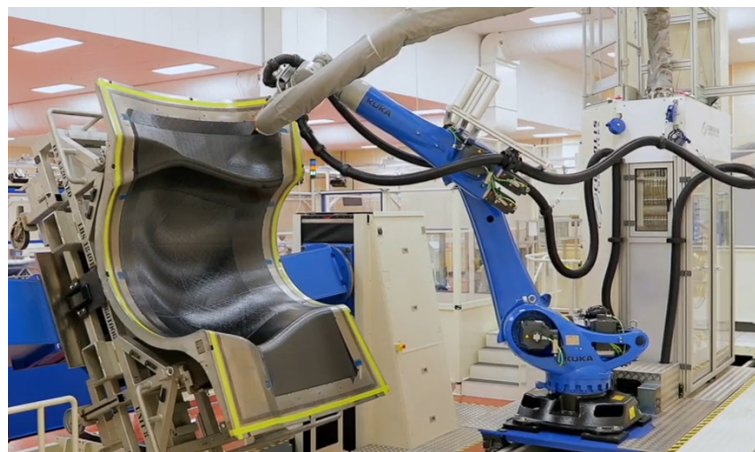
Figure 5.13: Safran Nacelles inner fixed structure AFP manufacturing [219]

Because of its geometry, AFP lay-up of the IFS includes steering and lay-up on a convex edge potentially causing out-of-plane buckling and tape peel-off.

5.4.1 Part description

As the original geometry of Safran Nacelles' IFS is a corporate secret, a generic IFS geometry was developed for the use case. The generic IFS is illustrated in Fig. 5.14 showing the simulation of the lay-up of a -45 ° track with the Coriolis 1/8-TS-AFP machine.
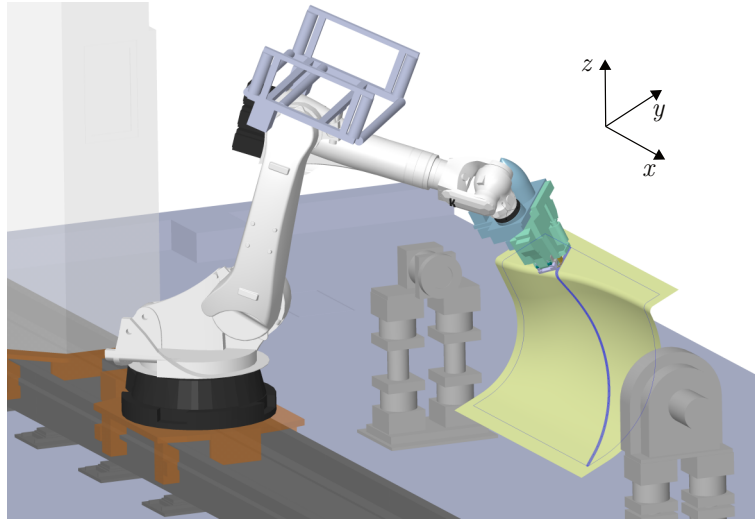
Figure 5.14: Inner fixed structure AFP manufacturing — CATFiber illustration

The length of the IFS is 2000 mm, the height is 750 mm, the curvature merges from $R480$ to $R700$, the edge radius is 40 mm, the minimum length after edge is 100 mm, and the total surface area of the part is 2.535 m^2. Further dimensions are shown in the technical drawing in Fig. A.18 of the appendix. In the use case, the most tack-sensitive lay-up situation — first-ply lay-up on a metal tool — was evaluated for the fiber directions 0 °, $+45$ °, -45 °, and 90 °. The tracks for each fiber direction were programmed using CATFiber from CORIOLIS GROUP SAS. Illustrations of the plies are shown in Fig. 5.15. In the $+45$ °, -45 °, and 90 ° plies tapes are placed over the convex edge which could lead to tape peel-off. The 0 ° and 90 ° plies are not subjected to any significant steering whereas the $+45$ ° and -45 ° plies are subjected to steering in certain areas.

To assess the steering radius, CATFiber offers a "Steering Analysis" which analyzes the local steering radius of each tape based on a discretization of the surface. Results can be highlighted visually with regard to a user defined threshold and data can be exported for quantitative analysis. Examples of the visualization for the -45 ° ply are shown in Fig. 5.16. The arbitrary steering limits underline the influence of the minimal possible steering radius on the manufacturability of the part. Lay-up defects have to be limited to a certain amount so that the mechanical properties of the cured part are not affected.

(a) 0 °

(b) +45 °

(c) −45 °

(d) 90 °
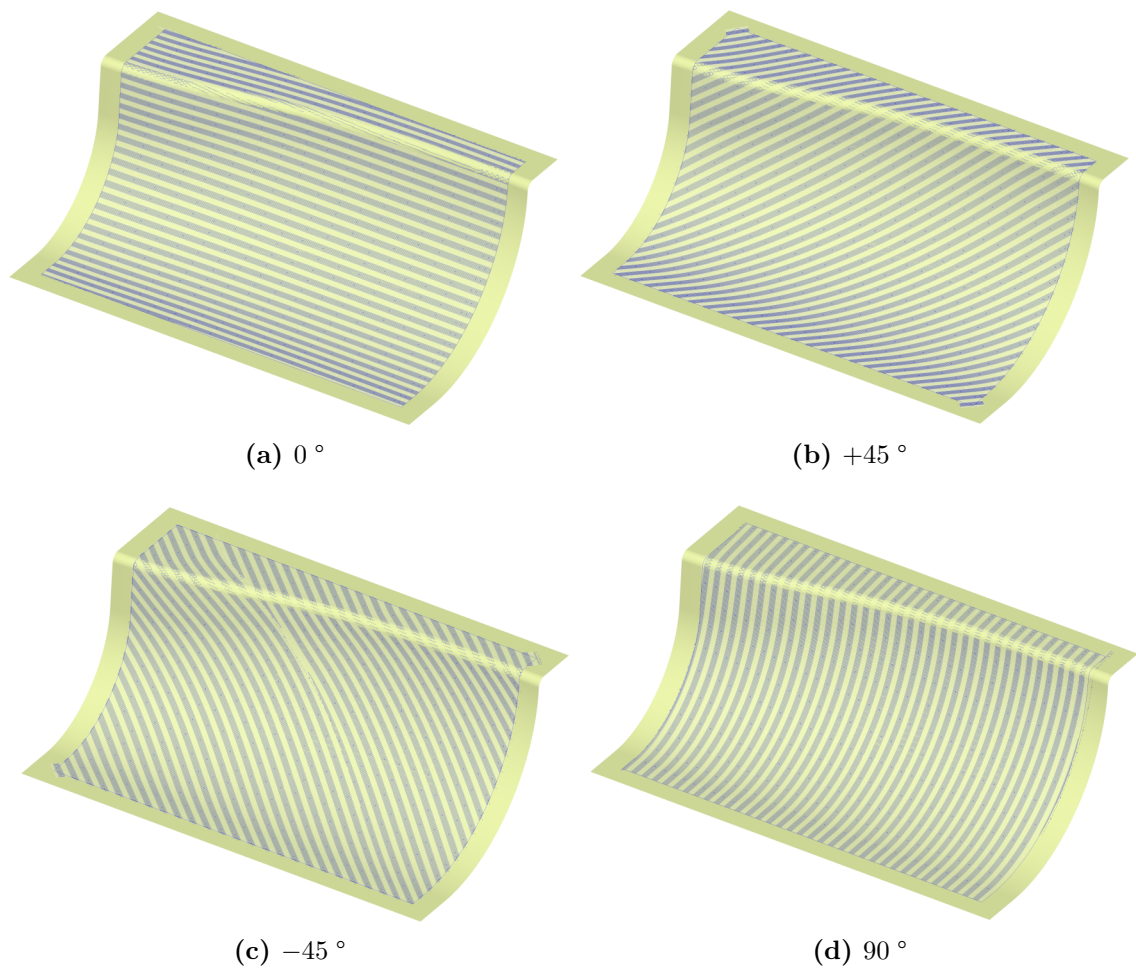
Figure 5.15: Inner fixed structure — simulated tapes in different fiber directions (tracks of eight tapes alternatingly colored in blue and white)

If it is not possible to stay below a certain steering limit, excessive defects will occur leading to scrapping of the ply or part.

The results of the parametric studies using the steering defect model and the tape peel-off model reveal that the probability of defect occurrence varies significantly as a function of out-time and material modification. Furthermore, they reveal that adjusting the process parameters is a feasible countermeasure to minimize the defect probability. To assess the consequences of material changes on the manufacturing of the IFS, the defect prediction models were used to determine the manufacturability and the lay-up time depending on the material properties.

(a) Steering limit 500 mm (b) Steering limit 700 mm

(c) Steering limit 900 mm (d) Steering limit 1100 mm
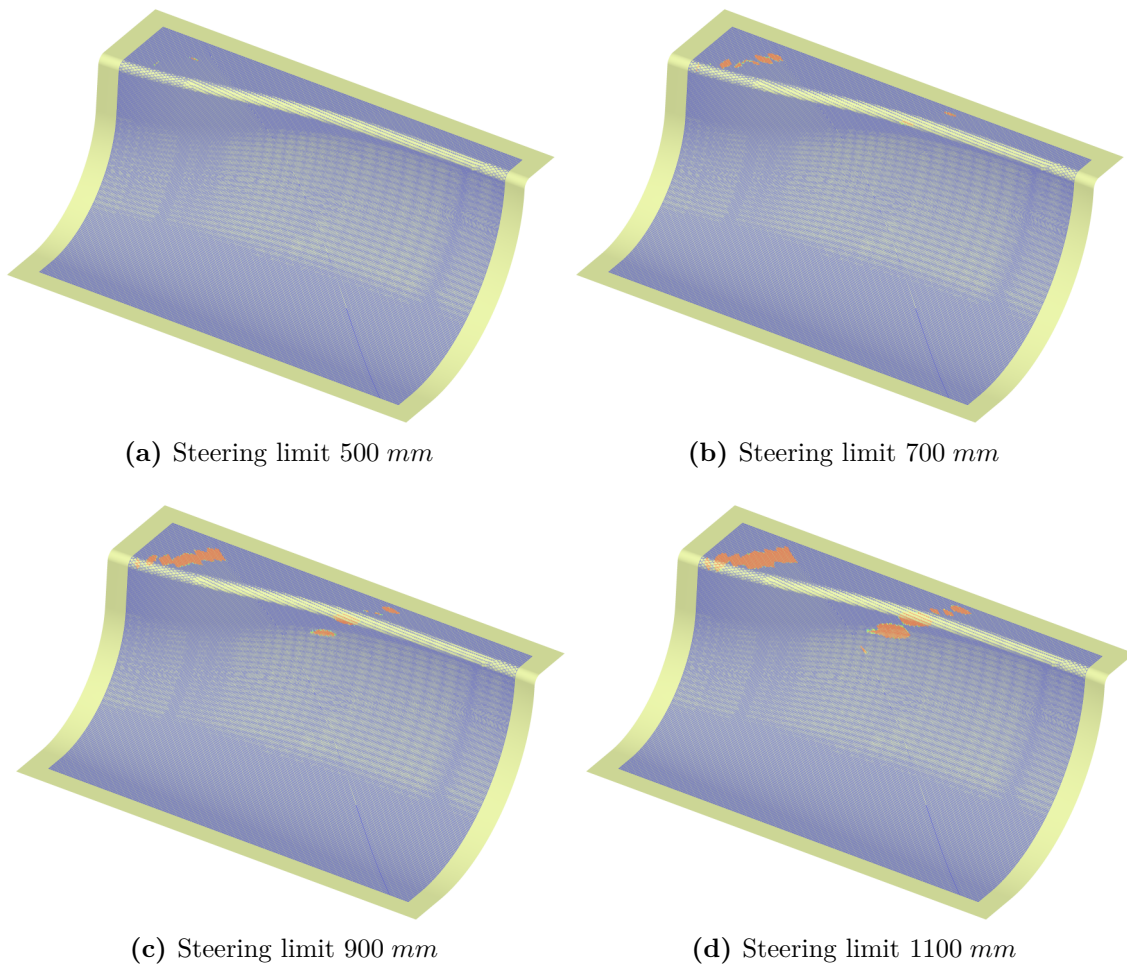
Figure 5.16: Inner fixed structure — steering analysis of simulated tapes of $-45\ °$ ply at different steering limits (blue: local steering radius above limit, red: local steering radius below limit)

5.4.2 Results

Besides avoiding defects, a principal objective during AFP manufacturing is minimizing the manufacturing time, i. e. maximizing the lay-up rate. Therefore, each fiber direction of the IFS was analyzed regarding maximum lay-up rate at which no defects occur. The limits of the process parameters were the ones of the Coriolis 1/8-TS-AFP machine — $v_{max} = 0.5\ m/s$, $F_{max} = 500\ N$, and $P_{IR,max} = 430\ W$. Using the data of the steering analysis, the minimum critical steering radius for the $+45\ °$ and $-45\ °$ plies were determined. Defining that the total defect area has to be $< 0.25\ \%$ of the total part area, the resulting critical steering radii are: $R_{crit}(+45\ °) = 1257.7\ mm$ and $R_{crit}(-45\ °) = 654.3\ mm$. The critical steering radii for $0\ °$ and $90\ °$ plies are considered infinite. As the robot movement causes

a slower lay-up rate during the lay-up on the edge, the maximum lay-up rate in the area around the edge ($A_{edge} = 0.222\ m^2$) was assessed for tape peel-off separately. To obtain peel-off results beyond the model's range of lay-up rate, the model results were extrapolated linearly as a function of lay-up rate. In the part area unaffected of peel-off, the maximum lay-up rate with regard to steering was assessed. To calculate the lay-up time per ply, the respective area was divided by the track width ($b_{track} = 8 \cdot 3.175\ mm$) and the respective lay-up rate as

$$t_{layup} = \frac{(A_{ply} - A_{edge})/b_{track}}{v_{max,steering}} + \frac{A_{edge}/b_{track}}{v_{max,peeloff}} \tag{5.24}$$

where A_{ply} is the total surface area of the ply, $v_{max,steering}$ is the maximum lay-up rate with regard to steering, and $v_{max,peeloff}$ is the maximum lay-up rate with regard to tape peel-off. The calculated lay-up time only considers the actual time when tapes are placed without considering robot movements during which no tapes are placed or other aspects of the total production time like vacuum debulking.

5.4.2.1 Out-time effects on IM7/8552

The maximum lay-up rates at which no out-of-plane buckling and no tape peel-off are expected for IM7/8552 are listed in Tab. 5.8. The process parameters compaction force and IR emitter power were set to the optimum value regarding steering based on the parametric study with the steering model — see Sec. 5.2.2.2. The study revealed that a higher compaction force leads to a lower critical steering radius at all out-times while the impact of IR emitter power depends on the out-time. The maximum lay-up rate with regard to steering $v_{max,steering}$ at the 0 ° and 90 ° plies is not affected by the out-time as the steering radii of these plies are considered infinite.

For the +45 ° plies, $v_{max,steering}$ is affected at 15 d out-time: to stay below the critical steering radius, the lay-up rate has to be lowered from 0.5 m/s to 0.21 m/s. For the −45 ° plies, the lay-up rate has to be adjusted to any out-time. At 1 d out-time, $v_{max,steering}$ is 0.2 m/s and at increasing out-times it has to be lowered down to 0.009 m/s at 15 d out-time. The maximum lay-up rate with regard to peel-off is also dependent on the out-time: while $v_{max,peeloff}$ is as high as 0.24 m/s at 5 d out-time, it has to be lowered down to 0.08 m/s at 15 d out-time to avoid tape peel-off. Yet, the results for maximum lay-up rate at 15 d out-time show that the material can still be used for all plies of the IFS even though the tack life is exceeded.

Table 5.8: Use case — maximum lay-up rate with regard to to steering and peel-off as a function of out-time of IM7/8552 material

t_{out} $[d]$	φ_{layup} $[°]$	F $[N]$	P $[W]$	$v_{max,steering}$ $[m/s]$	$v_{max,peeloff}$ $[m/s]$
	0	500	0	0.5	0.5
	+45	500	0	0.5	0.21
1	−45	500	0	0.2	0.21
	90	500	0	0.5	0.21
	0	500	0	0.5	0.5
	+45	500	0	0.5	0.24
5	−45	500	0	0.15	0.24
	90	500	0	0.5	0.23
	0	500	430	0.5	0.5
	+45	500	430	0.5	0.22
10	−45	500	430	0.06	0.22
	90	500	430	0.5	0.2
	0	500	430	0.5	0.5
	+45	500	430	0.21	0.08
15	−45	500	430	0.009	0.08
	90	500	430	0.5	0.08

Based on the results for the lay-up rate, the lay-up time was calculated using Eq. 5.24. The straightforward approach for this is using the lay-up rates from Tab. 5.8 as constant values for each ply. This leads to a steep increase in lay-up time as a function of out-time for the −45 ° ply as shown in Fig. 5.17a. Caused by the necessary lay-up rate of 0.009 m/s at 15 d out-time, the lay-up time of that ply increases by more than factor 20 compared to 1 d out-time. To reduce the lay-up time, the presented models can be used to divide the plies into areas with different critical steering radii so that the lay-up rate can be maximized for each area individually to minimize the lay-up time. For this, the critical steering radius at different lay-up rates ranging from 0.5 m/s to 0.009 m/s was calculated for the +45 ° and −45 ° plies. Using the data from the CATFiber steering analysis, the areas where the respective lay-up rate could be used was determined for each ply and out-time. Assuming that the lay-up rate is constant in each of these areas and neglecting acceleration and deceleration time, the lay-up time at higher out-times can be reduced significantly as shown in Fig. 5.17b.

Since the area with small critical steering radii is comparably small, the lay-up time can be reduced drastically at high out-times by adjusting the lay-up rate to the respective local critical steering radius.

(a) $v_{steering}$ constant for each ply   **(b)** $v_{steering}$ variable for each ply
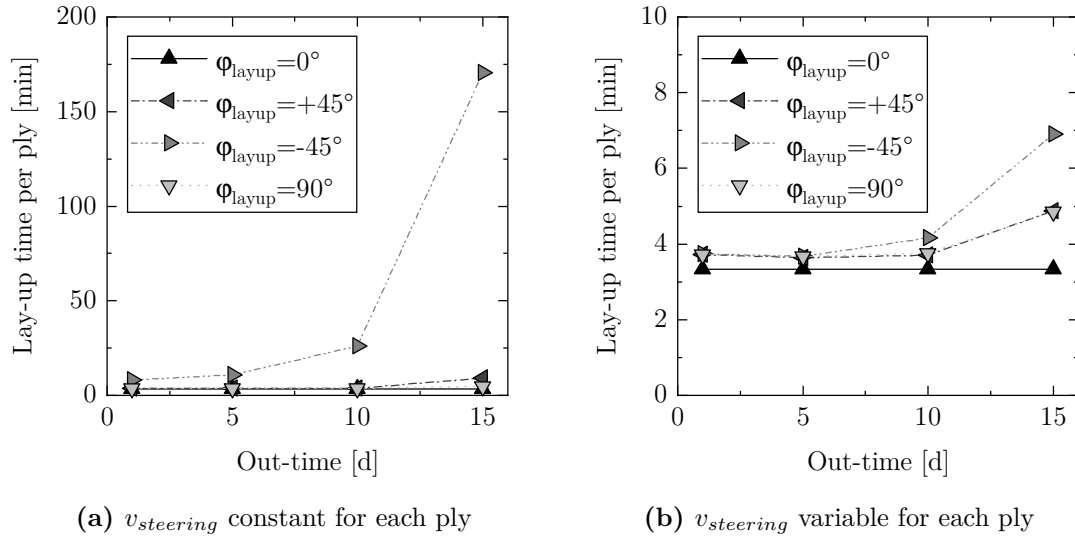
Figure 5.17: Use case — lay-up time per ply of IM7/8552

At 15 d out-time, the variable lay-up rate leads to a reduction of lay-up time for the -45 ° ply of 96 % compared to a constant lay-up rate. For the $+45$ ° ply, the reduction of lay-up time is 46 %. Besides that, Fig. 5.17b indicates that the lay-up time has to be increased to account for the out-time effects. E. g., the lay-up time for the -45 ° ply with variable lay-up rate is 3.8 *min* at 1 d out-time, 3.7 *min* at 5 d out-time, 4.2 *min* at 10 d out-time, and 6.9 *min* at 15 d out-time.

With the help of the presented results, manufacturers see that the material can still be used for all possible first plies of the IFS up to an out-time of 15 d. By optimizing the lay-up rate, the necessary increase in lay-up time at 15 d out-time can be reduced drastically compared to a constant lay-up rate for the whole ply. By that, manufacturers can decide whether they use the material with elevated out-time for the same part with adjusted lay-up rates or use it for parts with lower buckling and peel-off probability to avoid material waste.

5.4.2.2 Effects of modification

The analysis of the research materials reveals that the maximum lay-up rate of 0.5 m/s can be used for all plies of the IFS. Both materials are insensitive to out-of-plane buckling due to steering — see Sec. 5.2.2.3. For the unmodified material, tape peel-off is highly unlikely and for the modified material it is below the threshold in any configuration. To calculate the total lay-up time with the research materials, $v = 0.5\ m/s$ is used for the ply areas apart from the edge. At the edge area, the lay-up rate is set to $v = 0.25\ m/s$ since the robot movement has to be slowed down

to avoid exceeding velocity constraints of the individual robot axes regardless of the probability of tape peel-off. Using these values, the lay-up times are: 3.3 *min* for the 0 ° ply, 3.6 *min* for the −45 ° ply, 3.6 *min* for the −45 ° ply, and 3.6 *min* for the 90 ° ply. The lay-up times are slightly lower than the lay-up time for IM7/8552 at low out-times as the unmodified material's high tack and the modified material's high shear stiffness allow a higher lay-up rate.

5.4.2.3 Conclusion

Using the defect prediction models for the analysis of a real aerospace part — the aircraft nacelle inner fixed structure — emphasizes the benefit of the findings for practical applications. Combined with the analysis data from the offline programming software the defect models provide information on

- the suitability of a material for the manufacturing of a specific part,

- the constraints of a certain material regarding lay-up path complexity,

- the optimum process parameters to minimize manufacturing time while avoiding defects,

- the effects of out-time and modification and the respective optimum process parameters,

- the resulting lay-up time.

The use case with IM7/8552 at different out-times reveals that process parameters have to be adjusted to the out-time of the material. In particular at out-times greater than 5 *d*, keeping process parameters like the lay-up rate at the level of 1 *d* out-time would lead to excessive defects and therefore scrapping of the respective ply. Furthermore, the presented findings facilitate the minimization of the lay-up time by providing details on the maximum lay-up rate for distinct areas of a ply. By that, the lay-up rate can be maximized for each distinct area. In the considered case, the first-ply lay-up of a −45 ° ply on a metal surface is the most defect sensitive scenario. At this, the optimization of the lay-up rate led to a reduction in lay-up time of 96 % compared to a constant lay-up rate for the whole ply. Results obtained using the variable lay-up rate revealed that IM7/8552 can still be used for the inner fixed structure at 15 *d* out-time. The increase in lay-up time due to reduced lay-up rates for the −45 ° ply is 84 % compared to 1 *d* out-time.

The use case with the research materials demonstrates that both materials are well suited for the manufacturing of the inner fixed structure. Because of their

respective tack and shear stiffness, defects are unlikely to occur even at high lay-up rates. The modification of the material increases the probability of tape peel-off. Yet, the threshold for high probability was not exceeded in the investigated case. The lay-up time for the research material was slightly lower than the lay-up time for IM7/8552 at low out-times.

5.5 Intermediate summary

The presented chapter describes the theoretical models needed to predict the producibility of AFP parts based on the material properties obtained in the material characterization. For this, a thermal simulation was used to calculate the change in material temperature due to out-time and modification which is an input for the developed defect prediction models. To predict out-of-plane buckling due to steering, an existing model was enhanced to increase its scope and accuracy. The model enhancements include

- the determination of the position of the neutral bending axis,

- an accurate prediction of the temporal evolvement after lay-up,

- defect prediction as a function of AFP process parameters, and

- the implementation of material properties at different out-times.

Furthermore, the introduction of a conversion factor allows for the conversion between critical steering radius at which no defects occur to the estimated quantity of defects at a given steering radius. The parametric study with IM7/8552 affirms the strong influence of out-time on the critical steering radius. The results with regard to the process parameters allow for the determination of the optimum lay-up rate, IR emitter power, and compaction force at which no buckling occurs at a given out-time. By that, the suitability of a material for a part with steered paths can be evaluated and the manufacturing time can be minimized.

Parametric studies with the research materials showed that both material are less sensitive to buckling than IM7/8552 since the unmodified material has a very high tack and the modified material has a very high shear stiffness counteracting defect evolvement.

To predict tape peel-off on a convex edge, a new model was developed which is based on the difference between the strain energy due to bending and the separation energy to overcome tack. The main input parameters are the bending stiffness and the peel tack of the material, both of which were determined using

the respective newly developed test benches — see Sec. 3.3.2 and Sec. 3.5.3. The model is capable of indicating the risk of tape peel-off on a convex edge taking material properties, lay-up path, and process parameters into account. Again, increased out-time increases the defect probability and the most influential process parameter is the lay-up rate. The material modification via fillers leads to a higher risk of tape peel-off as it leads to a higher bending stiffness and a lower tack.

Applying the models to an AFP aerospace part — the aircraft nacelle inner fixed structure — reveals that IM7/8552 can be used for the part beyond its tack life of ten days. Yet, to avoid defects and to minimize the lay-up time, the process parameters have to be set accurately. Fig. 5.18 visualizes the impact of the presented defect prediction models on material usage and lay-up time.

Usually, process parameters are optimized for a material at low out-times. If the same process parameters are used for the same part at higher out-times ($\geq 10 \ d$ for IM7/8552), excessive defects occur and the material is scrapped. At the same process parameters, the material could still be used for a part with less complex paths. The limits of such less complex paths can be determined using the defect models. On the other hand, if process parameters are adjusted to the material process interaction at higher out-times, the material may still be used for the same part. The study on the inner fixed structure showed that if adjusted process parameters are used for the whole ply, the lay-up time increases significantly. In the investigated case, the lay-up time at $15 \ d$ out-time of the most critical $-45 \ °$ first-ply lay-up on a metal surface was factor 20.6 higher than the lay-up time at $1 \ d$ out-time. To reduce the lay-up time, the defect models can be used to determine local maximum lay-up rates on each ply depending on the local steering radius. With optimized process parameters the the lay-up time at $15 \ d$ out-time of the $-45 \ °$ first-ply lay-up was factor 1.8 higher than the lay-up time at $1 \ d$ out-time indicating that the material can still be used at $15 \ d$ out-time with moderate increase in lay-up time.
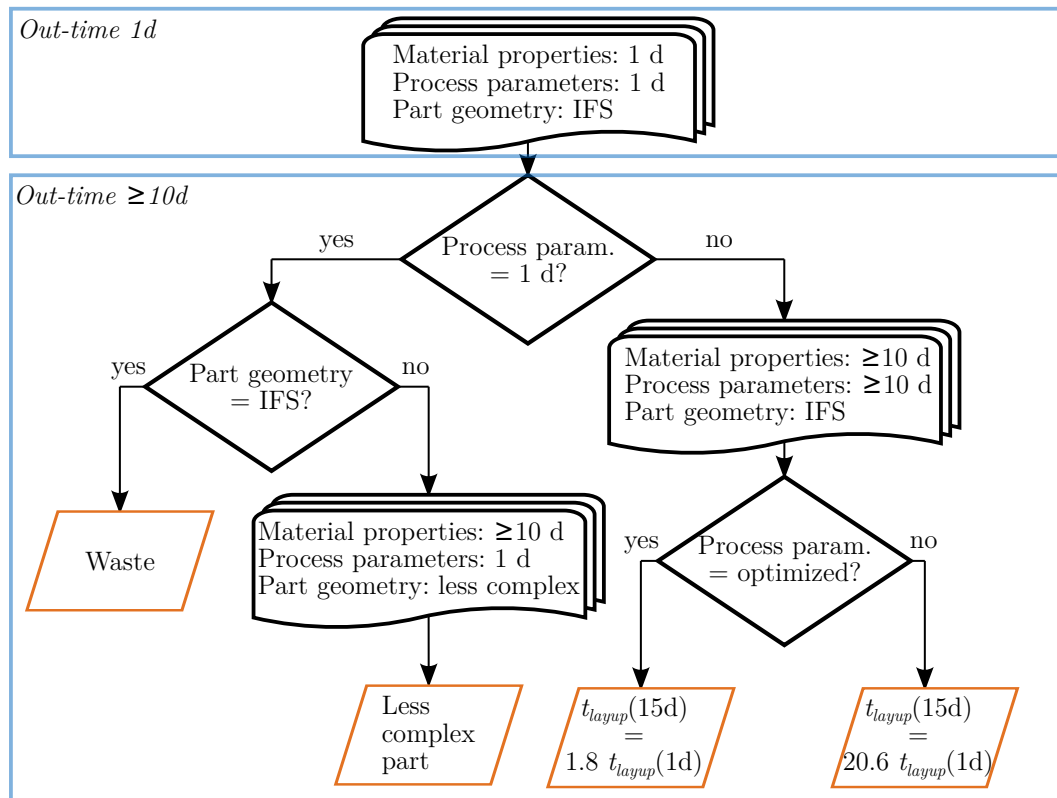
Figure 5.18: Simplified flowchart of material utilization during AFP manufacturing for the $-45\,°$ first-ply lay-up on a metal surface of the inner fixed structure (IFS: inner fixed structure, t_{layup}: lay-up time)

6 Conclusions and future work

A resource-efficient thermoset automated fiber placement (TS-AFP) manufacturing can only be achieved with profound knowledge of the prepreg material properties and their implications on the material process interaction. To reduce waste, minimize manufacturing time, and ease the development of new materials, the influences of material property changes on TS-AFP processing are investigated within the presented thesis. The methodology includes material characterization, lay-up experiments, and analytical defect prediction models. The main findings and the recommendations for future work are summarized in the following sections.

6.1 Conclusions

The basis of the presented work is the material characterization of prepreg in the uncured state which is the relevant state for TS-AFP processing. Since there are no test standards for most of the uncured prepreg properties, a *prepreg characterization procedure* was developed which takes all key properties affecting the material process interaction into account. The characterization procedure includes results from test method comparisons — e. g. for the in-plane shear modulus — as well as from the development of new test methods — i. e. for the peel tack and the bending stiffness. To analyze the tack of aerospace grade prepreg tapes, a new peel tack test method and test bench was developed. The test method allows for the reliable measurement of prepreg peel tack and comprises unprecedented capabilities such as: decoupling of deposition rate and peel rate, possibility to prepare specimens with AFP machine, possibility to measure at different times after deposition. The *prepreg characterization procedure*, which includes test methods for cure-related, tack, thermal, and mechanical properties, was used to quantify the affects of material changes due to storage at room temperature (out-time) and due to material modification via fillers. Both out-time and modification lead to a reduction in tack and an increase in mechanical properties and thermal conductivity. E. g., the peel tack decreases monotonously up to 100 % from 1 d to 15 d out-time and it decreases by an average of 79 % due to the presence of 15 $vol\%$ graphite fillers in the matrix. The in-plane shear modulus increases up to factor 3 from 1 d to 15 d out-time and

it increases up to factor 8.9 due to the modification via fillers. The temperature is the most influential test parameter for most properties which is explained by the viscoelastic behavior of the prepregs.

To quantify the impact of material property changes on AFP processing, a series of *lay-up experiments* was conducted. The experiments include the lay-up on concave and convex tool geometries as well as non-geodesic lay-up (steering) on a flat tool at different out-times with varying process parameters. The material's out-time has a strong effect on the steering defects out-of-plane buckling and tape pull-up because of the decrease in tack. Above the material's tack life of ten days, the defects increase significantly while some tapes did not adhere at all at high lay-up rate and low heat input. From $1\,d$ to $15\,d$ out-time the defect increase is between factor 5.2 and factor 13.3 depending on the process parameters. The most feasible countermeasure is a reduction in lay-up rate which affects the material temperature and the time of intimate contact. Similar results were obtained for tape peel-off on a convex edge where the averaged amount of defects increases by factor 16 from $1\,d$ to $15\,d$ out-time. In contrast, results for bridging on a concave edge do not reveal any out-time dependence. At the concave edge, the trajectory is geodesic before and after the edge reducing the sensitivity to a lower tack.

Using the novel peel tack test method at the same out-times and process parameters as the steering experiments provides insights on the correlation between steering defects and peel tack: there is a guide value of peel tack ($3.5\,mN/mm$ for HexPly IM7/8552 prepreg) below which the out-of-plane buckling increases significantly. This value can be used to assess the lay-up behavior of a material without doing lay-up experiments and it is a reference for the development of new materials.

The results of the material characterization and the lay-up experiments were both used as inputs for analytical *defect prediction models* to predict AFP lay-up defects. The developed *defect prediction model* for out-of-plane buckling during steering is based on an existing analytical model which was enhanced with regard to accuracy and capability of representing material property changes and process parameter influences. Due to the enhancements, the model is capable of predicting the defect probability as a function of steering radius, out-time, material modification, and AFP process parameters. By that, process parameters can be optimized with regard to given boundary conditions like lay-up trajectory and material condition.

For the tape peel-off on a convex edge, a new *defect prediction model* was developed which uses material properties from the newly developed peel tack and bending stiffness test methods as inputs. The comparison of the strain energy due

to bending to the separation energy needed to overcome the tack allows for the prediction of the probability of tape peel-off. Input variables of the model are the trajectory, the edge geometry, the out-time, the material modification, and the AFP process parameters.

The two defect prediction models were combined to assess an aerospace part currently being produced via TS-AFP — the aircraft nacelle inner fixed structure (IFS). The analysis of the IFS with a quasi-isotropic lay-up reveals that the reference material IM7/8552 can be used for the part manufacturing even after exceeding its tack life of ten days. The use case demonstrates an increase in out-time of 50 % during which the material can still be processed indicating a high potential for waste reduction. Furthermore, the models can be used to optimize the process parameters within each ply with regard to the local trajectory and the material condition. In the investigated case, the lay-up time at 15 d out-time can be reduced by 96 % for the most critical ply compared to the lay-up time at constant process parameters for the whole ply. Besides the out-time effects, the models enabled the evaluation of new research materials with and without modification via fillers. The assessment reveals that both materials are suitable for the manufacturing of the IFS. The defect probability increases due to the fillers since tack and bending stiffness increase. Yet, the modified material can still be processed at high lay-up rate during manufacturing of the IFS.

The presented use case demonstrates that using the *prepreg characterization procedure* and the *defect prediction models* allows for the assessment of new materials with regard to AFP production parts without doing lay-up experiments realizing a resource-efficient development of new prepregs. The models also enable the evaluation of new parts with given material properties.

6.2 Future work

The *prepreg characterization procedure* serves as a framework for future prepreg characterization. Prospective applications range from new materials — e. g. with different fillers — to refining and extending the range of test parameters. Besides slit-tapes, the characterization methods are suitable for towpregs (pre-impregnated rovings) which are currently used in filament winding and which show potential for the use in AFP. Other fields of application include fiber patch placement (FPP), where pre-impregnated spread tow patches are processed, as well as conventional hand lay-up manufacturing. Both the material characterization and the *lay-up experiments* were based on the first-ply lay-up on an aluminium substrate which is the most defect-sensitive case because of the adhesion between tape and aluminium

surface. To investigate other substrate options like release films or previously laid prepreg tapes, the developed test methods can be adapted to the respective case. With minor modifications of the peel tack test bench, even non-rigid or open surface substrates like honeycomb cores can be investigated opening up a wide range of applications for the test methods.

The presented *defect prediction models* represent a primary basis for the defect prediction during TS-AFP. As the model for out-of-plane buckling during steering was enhanced based on the *lay-up experiments*, future work can focus on the refinement of the model assumptions and boundary conditions so that empiric adjustments can be minimized. Out-of-plane buckling is considered rate dependent. Yet, the debonding rate during buckling is not yet fully understood. Hence, future studies can focus on determining the debonding rate and identifying if current test methods are capable of replicating said debonding rate. The steering defect tape pull-up is still a sparsely studied defect and has not yet been addressed in defect prediction models. Therefore, the development of a tape pull-up model is another possible field of activity. As the defect seems to occur after exceeding a certain threshold of steering radius at given material properties and process parameters, the model can be expressed as a buckling problem similar to the out-of-plane buckling. The newly developed model for tape peel-off on a convex edge comprises an empirical factor for the plastic deformation of the tape during bending. To verify the model assumptions, future work should aim at quantifying the degree of plastic deformation during lay-up on a convex edge. This work includes experimental characterization as well as developing a model that accounts for the deformation based on the material condition, lay-up path, and process parameters determining deformation rate and temperature.

Besides the analytical models, the presented results have the potential to serve as inputs for numerical models predicting AFP lay-up defects. Material characterization results for IM7/8552 may be used directly as input parameters. Furthermore, the presented out-time and modification-dependent property changes may serve as a reference for the influence of property changes of other prepreg materials. The results on the property changes are not only adjuvant for defect prediction models but also during current AFP production. By comparing a materials out-time or glass transition temperature to the presented findings, manufacturers can estimate the suitability of the material for the lay-up with a given lay-up path.

A Appendix

A.1 Material characterization

A.1.1 Process parameters

The results from AFP temperature measurements using thermocouples on the substrate are listed in Tab. A.1.

Table A.1: Results from AFP temperature measurements

v $[m/s]$	P_{IR} $[W]$	T mean $[°C]$	T std. dev. $[°C]$
0.03	150	26.253	1.745
0.03	350	39.002	4.179
0.06	150	25.545	0.962
0.06	350	34.319	2.879
0.10	150	24.762	0.839
0.10	350	31.310	2.113

A.1.2 Probe tack

The following tables Tab. A.2, Tab. A.3, and Tab. A.4 provide detailed results of the probe tack measurements with IM7/8552.

Table A.2: Maximum force per probe area of IM7/8552

T [$°C$]	v_{probe} [mm/s]	t_{out} [d]	Mean [N/mm^2]	Std. dev. [N/mm^2]	Min. [N/mm^2]	Max. [N/mm^2]
20	0.02	1	0.084	0.031	0.038	0.135
20	0.2	1	0.112	0.015	0.090	0.128
20	2	1	0.111	0.044	0.051	0.188
40	0.02	1	0.058	0.012	0.047	0.084
40	0.2	1	0.121	0.023	0.087	0.158
40	2	1	0.213	0.041	0.159	0.271
20	0.02	5	0.066	0.030	0.025	0.110
20	0.2	5	0.092	0.034	0.034	0.139
20	2	5	0.062	0.024	0.032	0.100
40	0.02	5	0.052	0.014	0.029	0.071
40	0.2	5	0.137	0.034	0.102	0.197
40	2	5	0.196	0.029	0.169	0.254
20	0.02	10	0.000	0.000	0.000	0.000
20	0.2	10	0.000	0.000	0.000	0.000
20	2	10	0.015	0.022	0.000	0.054
40	0.02	10	0.039	0.017	0.007	0.060
40	0.2	10	0.120	0.021	0.100	0.154
40	2	10	0.187	0.052	0.105	0.260
20	0.02	15	0.000	0.000	0.000	0.000
20	0.2	15	0.006	0.011	0.000	0.030
20	2	15	0.000	0.000	0.000	0.000
40	0.02	15	0.060	0.013	0.032	0.070
40	0.2	15	0.132	0.031	0.082	0.181
40	2	15	0.167	0.040	0.115	0.220

Table A.3: Work of adhesion per probe area of IM7/8552

T [°C]	v_{probe} [mm/s]	t_{out} [d]	Mean [$\mu J/mm^2$]	Std. dev. [$\mu J/mm^2$]	Min. [$\mu J/mm^2$]	Max. [$\mu J/mm^2$]
20	0.02	1	0.521	0.236	0.109	0.835
20	0.2	1	0.627	0.284	0.190	0.960
20	2	1	0.765	0.390	0.226	1.289
40	0.02	1	1.701	0.665	0.953	2.667
40	0.2	1	2.482	0.696	1.093	3.166
40	2	1	5.340	2.761	2.576	10.675
20	0.02	5	0.353	0.307	0.041	0.894
20	0.2	5	0.472	0.273	0.066	0.832
20	2	5	0.310	0.196	0.069	0.684
40	0.02	5	1.130	0.417	0.598	1.914
40	0.2	5	3.404	1.495	1.441	5.162
40	2	5	3.886	0.972	2.341	5.586
20	0.02	10	0.000	0.000	0.000	0.000
20	0.2	10	0.000	0.000	0.000	0.000
20	2	10	0.074	0.106	0.000	0.237
40	0.02	10	0.524	0.268	0.112	1.017
40	0.2	10	1.706	0.456	1.145	2.546
40	2	10	3.525	1.635	1.750	6.633
20	0.02	15	0.000	0.000	0.000	0.000
20	0.2	15	0.247	0.488	0.000	1.332
20	2	15	0.000	0.000	0.000	0.000
40	0.02	15	0.794	0.226	0.323	1.052
40	0.2	15	1.581	0.909	0.555	3.433
40	2	15	2.583	1.465	1.158	4.932

Table A.4: Tack stiffness per probe area of IM7/8552

T [$°C$]	v_{probe} [mm/s]	t_{out} [d]	Mean [N/mm^3]	Std. dev. [N/mm^3]	Min. [N/mm^3]	Max. [N/mm^3]
20	0.02	1	14.183	1.595	12.389	16.842
20	0.2	1	21.882	5.460	15.024	29.838
20	2	1	20.637	3.136	17.032	25.851
40	0.02	1	8.566	2.683	5.926	13.928
40	0.2	1	13.387	1.679	10.808	16.000
40	2	1	16.248	1.261	14.314	18.039
20	0.02	5	18.211	7.038	11.315	29.746
20	0.2	5	21.708	4.505	17.157	30.415
20	2	5	17.708	3.377	11.768	21.950
40	0.02	5	8.439	1.713	4.854	10.095
40	0.2	5	16.901	2.789	11.000	19.690
40	2	5	14.192	1.938	11.404	16.937
20	0.02	10	0.000	0.000	0.000	0.000
20	0.2	10	0.000	0.000	0.000	0.000
20	2	10	4.901	7.167	0.000	17.863
40	0.02	10	8.446	1.940	5.279	11.309
40	0.2	10	12.171	1.450	10.020	13.968
40	2	10	13.945	3.493	8.727	19.051
20	0.02	15	0.000	0.000	0.000	0.000
20	0.2	15	1.690	3.760	0.000	10.098
20	2	15	0.000	0.000	0.000	0.000
40	0.02	15	11.333	2.277	8.075	14.040
40	0.2	15	14.330	1.842	12.078	17.038
40	2	15	18.778	4.238	10.532	23.077

A.1.3 Peel tack

Tab. A.5 and Tab. A.6 detail the results of the peel tack measurements with IM7/8552.

Table A.5: Peel tack per width of IM7/8552 (part one)

v [m/s]	F [N]	P_{IR} [W]	t_{out} [d]	Mean [mN/mm]	Std. dev. [mN/mm]	Min. [mN/mm]	Max. [mN/mm]
0.03	200	150	1	11.355	3.531	5.817	14.402
0.03	400	150	1	9.350	4.713	3.331	13.621
0.03	200	350	1	13.595	7.492	5.910	26.550
0.03	400	350	1	12.699	5.097	5.024	19.381
0.06	200	150	1	4.026	2.690	1.297	8.052
0.06	400	150	1	4.764	2.745	1.205	8.989
0.06	200	350	1	10.900	1.757	8.075	12.487
0.06	400	350	1	8.587	3.594	2.194	12.340
0.1	200	150	1	6.540	1.311	4.851	8.808
0.1	400	150	1	5.656	2.061	2.885	8.790
0.1	200	350	1	6.434	2.522	2.845	9.472
0.1	400	350	1	8.110	3.056	3.646	11.823
0.03	200	150	5	4.818	1.291	3.176	7.031
0.03	400	150	5	4.200	2.109	0.613	6.737
0.03	200	350	5	4.163	2.207	1.683	7.429
0.03	400	350	5	4.664	1.551	1.868	6.296
0.06	200	150	5	3.857	1.291	2.187	5.872
0.06	400	150	5	3.491	1.541	1.677	5.388
0.06	200	350	5	3.981	1.499	1.200	5.244
0.06	400	350	5	6.443	0.611	5.578	7.156
0.1	200	150	5	4.080	0.863	2.858	5.429
0.1	400	150	5	4.304	0.571	3.517	5.081
0.1	200	350	5	3.094	0.460	2.401	3.623
0.1	400	350	5	3.281	1.567	0.735	5.659
0.03	200	150	10	3.398	1.745	1.328	5.835
0.03	400	150	10	1.822	0.290	1.249	2.044
0.03	200	350	10	2.961	1.105	1.678	4.280
0.03	400	350	10	1.956	1.056	0.084	3.049

Table A.6: Peel tack per width of IM7/8552 (part two)

v [m/s]	F [N]	P_{IR} [W]	t_{out} [d]	Mean [mN/mm]	Std. dev. [mN/mm]	Min. [mN/mm]	Max. [mN/mm]
0.06	200	150	10	2.936	1.073	1.124	4.038
0.06	400	150	10	3.193	0.797	2.332	4.280
0.06	200	350	10	2.595	1.351	0.468	4.352
0.06	400	350	10	3.090	1.789	0.204	5.438
0.1	200	150	10	4.215	1.445	2.293	6.625
0.1	400	150	10	3.741	2.029	0	6.001
0.1	200	350	10	3.329	1.879	0	5.369
0.1	400	350	10	1.618	1.891	0	5.011
0.03	200	150	15	0	0	0	0
0.03	400	150	15	3.448	4.704	0	12.379
0.03	200	350	15	2.096	1.699	0	4.124
0.03	400	350	15	1.645	3.289	0	8.224
0.06	200	150	15	2.500	3.105	0	7.065
0.06	400	150	15	1.656	2.867	0	7.344
0.06	200	350	15	0.924	1.206	0	2.969
0.06	400	350	15	1.377	1.810	0	4.482
0.1	200	150	15	0	0	0	0
0.1	400	150	15	0	0	0	0
0.1	200	350	15	0	0	0	0
0.1	400	350	15	0	0	0	0

A.1.4 Thermal conductivity

Details for the specimen density, specific heat capacity, thermal diffusivity, and resulting thermal conductivity for IM7/8552 are given in Tab. A.7 and Tab. A.8. Details for the research materials are given in Tab. A.9.

Table A.7: Thermal conductivity in thickness direction of IM7/8552 — specimen density, specific heat capacity, thermal diffusivity, resulting thermal conductivity (part one)

t_{out} [d]	T [°C]	ρ [g/cm³]	c_p [J/gK]	α_{diff} [mm²/s]	k_3 [W/mK]
1	21.8	1.489	1.028	0.302	0.462
1	21.7	1.517	1.028	0.31	0.484
1	21.8	1.568	1.028	0.274	0.442
1	21.4	1.566	1.027	0.273	0.439
1	21.3	1.558	1.027	0.273	0.437
1	40.5	1.513	1.089	0.301	0.496
1	41.0	1.493	1.091	0.297	0.484
1	42.6	1.498	1.098	0.281	0.462
1	41.6	1.493	1.094	0.297	0.485
5	41.3	1.440	1.096	0.318	0.502
5	41.6	1.489	1.098	0.296	0.484
5	39.2	1.487	1.089	0.304	0.492
5	21.0	1.509	1.025	0.308	0.476
5	19.9	1.495	1.022	0.301	0.460
5	19.4	1.495	1.021	0.31	0.473
5	21.8	1.482	1.028	0.313	0.477
5	21.5	1.484	1.027	0.323	0.492
5	39.9	1.512	1.091	0.308	0.508
5	44.4	1.481	1.109	0.309	0.507
10	21.6	1.475	1.030	0.329	0.500
10	21.9	1.480	1.031	0.32	0.488
10	21.4	1.460	1.029	0.327	0.491
10	20.9	1.426	1.028	0.348	0.510
10	21.5	1.524	1.029	0.312	0.489
10	40.5	1.502	1.095	0.322	0.530
10	42.8	1.473	1.104	0.319	0.519
10	42.3	1.463	1.102	0.315	0.508
10	40.4	1.474	1.094	0.31	0.500
10	42.4	1.507	1.102	0.306	0.508

Table A.8: Thermal conductivity in thickness direction of IM7/8552 — specimen density, specific heat capacity, thermal diffusivity, resulting thermal conductivity (part two)

t_{out} [d]	T [°C]	ρ [g/cm³]	c_p [J/gK]	α_{diff} [mm²/s]	k_3 [W/mK]
15	21.6	1.574	1.028	0.292	0.473
15	21.7	1.572	1.029	0.294	0.476
15	21.3	1.481	1.027	0.327	0.497
15	21.1	1.485	1.026	0.328	0.500
15	21.0	1.474	1.025	0.347	0.525
15	41.6	1.506	1.098	0.305	0.504
15	40.5	1.479	1.093	0.32	0.517
15	42.5	1.485	1.101	0.31	0.507
15	41.8	1.500	1.099	0.306	0.504
15	40.5	1.442	1.093	0.339	0.535

Table A.9: Thermal conductivity in thickness direction of the research materials — specimen density, specific heat capacity, thermal diffusivity, resulting thermal conductivity

Material	T [°C]	ρ [g/cm³]	c_p [J/gK]	α_{diff} [mm²/s]	k_3 [W/mK]
Unmodified	20.8	1.355	1.183	0.206	0.330
Unmodified	21.9	1.284	1.187	0.259	0.395
Unmodified	21.9	1.372	1.187	0.259	0.422
Unmodified	22.0	1.368	1.187	0.202	0.328
Unmodified	22.0	1.300	1.187	0.285	0.440
Unmodified	40.9	1.325	1.253	0.231	0.383
Unmodified	42.2	1.351	1.258	0.234	0.398
Unmodified	43.0	1.312	1.261	0.241	0.399
Unmodified	43.3	1.282	1.263	0.239	0.387
Unmodified	44.1	1.309	1.266	0.24	0.398
Modified	21.9	1.372	1.111	0.543	0.828
Modified	21.9	1.378	1.111	0.504	0.772
Modified	21.9	1.382	1.111	0.496	0.762
Modified	22.0	1.371	1.111	0.498	0.759
Modified	22.0	1.401	1.111	0.498	0.775
Modified	40.3	1.369	1.189	0.462	0.752
Modified	40.9	1.331	1.192	0.504	0.800
Modified	41.6	1.362	1.196	0.45	0.733
Modified	42.1	1.353	1.198	0.49	0.794
Modified	42.9	1.379	1.201	0.474	0.785

A.1.5 Transverse tensile modulus

The results for the transverse tensile modulus of IM7/8552 including standard deviation, minima, and maxima are listed in Tab. A.10.

Table A.10: Transverse tensile modulus of IM7/8552

T [$°C$]	$\dot{F}$ [N/min]	t_{out} [d]	Mean [MPa]	Std. dev. [MPa]	Min. [MPa]	Max. [MPa]
20	0.05	1	0.499	0.073	0.394	0.580
20	0.1	1	0.593	0.055	0.511	0.679
40	0.05	1	0.138	0.016	0.121	0.162
40	0.1	1	0.147	0.023	0.114	0.176
20	0.05	5	0.521	0.058	0.450	0.617
20	0.1	5	0.628	0.064	0.506	0.681
40	0.05	5	0.104	0.013	0.090	0.125
40	0.1	5	0.151	0.023	0.117	0.189
20	0.05	10	0.980	0.154	0.818	1.236
20	0.1	10	0.955	0.086	0.873	1.112
40	0.05	10	0.147	0.011	0.135	0.163
40	0.1	10	0.158	0.010	0.146	0.175
20	0.05	15	1.668	0.166	1.417	1.890
20	0.1	15	1.929	0.102	1.796	2.102
40	0.05	15	0.159	0.040	0.105	0.214
40	0.1	15	0.254	0.041	0.191	0.312

A.2 Experimental investigations on AFP lay-up defects

A.2.1 Investigation on temporal defect evolvement

Tables Tab. A.11–Tab. A.17 provide detailed information on the temporal buckle and pull-up evolvement analyzed in the steering investigations.

Table A.11: Steering investigation on temporal defect evolvement — buckling and pull-up results (excluding non-adhering tapes) (part one)

						Buckle		Pull-up	
t_{out} [d]	v [m/s]	F [N]	P_{IR} [W]	R [mm]	t_{after} [min]	Mean [%]	Std. dev. [%]	Mean [%]	Std. dev. [%]
1	0.03	200	150	400	1.5	3.067	1.566	73.588	19.419
1	0.03	200	150	400	5	5.596	2.517	81.829	9.086
1	0.03	200	150	400	10	6.464	2.773	81.245	10.543
1	0.03	200	150	400	20	7.036	2.835	81.692	9.685
1	0.03	200	150	400	40	8.082	3.434	81.673	10.136
1	0.06	400	150	400	1.5	4.378	4.234	64.509	9.303
1	0.06	400	150	400	5	6.147	4.342	65.376	9.938
1	0.06	400	150	400	10	7.303	4.791	65.175	10.072
1	0.06	400	150	400	20	8.626	4.722	65.391	9.986
1	0.06	400	150	400	40	9.855	4.506	69.222	8.062
1	0.06	200	150	600	1.5	2.394	3.180	50.091	20.492
1	0.06	200	150	600	5	3.076	3.345	52.222	19.486
1	0.06	200	150	600	10	4.549	3.183	52.935	18.568
1	0.06	200	150	600	20	5.518	3.954	53.281	18.438
1	0.06	200	150	600	40	6.694	4.080	53.176	18.512
1	0.03	400	150	800	1.5	2.010	0.990	0.000	0.000
1	0.03	400	150	800	5	3.296	1.087	0.000	0.000
1	0.03	400	150	800	10	4.305	0.891	0.000	0.000
1	0.03	400	150	800	20	5.124	1.649	0.000	0.000
1	0.03	400	150	800	40	6.016	2.102	0.000	0.000
1	0.1	200	150	600	1.5	1.817	1.580	61.765	14.612
1	0.1	200	150	600	5	3.784	2.501	63.588	15.454
1	0.1	200	150	600	10	5.127	2.598	64.234	15.685
1	0.1	200	150	600	20	5.581	3.015	65.585	13.596
1	0.1	200	150	600	40	6.765	3.425	65.154	13.636
1	0.1	400	150	800	1.5	4.335	3.118	0.000	0.000
1	0.1	400	150	800	5	5.798	3.300	6.914	13.829
1	0.1	400	150	800	10	7.792	4.825	6.766	13.533

Table A.12: Steering investigation on temporal defect evolvement — buckling and pull-up results (excluding non-adhering tapes) (part two)

						Buckle		Pull-up	
t_{out} [d]	v [m/s]	F [N]	P_{IR} [W]	R [mm]	t_{after} [min]	Mean [%]	Std. dev. [%]	Mean [%]	Std. dev. [%]
1	0.1	400	150	800	20	8.698	4.532	6.736	13.473
1	0.1	400	150	800	40	9.684	4.959	6.869	13.738
1	0.1	200	350	800	1.5	4.014	4.006	8.008	16.016
1	0.1	200	350	800	5	6.114	4.813	7.899	15.799
1	0.1	200	350	800	10	6.804	5.246	8.025	16.051
1	0.1	200	350	800	20	7.640	5.434	7.773	15.545
1	0.1	200	350	800	40	8.978	6.248	7.736	15.473
1	0.1	400	350	400	1.5	4.930	2.678	59.725	10.546
1	0.1	400	350	400	5	6.096	3.990	63.384	14.330
1	0.1	400	350	400	10	9.062	5.346	63.082	14.597
1	0.1	400	350	400	20	10.109	5.729	62.968	14.694
1	0.1	400	350	400	40	11.462	5.853	63.456	15.042
1	0.06	200	350	800	1.5	1.919	0.708	0.000	0.000
1	0.06	200	350	800	5	3.233	1.200	4.146	8.293
1	0.06	200	350	800	10	4.089	1.744	4.146	8.293
1	0.06	200	350	800	20	4.813	2.178	4.146	8.293
1	0.06	200	350	800	40	5.058	2.392	4.146	8.293
1	0.03	200	350	400	1.5	3.331	2.045	50.439	29.999
1	0.03	200	350	400	5	4.340	2.709	50.493	30.022
1	0.03	200	350	400	10	6.200	2.845	54.557	17.495
1	0.03	200	350	400	20	7.356	3.734	54.805	17.220
1	0.03	200	350	400	40	7.883	4.019	54.377	17.492
1	0.03	400	350	600	1.5	0.488	0.657	4.064	8.128
1	0.03	400	350	600	5	0.910	1.079	6.541	13.081
1	0.03	400	350	600	10	0.831	0.933	6.541	13.081
1	0.03	400	350	600	20	1.799	1.454	11.641	14.438
1	0.03	400	350	600	40	2.006	1.394	11.641	14.438
1	0.06	400	350	600	1.5	1.544	1.551	0.000	0.000
1	0.06	400	350	600	5	2.066	2.017	0.000	0.000
1	0.06	400	350	600	10	2.917	2.338	9.778	19.557
1	0.06	400	350	600	20	3.808	2.921	9.778	19.557
1	0.06	400	350	600	40	5.336	5.132	9.778	19.557
5	0.03	200	150	400	1.5	2.026	2.768	71.321	8.038
5	0.03	200	150	400	5	3.173	3.794	58.272	29.621
5	0.03	200	150	400	10	3.296	3.608	57.771	29.220
5	0.03	200	150	400	20	4.423	3.961	75.053	7.595

Table A.13: Steering investigation on temporal defect evolvement — buckling and pull-up results (excluding non-adhering tapes) (part three)

| | | | | | | Buckle | | Pull-up | |
| t_{out} | v | F | P_{IR} | R | t_{after} | Mean | Std. dev. | Mean | Std. dev. |
$[d]$	$[m/s]$	$[N]$	$[W]$	$[mm]$	$[min]$	$[\%]$	$[\%]$	$[\%]$	$[\%]$
5	0.03	200	150	400	40	5.698	3.843	76.576	6.279
5	0.06	400	150	400	1.5	1.099	0.828	57.295	16.154
5	0.06	400	150	400	5	2.261	2.148	57.533	15.489
5	0.06	400	150	400	10	2.817	2.475	60.509	11.238
5	0.06	400	150	400	20	3.306	2.749	65.859	6.158
5	0.06	400	150	400	40	3.500	2.799	66.594	6.073
5	0.06	200	150	600	1.5	0.993	0.493	41.874	7.761
5	0.06	200	150	600	5	2.107	1.915	45.577	9.657
5	0.06	200	150	600	10	2.660	2.163	45.638	9.329
5	0.06	200	150	600	20	3.364	2.864	45.603	9.870
5	0.06	200	150	600	40	4.002	3.011	45.557	9.004
5	0.03	400	150	800	1.5	0.725	0.892	0.000	0.000
5	0.03	400	150	800	5	1.164	1.261	0.000	0.000
5	0.03	400	150	800	10	1.988	2.048	0.000	0.000
5	0.03	400	150	800	20	2.715	1.990	0.000	0.000
5	0.03	400	150	800	40	3.402	2.602	0.000	0.000
5	0.1	200	150	600	1.5	3.590	2.654	36.869	35.009
5	0.1	200	150	600	5	4.312	3.194	47.846	30.380
5	0.1	200	150	600	10	5.365	3.750	52.903	18.762
5	0.1	200	150	600	20	6.337	3.436	55.817	19.498
5	0.1	200	150	600	40	6.730	3.832	56.212	20.298
5	0.1	400	150	800	1.5	2.453	2.230	0.000	0.000
5	0.1	400	150	800	5	4.185	3.111	0.000	0.000
5	0.1	400	150	800	10	5.086	3.192	0.000	0.000
5	0.1	400	150	800	20	5.935	3.660	0.000	0.000
5	0.1	400	150	800	40	6.416	3.887	0.000	0.000
5	0.1	200	350	800	1.5	4.176	3.060	32.720	40.501
5	0.1	200	350	800	5	5.220	3.342	32.438	40.024
5	0.1	200	350	800	10	5.457	3.524	32.432	40.019
5	0.1	200	350	800	20	6.030	3.960	32.432	40.019
5	0.1	200	350	800	40	6.805	4.395	33.498	41.553
5	0.1	400	350	400	1.5	9.591	6.862	73.564	7.434
5	0.1	400	350	400	5	12.064	8.216	74.229	8.719
5	0.1	400	350	400	10	13.939	8.690	74.961	8.886
5	0.1	400	350	400	20	14.857	9.094	76.227	10.290
5	0.1	400	350	400	40	15.865	9.752	78.651	11.645

Table A.14: Steering investigation on temporal defect evolvement — buckling and pull-up results (excluding non-adhering tapes) (part four)

						Buckle		Pull-up	
t_{out} [d]	v [m/s]	F [N]	P_{IR} [W]	R [mm]	t_{after} [min]	Mean [%]	Std. dev. [%]	Mean [%]	Std. dev. [%]
5	0.06	200	350	800	1.5	5.122	9.024	4.807	9.614
5	0.06	200	350	800	5	5.992	9.757	7.324	14.647
5	0.06	200	350	800	10	7.009	11.057	7.324	14.647
5	0.06	200	350	800	20	7.227	11.036	7.324	14.647
5	0.06	200	350	800	40	7.407	10.955	7.324	14.647
5	0.03	200	350	400	1.5	1.198	0.885	39.385	32.456
5	0.03	200	350	400	5	1.796	1.025	43.229	28.250
5	0.03	200	350	400	10	2.355	1.192	47.702	22.349
5	0.03	200	350	400	20	2.479	1.292	47.701	22.350
5	0.03	200	350	400	40	2.929	1.706	47.556	22.692
5	0.03	400	350	600	1.5	4.960	7.285	15.531	19.044
5	0.03	400	350	600	5	5.076	7.241	15.290	18.772
5	0.03	400	350	600	10	5.971	7.504	18.614	23.725
5	0.03	400	350	600	20	6.563	7.889	18.754	23.784
5	0.03	400	350	600	40	7.421	8.368	18.754	23.784
5	0.06	400	350	600	1.5	1.211	1.914	23.142	20.200
5	0.06	400	350	600	5	2.076	1.297	25.037	20.882
5	0.06	400	350	600	10	2.089	1.301	25.037	20.882
5	0.06	400	350	600	20	2.878	1.918	24.953	20.896
5	0.06	400	350	600	40	3.314	2.080	24.953	20.896
10	0.03	200	150	400	1.5	4.182	3.194	69.371	15.184
10	0.03	200	150	400	5	6.720	3.493	70.099	13.066
10	0.03	200	150	400	10	7.475	3.646	71.059	13.337
10	0.03	200	150	400	20	8.876	4.397	72.658	12.931
10	0.03	200	150	400	40	9.538	4.272	75.461	13.115
10	0.06	400	150	400	1.5	1.887	1.823	52.034	14.849
10	0.06	400	150	400	5	2.898	3.013	56.101	13.079
10	0.06	400	150	400	10	3.729	2.918	58.873	10.842
10	0.06	400	150	400	20	3.605	3.658	46.605	25.711
10	0.06	400	150	400	40	5.501	4.215	60.224	11.157
10	0.06	200	150	600	1.5	3.893	3.813	28.531	24.890
10	0.06	200	150	600	5	5.496	4.461	35.411	31.080
10	0.06	200	150	600	10	6.295	5.203	41.078	38.105
10	0.06	200	150	600	20	7.650	5.306	42.910	39.763
10	0.06	200	150	600	40	9.006	6.226	49.964	34.755
10	0.03	400	150	800	1.5	2.540	3.174	10.435	20.871

Table A.15: Steering investigation on temporal defect evolvement — buckling and pull-up results (excluding non-adhering tapes) (part five)

t_{out} [d]	v [m/s]	F [N]	P_{IR} [W]	R [mm]	t_{after} [min]	Buckle Mean [%]	Std. dev. [%]	Pull-up Mean [%]	Std. dev. [%]
10	0.03	400	150	800	5	2.995	3.751	10.427	20.855
10	0.03	400	150	800	10	4.535	5.867	10.191	20.382
10	0.03	400	150	800	20	5.061	6.453	10.058	20.116
10	0.03	400	150	800	40	5.340	6.836	10.173	20.345
10	0.1	200	150	600	1.5	3.714	4.470	36.885	32.827
10	0.1	200	150	600	5	4.384	4.658	48.460	29.960
10	0.1	200	150	600	10	5.049	4.826	49.649	29.067
10	0.1	200	150	600	20	6.148	5.918	50.784	30.188
10	0.1	200	150	600	40	6.784	6.022	50.958	30.294
10	0.1	400	150	800	1.5	6.780	6.872	0.000	0.000
10	0.1	400	150	800	5	8.292	7.854	0.000	0.000
10	0.1	400	150	800	10	8.673	8.388	0.000	0.000
10	0.1	400	150	800	20	10.205	9.035	5.237	10.474
10	0.1	400	150	800	40	11.030	9.686	5.237	10.474
10	0.1	200	350	800	1.5	4.754	3.162	31.072	38.178
10	0.1	200	350	800	5	6.781	4.237	38.221	35.248
10	0.1	200	350	800	10	7.689	4.624	38.027	34.949
10	0.1	200	350	800	20	8.345	4.915	41.661	39.056
10	0.1	200	350	800	40	9.468	6.067	41.124	38.484
10	0.1	400	350	400	1.5	4.733	6.452	42.251	25.758
10	0.1	400	350	400	5	6.438	7.814	68.450	17.702
10	0.1	400	350	400	10	7.782	9.245	68.610	17.333
10	0.1	400	350	400	20	9.735	9.961	68.935	17.894
10	0.1	400	350	400	40	10.984	9.946	68.405	17.198
10	0.06	200	350	800	1.5	0.934	1.328	15.047	30.094
10	0.06	200	350	800	5	2.169	2.193	16.062	32.125
10	0.06	200	350	800	10	2.762	2.948	21.165	31.967
10	0.06	200	350	800	20	3.320	3.564	20.356	30.418
10	0.06	200	350	800	40	3.851	4.234	22.419	30.896
10	0.03	200	350	400	1.5	2.018	1.874	20.188	25.978
10	0.03	200	350	400	5	3.056	3.482	27.697	34.145
10	0.03	200	350	400	10	4.486	5.368	30.507	31.764
10	0.03	200	350	400	20	5.302	6.775	30.478	31.724
10	0.03	200	350	400	40	5.659	7.177	30.475	31.720
10	0.03	400	350	600	20	0.320	0.392	26.246	12.139
10	0.03	400	350	600	40	0.380	0.473	26.390	12.090

Table A.16: Steering investigation on temporal defect evolvement — buckling and pull-up results (excluding non-adhering tapes) (part six)

						Buckle		Pull-up	
t_{out} [d]	v [m/s]	F [N]	P_{IR} [W]	R [mm]	t_{after} [min]	Mean [%]	Std. dev. [%]	Mean [%]	Std. dev. [%]
10	0.06	400	350	600	1.5	1.422	2.085	7.789	15.577
10	0.06	400	350	600	5	2.411	3.261	7.702	15.405
10	0.06	400	350	600	10	2.501	3.435	12.569	16.121
10	0.06	400	350	600	20	2.990	4.026	12.547	16.086
10	0.06	400	350	600	40	3.787	4.500	12.533	16.063
15	0.06	400	150	400	1.5	8.382	4.756	54.358	19.377
15	0.06	400	150	400	5	10.766	5.054	54.217	19.796
15	0.06	400	150	400	10	12.250	5.627	59.312	18.206
15	0.06	400	150	400	20	13.568	6.669	62.867	15.952
15	0.06	400	150	400	40	14.713	7.487	52.346	23.299
15	0.06	200	150	600	1.5	7.286	4.287	49.249	11.914
15	0.06	200	150	600	5	10.433	4.357	50.146	13.099
15	0.06	200	150	600	10	11.429	4.686	50.321	12.809
15	0.06	200	150	600	20	12.464	4.045	49.803	13.054
15	0.06	200	150	600	40	13.910	4.866	50.387	13.025
15	0.03	400	150	800	1.5	5.177	3.684	24.598	33.502
15	0.03	400	150	800	5	8.043	4.722	25.337	34.523
15	0.03	400	150	800	10	9.296	4.697	26.189	34.831
15	0.03	400	150	800	20	10.855	5.576	34.781	33.670
15	0.03	400	150	800	40	11.943	6.400	34.804	33.675
15	0.1	400	150	800	1.5	18.613	13.217	0.000	0.000
15	0.1	400	150	800	5	23.178	17.046	0.000	0.000
15	0.1	400	150	800	10	24.754	15.475	0.000	0.000
15	0.1	400	150	800	20	24.876	15.520	0.000	0.000
15	0.1	400	150	800	40	26.862	15.637	0.000	0.000
15	0.06	200	350	800	1.5	5.807	5.516	24.979	30.639
15	0.06	200	350	800	5	7.348	6.284	21.629	26.796
15	0.06	200	350	800	10	7.723	6.441	22.732	28.435
15	0.06	200	350	800	20	11.898	12.298	22.650	28.311
15	0.06	200	350	800	40	11.948	12.348	28.755	25.962
15	0.03	200	350	400	1.5	8.219	7.951	46.471	35.827
15	0.03	200	350	400	5	11.726	8.375	47.525	34.731
15	0.03	200	350	400	10	13.378	8.607	47.936	34.829
15	0.03	200	350	400	20	14.988	8.430	48.144	34.387
15	0.03	200	350	400	40	16.224	8.626	51.532	29.557
15	0.03	400	350	600	1.5	8.889	9.369	62.336	22.837

Table A.17: Steering investigation on temporal defect evolvement — buckling and pull-up results (excluding non-adhering tapes) (part seven)

						Buckle		Pull-up	
t_{out}	v	F	P_{IR}	R	t_{after}	Mean	Std. dev.	Mean	Std. dev.
[d]	[m/s]	[N]	[W]	[mm]	[min]	[%]	[%]	[%]	[%]
15	0.03	400	350	600	5	10.615	9.504	65.885	20.369
15	0.03	400	350	600	10	12.111	9.137	67.529	22.043
15	0.03	400	350	600	20	13.570	10.337	66.481	21.593
15	0.03	400	350	600	40	14.533	10.706	67.925	22.915
15	0.06	400	350	600	1.5	2.391	2.849	24.404	42.268
15	0.06	400	350	600	5	5.288	2.200	32.200	40.518
15	0.06	400	350	600	10	6.745	3.126	38.580	38.241
15	0.06	400	350	600	20	7.924	2.463	42.229	37.032
15	0.06	400	350	600	40	9.085	2.083	40.773	35.512

A.2.2 Investigation on process parameters

The results of the process parameter and out-time investigations during steering are listed in Tab. A.18 (out-of-plane buckling) and Tab. A.19 (tape pull-up).

Table A.18: Steering investigation on process parameters — relative buckle-free length

v [m/s]	F [N]	P_{IR} [W]	t_{out} [d]	Mean [-]	Std. dev. [-]	Min. [-]	Max. [-]
0.03	400	350	1	0.968	0.028	0.928	1.000
0.06	200	350	1	0.945	0.051	0.855	1.000
0.06	400	150	1	0.925	0.056	0.845	0.982
0.06	400	350	1	0.945	0.040	0.897	1.000
0.1	400	350	1	0.919	0.050	0.828	0.980
0.03	400	350	5	0.964	0.030	0.921	1.000
0.06	200	350	5	0.948	0.030	0.888	0.968
0.06	400	150	5	0.907	0.054	0.832	1.000
0.06	400	350	5	0.923	0.053	0.825	0.977
0.1	400	350	5	0.837	0.062	0.735	0.917
0.03	400	350	10	0.923	0.062	0.836	1.000
0.06	200	350	10	0.812	0.106	0.648	0.969
0.06	400	150	10	0.654	0.329	0.000	0.886
0.06	400	350	10	0.832	0.096	0.719	0.961
0.1	400	350	10	0.295	0.363	0.000	0.780
0.03	400	350	15	0.833	0.083	0.678	0.904
0.06	200	350	15	0.311	0.385	0.000	0.863
0.06	400	150	15	0.000	0.000	0.000	0.000
0.06	400	350	15	0.495	0.408	0.000	0.913
0.1	400	350	15	0.000	0.000	0.000	0.000

Table A.19: Steering investigation on process parameters — relative pull-up-free length

v [m/s]	F [N]	P_{IR} [W]	t_{out} [d]	Mean [-]	Std. dev. [-]	Min. [-]	Max. [-]
0.03	400	350	1	0.979	0.041	0.896	1.000
0.06	200	350	1	0.826	0.165	0.603	1.000
0.06	400	150	1	0.705	0.166	0.498	1.000
0.06	400	350	1	1.000	0.000	1.000	1.000
0.1	400	350	1	0.767	0.212	0.523	1.000
0.03	400	350	5	1.000	0.000	1.000	1.000
0.06	200	350	5	1.000	0.000	1.000	1.000
0.06	400	150	5	0.733	0.161	0.524	1.000
0.06	400	350	5	1.000	0.000	1.000	1.000
0.1	400	350	5	0.768	0.230	0.402	1.000
0.03	400	350	10	0.956	0.088	0.781	1.000
0.06	200	350	10	0.790	0.299	0.204	1.000
0.06	400	150	10	0.669	0.420	0.000	1.000
0.06	400	350	10	0.857	0.180	0.574	1.000
0.1	400	350	10	0.291	0.396	0.000	1.000
0.03	400	350	15	0.931	0.138	0.656	1.000
0.06	200	350	15	0.379	0.465	0.000	1.000
0.06	400	150	15	0.000	0.000	0.000	0.000
0.06	400	350	15	0.600	0.490	0.000	1.000
0.1	400	350	15	0.000	0.000	0.000	0.000

A.3 Theoretical models predicting lay-up defects

A.3.1 Steering defect model

Tab. A.20 and Tab. A.21 list the input parameters for the developed steering defect model.

Table A.20: Steering defect model — input parameters material: constant values

Parameter	Material		
	IM7/8552	Unmodified material	Modified material
$b\ [mm]$	3.175	3.175	3.175
$h\ [mm]$	0.125	0.09	0.09
$E_1\ [MPa]$	159000	115000	127000
$E_2\ [MPa]$	0.564	0.018	3.560
$\nu_{12}\ [-]$	0.24	0.24	0.24
$\nu_{21}\ [-]$	$8.513 \cdot 10^{-7}$	$3.757 \cdot 10^{-8}$	$6.728 \cdot 10^{-6}$

Table A.21: Steering defect model — input parameters material: $k_{tack,base}$ and G_{12}

Material	$t_{out}\ [d]$	$T\ [°C]$	$k_{tack,base}\ [N/mm^3]$	$G_{12}\ [MPa]$
IM7/8552	1	20	18.90	94
IM7/8552	1	40	12.73	39
IM7/8552	5	20	19.21	113
IM7/8552	5	40	13.18	44
IM7/8552	10	20	1.63	177
IM7/8552	10	40	11.52	44
IM7/8552	15	20	0.56	222
IM7/8552	15	40	14.81	49
Unmodified material	-	20	39.81	149
Unmodified material	-	40	17.09	54
Modified material	-	20	3.11	1480
Modified material	-	40	17.47	73

The MATLAB code of the developed steering defect model is depicted in Fig. A.1–Fig. A.3.

```matlab
%% process parameters

v = 0.21 ;                                           %[m/s]
P = 430 ;                                            %[W]
F = 500 ;                                            %[N]

T = 21.0 ;                                           %T_amb [°C]
d = 15 ;                                             %t_out [d]

T_layup_v003 = 0.0001116*P^2 + 0.0079474*P + T ;
T_layup_v006 = 0.0000683*P^2 + 0.0097229*P + T ;
T_layup_v010 = 0.0000514*P^2 + 0.0070352*P + T ;
T_layup_v_exp = [T_layup_v003 T_layup_v006 T_layup_v010]
v_exp = [0.03 0.06 0.1]
if (v >= 0) && (v <= 0.1)
    T_layup_v = interp1(v_exp, T_layup_v_exp, v, 'pchip') ;
elseif v > 0.1
    T_layup_v = interp1(v_exp, T_layup_v_exp, v, 'linear', 'extrap') ;
end

if T_layup_v < T
    T_layup = T ;
else
    T_layup = T_layup_v ;
end

t_intim = (0.0140841*F + 12.3057840)/(v*1000)

%% material parameters

b = 3.175 * 10^-3 ;                                  %[m]
h = 0.125 * 10^-3 ;                                  %[m]

E_1 = 159 * 10^9 ;                                   %[Pa]
E_2 = 0.564 * 10^6 ;                                 %[Pa]
ny_12 = 0.24 ;

G_12_days = [1 5 10 15];
G_12_T1_all = [0.094 0.113 0.177 0.222] * 10^9 ;   %[Pa]
T1_G = 20 ;                                          %[°C]
G_12_T2_all = [0.039 0.044 0.044 0.049] * 10^9 ;   %[Pa]
T2_G = 40 ;                                          %[°C]

k_base_days = [1 5 10 15];                           %[d]
k_base_T1_all = [18.90 19.21 1.63 0.56] * 10^9;    %[N/m³]
T1_k = 20 ;                                          %[°C]
k_base_T2_all = [12.73 13.18 11.52 14.81] * 10^9;  %[N/m³]
T2_k = 40 ;                                          %[°C]
```

Figure A.1: Steering defect model — MATLAB code (part one)

```matlab
%% inter-/extrapolation of material paramters

G_12_T1 = interp1(G_12_days, G_12_T1_all, d);
G_12_T2 = interp1(G_12_days, G_12_T2_all, d);

k_base_T1 = interp1(k_base_days, k_base_T1_all, d);
k_base_T2 = interp1(k_base_days, k_base_T2_all, d);

c_G12 = 0.1
G_12 = c_G12*(G_12_T1 + ((G_12_T2 - G_12_T1)/(T2_G - T1_G)) * (T -↙
T1_G)) ;
k_base = k_base_T1 + ((k_base_T2 - k_base_T1)/(T2_k - T1_k)) * (T -↙
T1_k) ;
k_base_layup = k_base_T1 + ((k_base_T2 - k_base_T1)/(T2_k - T1_k)) *↙
(T_layup - T1_k) ;

%% correction parameters of tack stiffness

zeta_time = 0.93 ;
tau_k = 7 ;

c_outtime_days = [1 5 10 15]
c_outtime_all = [1 0.859 1.076 0.270];
c_outtime = interp1(c_outtime_days, c_outtime_all, d, 'pchip') ;

c_Temp = k_base_layup/k_base ;

c_tintim = 1.3009*t_intim^0.2282 ;

k_start = k_base * c_Temp * c_tintim * c_outtime ;
k_infinite = zeta_time * k_start ;
k_1 = k_start - k_infinite ;

%% calculated parameters

G = G_12 * h
ny_21 = ny_12 * (E_2 / E_1) ;
Q_11 = E_1 / (1- ny_12 * ny_21) ;
D_11 = (h^3 * Q_11) / 12 ;
Q_22 = E_2 / (1- ny_12 * ny_21) ;
D_22 = (h^3 * Q_22) / 12 ;
Q_66 = G_12 ;
D_66 = (h^3 * Q_66) / 12 ;
Q_12 = (E_2 * ny_12) / (1- ny_12 * ny_21) ;
D_12 = (h^3 * Q_12) / 12 ;
```

Figure A.2: Steering defect model — MATLAB code (part two)

```matlab
%% calculation of the time-dependent critical steering radius

t = 1 ;                                              %[min]
R_cr_t = [] ;
conv = 1 ;

while conv > 10^-6
    k = k_infinite + k_1 * exp(-t/tau_k);
    z = 0 ;                                          %[m]

    for p = 1:1000
    alpha = b / ((0.5 * b) + z) ;
    R_cr = ((6-alpha) * E_1 * h * b^3 * sqrt(D_11 * (180 * D_22 + 9 *↙
k * b^4 + 60 * G * b^2))) / (2 * alpha * (360 * sqrt(3) * D_22 * D_11↙
+ 18 * sqrt(3) *...
    k * b^4 * D_11 + 120 * sqrt(3) * G * b^2 * D_11 + 2 * sqrt(D_11 *↙
(180 * D_22 + 9 * k * b^4 + 60 * G * b^2)) * (40 * D_66 - 10 * D_12)↙
+...
    3 * G * b^2 * sqrt(D_11 * (180 * D_22 + 9 * k * b^4 + 60 * G *↙
b^2)))) ;
    e_b = b * (1 / R_cr) * 0.5;
    z = (b / 2) * (1 + ( 1 / (e_b * (E_1 / G_12))) * (1 - sqrt(1 + (4↙
* e_b * (E_1 / G_12)))))) ;     %[m]
    end

    R_cr_t(t,1) = t ;
    R_cr_t(t,2) = R_cr ;
    if t>=2
        conv_q = (R_cr_t(t,2) / R_cr_t(t-1,2))  ;
        if conv_q>1
            conv = conv_q -1;
        else
            conv = 1 - conv_q;
        end
    end
    t = t + 1 ;
end

R_cr_mm=R_cr*1000

%% output results
plot(R_cr_t(:,1),R_cr_t(:,2))
xlabel('time [min]')
ylabel('Rcr [m]')
```

Figure A.3: Steering defect model — MATLAB code (part three)

The results of the parameter variation for IM7/8552 and the research materials are illustrated in the contour plots in Fig. A.4–Fig. A.9.

(a) Legend

(b) $F = 50\ N$

(c) $F = 200\ N$

(d) $F = 400\ N$

(e) $F = 600\ N$
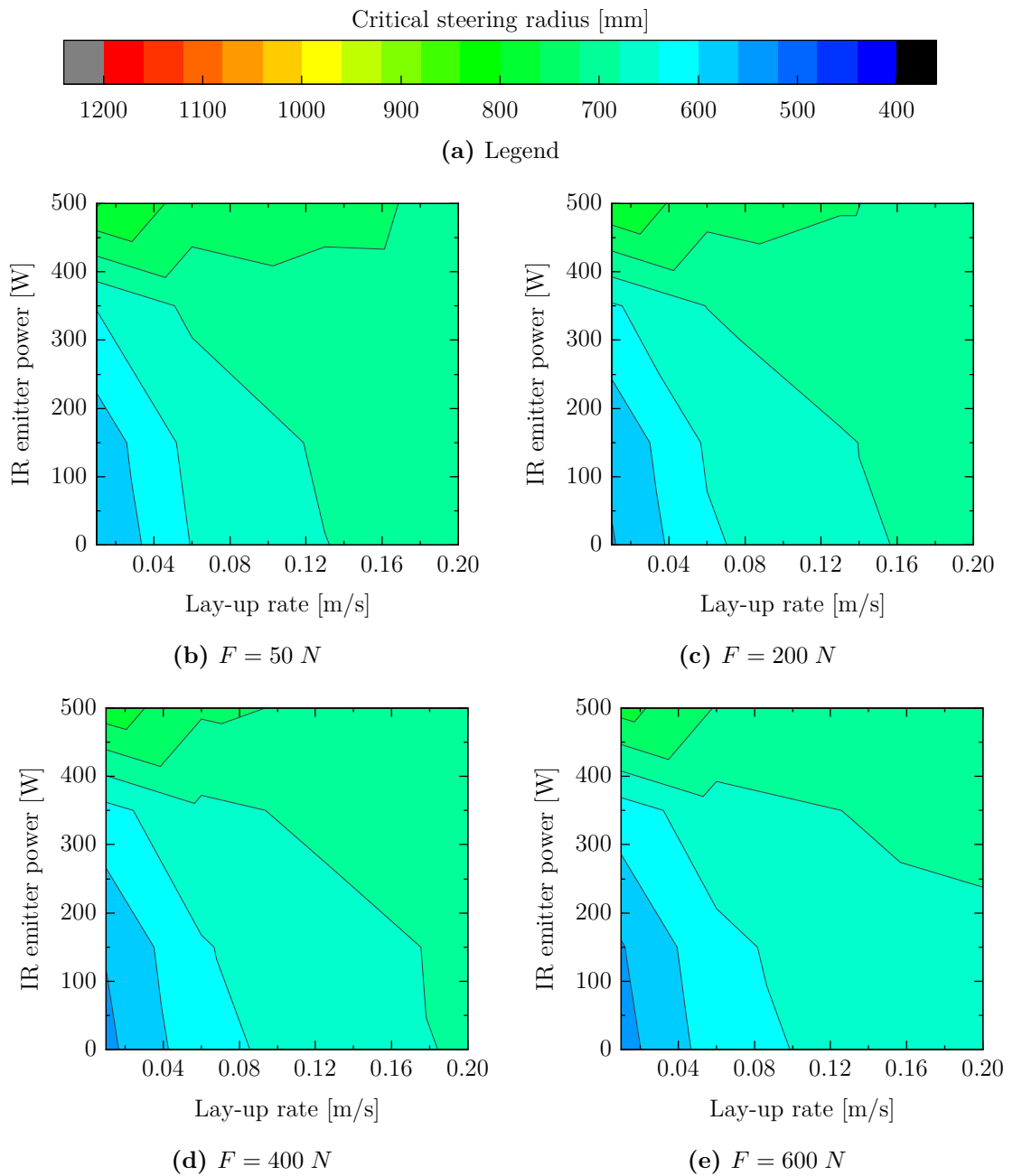
Figure A.4: Steering model — critical steering radius at $t_{after} = 40\ min$ as a result of process parameter variation for IM7/8552 at 1 d out-time

(a) Legend

(b) $F = 50\ N$

(c) $F = 200\ N$

(d) $F = 400\ N$

(e) $F = 600\ N$
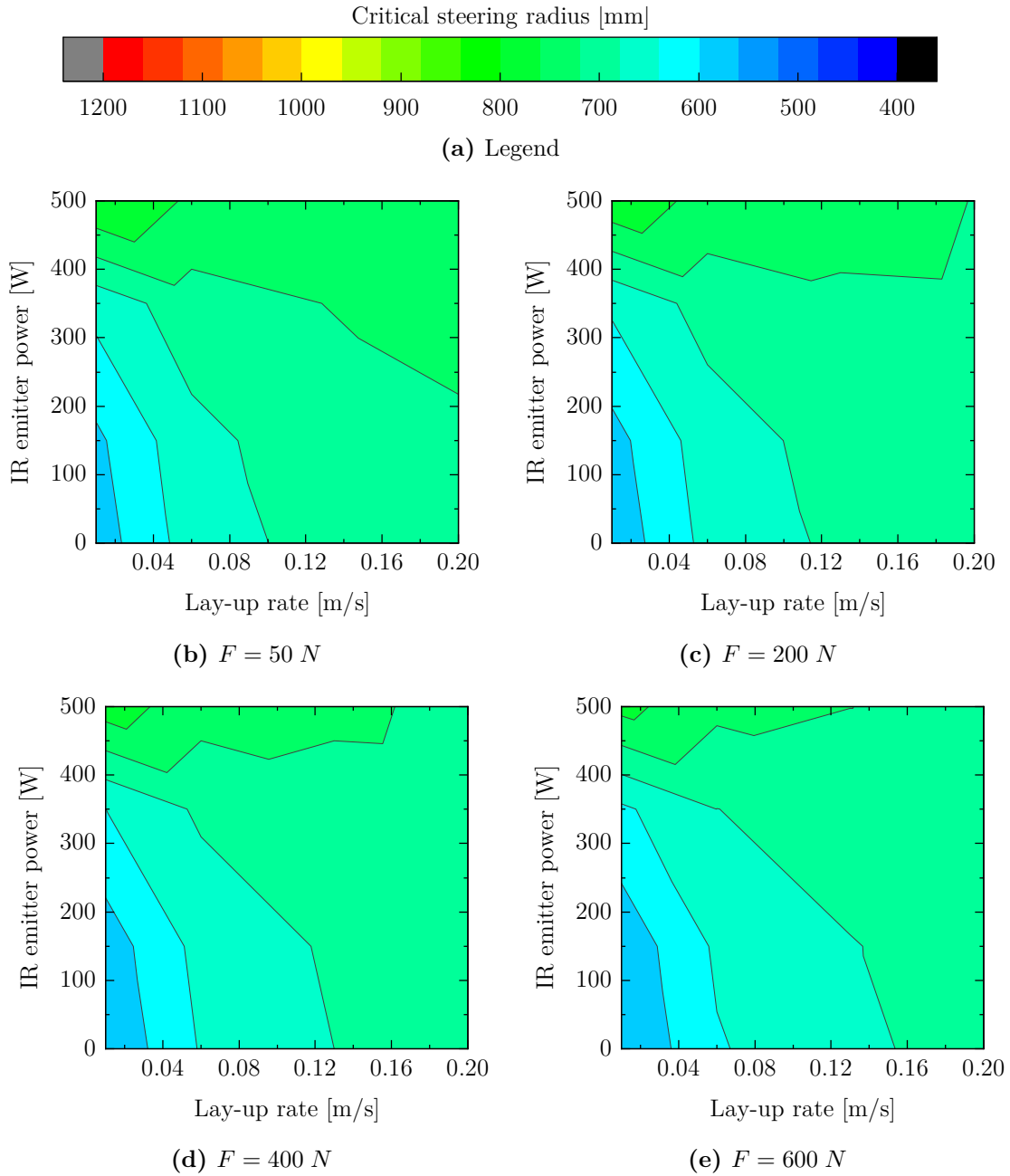
Figure A.5: Steering model — critical steering radius at $t_{after} = 40\ min$ as a result of process parameter variation for IM7/8552 at $5\ d$ out-time
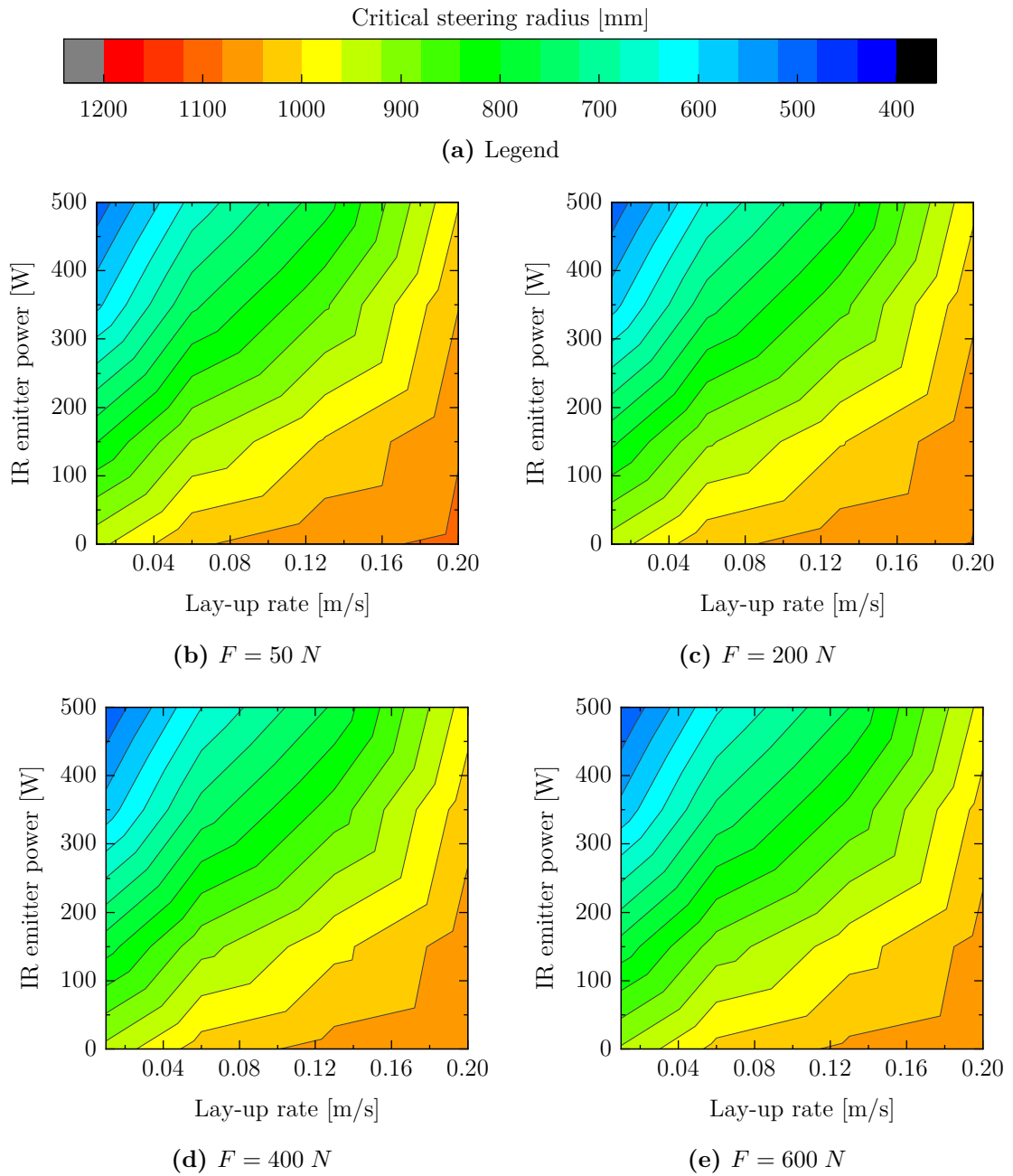
Figure A.6: Steering model — critical steering radius at $t_{after} = 40 \; min$ as a result of process parameter variation for IM7/8552 at 10 d out-time

(a) Legend

(b) $F = 50\ N$

(c) $F = 200\ N$

(d) $F = 400\ N$

(e) $F = 600\ N$
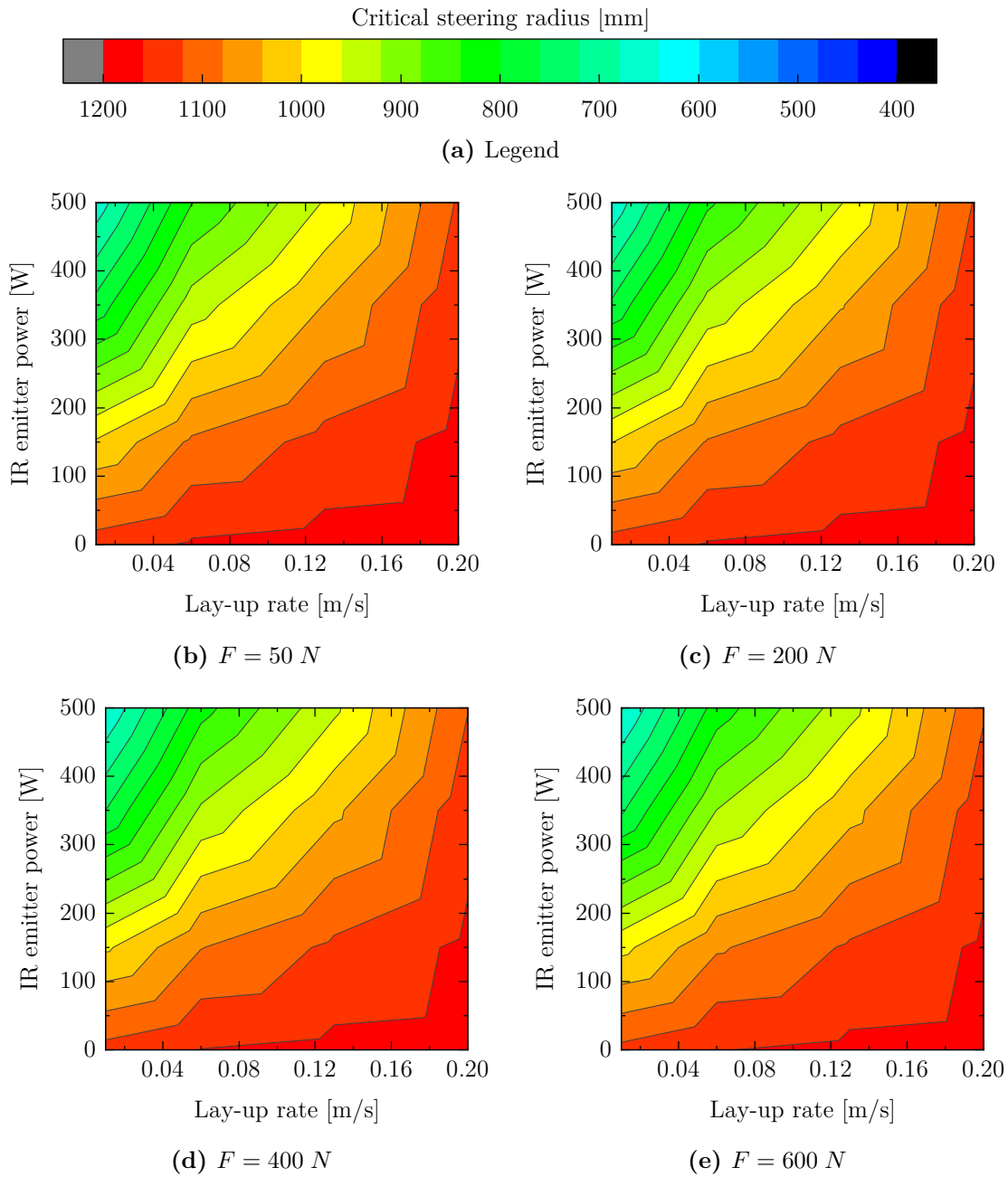
Figure A.7: Steering model — critical steering radius at $t_{after} = 40\ min$ as a result of process parameter variation for IM7/8552 at 15 d out-time

(a) Legend

(b) $F = 50\ N$

(c) $F = 200\ N$

(d) $F = 400\ N$

(e) $F = 600\ N$
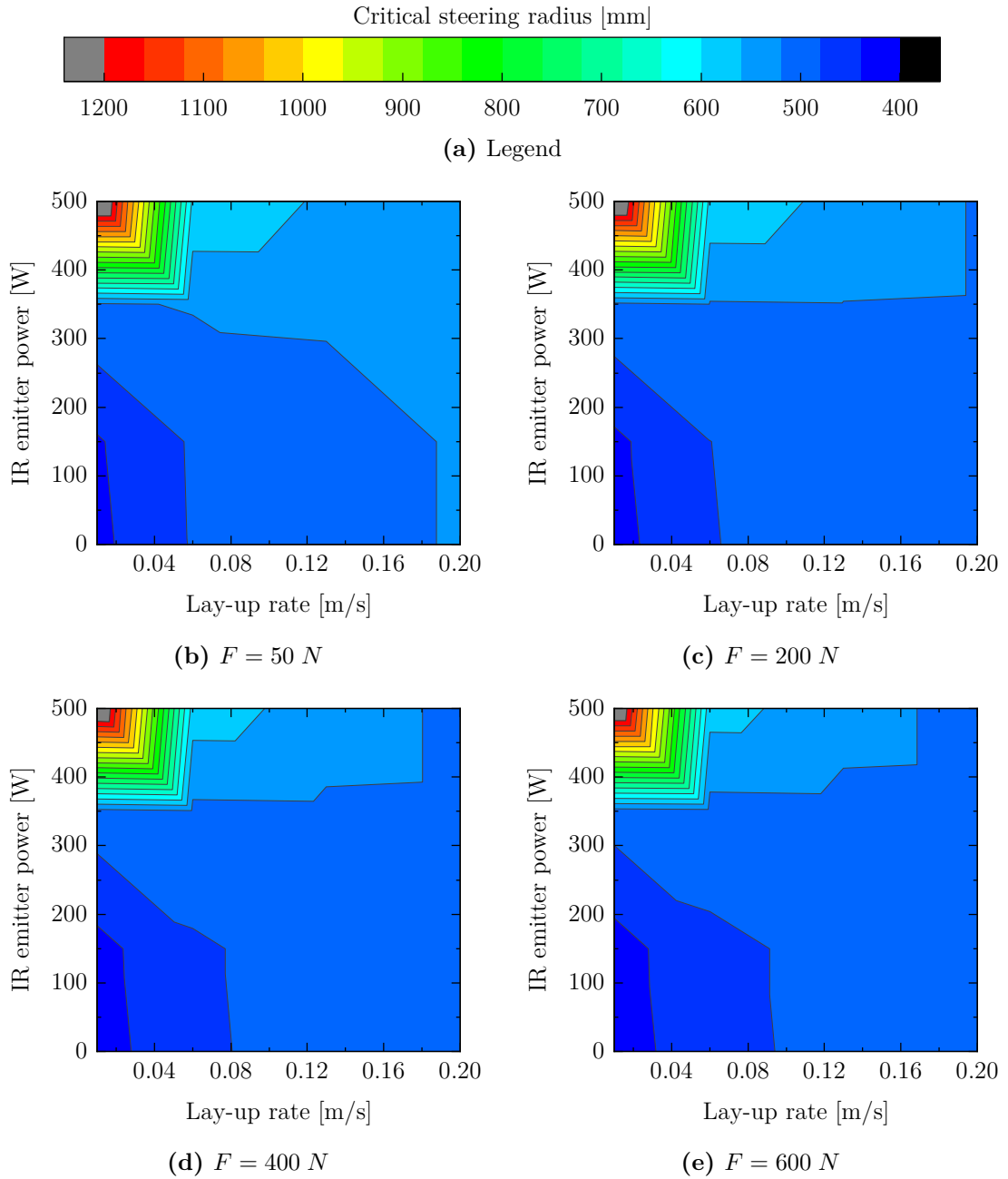
Figure A.8: Steering model — critical steering radius at $t_{after} = 40\ min$ as a result of process parameter variation for unmodified material

Critical steering radius [mm]

(a) Legend

(b) $F = 50\ N$

(c) $F = 200\ N$

(d) $F = 400\ N$

(e) $F = 600\ N$
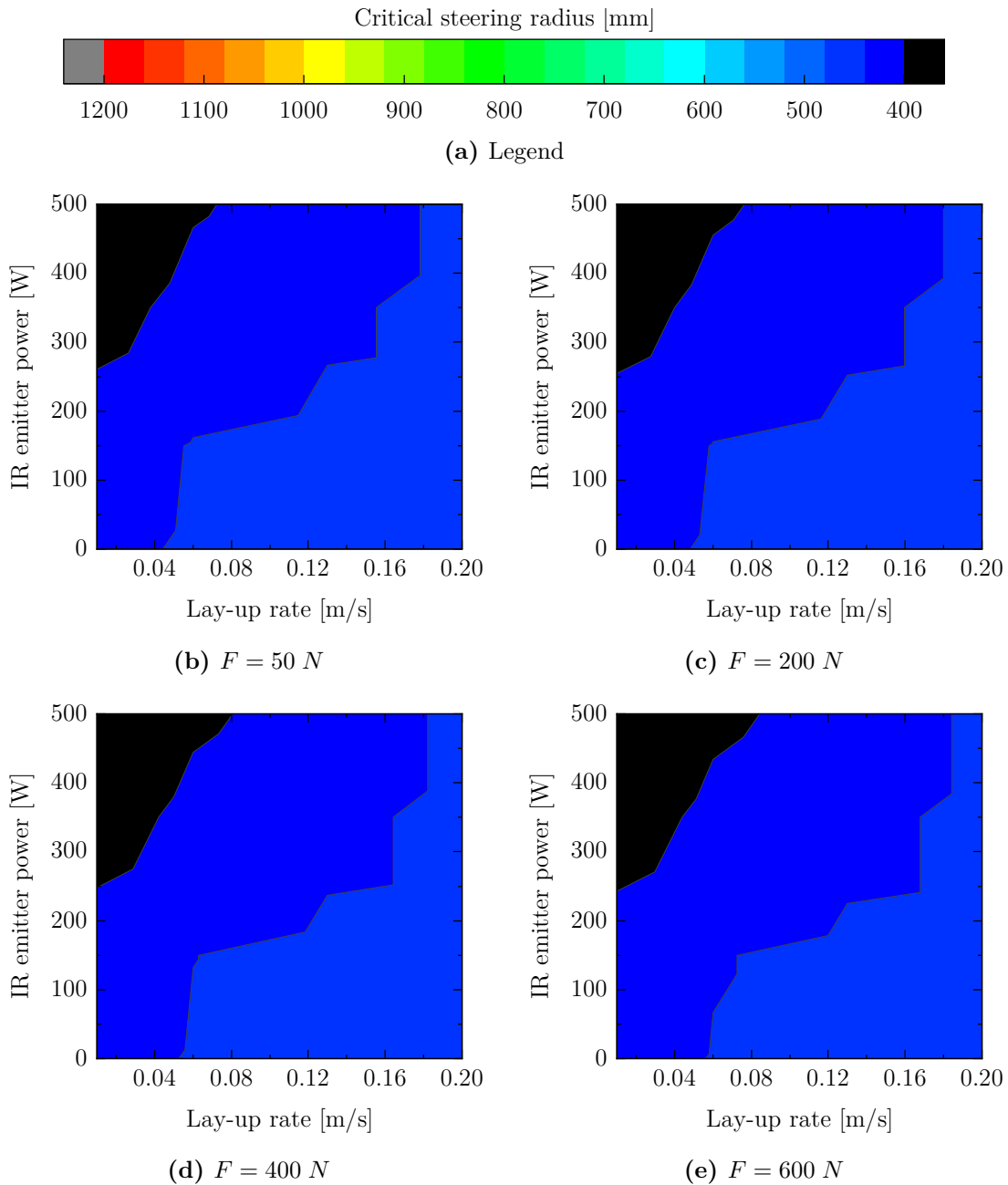
Figure A.9: Steering model — critical steering radius at $t_{after} = 40\ min$ as a result of process parameter variation for modified material

A.3.2 Tape peel-off model

The MATLAB code of the developed peel-off model is depicted in Fig. A.10 and Fig. A.11.

```matlab
%% geometric parameters and process parameters

L_edge = 100 * 10^-3 ;                  %[m]
beta = 0 * (pi/180);                     %90° minus phi_layup [°]
r = 40 * 10^-3 ;                         %R_edge [m]
alpha = 90 * (pi/180);                   %opening angle of edge tool [°]

v = 0.03 ;                               %[m/s]
P = 350 ;                                %[W]
F = 400 ;                                %[N]

%% material parameters

T = 21.0 ;                               %T_amb [°C]
d = 15 ;                                 %t_out [d]

b = 3.175 * 10^-3 ;                      %[m]
h = 0.125 * 10^-3 ;                      %[m]

I = b*h^3/12 ;                           %[m^2]

T_layup_v003 = 0.0001116*P^2 + 0.0079474*P + T ;
T_layup_v006 = 0.0000683*P^2 + 0.0097229*P + T ;
T_layup_v010 = 0.0000514*P^2 + 0.0070352*P + T ;
T_layup_v_exp = [T_layup_v003 T_layup_v006 T_layup_v010]
v_exp = [0.03 0.06 0.1]
if (v >= 0) && (v <= 0.1)
    T_layup_v = interp1(v_exp, T_layup_v_exp, v, 'pchip') ;
elseif v > 0.1
    T_layup_v = interp1(v_exp, T_layup_v_exp, v, 'linear', 'extrap') ;
end

if T_layup_v < T
    T_layup = T ;
else
    T_layup = T_layup_v ;
end

%% inter-/extrapolation E_flex*I

E_days = [4.87 8.11 10.5 15.02];                         %[d]
E_T1_all = [40282.16 44391.33 57680.95 60017.29] * 10^6;  %[N/m²]
T1_E = 23.5 ;                                            %[°C]
E_T2_all = [27189.26 14822.55 14830.29 16127.81] * 10^6;  %[N/m²]
T2_E = 40 ;                                              %[°C]

E_T1 = interp1(E_days, E_T1_all, d, 'linear', 'extrap');
E_T2 = interp1(E_days, E_T2_all, d, 'linear', 'extrap');
```

Figure A.10: Tape peel-off model — MATLAB code (part one)

```matlab
E = E_T1 + ((E_T2 - E_T1)/(T2_E - T1_E)) * (T_layup - T1_E) ;

if E > 0
    E = E_T1 + ((E_T2 - E_T1)/(T2_E - T1_E)) * (T_layup - T1_E) ;
else
    E = 0 ;
end

%% inter-/extrapolation peel tack

k_v = [0.03 0.06 0.1] ;
k_P = [150 350] ;
k_F = [200 400] ;
k_days = [1 5 10 15] ;
K_01d = [11.355 4.026 6.540; 13.595 10.900 6.434] ;
K_01d(:,:,2) = [9.350 4.764 5.656; 12.699 8.587 8.110] ;
K_05d = [4.818 3.857 4.080; 4.163 3.981 3.094] ;
K_05d(:,:,2) = [4.200 3.491 4.304; 4.664 6.443 3.281] ;
K_10d = [3.398 2.936 4.215; 2.961 2.595 3.329] ;
K_10d(:,:,2) = [1.822 3.193 3.741; 1.956 3.090 1.618] ;
K_15d = [0 2.500 0; 2.096 0.924 0] ;
K_15d(:,:,2) = [3.448 1.656 0; 1.645 1.377 0] ;

e_tack_01d = interp3(k_v,k_P,k_F,K_01d,v,P,F,'makima') ;
e_tack_05d = interp3(k_v,k_P,k_F,K_05d,v,P,F,'makima') ;
e_tack_10d = interp3(k_v,k_P,k_F,K_10d,v,P,F,'makima') ;
e_tack_15d = interp3(k_v,k_P,k_F,K_15d,v,P,F,'makima') ;
e_tack_days = [e_tack_01d e_tack_05d e_tack_10d e_tack_15d] ;
e_tack = interp1(k_days, e_tack_days, d) ;

if e_tack > 0
    e_tack = interp1(k_days, e_tack_days, d) ;
else
    e_tack = 0 ;
end

%% correction factor

r_eff = sqrt((r * alpha)^2 + (tan(beta)*r*alpha)^2)/alpha;   %[m]
l = r_eff * alpha ;                                          %[m]

c_p0 = 0.1 ;
c_p = c_p0 + r_eff*(1-c_p0)/0.04 ;

%% calculation of the  peel-off energy

U_B = c_p * ((E*I*l) / (2 * r_eff^2)) ;                      %[J]
U_T = b * (L_edge + r_eff * alpha) * e_tack ;               %[J]
U_peeloff = U_B - U_T
```

Figure A.11: Tape peel-off model — MATLAB code (part two)

Tab. A.22–Tab. A.24 detail the input parameters for the peel-off model.

Table A.22: Peel-off model — input parameters material: e_{tack} (part one)

Material	t_{out} [d]	v [m/s]	F [N]	P_{IR} [W]	e_{tack} [N/m]
IM7/8552	1	0.03	200	150	11.355
IM7/8552	1	0.03	400	150	9.350
IM7/8552	1	0.03	200	350	13.595
IM7/8552	1	0.03	400	350	12.699
IM7/8552	1	0.06	200	150	4.026
IM7/8552	1	0.06	400	150	4.764
IM7/8552	1	0.06	200	350	10.900
IM7/8552	1	0.06	400	350	8.587
IM7/8552	1	0.1	200	150	6.540
IM7/8552	1	0.1	400	150	5.656
IM7/8552	1	0.1	200	350	6.434
IM7/8552	1	0.1	400	350	8.110
IM7/8552	5	0.03	200	150	4.818
IM7/8552	5	0.03	400	150	4.200
IM7/8552	5	0.03	200	350	4.163
IM7/8552	5	0.03	400	350	4.664
IM7/8552	5	0.06	200	150	3.857
IM7/8552	5	0.06	400	150	3.491
IM7/8552	5	0.06	200	350	3.981
IM7/8552	5	0.06	400	350	6.443
IM7/8552	5	0.1	200	150	4.080
IM7/8552	5	0.1	400	150	4.304
IM7/8552	5	0.1	200	350	3.094
IM7/8552	5	0.1	400	350	3.281
IM7/8552	10	0.03	200	150	3.398
IM7/8552	10	0.03	400	150	1.822
IM7/8552	10	0.03	200	350	2.961
IM7/8552	10	0.03	400	350	1.956
IM7/8552	10	0.06	200	150	2.936
IM7/8552	10	0.06	400	150	3.193
IM7/8552	10	0.06	200	350	2.595
IM7/8552	10	0.06	400	350	3.090
IM7/8552	10	0.1	200	150	4.215
IM7/8552	10	0.1	400	150	3.741
IM7/8552	10	0.1	200	350	3.329
IM7/8552	10	0.1	400	350	1.618

Table A.23: Peel-off model — input parameters material: e_{tack} (part two)

Material	t_{out} [d]	v [m/s]	F [N]	P_{IR} [W]	e_{tack} [N/m]
IM7/8552	15	0.03	200	150	0
IM7/8552	15	0.03	400	150	3.448
IM7/8552	15	0.03	200	350	2.096
IM7/8552	15	0.03	400	350	1.645
IM7/8552	15	0.06	200	150	2.500
IM7/8552	15	0.06	400	150	1.656
IM7/8552	15	0.06	200	350	0.924
IM7/8552	15	0.06	400	350	1.377
IM7/8552	15	0.1	200	150	0
IM7/8552	15	0.1	400	150	0
IM7/8552	15	0.1	200	350	0
IM7/8552	15	0.1	400	350	0
Unmodified material	-	0.03	200	150	7.969
Unmodified material	-	0.03	400	150	12.313
Unmodified material	-	0.03	200	350	6.646
Unmodified material	-	0.03	400	350	12.083
Unmodified material	-	0.06	200	150	33.477
Unmodified material	-	0.06	400	150	47.034
Unmodified material	-	0.06	200	350	13.737
Unmodified material	-	0.06	400	350	28.318
Unmodified material	-	0.1	200	150	17.080
Unmodified material	-	0.1	400	150	21.098
Unmodified material	-	0.1	200	350	8.958
Unmodified material	-	0.1	400	350	23.351
Modified material	-	0.03	200	150	5.472
Modified material	-	0.03	400	150	2.649
Modified material	-	0.03	200	350	1.952
Modified material	-	0.03	400	350	6.699
Modified material	-	0.06	200	150	2.486
Modified material	-	0.06	400	150	4.741
Modified material	-	0.06	200	350	1.714
Modified material	-	0.06	400	350	3.374
Modified material	-	0.1	200	150	6.877
Modified material	-	0.1	400	150	9.060
Modified material	-	0.1	200	350	0.562
Modified material	-	0.1	400	350	1.624

Table A.24: Peel-off model — input parameters material: E_{flex}

Material	Equiv. t_{out} [d]	T [°C]	E_{flex} [MPa]
IM7/8552	4.9	23.5	40282.16
IM7/8552	8.1	23.5	44391.33
IM7/8552	10.5	23.5	57680.95
IM7/8552	15.0	23.5	60017.29
IM7/8552	4.9	40.0	27189.26
IM7/8552	8.1	40.0	14822.55
IM7/8552	10.5	40.0	14830.29
IM7/8552	15.0	40.0	16127.81
Unmodified material	-	23.2	2911.23
Unmodified material	-	40.0	0
Modified material	-	23.2	31579.68
Modified material	-	40.0	24574.88

The results of the parameter variation for IM7/8552 and the research materials are illustrated in the contour plots in Fig. A.12–Fig. A.17.

(a) Legend

(b) $F = 200\ N$

(c) $F = 300\ N$

(d) $F = 400\ N$
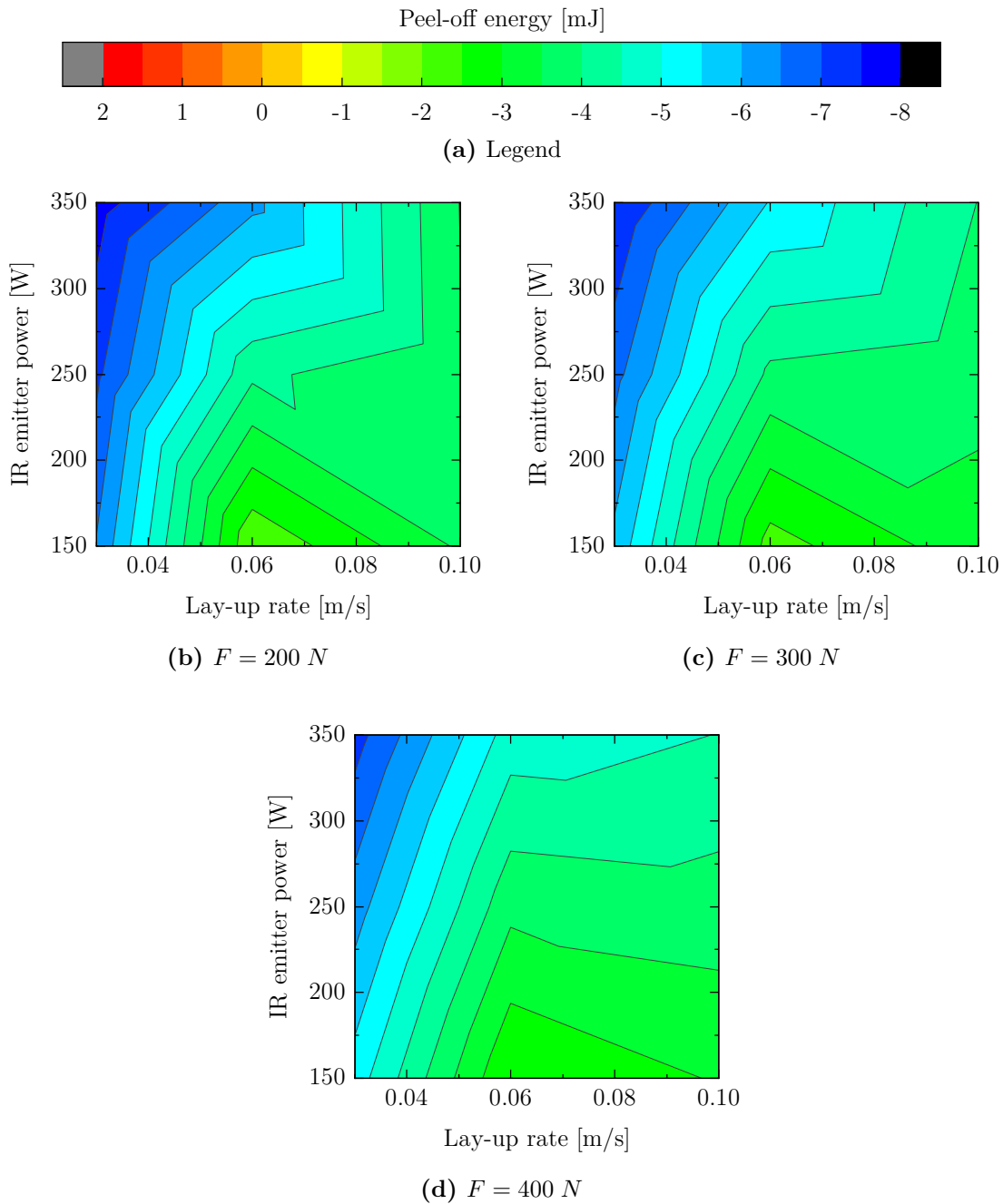
Figure A.12: Peel-off model — peel-off energy as a result of process parameter variation for IM7/8552 at 1 d out-time

(a) Legend

(b) $F = 200\ N$

(c) $F = 300\ N$

(d) $F = 400\ N$
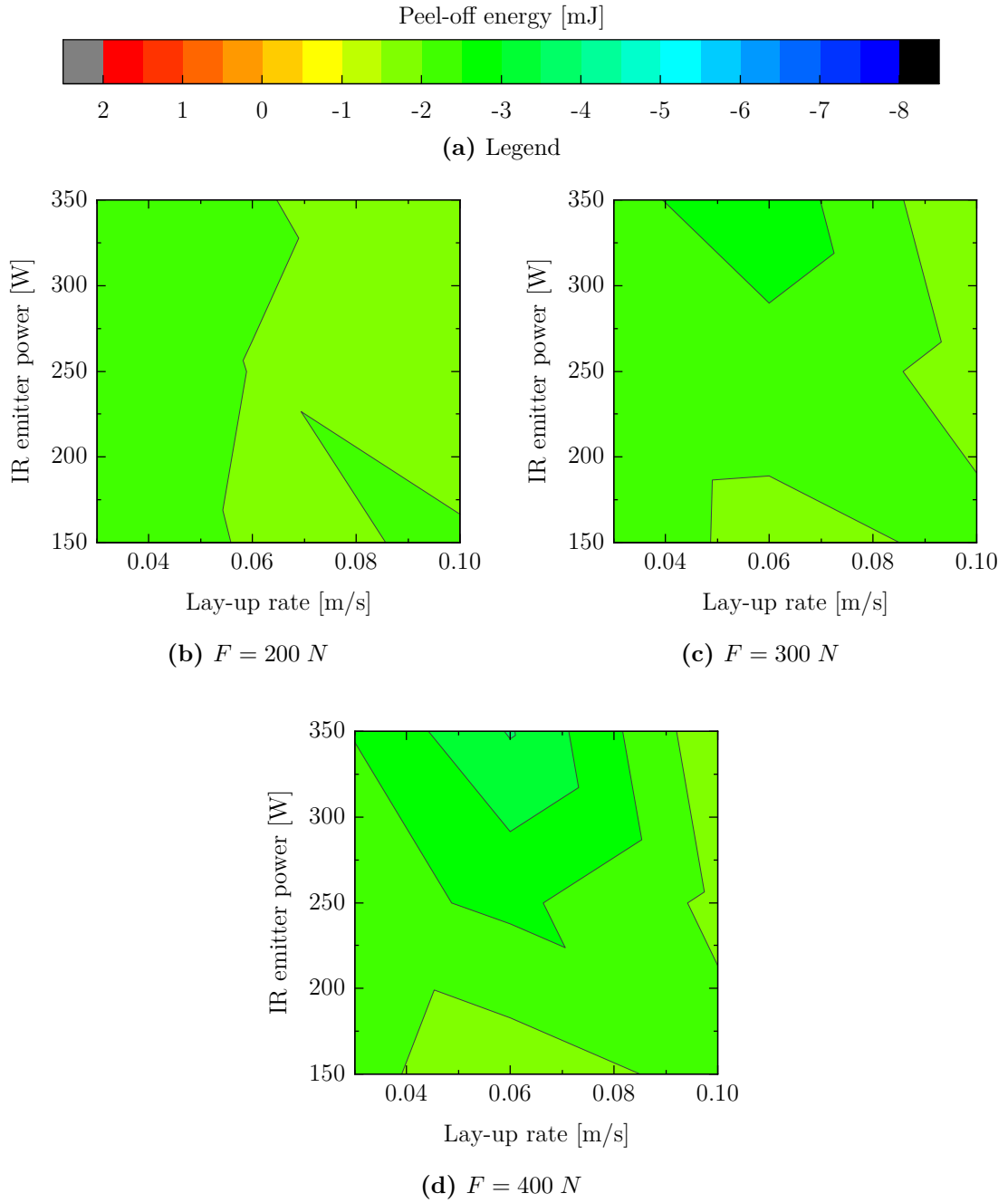
Figure A.13: Peel-off model — peel-off energy as a result of process parameter variation for IM7/8552 at 5 d out-time

(a) Legend

(b) $F = 200\ N$

(c) $F = 300\ N$

(d) $F = 400\ N$
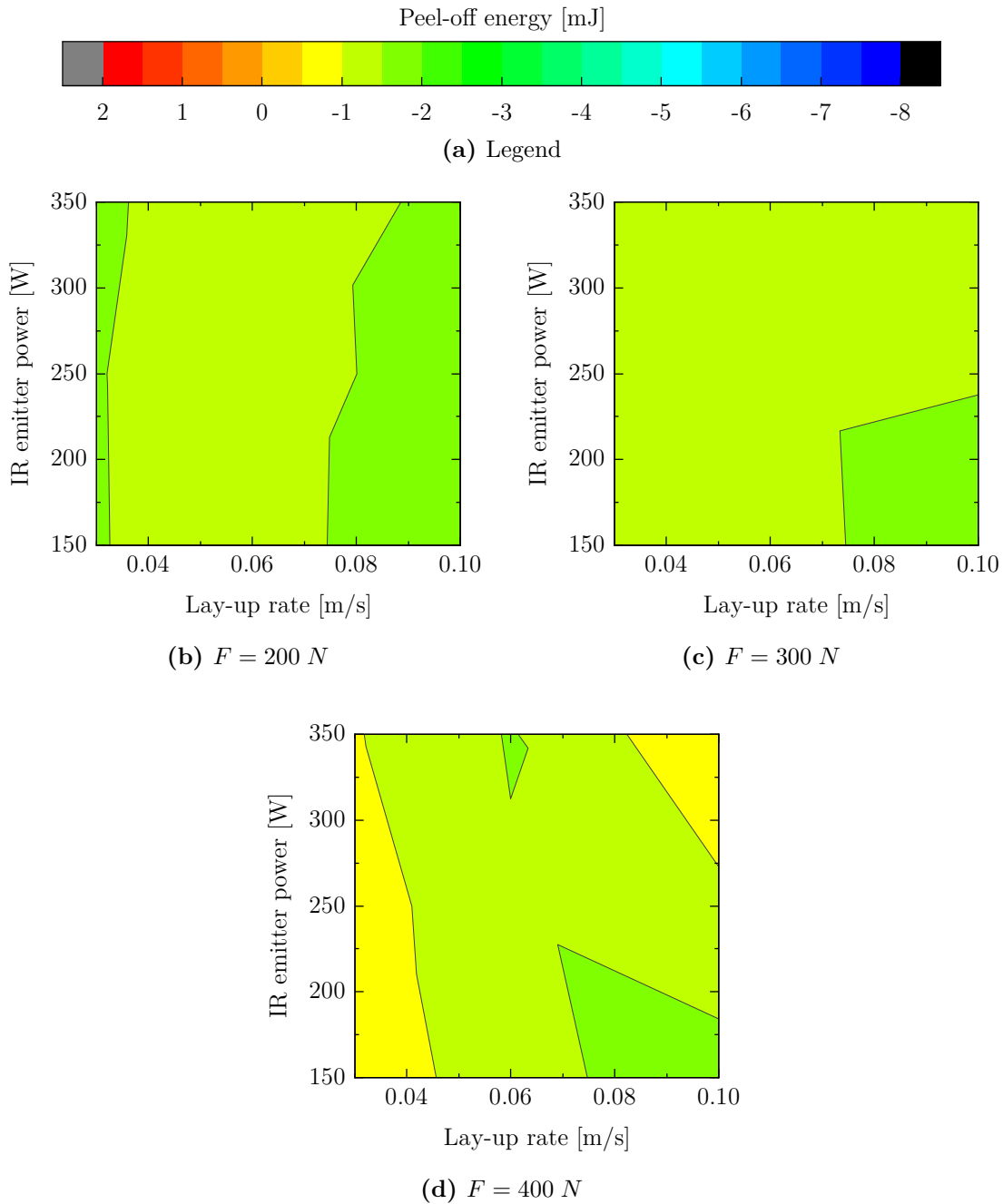
Figure A.14: Peel-off model — peel-off energy as a result of process parameter variation for IM7/8552 at 10 d out-time

Peel-off energy [mJ]

(a) Legend

(b) $F = 200\ N$

(c) $F = 300\ N$

(d) $F = 400\ N$
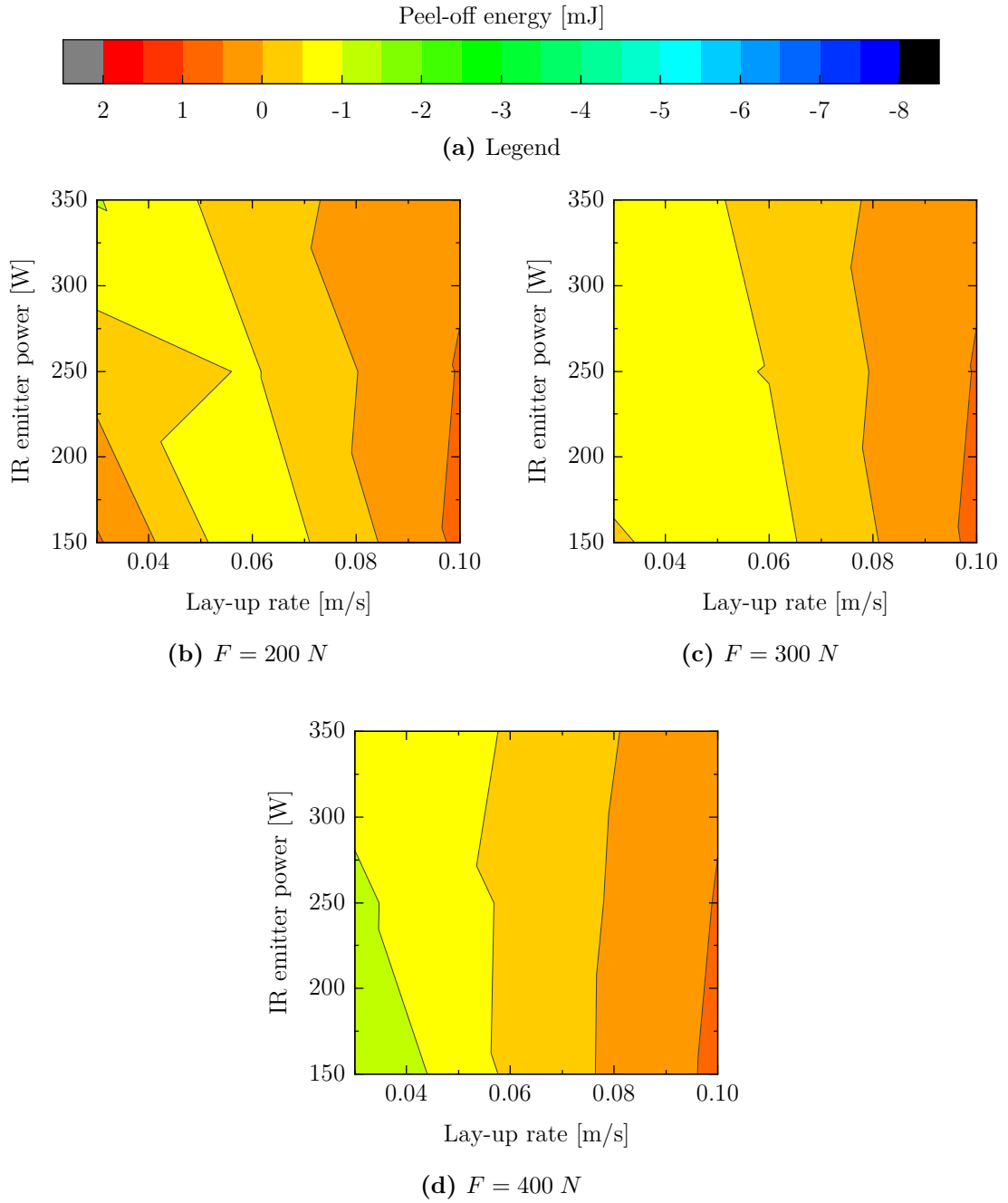
Figure A.15: Peel-off model — peel-off energy as a result of process parameter variation for IM7/8552 at 15 d out-time

(a) Legend

(b) $F = 300\ N$

(c) $F = 300\ N$

(d) $F = 400\ N$
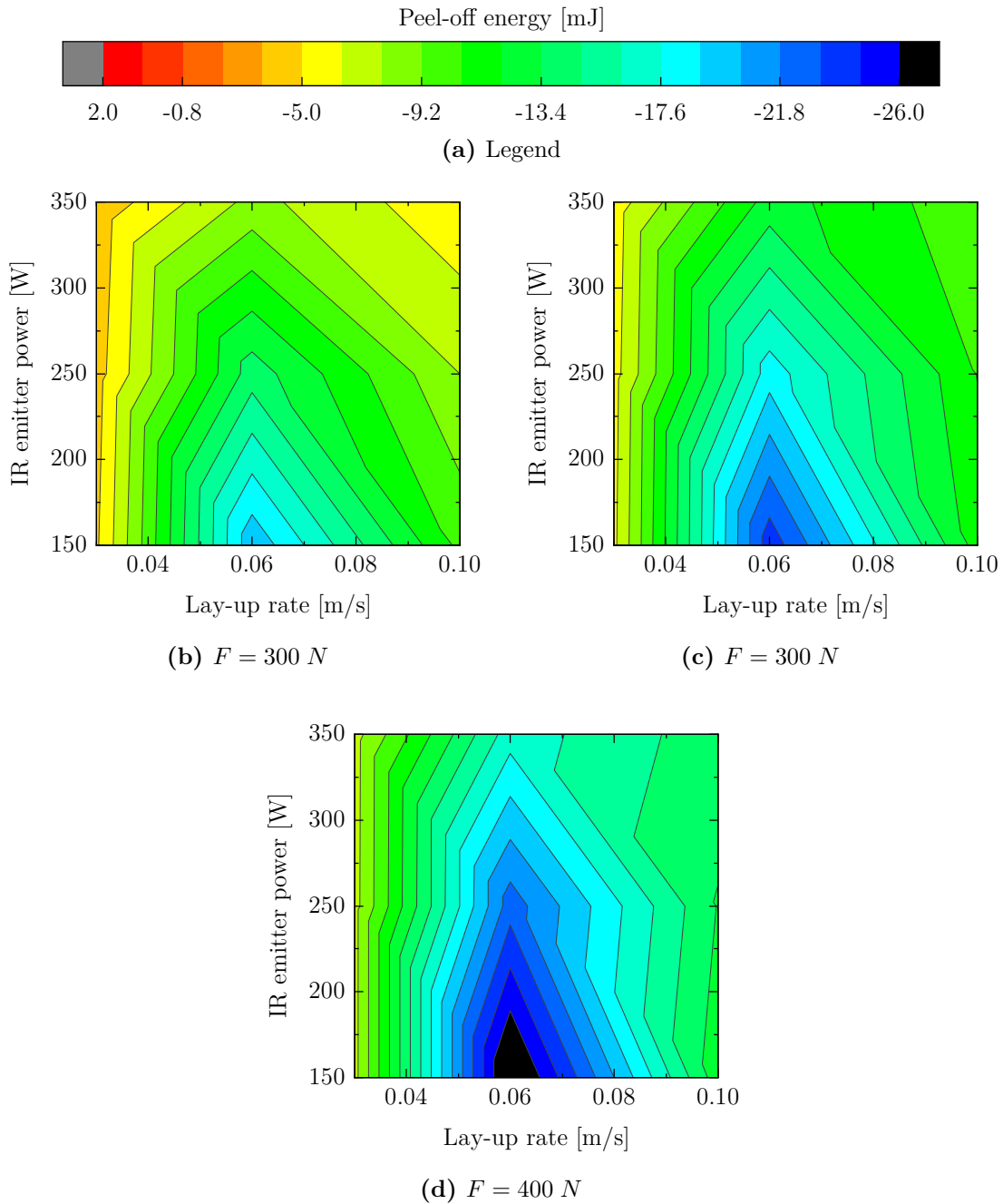
Figure A.16: Peel-off model — peel-off energy as a result of process parameter variation for unmodified material

Peel-off energy [mJ]

(a) Legend

(b) $F = 300\ N$

(c) $F = 300\ N$

(d) $F = 400\ N$
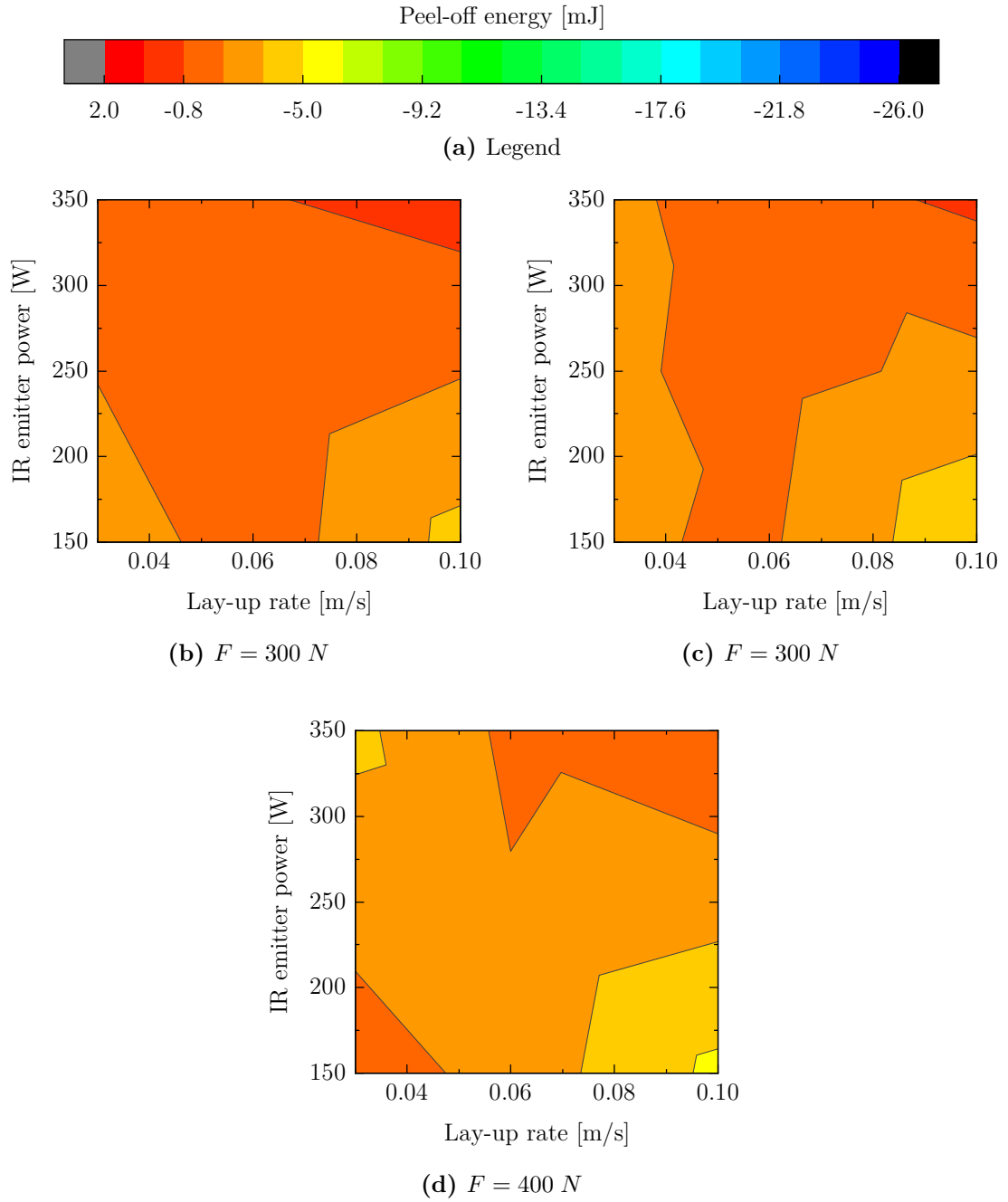
Figure A.17: Peel-off model — peel-off energy as a result of process parameter variation for modified material

A.3.3 Use case: aircraft nacelle inner fixed structure

Details of the generic inner fixed structure used for the use case are given in Fig. A.18.
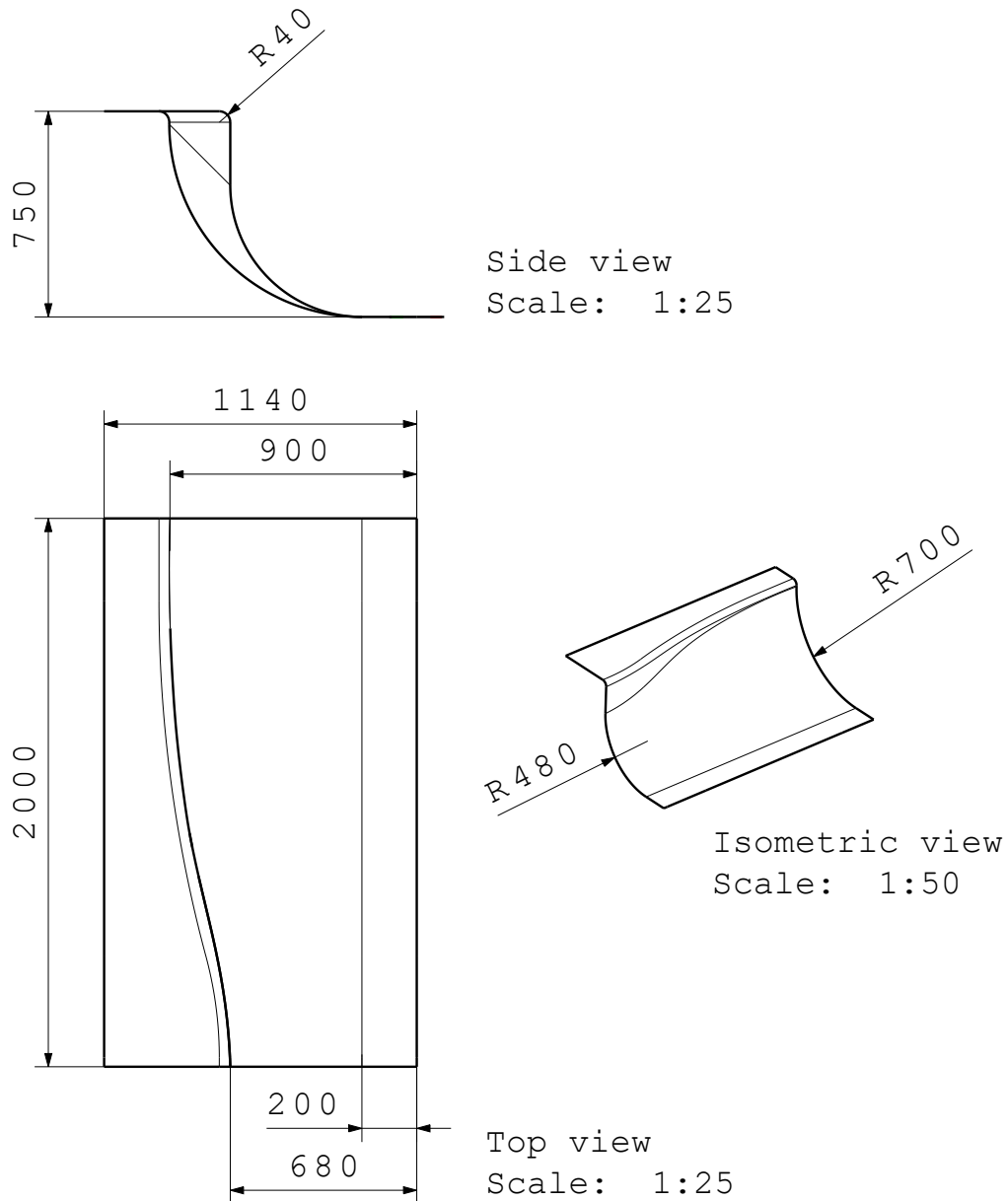
Figure A.18: Inner fixed structure — dimensions

B Publications

Journal Paper

[J1] K. Heller, M. Hallmannseder, D. Colin, K. Kind, K. Drechsler. Comparing
      Test Methods for the Intra-ply Shear Properties of Uncured Prepreg Tapes.
      Science and Engineering of Composites. 2020; 27:89-96. doi: 10.1515/secm-
      2020-0009.

[J2] K. Heller, D. Colin, K. Drechsler. Quantifying the Influence of Out-time
      on Prepreg Material Properties and Out-of-plane Steering Defects during
      Automated Fiber Placement. *Frontiers in Materials.* 2022; 9:825809. doi:
      10.3389/fmats.2022.825809.

Conference

[C1] K. Heller, B. Böckl, C. Ebel, K. Drechsler. Influence of Prepreg Aging and
      Tack on Lay-Up Effects/defects in Thermoset Automated Fiber Placement.
      In: *ECCM18: 18th European Conference on Composite Materials*, 24-28 June
      2018, Athens, Greece.

[C2] K. Heller, M. Hallmannseder, D. Colin, K. Kind, K. Drechsler. Compar-
      ing Test Methods for the Deformation Behavior of Uncured Prepreg Tapes.
      In: *ACM4 - The Fourth International Symposium on Automated Composites
      Manufacturing*, 25-26 April 2019, Montreal, Canada.

[C3] K. Heller, S. Seyfferth, K. Kind, K. Drechsler. A Post Lay-up Tack Peel Test
      for Aerospace Grade Prepreg Tapes. In: *Proceedings SE Conference Amster-
      dam 20*, SAMPE Europe Conference and Exhibition 2020, 29 September - 1
      October 2020, Amsterdam, Netherlands.

[C5]   B. Böckl, C. Jetten, K. Heller, C. Ebel, K. Drechsler. Assessment of the tack of prepreg slit tapes during the Automated Fiber Placement process. In: *SICOMP29 - 29th Conference on Manufacturing and Design of Composites*, 28-29 May 2018, Lulea, Sweden.

[C4]   B. Böckl, C. Jetten, K. Heller, C. Ebel, K. Drechsler. Online Monitoring System for the Tack of Prepreg Slit Tapes Used in Automated Fiber Placement. In: *ECCM18: 18th European Conference on Composite Materials*, 24-28 June 2018, Athens, Greece.

[C5]   N. Siemen, K. Heller. Composite Prepregs Tack Change Along the Process Chain. In: *ECCM20: 20th European Conference on Composite Materials*, 26-30 June, 2022, Lausanne, Switzerland.

C Supervised student theses

[S1] M. Gueffroy. Aufbau eines Prüfstands zur Untersuchung des Ablegeverhaltens beim Automated Fiber Placement. Bachelor's Thesis. 2017.

[S2] T. Zessack. Konzeptentwicklung und Auslegung einer Luftfahrt-Generatorkomponente in Faserverbundbauweise. Master's Thesis. 2017.

[S3] M. Hallmannseder. Entwicklung einer Methodik zur Charakterisierung von duroplastischen Prepreg-Tapes. Term Project. 2018.

[S4] A. Benda. Weiterentwicklung eines Prüfstands zur Untersuchung des Ablegeverhaltens beim Automated Fiber Placement. Bachelor's Thesis. 2018.

[S5] J. Wortmann. Erweiterung eines Prozesses zur effizienten Fertigung von Luftfahrtbauteilen mit vorimprägnierten Faserbändern. Bachelor's Thesis. 2018.

[S6] M. Hallmannseder. Entwicklung von Prüfmethoden für das Formbarkeitsverhalten von unausgehärteten duroplastischen Prepreg-Tapes. Master's Thesis. 2018.

[S7] T. Moriz. Mechanische Charakterisierung von zukünftigen Prepreg-Materialien im Verarbeitungszustand für das Automated Fiber Placement. Bachelor's Thesis. 2019.

[S8] S. Seyfferth. Entwicklung eines mobilen Prüfstands zur Ermittlung der Klebrigkeit von Prepreg Tapes. Master's Thesis. 2019.

[S9] A. Pilger. Weiterentwicklung eines Biegeprüfstands zur Charakterisierung von Prepreg-Materialien für Luftfahrtanwendungen. Term Project. 2019.

[S10] J. Drexler. Evaluation von Fiber-Patch-Placement hinsichtlich der Verwendung von vorimprägniertem Fasermaterial. Term Project. 2020.

[S11] M. Bulzacchi. Experimentelle Untersuchung und Matlab unterstützte numerische Simulation von neuen CFK-Prepreg Materialien für das Automated-Fiber-Placement. Bachelor's Thesis. 2020.

[S12] D. de Haes. Entwicklung eines analytischen Modells zur Vorhersage von Ablegedefekten im Automated-Fiber-Placement-Prozess. Master's Thesis. 2020.

[S13] J. Torresano Gómez. Mehrfaktorielle Untersuchung verschiedener Einflussvariablen auf die Klebrigkeit beim Automated Fiber Placement. Research Internship. 2021.

[S14] J. Neszvecsko. Grundlagenforschung zur Entwicklung neuer Luftfahrtmaterialien im Bereich elektrisches Fliegen. Research Internship. 2021.

Parts of the following theses contributed to the underlying doctoral thesis: [S1], [S3], [S6–S9], [S11–S14]. The specific contributions are also indicated within the text.

Bibliography

[1] United Nations Department of Economic and Social Affairs. Transforming our world: the 2030 Agenda for Sustainable Development, 09.06.2021. URL https://sdgs.un.org/2030agenda.

[2] United Nations Department of Economic and Social Affairs. *The Sustainable Development Goals Report 2020.* UNITED NATIONS, [S.l.], 2020. ISBN 978-92-1-101425-9.

[3] E. P. Penner, D. H. Lister, D. J. Griggs, D. J. Dokken, and M. McFarland. IPCC Special Report: Aviation and the Global Atmosphere: a special report of IPCC Working Groups I and III in collaboration with the Scientific Assessment Panel to the Montreal Protocol on Substances that Deplete the Ozone Layer, 10.06.2021. URL https://www.ipcc.ch/report/aviation-and-the-global-atmosphere-2/.

[4] A. J. Timmis, A. Hodzic, L. Koh, M. Bonner, C. Soutis, A. W. Schäfer, and L. Dray. Environmental impact assessment of aviation emission reduction through the implementation of composite materials. *The International Journal of Life Cycle Assessment*, 20(2):233–243, 2015. ISSN 0948-3349. doi: 10.1007/s11367-014-0824-0.

[5] M. Biron. *A practical guide to plastics sustainability: Concept, solutions, and implementation.* Plastics design library. William Andrew, Applied Science Publishers, Kidlington, Osford and Cambridge, MA, 2020. ISBN 978-0-12-821539-5.

[6] D. H.-J. A. Lukaszewicz, C. Ward, and K. Potter. The engineering aspects of automated prepreg layup: History, present and future. *Composites Part B: Engineering*, 43(3):997–1009, 2012. ISSN 13598368. doi: 10.1016/j.compositesb.2011.12.003.

[7] M. K. Hagnell and M. Åkermo. A composite cost model for the aeronautical industry: Methodology and case study. *Composites Part B: Engineering*, 79: 254–261, 2015. ISSN 13598368. doi: 10.1016/j.compositesb.2015.04.043.

[8] B. Ellis, editor. *Chemistry and Technology of Epoxy Resins*. Blackie Academic & Professional, London and New York, 1993. ISBN 978-94-010-5302-0. doi: 10.1007/978-94-011-2932-9.

[9] K. Heller, B. Böckl, C. Ebel, and K. Drechsler. Influence of Prepreg Aging and Tack on Lay-up Effects/Defects in Thermoset Automated Fiber Placement. In *ECCM 2018 - 18th European Conference on Composite Materials*. Applied Mechanics Laboratory, 2018. ISBN 978-151089693-2.

[10] S. Bard, M. Demleitner, M. Radtke, and V. Altstädt. Transverse Thermal Conductivity of Epoxy Carbon Fiber Prepreg Laminates with a Graphite Filled Matrix. *Journal of Composites Science*, 3(2):44, 2019. doi: 10.3390/jcs3020044.

[11] S. Bard, F. Schönl, M. Demleitner, and V. Altstädt. Copper and Nickel Coating of Carbon Fiber for Thermally and Electrically Conductive Fiber Reinforced Composites. *Polymers*, 11(5), 2019. doi: 10.3390/polym11050823.

[12] J. C. Halpin, J. L. Kardos, and M. P. Dudukovic. Processing science: an approach for prepreg composite systems. *Pure and Applied Chemistry*, 55(5): 893–906, 1983. ISSN 0033-4545. doi: 10.1351/pac198355050893.

[13] H. Lengsfeld, F. Wolff-Fabris, J. Krämer, J. Lacalle, and V. Altstädt. *Composite technology: Prepregs and monolithic part fabrication technologies*. Hanser Publishers and Hanser Publications, Munich and Cincinnati, 2016. ISBN 978-1-56990-599-9.

[14] T. Gutowski, editor. *Advanced composites manufacturing*. A Wiley inter-science publication. Wiley, New York, NY, 1997. ISBN 978-0471153016.

[15] J. C. Seferis, C. N. Velisaris, and V. M. Drakonakis. Prepreg Manufacturing. In L. Nicolais and S. M. Lee, editors, *Wiley encyclopedia of composites*. Wiley Interscience, Hoboken, NY, 2011. ISBN 9781118097298. doi: 10.1002/9781118097298.weoc196.

[16] S. T. Peters, editor. *Handbook of Composites*. Springer US, Boston, MA and s.l., second edition edition, 1998. ISBN 978-1-4615-6389-1. doi: 10.1007/978-1-4615-6389-1.

[17] C. Haller. Hexcel quote 50QU001016 for HexPly 8552/33%/268/IM7: E-mail message, 19.03.2019.

[18] D. H.-J. A. Lukaszewicz and K. Potter. The internal structure and conformation of prepreg with respect to reliable automated processing. *Composites Part A: Applied Science and Manufacturing*, 42(3):283–292, 2011. ISSN 1359835X. doi: 10.1016/j.compositesa.2010.11.014.

[19] Hexcel Corporation. HexPly 8552 Epoxy matrix: Product Data Sheet, 22.07.2021. URL https://www.hexcel.com/user_area/content_media/raw/HexPly_8552_eu_DataSheet.pdf.

[20] Hexcel Corporation. HexTow IM7 Carbon Fiber: Product Data Sheet, 22.07.2021. URL https://www.hexcel.com/user_area/content_media/raw/IM7_HexTow_DataSheet.pdf.

[21] B. Thorfinnson and T. F. Biermann. Degree of Impregnation of Prepregs - Effects on Porosity. In R. Carson and M. Burg, editors, *Advanced Materials Technology '87*, volume 32, pages 1500–1509. SAMPE, Covina, Calif., 1987. ISBN 0938994344.

[22] K. Potter. In-plane and out-of-plane deformation properties of unidirectional preimpregnated reinforcement. *Composites Part A: Applied Science and Manufacturing*, 33(11):1469–1477, 2002. ISSN 1359835X. doi: 10.1016/S1359-835X(02)00138-0.

[23] A. Beakou, M. Cano, J.-B. Le Cam, and V. Verney. Modelling slit tape buckling during automated prepreg manufacturing: A local approach. *Composite Structures*, 93(10):2628–2635, 2011. ISSN 02638223. doi: 10.1016/j.compstruct.2011.04.030.

[24] D. Budelmann, C. Schmidt, and D. Meiners. Prepreg tack: A review of mechanisms, measurement, and manufacturing implication. *Polymer Composites*, 41(9):3440–3458, 2020. ISSN 0272-8397. doi: 10.1002/pc.25642.

[25] T. Orth. A review of radiative heating in automated layup and its modelling. *Zeitschrift Kunststofftechnik*, 2:91–125, 2017. ISSN 18642217. doi: 10.3139/o999.01022017.

[26] Y. R. Larberg, M. Åkermo, and M. Norrby. On the in-plane deformability of cross-plied unidirectional prepreg. *Journal of Composite Materials*, 46(8):929–939, 2012. ISSN 0021-9983. doi: 10.1177/0021998311412988.

[27] W. Grellmann, S. Seidler, and V. Altstädt, editors. *Polymer testing*. Hanser, München, 2007. ISBN 978-1-56990-410-7.

[28] K. J. Ahn, J. C. Seferis, T. Pelton, and M. Wilhelm. Analysis and characterization of prepreg tack. *Polymer Composites*, 13(3):197–206, 1992. ISSN 0272-8397. doi: 10.1002/pc.750130308.

[29] R. M. Christensen. Effective viscous flow properties for fiber suspensions under concentrated conditions. *Journal of Rheology*, 37(1):103–121, 1993. ISSN 0148-6055. doi: 10.1122/1.550459.

[30] R. Banks, A. P. Mouritz, S. John, F. Coman, and R. Paton. Development of a new structural prepreg: characterisation of handling, drape and tack properties. *Composite Structures*, 66(1-4):169–174, 2004. ISSN 02638223. doi: 10.1016/j.compstruct.2004.04.034.

[31] M. Belhaj and M. Hojjati. Wrinkle formation during steering in automated fiber placement: Modeling and experimental verification. *Journal of Reinforced Plastics and Composites*, 37(6):396–409, 2018. ISSN 0731-6844. doi: 10.1177/0731684417752872.

[32] B. Prime. Thermosets. In E. Turi, editor, *Thermal Characterization of Polymeric Materials*, pages 435–569. Elsevier, 1981. ISBN 9780127037806. doi: 10.1016/B978-0-12-703780-6.50010-9.

[33] G. Wisanrakkit and J. K. Gillham. The glass transition temperature (Tg) as an index of chemical conversion for a high-Tg amine/epoxy system: Chemical and diffusion-controlled reaction kinetics. *Journal of Applied Polymer Science*, 41(1112):2885–2929, 1990. ISSN 00218995. doi: 10.1002/APP.1990.070411129.

[34] K. J. Ahn, L. Peterson, J. C. Seferis, D. Nowacki, and H. G. Zachmann. Prepreg aging in relation to tack. *Journal of Applied Polymer Science*, 45(3): 399–406, 1992. ISSN 00218995. doi: 10.1002/app.1992.070450304.

[35] A. Endruweit, G. Y. H. Choong, S. Ghose, B. A. Johnson, D. R. Younkin, N. A. Warrior, and D. S. A. de Focatiis. Characterisation of tack for unidirectional prepreg tape employing a continuous application-and-peel test method. *Composites Part A: Applied Science and Manufacturing*, 114:295–306, 2018. ISSN 1359835X. doi: 10.1016/j.compositesa.2018.08.027.

[36] D. Budelmann, H. Detampel, C. Schmidt, and D. Meiners. Interaction of process parameters and material properties with regard to prepreg tack in automated lay-up and draping processes. *Composites Part A: Applied Science*

and Manufacturing, 117:308–316, 2019. ISSN 1359835X. doi: 10.1016/j. compositesa.2018.12.001.

[37] A. W. Smith, A. Endruweit, G. Y. H. Choong, D. S. A. de Focatiis, and P. Hubert. Adaptation of material deposition parameters to account for out-time effects on prepreg tack. *Composites Part A: Applied Science and Manufacturing*, 133:105835, 2020. ISSN 1359835X. doi: 10.1016/j.compositesa. 2020.105835.

[38] E. B. Stark, A. M. Ibrahim, T. E. Munns, and J. C. Seferis. Moisture effects during cure of high-performance epoxy matrices. *Journal of Applied Polymer Science*, 30(4):1717–1731, 1985. ISSN 00218995. doi: 10.1002/app.1985. 070300436.

[39] N. Sharp, C. Li, A. Strachan, D. Adams, and R. B. Pipes. Effects of water on epoxy cure kinetics and glass transition temperature utilizing molecular dynamics simulations. *Journal of Polymer Science Part B: Polymer Physics*, 55(15):1150–1159, 2017. ISSN 08876266. doi: 10.1002/polb.24357.

[40] O. Dubois, J.-B. Le Cam, and A. Béakou. Experimental Analysis of Prepreg Tack. *Experimental Mechanics*, 50(5):599–606, 2010. ISSN 0014-4851. doi: 10.1007/s11340-009-9236-7.

[41] Aerospace Engineer. Temperature and humidity in prepreg lamination workshops: Telephone, 07/02/2020.

[42] D. A. Scola, J. Vontell, and M. Felsen. Effects of ambient aging of 5245C/-graphite prepreg on composition and mechanical properties of fabricated composites. *Polymer Composites*, 8(4):244–252, 1987. ISSN 0272-8397. doi: 10.1002/pc.750080406.

[43] K. C. Cole, D. Noël, J.-J. Hechler, A. Chouliotis, and K. C. Overbury. Room temperature aging of Narmco 5208 carbon-epoxy prepreg. Part I: Physico-chemical characterization. *Polymer Composites*, 10(3):150–161, 1989. ISSN 0272-8397. doi: 10.1002/pc.750100303.

[44] M. Frigione and J. M. Kenny. Thermokinetic effect of the aging of epoxy matrix prepregs for high performance composites. *Polymer Composites*, 23 (4):530–537, 2002. ISSN 0272-8397. doi: 10.1002/pc.10454.

[45] K. J. Ji, C. Y. Wei, W. H. Deng, Y. S. Zhang, Y. J. Liu, R. Z. Mao, and X. Wang. Evaluation of Glass Fibre/Epoxy Prepreg Quality during

Storage. *Polymers and Polymer Composites*, 10(8):599–606, 2002. doi: 10.1177/096739110201000803.

[46] R. W. Jones, Y. Ng, and J. F. McClelland. Monitoring ambient-temperature aging of a carbon-fiber/epoxy composite prepreg with photoacoustic spectroscopy. *Composites Part A: Applied Science and Manufacturing*, 39(6): 965–971, 2008. ISSN 1359835X. doi: 10.1016/j.compositesa.2008.03.015.

[47] S. G. Miller, T.-H. Hou, J. K. Sutter, D. A. Scheiman, R. E. Martin, M. Maryanski, M. Schlea, J. M. Gardner, and Z. R. Schiferl. Out-life characteristics of IM7/977-3 composites. In S. W. Beckwith, editor, *Advanced materials and processes*. SAMPE, Covina, Calif., 2010. ISBN 978-193455108-0.

[48] L. K. Grunenfelder and S. R. Nutt. Prepreg age monitoring via differential scanning calorimetry. *Journal of Reinforced Plastics and Composites*, 31(5): 295–302, 2012. ISSN 0731-6844. doi: 10.1177/0731684411431020.

[49] D. Blass, S. Kreling, and K. Dilger. The impact of prepreg aging on its processability and the postcure mechanical properties of epoxy-based carbon-fiber reinforced plastics. *Proceedings of the Institution of Mechanical Engineers, Part L: Journal of Materials: Design and Applications*, 231(1-2):62–72, 2017. ISSN 1464-4207. doi: 10.1177/1464420716665413.

[50] O. de Andrade Raponi, J. E. Baldo Junior, P. de Souza Leite, A. C. Ancelotti Junior, and A. Guimarães. Prepreg aging effects on its properties, curing process and final composite behavior characterized by dynamic mechanical analysis. *Journal of Reinforced Plastics and Composites*, 38(16):749–759, 2019. ISSN 0731-6844. doi: 10.1177/0731684419845474.

[51] O. de Andrade Raponi, L. C. M. Barbosa, J. E. Baldo Junior, Ancelotti Junior, A. C. A., and A. Guimarães. Effects of the exposition of an autoclave prepreg to the processing environment on its properties, curing cycle and final composite behavior. *The International Journal of Advanced Manufacturing Technology*, 106(11-12):5129–5136, 2020. ISSN 0268-3768. doi: 10.1007/s00170-020-05022-5.

[52] Y. Gu, M. Li, Z. Zhang, and Y. Li. Effects of resin storage aging on rheological property and consolidation of composite laminates. *Polymer Composites*, 30 (8):1081–1090, 2009. ISSN 0272-8397. doi: 10.1002/pc.20659.

[53] L. K. Grunenfelder and S. R. Nutt. Out-time effects on VBO (vacuum bag only) prepreg and laminate properties. *SAMPE Journal*, 47(5):6–13, 2011.

[54] D. Kim, T. Centea, and S. R. Nutt. In-situ cure monitoring of an out-of-autoclave prepreg: Effects of out-time on viscosity, gelation and vitrification. *Composites Science and Technology*, 102:132–138, 2014. ISSN 02663538. doi: 10.1016/j.compscitech.2014.07.027.

[55] Z. N. Sanjana, W. H. Schaefer, and J. R. Ray. Effect of aging and moisture on the reactivity of a graphite epoxy prepreg. *Polymer Engineering and Science*, 21(8):474–482, 1981. ISSN 0032-3888. doi: 10.1002/pen.760210807.

[56] L. K. Grunenfelder and S. R. Nutt. Void formation in composite prepregs – Effect of dissolved moisture. *Composites Science and Technology*, 70(16): 2304–2309, 2010. ISSN 02663538. doi: 10.1016/j.compscitech.2010.09.009.

[57] D. Kim, T. Centea, and S. R. Nutt. Modelling and monitoring of out-time and moisture absorption effects on cure kinetics and viscosity for an out-of-autoclave (OoA) prepreg. *Composites Science and Technology*, 138:201–208, 2017. ISSN 02663538. doi: 10.1016/j.compscitech.2016.11.023.

[58] S. Minakuchi, K. Nakamura, T. Mizutani, K. Kitamoto, S. Ogihara, and N. Takeda. Life-cycle evaluation of the moisture absorption and desorption behaviors of prepreg-based carbon fiber reinforced plastic. *Advanced Composite Materials*, 30(sup2):17–33, 2021. ISSN 0924-3046. doi: 10.1080/09243046. 2020.1794353.

[59] P. Hubert, A. Johnston, A. Poursartip, K. Nelson, and Saremi F.F. Repecka L. Cure kinetics and viscosity models for Hexcel 8552 epoxy resin. *International SAMPE Symposium and Exhibition (Proceedings)*, 46 II, 2001. ISSN 08910138.

[60] Y. Yu, H. Su, and W. Gan. Effects of Storage Aging on the Properties of Epoxy Prepregs. *Industrial & Engineering Chemistry Research*, 48(9):4340–4345, 2009. ISSN 0888-5885. doi: 10.1021/ie8018005.

[61] L. K. Grunenfelder, T. Centea, P. Hubert, and S. R. Nutt. Effect of room-temperature out-time on tow impregnation in an out-of-autoclave prepreg. *Composites Part A: Applied Science and Manufacturing*, 45:119–126, 2013. ISSN 1359835X. doi: 10.1016/j.compositesa.2012.10.001.

[62] D. Kim, T. Centea, and S. R. Nutt. Out-time effects on cure kinetics and viscosity for an out-of-autoclave (OOA) prepreg: Modelling and monitoring. *Composites Science and Technology*, 100:63–69, 2014. ISSN 02663538. doi: 10.1016/j.compscitech.2014.05.027.

[63] A. Kuliaei, I. Amiri Amraei, and S. R. Mousavi. Investigating the relationship between tack and degree of conversion in DGEBA-based epoxy resin cured with dicyandiamide and diuron. *Journal of Polymer Engineering*, 41(7):537–545, 2021. ISSN 0334-6447. doi: 10.1515/polyeng-2020-0340.

[64] K. C. Cole, D. Noël, J.-J. Hechler, P. Cielo, J.-C. Krapez, A. Chouliotis, and K. C. Overbury. Room-temperature aging of Narmco 5208 carbon-epoxy prepreg. Part II: Physical, mechanical, and nondestructive characterization. *Polymer Composites*, 12(3):203–212, 1991. ISSN 0272-8397. doi: 10.1002/pc.750120311.

[65] C. D. Nguyen and C. Krombholz. Influence of process parameters and material aging on the adhesion of prepreg in AFP processes. In *ECCM17 - 17th European Conference on Composite Materials*, 2016. ISBN 3000533877.

[66] B. Böckl, C. Jetten, K. Heller, C. Ebel, and K. Drechsler. Online Monitoring System for the Tack of Prepreg Slit Tapes Used in Automated Fiber Placement. In *ECCM 2018 - 18th European Conference on Composite Materials*. Applied Mechanics Laboratory, 2018. ISBN 978-151089693-2.

[67] J. McHugh and W. Stark. Determination and interpretation of changes in thermophysical properties of a carbon-fibre prepreg during cure. *Polymer Testing*, 49:115–120, 2016. ISSN 01429418. doi: 10.1016/j.polymertesting.2015.11.015.

[68] B.-Ch. Chern, T. J. Moon, J. R. Howell, and W. Tan. New Experimental Data for Enthalpy of Reaction and Temperature- and Degree-of-Cure-Dependent Specific Heat and Thermal Conductivity of the Hercules 3501-6 Epoxy System. *Journal of Composite Materials*, 36(17):2061–2072, 2002. ISSN 0021-9983. doi: 10.1177/0021998302036017238.

[69] B. Garnier and A. Sommier. Thermal Property Measurements During Curing of Thermoset Resins Using Steady Periodic Conditions. *Journal of Reinforced Plastics and Composites*, 21(13):1193–1203, 2002. ISSN 0731-6844. doi: 10.1177/073168402128987725.

[70] E. P. Scott and J. V. Beck. Estimation of Thermal Properties in Carbon/Epoxy Composite Materials during Curing. *Journal of Composite Materials*, 26(1):20–36, 1992. ISSN 0021-9983. doi: 10.1177/002199839202600102.

[71] H. H. Friis-Pedersen, J. H. Pedersen, L. Haussler, and B. K. Storm. On-line measurement of thermal diffusivity during cure of an epoxy composite. *Polymer Testing*, 25(8):1059–1068, 2006. ISSN 01429418. doi: 10.1016/j.polymertesting.2006.07.005.

[72] S. Sourour and M. R. Kamal. A new apparatus to measure the thermal conductivity and diffusivity of thermoplastic and thermosetting polymers. *Polymer Engineering and Science*, 16(7):480–489, 1976. ISSN 0032-3888. doi: 10.1002/pen.760160704.

[73] G. Struzziero, B. Remy, and A. A. Skordos. Measurement of thermal conductivity of epoxy resins during cure. *Journal of Applied Polymer Science*, 136(5):47015, 2019. ISSN 00218995. doi: 10.1002/app.47015.

[74] A. Margossian, S. Bel, and R. Hinterhoelzl. On the characterisation of transverse tensile properties of molten unidirectional thermoplastic composite tapes for thermoforming simulations. *Composites Part A: Applied Science and Manufacturing*, 88:48–58, 2016. ISSN 1359835X. doi: 10.1016/j.compositesa.2016.05.019.

[75] C. L. Tucker. Forming of Advanced Composites. In T. Gutowski, editor, *Advanced composites manufacturing*, A Wiley interscience publication, pages 297–372. Wiley, New York, NY, 1997. ISBN 978-0471153016.

[76] A. C. Long. *Composites forming technologies*, volume 61 of *Woodhead Publishing series in textiles*. Woodhead, Cambridge, 2007. ISBN 978-1-84569-253-7. URL http://www.sciencedirect.com/science/book/9781845690335.

[77] S. P. Haanappel and R. Akkerman. Shear characterisation of uni-directional fibre reinforced thermoplastic melts by means of torsion. *Composites Part A: Applied Science and Manufacturing*, 56:8–26, 2014. ISSN 1359835X. doi: 10.1016/j.compositesa.2013.09.007.

[78] Y. R. Larberg. *Forming of stacked unidirectional prepreg materials*. Dissertation, KTH Royal Institute of Technology, Stockholm, 2012. URL http://kth.diva-portal.org/smash/record.jsf?pid=diva2%3A573621&dswid=-878.

[79] K. Potter. Bias extension measurements on cross-plied unidirectional prepreg. *Composites Part A: Applied Science and Manufacturing*, 33(1):63–73, 2002. ISSN 1359835X. doi: 10.1016/S1359-835X(01)00057-4.

[80] P. Harrison, M. J. Clifford, and A. C. Long. Shear characterisation of viscous woven textile composites: a comparison between picture frame and bias extension experiments. *Composites Science and Technology*, 64(10-11):1453–1465, 2004. ISSN 02663538. doi: 10.1016/j.compscitech.2003.10.015.

[81] A. Margossian, P. Hörmann, K. Zemliana, L. Avila-Gray, S. Bel, and R. Hinterhoelzl. Shear characterisation of unidirectional thermoset pre-impregnated composites using a rheometre. In *Comptes Rendus des JNC 19 – Lyon*, 2015.

[82] D. M. Leutz. *Forming simulation of AFP material layups: Material characterization, simulation and validation.* Dissertation, Technische Universität München, München, 2016. URL http://nbn-resolving.de/urn/resolver.pl?urn:nbn:de:bvb:91-diss-20160701-1275863-1-7.

[83] A. Margossian. *Forming of tailored thermoplastic composite blanks: material characterisation, simulation and validation.* Dissertation, Universitätsbibliothek der TU München, München, 2017.

[84] Y. Wang, M. K. Chea, J. P.-H. Belnoue, J. Kratz, D. S. Ivanov, and S. R. Hallett. Experimental characterisation of the in-plane shear behaviour of UD thermoset prepregs under processing conditions. *Composites Part A: Applied Science and Manufacturing*, 133:105865, 2020. ISSN 1359835X. doi: 10.1016/j.compositesa.2020.105865.

[85] N. Ersoy, T. Garstka, K. Potter, M. R. Wisnom, D. Porter, M. Clegg, and G. Stringer. Development of the properties of a carbon fibre reinforced thermosetting composite through cure. *Composites Part A: Applied Science and Manufacturing*, 41(3):401–409, 2010. ISSN 1359835X. doi: 10.1016/j.compositesa.2009.11.007.

[86] C. Chen, A. Poursartip, and G. Fernlund. Influence of the glass transition of interlaminar particles on shear behaviour during cure of interlayer toughened thermoset composites. *Composites Part A: Applied Science and Manufacturing*, 147:106447, 2021. ISSN 1359835X. doi: 10.1016/j.compositesa.2021.106447.

[87] D. J. O'Brien, N. R. Sottos, and S. R. White. Cure-dependent Viscoelastic Poisson's Ratio of Epoxy. *Experimental Mechanics*, 47(2):237–249, 2007. ISSN 0014-4851. doi: 10.1007/s11340-006-9013-9.

[88] S. Saseendran, M. Wysocki, and J. Varna. Cure-state dependent viscoelastic Poisson's ratio of LY5052 epoxy resin. *Advanced Manufacturing: Polymer*

& Composites Science, 3(3):92–100, 2017. ISSN 2055-0340. doi: 10.1080/ 20550340.2017.1348002.

[89] J. Wang, A. C. Long, and M. J. Clifford. Experimental measurement and predictive modelling of bending behaviour for viscous unidirectional composite materials. *International Journal of Material Forming*, 3(S2):1253–1266, 2010. ISSN 1960-6206. doi: 10.1007/s12289-009-0670-y.

[90] L. D. Bloom, M. Elkington, C. Ward, A. Chatzimichali, and K. Potter. On prepreg properties and manufacturability. In International Committee on Composite Materials, editor, *ICCM19*, Montreal, 2013. International Committee on Composite Materials.

[91] H. Alshahrani and M. Hojjati. A new test method for the characterization of the bending behavior of textile prepregs. *Composites Part A: Applied Science and Manufacturing*, 97:128–140, 2017. ISSN 1359835X. doi: 10. 1016/j.compositesa.2017.02.027.

[92] A. V. Shenoy. *Rheology of Filled Polymer Systems*. Springer Netherlands, Dordrecht and s.l., 1999. ISBN 978-94-015-9213-0. doi: 10.1007/978-94-015-9213-0.

[93] S. Bard, G. Bakis, M. Radtke, and V. Altstädt. Thermal and Electrical Conductivity of Epoxy-Carbon Fiber Prepreg Laminates Filled with Different Sizes of Graphite Particles. In *ECCM 2018 - 18th European Conference on Composite Materials*. Applied Mechanics Laboratory, 2018. ISBN 978-151089693-2.

[94] N. A. Siddiqui, S. U. Khan, P. C. Ma, C. Y. Li, and J.-K. Kim. Manufacturing and characterization of carbon fibre/epoxy composite prepregs containing carbon nanotubes. *Composites Part A: Applied Science and Manufacturing*, 42(10):1412–1420, 2011. ISSN 1359835X. doi: 10.1016/j.compositesa.2011. 06.005.

[95] K. Tao, S. Yang, J. C. Grunlan, Y.-S. Kim, B. Dang, Y. Deng, R. L. Thomas, B. L. Wilson, and X. Wei. Effects of carbon nanotube fillers on the curing processes of epoxy resin-based composites. *Journal of Applied Polymer Science*, 102(6):5248–5254, 2006. ISSN 00218995. doi: 10.1002/app.24773.

[96] D. Puglia, L. Valentini, I. Armentano, and J. M. Kenny. Effects of single-walled carbon nanotube incorporation on the cure reaction of epoxy resin

and its detection by Raman spectroscopy. *Diamond and Related Materials*, 12(3-7):827–832, 2003. ISSN 09259635. doi: 10.1016/S0925-9635(02)00358-8.

[97] M. Mauro, M. R. Acocella, C. E. Corcione, A. Maffezzoli, and G. Guerra. Catalytic activity of graphite-based nanofillers on cure reaction of epoxy resins. *Polymer*, 55(22):5612–5615, 2014. ISSN 00323861. doi: 10.1016/j. polymer.2014.09.019.

[98] Z. Yang, K. McElrath, J. Bahr, and N. A. D'Souza. Effect of matrix glass transition on reinforcement efficiency of epoxy-matrix composites with single walled carbon nanotubes, multi-walled carbon nanotubes, carbon nanofibers and graphite. *Composites Part B: Engineering*, 43(4):2079–2086, 2012. ISSN 13598368. doi: 10.1016/j.compositesb.2012.01.049.

[99] S. S. Rahatekar, K. K. K. Koziol, S. A. Butler, J. A. Elliott, M. S. P. Shaffer, M. R. Mackley, and A. H. Windle. Optical microstructure and viscosity enhancement for an epoxy resin matrix containing multiwall carbon nanotubes. *Journal of Rheology*, 50(5):599–610, 2006. ISSN 0148-6055. doi: 10.1122/1.2221699.

[100] J. Xu, S. Chatterjee, K. W. Koelling, Y. Wang, and S. E. Bechtel. Shear and extensional rheology of carbon nanofiber suspensions. *Rheologica Acta*, 44(6):537–562, 2005. ISSN 0035-4511. doi: 10.1007/s00397-005-0436-5.

[101] K. H. Wang, M. H. Choi, C. M. Koo, M. Xu, I. J. Chung, M. C. Jang, S. W. Choi, and H. H. Song. Morphology and physical properties of polyethylene/-silicate nanocomposite prepared by melt intercalation. *Journal of Polymer Science Part B: Polymer Physics*, 40(14):1454–1463, 2002. ISSN 08876266. doi: 10.1002/polb.10201.

[102] Ş. Yazman, M. Uyaner, F. Karabörk, and A. Akdemir. Effects of nano reinforcing/matrix interaction on chemical, thermal and mechanical properties of epoxy nanocomposites. *Journal of Composite Materials*, page 002199832110370, 2021. ISSN 0021-9983. doi: 10.1177/00219983211037059.

[103] M. Abdalla, D. Dean, P. Robinson, and E. Nyairo. Cure behavior of epoxy/M-WCNT nanocomposites: The effect of nanotube surface modification. *Polymer*, 49(15):3310–3317, 2008. ISSN 00323861. doi: 10.1016/j.polymer.2008. 05.016.

[104] A. Allaoui. Mechanical and electrical properties of a MWNT/epoxy composite. *Composites Science and Technology*, 62(15):1993–1998, 2002. ISSN 02663538. doi: 10.1016/S0266-3538(02)00129-X.

[105] J. Bai. Evidence of the reinforcement role of chemical vapour deposition multi-walled carbon nanotubes in a polymer matrix. *Carbon*, 41(6):1325–1328, 2003. ISSN 00086223. doi: 10.1016/S0008-6223(03)00034-4.

[106] L. Liu and H. D. Wagner. Rubbery and glassy epoxy resins reinforced with carbon nanotubes. *Composites Science and Technology*, 65(11-12):1861–1868, 2005. ISSN 02663538. doi: 10.1016/j.compscitech.2005.04.002.

[107] Q. Guo, editor. *Thermosets: Structure, properties and applications*. Woodhead publishing in materials. Woodhead Publ, Oxford, 2012. ISBN 978-0-85709-763-7. URL http://www.loc.gov/catdir/enhancements/fy1403/2012911034-b.html.

[108] M. Xie, Z. Zhang, Y. Gu, M. Li, and Y. Su. A new method to characterize the cure state of epoxy prepreg by dynamic mechanical analysis. *Thermochimica Acta*, 487(1-2):8–17, 2009. ISSN 00406031. doi: 10.1016/j.tca.2009.01.001.

[109] D. J. Crabtree. Quantitative Analysis of Resin Matrix Aging by Gel Permeation Chromatography and Differential Scanning Calorimetry. In C. A. May, editor, *Resins for Aerospace*, volume 132 of *ACS Symposium Series*, pages 459–468. AMERICAN CHEMICAL SOCIETY, WASHINGTON, D. C., 1980. ISBN 9780841205673. doi: 10.1021/bk-1980-0132.ch033.

[110] R. J. Crossley, P. J. Schubel, and D. S. A. de Focatiis. Time–temperature equivalence in the tack and dynamic stiffness of polymer prepreg and its application to automated composites manufacturing. *Composites Part A: Applied Science and Manufacturing*, 52:126–133, 2013. ISSN 1359835X. doi: 10.1016/j.compositesa.2013.05.002.

[111] O. de Andrade Raponi, B. R. de Souza, J. E. Baldo Junior, A. C. Ancelotti Junior, and A. Guimarães. Dielectric analysis as a low-complexity methodology for tracking prepreg out-time and its effects on the curing cycle. *Journal of Composite Materials*, 53(28-30):4035–4042, 2019. ISSN 0021-9983. doi: 10.1177/0021998319853325.

[112] J. P. Pascault and R. J. J. Williams. Glass transition temperature versus conversion relationships for thermosetting polymers. *Journal of Polymer*

Science Part B: Polymer Physics, 28(1):85–95, 1990. ISSN 08876266. doi: 10.1002/polb.1990.090280107.

[113] DIN Deutsches Institut für Normung e. V. DIN EN ISO 11357-3:2018-07, Plastics - Differential scanning calorimetry (DSC) - Part 3: Determination of temperature and enthalpy of melting and crystallization (ISO 11357-3:2018); German version EN ISO 11357-3:2018, 2018.

[114] ASTM International. ASTM D3418-15 Test Method for Transition Temperatures and Enthalpies of Fusion and Crystallization of Polymers by Differential Scanning Calorimetry, 2015.

[115] DIN Deutsches Institut für Normung e. V. DIN EN ISO 11357-2:2020-08, Plastics - Differential scanning calorimetry (DSC) - Part 2: Determination of glass transition temperature and step height (ISO_11357-2:2020); German version EN ISO 11357-2:2020, 2020.

[116] ASTM International. ASTM E1356-08(2014) Test Method for Assignment of the Glass Transition Temperatures by Differential Scanning Calorimetry, 2014.

[117] ASTM International. ASTM E2602-09(2015) Test Method for the Assignment of the Glass Transition Temperature by Modulated Temperature Differential Scanning Calorimetry, 2015.

[118] A. T. DiBenedetto. Prediction of the glass transition temperature of polymers: A model based on the principle of corresponding states. *Journal of Polymer Science Part B: Polymer Physics*, 25(9):1949–1969, 1987. ISSN 08876266. doi: 10.1002/polb.1987.090250914.

[119] K. Fischer. Neues Verfahren zur maßanalytischen Bestimmung des Wassergehaltes von Flüssigkeiten und festen Körpern. *Angewandte Chemie*, 48(26): 394–396, 1935. ISSN 00448249. doi: 10.1002/ange.19350482605.

[120] DIN Deutsches Institut für Normung e. V. DIN EN ISO 3219-2:2021-08, Rheology - Part 2: General principles of rotational and oscillatory rheometry (ISO 3219-2:2021); German version EN ISO 3219-2:2021, 2021.

[121] A. M. Gillanders, S. Kerr, and T. J. Martin. Determination of prepreg tack. *International Journal of Adhesion and Adhesives*, 1(3):125–134, 1981. ISSN 01437496. doi: 10.1016/0143-7496(81)90035-X.

[122] J. W. Putnam, J. C. Seferis, T. Pelton, and M. Wilhelm. Perceptions of Prepreg Tack for Manufacturability in Relation to Experimental Measures. *Science and Engineering of Composite Materials*, 4(3), 1995. ISSN 2191-0359. doi: 10.1515/SECM.1995.4.3.143.

[123] B. S. Hayes, J. C. Seferis, and J. S. Chen. Development and hot-melt impregnation of a model controlled flow prepreg system. *Polymer Composites*, 17(5):730–742, 1996. ISSN 0272-8397. doi: 10.1002/pc.10665.

[124] F.U Buehler and J.C Seferis. Effect of reinforcement and solvent content on moisture absorption in epoxy composite materials. *Composites Part A: Applied Science and Manufacturing*, 31(7):741–748, 2000. ISSN 1359835X. doi: 10.1016/S1359-835X(00)00036-1.

[125] C. Wohl, F. L. Palmieri, A. Forghani, C. Hickmott, H. Bedayat, B. Coxon, A. Poursartip, and B. Grimsley. Tack measurements of prepreg tape at variable temperature and humidity. In *Composites and Advanced Materials Expo (CAMX 2017)*, September, 2017.

[126] A. Forghani, C. Hickmott, V. Hutten, H. Bedayat, C. Wohl, B. Grimsley, B. Coxon, and A. Poursartip. Experimental calibration of a numerical model of prepreg tack for predicting afp process related defects. In S. W. Beckwith, editor, *SAMPE Conference & Exhibition*. Society for the Advancement of Material and Process Engineering, Diamond Bar, CA, 2018. ISBN 978-193455127-1.

[127] E. J. Smith, C. Grubb, J. Misasi, and N. Larson. Developing a procedure for prepreg tack characterization. In *CAMX 2019 - Composites and Advanced Materials Expo*. The Composites and Advanced Materials Expo (CAMX), 2019.

[128] S. Rao, R. Umer, J. Thomas, and W. J. Cantwell. Investigation of peel resistance during the fibre placement process. *Journal of Reinforced Plastics and Composites*, 35(4):275–286, 2015. ISSN 0731-6844. doi: 10.1177/0731684415613634.

[129] M. Belhaj, A. Dodangeh, and M. Hojjati. Experimental investigation of prepreg tackiness in automated fiber placement. *Composite Structures*, 262: 113602, 2021. ISSN 02638223. doi: 10.1016/j.compstruct.2021.113602.

[130] R. J. Crossley, P. J. Schubel, and N. A. Warrior. The experimental determination of prepreg tack and dynamic stiffness. *Composites Part A: Applied Science and Manufacturing*, 43(3):423–434, 2012. ISSN 1359835X. doi: 10.1016/j.compositesa.2011.10.014.

[131] G. Y. H. Choong, A. Endruweit, and D. S. A. de Focatiis. Analysis of contact area in a continuous application-and-peel test method for prepreg tack. *International Journal of Adhesion and Adhesives*, 107:102849, 2021. ISSN 01437496. doi: 10.1016/j.ijadhadh.2021.102849.

[132] C. D. Nguyen and D. Delisle. First Ply Tack of an AFP Process – Influence of Heatabale Mould Surface, Release Films and Process Parameters. In *SAMPE Europe Conference & Exhibition 2017 Stuttgart*, Red Hook, NY, 2018. Curran Associates Inc. ISBN 978-1-5108-6128-2.

[133] S. Rajan, M. A. Sutton, W. McMakin, E. Compton, A. Kidane, Z. Gurdal, R. Wehbe, and Y. Farzana. Characterization of Mode I and Mode II traction–separation laws for cohesive separation of uncured thermoset tows. *International Journal of Fracture*, 221(1):25–38, 2020. ISSN 0376-9429. doi: 10.1007/s10704-019-00399-1.

[134] ASTM International. ASTM D2979-16 Test Method for Pressure-Sensitive Tack of Adhesives Using an Inverted Probe Machine, 2016.

[135] V. Hutten, A. Forghani, P. Silva, C. Hickmott, T. Sreekantamurthy, C. Wohl, B. Grimsley, B. Coxon, and A. Poursartip. A Validation Study of a Physics-based Tack Model for an Automated Fiber Placement Process Simulation. In *SAMPE 2019 - Charlotte, NC*. SAMPE, 2019. doi: 10.33599/nasampe/s.19. 1512.

[136] ASTM International. ASTM D6862-11(2021) Test Method for 90 Degree Peel Resistance of Adhesives, 2021.

[137] ASTM International. ASTM D3167-10(2017) Test Method for Floating Roller Peel Resistance of Adhesives, 2017.

[138] DIN Deutsches Institut für Normung e. V. DIN EN ISO 11339:2010-06, Adhesives - T-peel test for flexible-to-flexible bonded assemblies (ISO 11339:2010); German version EN ISO 11339:2010, 2010.

[139] T. Centea and P. Hubert. Measuring the impregnation of an out-of-autoclave prepreg by micro-CT. *Composites Science and Technology*, 71(5):593–599, 2011. ISSN 02663538. doi: 10.1016/j.compscitech.2010.12.009.

[140] J. Sun, M. Li, Y. Gu, D. Zhang, Y. Li, and Z. Zhang. Interply friction of carbon fiber/epoxy prepreg stacks under different processing conditions. *Journal of Composite Materials*, 48(5):515–526, 2014. ISSN 0021-9983. doi: 10.1177/0021998313476320.

[141] ASTM International. ASTM E1269-11(2018) Test Method for Determining Specific Heat Capacity by Differential Scanning Calorimetry, 2018.

[142] DIN Deutsches Institut für Normung e. V. DIN EN ISO 11357-4:2021-05, Plastics - Differential scanning calorimetry (DSC) - Part 4: Determination of specific heat capacity (ISO 11357-4:2021); German version EN ISO 11357-4:2021, 2021.

[143] ASTM International. ASTM C177-04 Test Method for Steady-State Heat Flux Measurements and Thermal Transmission Properties by Means of the Guarded-Hot-Plate Apparatus, 2004.

[144] J.-L. Bailleul, D. Delaunay, Y. Jarny, and T. Jurkowski. Thermal Conductivity of Unidirectional Reinforced Composite Materials—Experimental Measurement as a Function of State of Cure. *Journal of Reinforced Plastics and Composites*, 20(1):52–64, 2001. ISSN 0731-6844. doi: 10.1106/UE8K-1RVA-WE2B-8V9D.

[145] ASTM International. ASTM E1461-13 Test Method for Thermal Diffusivity by the Flash Method, 2013.

[146] ASTM International. ASTM D5930-09 Test Method for Thermal Conductivity of Plastics by Means of a Transient Line-Source Technique, 2009.

[147] ASTM International. ASTM D3039 / D3039M-17 Test Method for Tensile Properties of Polymer Matrix Composite Materials, 2017.

[148] R. M. Jones. *Mechanics of composite materials.* Taylor & Francis, New York, 2. ed. edition, 1999. ISBN 1-56032-712-X. URL http://www.loc.gov/catdir/enhancements/fy0647/98018290-d.html.

[149] P. Hörmann. *Thermoset automated fibre placement – on steering effects and their prediction.* Dissertation, Technische Universität München, München, 21.12.2015.

[150] S. M. Spivak and L. R. G. Treloar. The Behavior of Fabrics in Shear. *Textile Research Journal*, 38(9):963–971, 1968. ISSN 0040-5175. doi: 10.1177/004051756803800911.

[151] J. Skelton. Fundamentals of Fabric Shear. *Textile Research Journal*, 46(12): 862–869, 1976. ISSN 0040-5175. doi: 10.1177/004051757604601202.

[152] K. Potter. The influence of accurate stretch data for reinforcements on the production of complex structural mouldings. *Composites*, 10(3):161–167, 1979. ISSN 00104361. doi: 10.1016/0010-4361(79)90291-X.

[153] N. W. Tschoegl, W. G. Knauss, and I. Emri. Poisson's Ratio in Linear Viscoelasticity – A Critical Review. *Mechanics of Time-Dependent Materials*, 6(1):3–51, 2002. ISSN 13852000. doi: 10.1023/A:1014411503170.

[154] O. I. Okoli and G. F. Smith. The effect of strain rate and fibre content on the Poisson's ratio of glass/epoxy composites. *Composite Structures*, 48(1-3): 157–161, 2000. ISSN 02638223. doi: 10.1016/S0263-8223(99)00089-6.

[155] S. Pandini and A. Pegoretti. Time, temperature, and strain effects on viscoelastic Poisson's ratio of epoxy resins. *Polymer Engineering and Science*, 48(7):1434–1441, 2008. ISSN 0032-3888. doi: 10.1002/pen.21060.

[156] S. Erland, T. J. Dodwell, and R. Butler. Characterisation of bending mechanics in uncured laminated materials using a modified Dynamic Mechanical Analysis, 13.09.2021. URL https://arxiv.org/pdf/1709.07940.

[157] S. Rajan, M. A. Sutton, R. Wehbe, Z. Gurdal, A. Kidane, and I. Emri. Characterization of viscoelastic bending stiffness of uncured carbon-epoxy prepreg slit tape. *Composite Structures*, 275:114295, 2021. ISSN 02638223. doi: 10.1016/j.compstruct.2021.114295.

[158] ASTM International. ASTM D1388-18 Test Method for Stiffness of Fabrics, 2018.

[159] D. G. Fertis. *Nonlinear Structural Engineering: With Unique Theories and Methods to Solve Effectively Complex Nonlinear Problems.* Springer-Verlag Berlin Heidelberg, Berlin, Heidelberg, 2006. ISBN 978-3-540-32976-3. doi: 10.1007/978-3-540-32976-3.

[160] B. Liang, N. Hamila, M. Peillon, and P. Boisse. Analysis of thermoplastic prepreg bending stiffness during manufacturing and of its influence on wrinkling simulations. *Composites Part A: Applied Science and Manufacturing*, 67: 111–122, 2014. ISSN 1359835X. doi: 10.1016/j.compositesa.2014.08.020.

[161] U. Sachs. *Friction and bending in thermoplastic composites forming processes.* Dissertation, University of Twente, Enschede, The Netherlands, 2014.

[162] S. Ropers, M. Kardos, and T. A. Osswald. A thermo-viscoelastic approach for the characterization and modeling of the bending behavior of thermoplastic composites. *Composites Part A: Applied Science and Manufacturing*, 90: 22–32, 2016. ISSN 1359835X. doi: 10.1016/j.compositesa.2016.06.016.

[163] A. Margossian, S. Bel, and R. Hinterhoelzl. Bending characterisation of a molten unidirectional carbon fibre reinforced thermoplastic composite using a Dynamic Mechanical Analysis system. *Composites Part A: Applied Science and Manufacturing*, 77:154–163, 2015. ISSN 1359835X. doi: 10.1016/j.compositesa.2015.06.015.

[164] F. T. Peirce. 26—THE "HANDLE" OF CLOTH AS A MEASURABLE QUANTITY. *Journal of the Textile Institute Transactions*, 21(9):T377–T416, 1930. ISSN 1944-7027. doi: 10.1080/19447023008661529.

[165] E. de Bilbao, D. Soulat, G. Hivet, and A. Gasser. Experimental Study of Bending Behaviour of Reinforcements. *Experimental Mechanics*, 50(3):333–351, 2010. ISSN 0014-4851. doi: 10.1007/s11340-009-9234-9.

[166] S. V. Lomov, I. Verpoest, M. Barburski, and J. Laperre. Carbon composites based on multiaxial multiply stitched preforms. Part 2. KES-F characterisation of the deformability of the preforms at low loads. *Composites Part A: Applied Science and Manufacturing*, 34(4):359–370, 2003. ISSN 1359835X. doi: 10.1016/S1359-835X(03)00025-3.

[167] D. Soteropoulos, K. Fetfatsidis, J. A. Sherwood, and J. Langworthy. Digital Method of Analyzing the Bending Stiffness of Non-Crimp Fabrics. In *AIP Conference Proceedings*, AIP Conference Proceedings, pages 913–917. AIP, 2011. doi: 10.1063/1.3589632.

[168] S. Kawabata. *The Standardization and Analysis of Hand Evaluation.* Hand Evaluation Standardization Committee, Japan, 2nd edition, 1980.

[169] A. Brasington, C. Sacco, J. Halbritter, R. Wehbe, and R. Harik. Automated fiber placement: A review of history, current technologies, and future paths forward. *Composites Part C: Open Access*, 6:100182, 2021. ISSN 26666820. doi: 10.1016/j.jcomc.2021.100182.

[170] T. Orth, M. Krahl, P. Parlevliet, and N. Modler. Optical thermal model for LED heating in thermoset-automated fiber placement. *Advanced Manufacturing: Polymer & Composites Science*, 4(3):73–82, 2018. ISSN 2055-0340. doi: 10.1080/20550340.2018.1507798.

[171] J. Cheng, D. Zhao, K. Liu, Y. Wang, and H. Chen. Modeling and impact analysis on contact characteristic of the compaction roller for composite automated placement. *Journal of Reinforced Plastics and Composites*, 37 (23):1418–1432, 2018. ISSN 0731-6844. doi: 10.1177/0731684418798151.

[172] N. Bakhshi and M. Hojjati. Effect of compaction roller on layup quality and defects formation in automated fiber placement. *Journal of Reinforced Plastics and Composites*, 39(1-2):3–20, 2020. ISSN 0731-6844. doi: 10.1177/0731684419868845.

[173] Q. Chu, Y. Li, J. Xiao, D. Huan, and X. Zhang. Placeability restricted by in-complete contact between laying roller and mould in an automated fiber placement process. *Journal of Reinforced Plastics and Composites*, 37(7): 475–489, 2018. ISSN 0731-6844. doi: 10.1177/0731684417752871.

[174] G. Rousseau, R. Wehbe, J. Halbritter, and R. Harik. Automated Fiber Placement Path Planning: A state-of-the-art review. *Computer-Aided Design and Applications*, 16(2):172–203, 2018. doi: 10.14733/cadaps.2019.172-203.

[175] F. Heinecke and C. Willberg. Manufacturing-Induced Imperfections in Composite Parts Manufactured via Automated Fiber Placement. *Journal of Composites Science*, 3(2):56, 2019. doi: 10.3390/jcs3020056.

[176] J. Chen, T. Chen-Keat, M. Hojjati, A. J. Vallee, M.-A. Octeau, and A. Yousefpour. Impact of layup rate on the quality of fiber steering/cut-restart in automated fiber placement processes. *Science and Engineering of Composite Materials*, 22(2):165–173, 2015. ISSN 2191-0359. doi: 10.1515/secm-2013-0257.

[177] M. Y. Matveev, P. J. Schubel, A. C. Long, and I. A. Jones. Understanding the buckling behaviour of steered tows in Automated Dry Fibre Placement (ADFP). *Composites Part A: Applied Science and Manufacturing*, 90:451–456, 2016. ISSN 1359835X. doi: 10.1016/j.compositesa.2016.08.014.

[178] R. P. Smith, Z. Qureshi, R. J. Scaife, and H. M. El-Dessouky. Limitations of processing carbon fibre reinforced plastic/polymer material using automated fibre placement technology. *Journal of Reinforced Plastics and Composites*, 35(21):1527–1542, 2016. ISSN 0731-6844. doi: 10.1177/0731684416659544.

[179] C. Zhao, J. Xiao, W. Huang, X. Huang, and S. Gu. Layup quality evaluation of fiber trajectory based on prepreg tow deformability for automated fiber placement. *Journal of Reinforced Plastics and Composites*, 35(21):1576–1585, 2016. ISSN 0731-6844. doi: 10.1177/0731684416659933.

[180] N. Bakhshi and M. Hojjati. An experimental and simulative study on the defects appeared during tow steering in automated fiber placement. *Composites Part A: Applied Science and Manufacturing*, 113:122–131, 2018. ISSN 1359835X. doi: 10.1016/j.compositesa.2018.07.031.

[181] N. Bakhshi and M. Hojjati. Time-dependent wrinkle formation during tow steering in automated fiber placement. *Composites Part B: Engineering*, 165: 586–593, 2019. ISSN 13598368. doi: 10.1016/j.compositesb.2019.02.034.

[182] S. Rajan, M. A. Sutton, R. Wehbe, B. Tatting, Z. Gürdal, A. Kidane, and R. Harik. Experimental investigation of prepreg slit tape wrinkling during automated fiber placement process using StereoDIC. *Composites Part B: Engineering*, 160:546–557, 2019. ISSN 13598368. doi: 10.1016/j.compositesb. 2018.12.017.

[183] R. Wehbe, B. Tatting, S. Rajan, R. Harik, M. Sutton, and Z. Gürdal. Geometrical modeling of tow wrinkles in automated fiber placement. *Composite Structures*, 246:112394, 2020. ISSN 02638223. doi: 10.1016/j.compstruct. 2020.112394.

[184] R. Wehbe, C. Sacco, A. Baz Radwan, M. Albazzan, and R. Harik. Influence of process parameters in AFP fiber steering on cylinders: Constant curvature paths. *Composites Part C: Open Access*, 2:100036, 2020. ISSN 26666820. doi: 10.1016/j.jcomc.2020.100036.

[185] W. Qu, J. Gao, Y. Di, R. He, Q. Yang, L. Cheng, and Y. Ke. Automated fiber placement path generation method based on prospective analysis of path performance under multiple constraints. *Composite Structures*, 255:112940, 2021. ISSN 02638223. doi: 10.1016/j.compstruct.2020.112940.

[186] R. Lichtinger, J. Lacalle, R. Hinterhölzl, U. Beier, and K. Drechsler. Simulation and experimental validation of gaps and bridging in the automated fiber placement process. *Science and Engineering of Composite Materials*, 22(2), 2015. ISSN 2191-0359. doi: 10.1515/secm-2013-0158.

[187] E. Oromiehie, B. G. Prusty, P. Compston, and G. Rajan. Automated fibre placement based composite structures: Review on the defects, impacts and inspections techniques. *Composite Structures*, 224:110987, 2019. ISSN 02638223. doi: 10.1016/j.compstruct.2019.110987.

[188] S. Sun, Z. Han, H. Fu, H. Jin, J. S. Dhupia, and Y. Wang. Defect Characteristics and Online Detection Techniques During Manufacturing of FRPs

Using Automated Fiber Placement: A Review. *Polymers*, 12(6), 2020. doi: 10.3390/polym12061337.

[189] W. Ritz. Über eine neue Methode zur Lösung gewisser Variationsprobleme der mathematischen Physik. *Journal für die reine und angewandte Mathematik (Crelles Journal)*, 1909(135):1–61, 1909. ISSN 0075-4102. doi: 10.1515/crll.1909.135.1.

[190] A. E. H. Love. XVI. The small free vibrations and deformation of a thin elastic shell. *Philosophical Transactions of the Royal Society of London. (A.)*, 179: 491–546, 1888. ISSN 0264-3820. doi: 10.1098/rsta.1888.0016.

[191] S. P. Timoshenko and J. M. Gere. *Theory of elastic stability.* Engineering societies monographs. McGraw-Hill, Auckland, 2. ed., [nachdr.], internat. student ed. edition, 2000. ISBN 0070858217.

[192] I. E. Avramidis and K. Morfidis. Bending of beams on three-parameter elastic foundation. *International Journal of Solids and Structures*, 43(2):357–375, 2006. ISSN 00207683. doi: 10.1016/j.ijsolstr.2005.03.033.

[193] S. Rajan, M. A. Sutton, S. Sockalingam, W. McMakin, Z. Gurdal, and A. Kidane. Simulations and experiments for automated fiber placement of prepreg slit tape: Wrinkle formation and fundamental observations. *Composites Part B: Engineering*, 201:108287, 2020. ISSN 13598368. doi: 10.1016/j.compositesb.2020.108287.

[194] H. R. Hertz. Ueber die Berührung fester elastischer Körper. *Journal für die reine und angewandte Mathematik (Crelles Journal)*, 1882(92):156–171, 1882. ISSN 0075-4102. doi: 10.1515/crll.1882.92.156.

[195] J. Jiang, Y. He, and Y. Ke. Pressure distribution for automated fiber placement and design optimization of compaction rollers. *Journal of Reinforced Plastics and Composites*, 38(18):860–870, 2019. ISSN 0731-6844. doi: 10.1177/0731684419850896.

[196] J. Jiang, Y. He, H. Wang, and Y. Ke. Modeling and experimental validation of compaction pressure distribution for automated fiber placement. *Composite Structures*, 256:113101, 2021. ISSN 02638223. doi: 10.1016/j.compstruct.2020.113101.

[197] W. Qu, R. He, L. Cheng, Y. Di, J. Gao, H. Wang, Q. Yang, and Y. Ke. Placement suitability analysis of automated fiber placement on curved surfaces

considering the influence of prepreg tow, roller and AFP machine. *Composite Structures*, 262:113608, 2021. ISSN 02638223. doi: 10.1016/j.compstruct. 2021.113608.

[198] T. J. Dodwell, R. Butler, and G. W. Hunt. Out-of-plane ply wrinkling defects during consolidation over an external radius. *Composites Science and Technology*, 105:151–159, 2014. ISSN 02663538. doi: 10.1016/j.compscitech. 2014.10.007.

[199] Teijin Carbon Europe GmbH. Tenax Filament Yarn - Product Data Sheet, 23.09.2021. URL https://www.teijincarbon.com/fileadmin/PDF/Datenbl% C3%A4tter_en/Product_Data_Sheet_TSG01en___EU_Filament_.pdf.

[200] Hexion Inc. EPIKOTE Resin 496 - Technical Data Sheet, 24.09.2021. URL https://www.hexion.com/CustomServices/PDFDownloader.aspx?type= tds&pid=d548dd3b-5814-6fe3-ae8a-ff0300fcd525.

[201] Imerys Graphite & Carbon Switzerland Ltd. Specialty Carbons for Thermally Conductive Polymers, 24.09.2021. URL https://www.imerys-graphite-and- carbon.com/?dl_name=TB_Thermal_Conductivity_Brochure_web_ 2021_09.pdf.

[202] Tekscan, Inc. Pressure Mapping Sensor 5101, 10.10.2021. URL https://www. tekscan.com/products-solutions/pressure-mapping-sensors/5101.

[203] TA Instruments. Accessories, Parts, & Consumables: Effective January 2021, 28.09.2021. URL https://www.tainstruments.com/wp-content/ uploads/Parts-and-Accessories-Guide.pdf.

[204] D. van Ee and A. Poursartip. HexPly 8552 Material Properties Database for use with COMPRO CCA and Raven: Created for NCAMP National Center for Advanced Materials Performance, 28.09.2021. URL https://www.wichita.edu/industry_and_defense/NIAR/ Research/hexcel-8552/Additional-Documents-2.pdf.

[205] R. Rousseau, L. Egghe, and R. Guns. Statistics. In R. Rousseau, L. Egghe, and R. Guns, editors, *Becoming Metric-Wise*, pages 67–97. Chandos Publishing is an imprint of Elsevier, Cambridge, MA, 2018. ISBN 9780081024751. doi: 10.1016/B978-0-08-102474-4.00004-2.

[206] D. Stelzl, R. M. Carsi, M. Hollerith, J. Roth, J. Lacalle, and K. Drechsler. A Peel Tack Test Bench for Automated Fibre Placement Processes. In KU Leuven, editor, *COMPOSITES WEEK @ LEUVEN*. KU Leuven, 2013.

[207] R. Lichtinger. *Thermo-mechanical coupled simulation of the Thermoset automated fibre placement process*. Dissertation, Technische Universität München, München, 2015.

[208] DIN Deutsches Institut für Normung e. V. DIN EN ISO 29862:2019-09, Self adhesive tapes - Determination of peel adhesion properties (ISO 29862:2018); German version EN ISO 29862:2019, 2019.

[209] M. T. Saad, S. G. Miller, and T. Marunda. Thermal Characterization of IM7/8552-1 Carbon-Epoxy Composites. In *Proceedings of the ASME International Mechanical Engineering Congress and Exposition – 2014*, page V08BT10A091, New York, N.Y., 2015. ASME. ISBN 978-0-7918-4956-9. doi: 10.1115/IMECE2014-40030.

[210] NETZSCH-Gerätebau GmbH. Laser Flash Apparatus LFA 457 MicroFlash, 12.11.2021. URL https://www.netzsch-thermal-analysis.com/media/thermal-analysis/brochures/LFA_457_MicroFlash_en_web_01.pdf.

[211] Y. Wang, J. P.-H. Belnoue, D. S. Ivanov, and S. R. Hallett. Hypo-viscoelastic modelling of in-plane shear in UD thermoset prepregs. *Composites Part A: Applied Science and Manufacturing*, 146:106400, 2021. ISSN 1359835X. doi: 10.1016/j.compositesa.2021.106400.

[212] J. Krollmann, D. Colin, L. Avila Gray, and K. Drechsler. Bending characterization of axis and off-axis fiber-reinforced hinges at large deflection. In Society for the Advancement of Material and Process Engineering, editor, *SAMPE Long Beach 2016 Conference and Exhibition*, Covina, 2016. Soc For Adv Of Materials. ISBN 9781934551233.

[213] M. Leyendecker. *Numerische Simulation des thermochemischen und mechanischen Verhaltens von Prepregs während des "Automated-Fiber-Placement"-Prozesses mit Matlab auf Basis der Finite-Differenzen-Methode*. Term project, Technische Universität München, München, 18.06.2013.

[214] Toho Tenax Europe GmbH. Delivery programme and characteristics for Tenax HTS filament yarn, 17.12.2021. URL https://www.havel-composites.com/uploads/files/products/14/e5aa6cb10c0311278834d407273bf1b427421284.pdf.

[215] W. H. Francis. *Mechanics of post-microbuckled compliant-matrix composites*. Master's thesis, University of Colorado, Boulder, 2008.

[216] The MathWorks, Inc. makima: Modified Akima piecewise cubic Hermite interpolation, 03.02.2022. URL https://de.mathworks.com/help/matlab/ref/makima.html#mw_e8ee1c8c-2cc3-46c4-90c4-c3208804ff4e.

[217] K. Kozaczuk. Engine nacelles design – Problems and challenges. *Proceedings of the Institution of Mechanical Engineers, Part G: Journal of Aerospace Engineering*, 231(12):2259–2265, 2017. ISSN 0954-4100. doi: 10.1177/0954410017706993.

[218] Safran S.A. New UK clean room facility contributes to Aircelle's nacelle production ramp-up, 07.02.2022. URL https://www.safran-group.com/news/new-uk-clean-room-facility-contributes-aircelles-nacelle-production-ramp-2016-02-05.

[219] Coriolis Composites SAS. Extrait Video Safran Nacelles, 06.02.2022. URL https://www.coriolis-composites.com/wp-content/uploads/2019/10/Extrait_Video_Safran_Nacelles.png.